2021

Electrochemical Reduction of Carbon Dioxide to Formate

Jinshuo Zou

Electrochemical Reduction of Carbon Dioxide to Formate

Jinshuo Zou

PhD Candidate, University of Wollongong

Submitted in fulfillment of the requirements for the award

of the degree of Doctor of Philosophy

Conducted at the University of Wollongong- Intelligent Polymer Research Institute,

ARC Centre of Excellence for Electromaterials Science, Wollongong, NSW, Australia.

September 2021

Certifications

I, Jinshuo Zou, declare that this thesis, submitted in fulfilment of the requirements for the award of Doctor of Philosophy, at the Australian Institute for Innovative Materials, University of Wollongong, is original work carried out by myself. This document is submitted as a thesis by compilation, containing four published articles and a manuscript in preparation as the main body. The document has not been submitted for qualifications at any other academic institution.

Jinshuo Zou

September 2021

Acknowledgements

I would like to express my deep gratitude to my principal supervisor, Dr. Chong-Yong Lee for his academic guidance, continuous support and valuable advices during my PhD study at the University of Wollongong. His profound knowledge and valuable experience in electrochemistry broadened my academic horizon. He also spent large amount of time and efforts on teaching me scientific paper writing skills which will remain with me as an invaluable part of my research career.

I am highly grateful to my co-supervisor, Prof. Gordon G. Wallace for the opportunity to perform my PhD study at IPRI and his helpful supervision. His acute scientific insight and feedback in my research not only helped solve the problems I encountered, but also prompted me to think deeper in my project. His guidance and strong support also encouraged me to face the challenges and carry out impactful researches.

I deeply appreciate the Matching Scholarship & International Postgraduate tuition award to support my study at UOW. I also thank ARC Centre of Excellence for Electromaterials Science (ACES) for the support of my research and the opportunities of attending highly quality seminars, workshops, and conferences, in which I can learn a lot in my research area.

I am also thankful to my collaborators, Prof. Douglas R. Macfarlane at Monash University, Prof. Yusuke Yamauchi at the University of Queensland, Dr. Caiyun Wang at IPRI, for their contributions to research ideas and manuscript revising. I wish to thank Prof. Jun Chen, Dr. Klaudia Wagner, Dr. Andrew Nattestad, Dr. Xiao Liu, Dr. Andres Ruland Palaia at IPRI for their

help with my experiments. I also wish to thank my friends in IPRI, Amuruthalakshimi Vijayakumar, Chunyan Qin, Dandan Cui, Dan Yang, Habib Dalal, Zhiqi Chen, Lisha Jia, Shuai Zhang, Yong Zhao, Yuetong Zhou, Yunfeng Chao and Yuqing Liu, for their kind help in both my research work and life.

Additionally, I would like to thank Phil Smugreski, Toni Campbell, Tracey Hanley, Naomi Davies, Joanne George, Candace Gabelish, and Narelle Badger for their supports during my PhD study. Moreover, I wish to acknowledge the Electron Microscopy Centre (EMC) for access to its facilities. I would like to thank Dr. Tony Romeo for his help with SEM training and Dr. David R. G. Mitchell for his help with TEM training and technical support. Many thanks to Dr Patricia Hayes for her great help with NMR, UV-Vis, Raman, and FTIR analyses. I greatly appreciate Dr. Dongqi Shi for tube furnace and XPS training. I thank Dr. Sepidar Sayyar and Dr. Germanas Peleckis for the XRD training. In addition, I also wish to show my thanks to Dr. Ali Jeiranikhameneh for the 3D printing training and Dr. Adam Taylor for the laser cutter training.

Finally, I would like to thank my parents and my husband Dr. Gemeng Liang for their great support and encouragement during my PhD study. Their constant love is always promoting me to solve problems and meet challenges.

Jinshuo Zou

September 16, 2021

Abstract

Electrochemical CO_2 reduction (CO_2RR) is an environmentally friendly approach to transform greenhouse CO_2 to value-added chemical feedstocks and fuels. One of the promising CO_2RR products is formate which is widely applied in chemical, food and energy related industrials. The ideal CO_2RR to formate electrolysers should possess features such as high formate conversion Faradaic efficiencies ($FE_{formate}$) at low overpotentials, high current densities, and outstanding stability to meet industrial requirements. In this thesis, highly selective formate producing catalysts were designed and prepared. The effects of CO_2RR catalysts' structures, the electrolyte alkalinity, the cell configuration, and the full-cell assembly in combination with an oxygen evolution anode toward CO_2RR performance were systematically studied.

To study catalyst structural effects on formate selectivity, a novel hierarchical structure of 3 dimensional (3D) mesoporous Pd on highly ordered TiO_2 nanotubes were prepared via the electrodeposition method. The product selectivity was found to depend on the TiO_2 nanotube length, resulting from the influence of mass transports of CO_2, protons and products in the tubes. This work demonstrates the importance of designing efficient hierarchical structures to optimise reactant/product mass transport and electrochemical kinetics.

The electrochemical flow cell was employed to overcome the low current density and mass transfer challenge encountered in H-cell using SnS nanosheet-based catalysts. Alkaline electrolyte (1.0 M KOH) successfully suppressed the hydrogen evolution across all potentials particularly at the less negative potentials, and CO evolution at more negative potentials. This in turn widened the electrochemical potential window for formate conversion. A comparative study to SnO_x

counterpart indicated sulfur also acts to suppress hydrogen evolution, although electrolyte alkalinity resulting in a greater suppression. Moreover, to achieve a long-term current stability, it is necessary to buffer the carbonate/bicarbonate formed from chemical reactions between CO_2 and KOH.

High performance oxygen evolution reaction (OER) catalyst is required to be coupled with CO_2RR cathode for the full-cell electrolyser assembly. The ultrathin amorphous iron oxyhydroxide nanosheets were synthesized via cyclic voltammetry (CV) potential modulations on thermally treated iron foils. The size and thickness of nanosheets were controlled by tuning CV cycles, potential range, duration, and electrolytes. By loading of Ni species onto the nanosheets, the OER activity was significantly enhanced, indicating iron oxyhydroxide nanosheets can act as excellent 2D supports to achieve synergies effect of bimetallic catalysis.

A single full-cell CO_2 electrolyser under electrochemical flow configuration was developed by employed CO_2RR active Bi nanoparticles (NPs)-based cathode and earth-abundant NiFe layered double hydroxide (LDH) anode. The rate determining step of CO_2RR to formate is the formation of *OCHO via one electron transfer. The combination of highly active NiFe LDH anode, highly efficient Bi NPs cathode, and highly conductive KOH electrolyte operated in flow cell configuration, all contribute to high-performance non-precious metal catalyst-based electrolyser.

This thesis successfully developed several formate producing CO_2RR catalysts, and systematically studied effects of mass transports, electrolyte alkalinity, cell configuration, and anode activity for CO_2RR to formate. Such studies in catalyst development and understanding the factors influencing CO_2RR performance would assist in developing commercial-relevant large-scale electrolysers.

Table of Contents

List of Figures

List of Tables

List of publications

[1] **Jinshuo Zou**, Germanas Peleckis, Chong-Yong Lee, Gordon G Wallace. Facile electrochemical synthesis of ultrathin iron oxyhydroxide nanosheets for the oxygen evolution reaction. *Chemical Communications*, 2019, *55*(60), 8808-8811.

[2] **Jinshuo Zou**, Muhammad Iqbal, Amruthalakshmi Vijayakumar, Caiyun Wang, Douglas R. Macfarlane, Yusuke Yamauchi, Chong-Yong Lee, Gordon G. Wallace. Hierarchical architectures of mesoporous Pd on highly ordered TiO_2 nanotube arrays for electrochemical CO_2 reduction. *Journal of Materials Chemistry A*, 2020, 8(16): 8041-8048.

[3] **Jinshuo Zou**, Chong-Yong Lee, Gordon G Wallace, Boosting formate production from CO_2 at high current densities over a wide electrochemical potential window on a SnS catalyst, *Advanced Science*, 2021, 2004521.

[4] **Jinshuo Zou**, Chong-Yong Lee, Gordon G Wallace, A non-noble metal catalyst-based electrolyser for efficient CO_2-to-formate conversion. *ACS Sustainable Chem. Eng.*, 2021, DOI: 10.1021/acssuschemeng.1c06295

[5] **Jinshuo Zou**, Chong-Yong Lee, Gordon G Wallace, Recent progress on electrocatalysts and cell designs for electrochemical CO_2 reduction to formate. In preparation. (Note: a review article adapted from introductory chapter 1)

Thesis by compilation declaration

The author of this thesis is the first author of the above papers, which are either in print, or in preparation, as stated. These substantiate the main body of this thesis.

List of abbreviations and notation

A - Ampere
AEM - Anion exchange membrane
a.u. - Arbitrary unit
C - Coulomb
CEM - Cation exchange membrane
cm - Centimeter
CO_2RR - CO_2 reduction reaction
CV - Cyclic voltammetry
DFT - Density functional theory
EDS - Energy-Dispersive X-ray Spectroscopy
EIS - Electrochemical impedance spectroscopy
FE - Faradaic efficiency
FID - Flame ionization detector
FTIR - Fourier transform infrared spectroscopy
GC - Gas chromatography
h - Hour
HER - Hydrogen evolution reaction
HRTEM - High resolution tem
j - Current density
LDH - Layer double hydroxide
LSV - Linear sweep voltammetry
M - Mole per liter
mA - Milliampere
MHz - Megahertz
min - Minute
mV - Millivolt
nm - Nanometer

NMR - Nuclear magnetic resonance

NPs - Nanoparticles

NWs - Nanowires

OER - Oxygen evolution reaction

psi - Pounds per square inch

RHE - Reversible hydrogen electrode

s - Second

SHE - Standard hydrogen electrode

SEM - Scanning electron microscope

TEM - Transmission electron microscope

TCD - Thermal conductivity detector

V - Volt

XRD - X-ray Diffraction

XPS - X-ray Photoelectron Spectroscopy

Ω - Ohm

μ - Micro

1D - One-dimensional

2D - Two-dimensional

3D - Three-dimensional

Chapter 1 Introduction

Preface

This chapter is divided into five sections. The first provides a general background of electrochemical CO_2 reduction to formate. The second section describes the fundamentals of the electrochemical CO_2 reduction to formate, including the reaction mechanisms and performance metrics. The post-transition (p-block) and transitional metal electrocatalysts for formate conversion and their design strategies are discussed in section three. The fourth section details the cell designs including H-cell, flow-cell and full cell assemblies for CO_2 reduction to formate. The thesis aims and structure are summarized in the final section.

1.1 Background of electrochemical CO_2 reduction to formate

The concentration of atmospheric CO_2 continues in an upward trajectory as a result of explosive growth in fossil fuel burning since the industrial revolution began. CO_2 can absorb and emit radiant energy of the thermal infrared range, having harmful effects on the climate, ecosystem, environment and human livelihoods.[1-3] Without efficient measures, a much greater climate change impact caused by global warming is expected as the atmospheric CO_2 concentration is projected to increase from 406 ppm to 983 ppm by the end of this century.[4] One of the potential solutions to control the CO_2 level in the atmosphere is the capture and recycling of CO_2 into useful industrial chemicals or fuels, thus concurrently alleviating environmental and energy crises. Several strategies have been investigated: (i) biological CO_2 fixation through nonphotosynthetic microorganisms;[5] (ii) photocatalytic CO_2 reduction reaction by photo-induced electrons at the surface of semiconductors;[6-8] (iii) room

temperature electrochemical CO_2 reduction reaction (CO_2RR) ;[9-10] and (iv) thermochemical synthesis at high temperature (>1000 ^oC).[11-13] Among them, CO_2RR is an environmentally friendly approach to transform CO_2 to value-added chemical products and fuels at ambient temperature and pressure, which can be powered by using clean and renewable energy sources such as solar, wind, hydro, and nuclear energy (Figure 1.1).[14] In addition, the scalability, relatively low capital and operation costs of electrochemical technology makes it attractive for industrial applications.[15]

Electrochemical CO_2RR involves multi-electron and proton transferring reactions. An additional overpotential is required to overcome thermodynamic and kinetic barriers for the stable CO_2 molecule. In an aqueous electrolyte, water is a proton source, hence hydrogen evolution is a main competing reaction which has to be suppressed to increase the efficiency in obtaining high selectivity toward desirable carbon-based CO_2RR fuels and chemical feedstocks. CO_2 can be reduced to a wide range of products such as gaseous CO, methane (CH_4), ethylene (C_2H_4), liquid formate, methanol (CH_3OH), ethanol (CH_3CH_2OH) and formaldehyde (HCHO). The mechanistic pathways of a typical electrochemical CO_2 reduction reaction depend on factors such as the type of catalyst and electrolyte employed. The potential (vs reversible hydrogen electrode, RHE) needed for the single- or multi-electron steps of CO_2RR, and the products from such reactions are summarized in Figure 1.2(a).[16] The selectivity of CO_2RR catalysts are influenced by the surface stabilization of adsorbed intermediates, such as $^*CO_2^{\cdot-}$, $^*COOH$, and $OCHO^*$. If the catalyst structure strongly binds the reaction intermediate, this species can be further reduced to products requiring more than 2-electron transfers, such as hydrocarbon or alcohols.[17-19] Otherwise, the weakly adsorbed intermediate may desorb from the metallic surface before the subsequent reduction process. However, if CO intermediate, CO* binds to the catalyst surface strongly, further reduction to

multi-carbon products may be inhibited. In addition, consistent with the Sabatier principle, the scaling relationships of different C-bound intermediates corresponding to different CO_2RR reaction routes on catalyst surface, make it difficult to optimize the binding energies and the selectivity toward targeted products.[18] Optimal catalysts should lead to a CO_2 electrolyser with an enhanced CO_2RR reaction rate at low overpotential, excellent selectivity and outstanding stability.

Formate in near neutral media or the counterpart formic acid in acidic media is one of the most promising CO_2RR products with significant market value (600 kilotons in 2020 according to the report of Mordor Intelligence).[20] Livestock offers a substantial formic acid marketplace as formic acid is a good food preservative which helps to prevent bacterial growth.[21-22] As an industrial chemical, formic acid is employed in leather tanning, pharmaceutical engineering, and rubber manufacturing.[23] The biodegradable properties of formic acid make it an ideal replacement for hydrochloric or sulfuric acid. In addition, its excellent hydrogen storage capacity (53.4 g L^{-1}) under ambient conditions and its ease of transport mean that formic acid is an outstanding liquid-phase hydrogen storage medium.[24] In addition, the development of a direct formic acid fuel cell means it could be a significant fuel material.[25-26] Therefore, the development of CO_2RR electrolysers with excellent selectivity and efficiency toward formate production at high reaction rates is highly desirable, being driven and motivated by economic and environmental benefits.

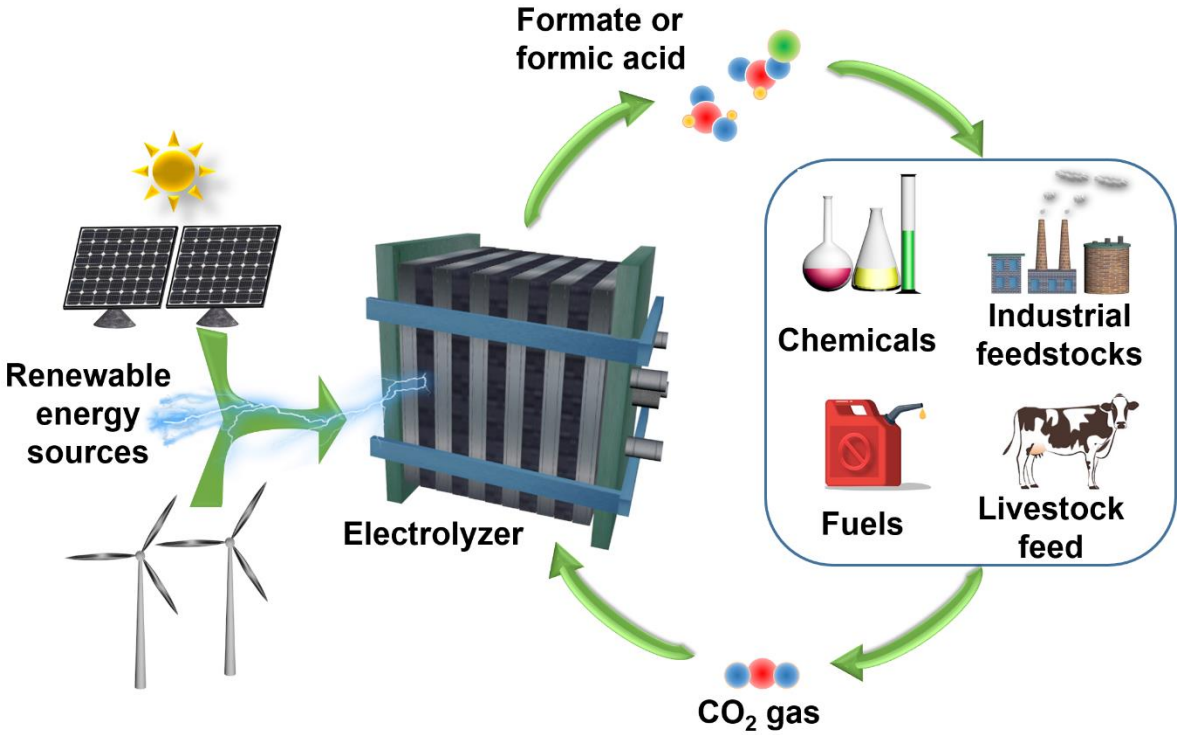

Figure 1.1 Schematics of electrochemical synthesis of CO_2 to formate powered by renewable energy sources such as solar and wind. Formate has wide industrial applications such as in chemicals, fuels, industrial feedstocks, and livestock feed, whilst the released CO_2 can be recycled.

The emergence of nanotechnology, especially a range of nanostructuring strategies to tailor, design, and synthesis electrocatalysts for CO_2 reduction to formate has resulted in significant advances in catalyst performance such as operating potential window, stabilities, conversion efficiencies, and current densities. Different attributes of catalyst structure such as size, shape, exposed crystal surface, and defects have been intensively studied. Electrochemical cell design is one of the key factors that influences the CO_2RR performance. Recent encouraging progress in cell design, the catalyst and electrolyte used, have significantly improved performance for the electrochemical reduction of CO_2.

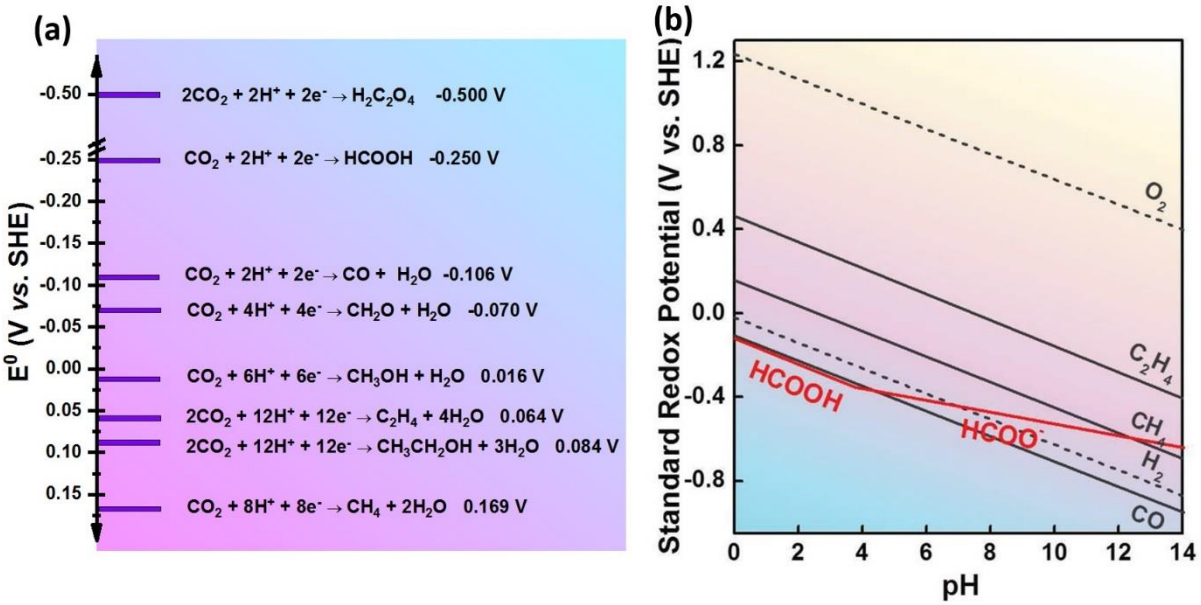

Figure 1.2 (a) Standard reduction potential (vs. Standard hydrogen electrode SHE) needed for the single- or multi-electron steps of CO_2RR, (b) Standard redox potentials of electrochemical CO_2RR into different products as well as HER and OER as a function of the solution pH, reproduced with permission.[27] Copyright, 2019, Wiley.

1.2 Fundamentals of electrochemical CO_2 reduction to formate

1.2.1 Electrochemical CO_2 reduction to formate mechanism

Electrochemical CO_2 reduction is a multi-electron transfer and multi-step process involving the adsorption of reactant CO_2 on the catalyst active sites, electron transferring to create new chemical bonds, hydrogenation on carbon or oxygen atoms, and desorption of newly formed products from the catalyst surface. It is well known that the selectivity toward different CO_2RR products depends on the intermediates and the pathways.[28-29] However, the complex intermediates and the corresponding pathways vary on different electrocatalysts, which makes it difficult to tune the selectivity. For example, Sn based catalysts, especially at more negative potential (eg. -0.9 V vs RHE) have an optimal binding energy for the *OCHO intermediate to produce formate, while Au, Ag are preferred to bind *COOH intermediate to produce CO.[30]

CO_2 reduction to formate involves a two-electron transfer step. The advanced in-situ characterization in combination with theoretical studies have deepened the mechanistic understanding of formate generation. Generally, there are four possible main pathways which depend on the key reaction intermediates as shown in Figure 1.3: (i) direct formation of *OCHO intermediate[27] by one electron transferring to the surface adsorbed CO_2 where the oxygen atom binds to the catalyst surface; (ii) *COOH intermediate where the carbon atom binds to the catalyst surface;[31] (iii) metal carbonate intermediate resulting from the insertion of CO_2 to M-OH (where M denotes the metal catalyst)[32-35]; and (iv) M-H intermediate[36-37] followed by insertion of CO_2 to form formate. Among these four pathways, (i) is the most recognized for formate formation as the *OCHO intermediate is energetically the most favourable one[38] and widely referred mechanistic pathway.[27, 31, 39-40] In pathway (ii), after the formation of *COOH, the subsequent electron and proton transfer might lead to both CO and formate products. However, CO route is more favourable as according to most reported DFT studies, where many researchers proposed *COOH as a specific intermediate toward CO.[41-42] Bocarsly and co-workers proposed the pathway (iii) as examined by in-situ ATR-IR spectroscopy study on Sn, In, and Ga_2O_3 electrodes.[32, 35, 43] They proposed that the reduction of CO_2 is preceded by a two-electron reduction of the electrode from a native metal oxide to a metal oxyhydroxide, which is followed by the insertion of CO_2. Note that all pathways except (ii) involve the formation of oxygen bridged *OCHO intermediates. Therefore, an ideal catalyst that favours formate should bind the *OCHO intermediate suitably, neither too weak nor too strong. If the *OCHO binding on the catalyst is too strong (e.g. Ni), the product desorption would be difficult, while if the binding is too weak (e. g. Au, Ag), the reduction will go through pathways involving other atom bound intermediates such as *COOH, *CHO, *CHOH, *H. Typically, p-block post-transition metals such as Sn, Bi, In, Pb and their corresponding oxides,

sulphides are ideal catalyst candidates as they always have relatively moderate binding energies to *OCHO over *COOH, or *H.

It should be noted that in most cases, multi-intermediates including *OCHO, *COOH, *CHO, and *H may coexist and the competing reactions can consume electrons and thus limit the further improvement of formate production efficiency. The nature of catalysts plays an important role in this. Firstly, the commonly used catalysts are often polycrystalline with a series of exposed crystal planes. The binding energies of intermediates on those various crystal planes are different, which make it complex to obtain the desired pathways.[44-45] Secondly, defects derived from doping, vacancies, grain boundary, step and terraces, corresponding to different electronic structures of the catalysts and which influence the types of bound intermediates, always coexist and are unavoidable in most circumstances during synthesizing.[38] In addition, the scaling relationship between the intermediate binding energies can increase the difficulty of adjusting the catalyst surface intermediates.[18, 46] Intermediates with the same binding atom on catalysts are always linearly scaled and any modification can cause a series of changes on the binding energy of different intermediates.[47-48]

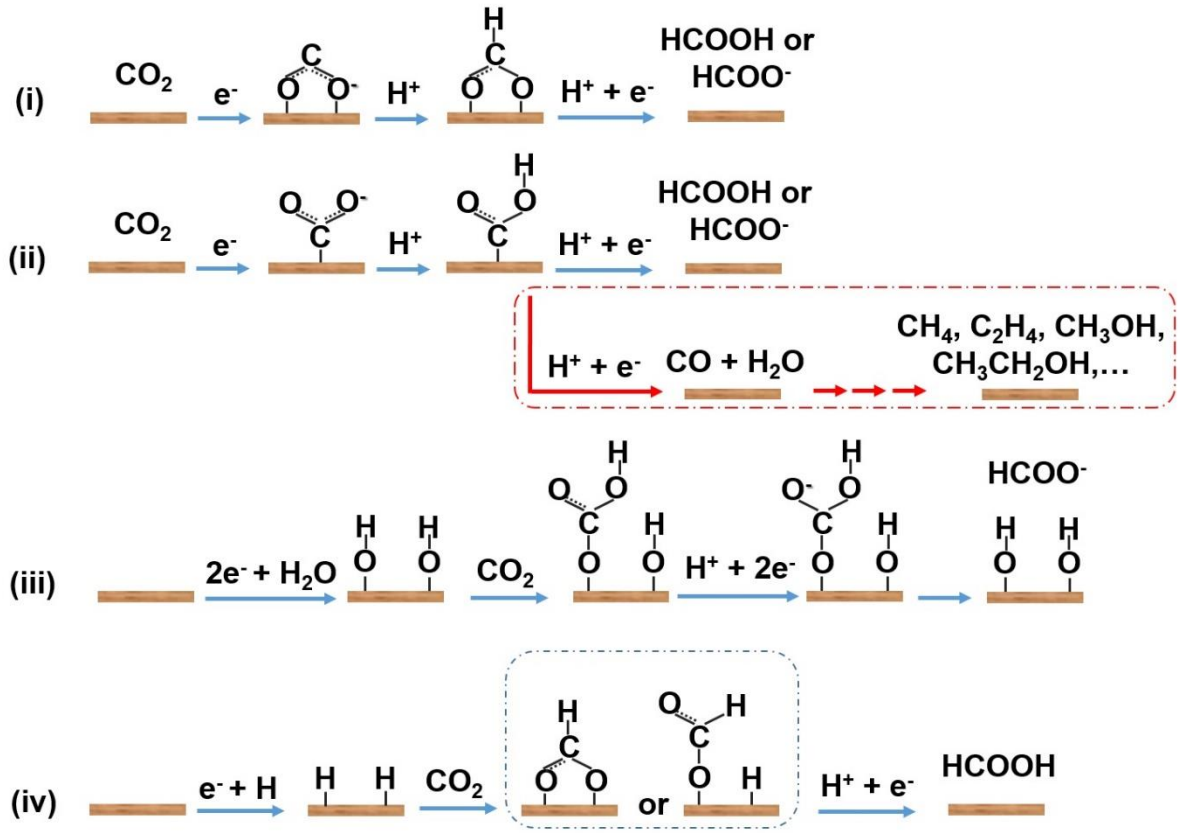

Figure 1.3 Reaction pathways for electrochemical CO_2 reduction to formate and the competing reactions.

The employed electrolytes should be taken into consideration as they can greatly affect the adsorption of intermediates and the corresponding pathways, hence influencing the CO_2RR activities. The pH of the electrolyte is one of the most important factors as both CO_2RR and HER involve the proton-coupled electron transfer. The standard redox potential for formate or formic acid is not linearly pH dependent according to Li et al (Figure 1.2b).[27] At pH < 3.75, the product is formic acid and the CO_2RR to formic acid pathway is thermodynamically the least favoured. However, when at the region of pH > 3.75, formate gradually becomes the main product and thermodynamically more favourable compared with CO formation. At pH > 7, the standard redox potential of CO_2RR to formate is even lower than that of hydrogen evolution. Sargent and co-workers experimentally identified that the increased alkaline

concentration in electrolyte favours the pathway toward formate instead of CO on a silver electrocatalyst.[49] Bumroongsakulsawat et al. also found the tendency that low proton concentration can increase the ratio of CO and formate.[50] Therefore, electrolytes with higher pH could increase the selectivity toward formate production. Generally, the local electrochemical interfaces are complex as the CO_2 concentration gradient, the localised change in electrolyte pH, the accessibility of CO_2 to catalyst active sites and the interaction of CO_2 and electrolyte potentially contribute to the thermodynamic electrochemical conditions.

It has been reported that alkaline metal ion cations can influence the selectivity of CO_2RR.[51-52] Cations of different sizes in electrolytes correspond to different pK_a of cation hydrolysis occurring near the cathode. Singh and coworkers reported that the p*K*a for cation hydrolysis decreases with the increase in cation size, and consequently the buffering capability and the polarization loss decrease in the order of $Li^+ < Na^+ < K^+ < Rb^+ < Cs^+$.[53] The buffering capability which is closely related to the local pH at the cathode surface could affect the selectivity as higher pH favours the selectivity toward formate production. Since the applied potential is a sum of polarization loss and kinetic overpotential, the current density increases correspondingly with the increase of cation size. Zhao et al reported the effect of the hydrophilic/hydrophobic nature of cations on selectivity by introducing Li^+, Na^+, and K^+ cations into the solvent model on a Pb(111) surface.[54] They found that hydrophilic Li^+ and Na^+ can form cations and adsorb onto the Pb surface, while K^+ is hydrophobic and has to be adsorbed directly onto the surface. The larger hydrophilic cations are beneficial in promoting the formation of formate as the intermediate is easier to be removed from the catalyst in the K^+ system (E_{ad} = - 3.76 eV) than that in Li^+ (E_{ad} = - 4.53 eV) and Na^+ (E_{ad} = - 4.49 eV). Wu and co-workers compared the alkaline metal ions, Na^+, K^+ and Cs^+ on Sn cathode and found the smallest ion, Na^+ electrolyte benefits the stability and Faradaic efficiency while Cs^+ electrolyte

resulted in the highest current density. [55] They concluded that K^+ may be the optimal cation for formate production.

The effects of anions are always intertwined and is essential when selecting a suitable electrolyte for a CO_2 electrolyser. The buffer capacity of the anions is one of the reasons that affects the selectivity.[56] Although CO_2 is flowed continuously into the electrolyte, the consumption of local CO_2 through CO_2 reduction and the mass transfer limitation in the electrolyte may result in a low CO_2 concentration at the catalyst surface. If the buffer capacity of anions is strong enough to compensate the pH change, the CO_2RR will be less affected by local CO_2 concentration change and thus a stable electrolysis can be obtained. Bicarbonate could be a source of protons, and the consumption may impose a mass transfer issue for the competing proton reduction reaction, which would then favour the CO_2RR instead of HER.[57] However, according to some recent studies, HCO_3^- may also function as a source of carbon that can be reduced, hence add complexity to the product selectivity due to the HCO_3^- depletion.[58-59] Recently, alkaline electrolytes containing OH^- have been identified to promote the selectivity toward formate.[49, 60] Kim et al. studied the anion effects on Sn electrode by comparing the performance in KOH, $KHCO_3$, KCl, and $KHSO_4$ and found that KOH had the highest HCOOH production efficiency, which was attributed to the suppression of HER in the KOH electrolyte.[61] Furthermore, it has been identified that halide ions can be adsorbed on catalysts and affect the performance.[62] Yoon et al. studied the effects of halide anions on CO_2 reduction to formic acid on Bi (012) surfaces using DFT and found that the CO_2 molecules prefer to coordinate directly with hydrated Bi atoms via the oxygen bidentate mode.[63] By comparing the free energy in Cs^+/Cl^-, Cs^+/Br^-, and Cs^+/I^- to form formic acid, they found that Cl^- is more favourable than Br^- and I^- in both the CO_2 adsorption and the HCOOH desorption steps, indicating that Cl^- is most favoured for CO_2 reduction on Bi. Some researchers attribute

the halide effects to the modification catalyst structure and morphology by halide. Gao et al found that the halide ions induced significant nanostructuring on the oxidized Cu surface, including at open circuit potential, resulting in positive impacts of enhanced current density and intrinsically high selectivity.[62] The suppression of hydrogen evolution may be another reason for the enhanced CO_2 reduction selectivity. Varela and co-workers presented the results that Cl^- and Br^- can suppress the hydrogen production while I^- can only suppress at low overpotentials.[64] Therefore, halide anions can be used to tune the CO_2 reduction performance.

1.2.2 Performance metrics of electrochemical CO_2 reduction to formate

1.2.2.1 Onset potential and overpotential

The electrochemical onset potential for formate is the potential where CO_2 reduction to formate starts. It is not easy to measure from the polarization curve as there are some competing reactions such as hydrogen evolution and CO evolution. Overpotential (ΔE) illustrates the potential difference of the required potential for formate generation and the thermodynamically equilibrium potential. In comparison to onset potential, overpotential is a more practical parameter for CO_2 reduction research as both the required potential and the equilibrium potential are available. Generally, the overpotential varies with different electrocatalysts. For example, Sn-related catalysts have a higher overpotential than Pd-related catalysts for formate production, the latter's is near to zero.[65-67] To minimise the required electrical energy in operating the CO_2 electrolyser, strategies in lowering the reaction overpotential whilst maintaining high product conversion efficiency is highly desirable.

1.2.2.2 Faradaic efficiency

Faradaic efficiency indicates the selectivity of an electrocatalyst at a given potential, referring to the ratio of transferred electrons to the target product over the total consumed electrons during the electrolysis. The calculation equation is: FE = znF/Q, where z is the electron number required to form one mole of product (z for formate is 2), n is the molar amount of a target product, F is the Faraday's constant (F = 96485 C mol^{-1}), and Q is the charge consumed during the electrolysis. High Faradaic efficiency means efficient use of energy in conversion of charge to a targeted product. However, side reactions such as hydrogen evolution, catalyst corrosion, and the evolution of other non-targeted CO_2RR products (eg. all CO_2RR products except formate and formic acid) can decrease the Faradaic efficiency of a targeted product. Therefore, suppression of side reactions and improving the Faradaic efficiency of a targeted product is one of the most important tasks in enhancing the CO_2RR activity.

1.2.2.3 Partial current density

The total current density (j_{total}) is the current normalised by the surface area or the weight of electrocatalysts. Partial current density ($j_{formate}$) illustrates the effective part of the total current density that is used for the generation of the targeted product, formate. It is often calculated by the equation: $j_{formate} = FE \times j_{total}$. For industrially relevant CO_2 electrolysis, the partial current density should be higher than 100 mA cm^{-2}.[68] However, the $j_{formate}$ in most of the earlier studies, using H-cell could not reach this level due to the concentration limitation of dissolved CO_2 and the relatively low conductivity in bicarbonate electrolyte. An electrochemical flow-cell system employing the gas diffusion electrode and electrolyte other than bicarbonates has been an increasingly employed strategy to overcome both the CO_2 mass transfer and the electrolyte conductivity issues. The electrolyser design to improve the $j_{formate}$ will be discussed later in the cell design section.

1.2.2.4 Tafel plots

The Tafel plot represents the relationship of an overpotential and logarithm of the partial current density of the product (formate). In the Tafel equation, $\Delta E = a + b\log j_{formate}$, the Tafel slope b is inherently related to the electrokinetics and can reflect the rate-determining step (RDS). Usually, a slope of ~118 mV dec^{-1} corresponds to the RDS of a one-electron transfer to form CO_2^- intermediates, while a slope of ~59 mV dec^{-1} indicates the RDS of a chemical step following the fast one-electron transfer.[69] Lower Tafel slope values indicate fast reaction kinetics and thus the kinetic enhancement of a catalyst can be verified by detecting the change of the Tafel slope.

1.2.2.5 Long term stability

The long term stability of a CO_2RR describes the electrolyser's durability, with respect to the selectivity and current density. To achieve industrial applications, the stability of an electrolyser should be more than 4,000 h with a relatively high formate Faradaic efficiency and partial current density.[70] However, most of the reported stability data only last dozens of hours, which falls far short of what is required for commercial applications. Catalyst poisoning can be one of the main reasons that limits the CO_2 electrolyser performance stabilities. The poisoning may come from the contamination of the electrolyte in the electrolyser and the selective adsorption of CO or other intermediates. Catalyst degradation due to corrosion or composition change is also a common factor that causes the decrease in selectivity and current density. In addition, the local electrolyte pH change during electrocatalysis influences not only the reaction pathways and the selectivities, but also stability. It should be noted that the above factors may coexist and interplay with each other, making it still a great challenge to design stable electrolysers that can last for months/years.

1.3. Catalysts for electrochemical CO_2 reduction to formate

In this section, the p-block post-transition metals (Sn, Bi, In, Pb, and Sb) and the transition metals (Cu, Pd, Co) that emerged in recent years as active electrocatalysts for formate production will be reviewed. In addition, a summary of the catalyst design strategies will also be given, including crystal facet tailoring, morphology regulation, defect engineering, alloying treatment, and surface functionalization. Table 1.1 summarizes the typically employed electrocatalysts for formate production, and their corresponding performances. Generally, p-block post-transition metal-based catalysts exhibited high selectivity to formate, but at relatively higher overpotentials (> 300 mV). In contrast, transition metal-based catalysts such as noble metal Pd have a relatively low overpotential, however, the high cost and operation at a lower potential region (hence low current densities) may limit their application. In addition to catalysts, factors such as cell configuration and the employed electrolyte are critical to CO_2 conversion to formate performance, and they are included in this table and will be discussed later.

Table 1.1 Summary of electrocatalysts and the corresponding performance collated from the recent literatures.

Electrocatalysts	Cell type	Electrolyte	$FE_{formate}$	j(mA cm^{-2})	Ref.
SnS_2 monolayers (0.58 ± 0.04 nm)	H-cell	0.1 M $KHCO_3$	94 ± 5% at -0.8 V vs. RHE	~45.2 mA cm^{-2} at -0.8 V vs. RHE	[71]
SnO_2 nanoparticles	H-cell	0.1 M $KHCO_3$	85% at -1.1 V vs. RHE	23.7 mA cm^{-2} at -1.1 V vs. RHE	[72]
N-enriched Sn(S) nanosheets	Flow-cell	0.1 M $KHCO_3$	93.3% at -0.7 V vs. RHE	~25 mA cm^{-2} at -0.65 to -0.9 V vs. RHE	[73]
SnO_2/Sn_3O_4	H-cell	0.5 mol L^{-1} $KHCO_3$	88.3% at -0.9 V vs. RHE	19.03 mA cm^{-2} at -0.9 V vs. RHE	[74]
Sn foil coated with N doped graphene	H-cell	0.5 M $KHCO_3$	92.0% at -1.0 V vs. RHE	21.3 mA cm^{-2} at -1.0 V vs. RHE	[75]

SnO_x covered by hydroxyl	H-cell	0.1 M KCl	93.1% at -1.6 V vs. Ag/AgCl	10.7 mA cm^{-2} at -1.6 V vs. Ag/AgCl	[76]
Sn-gas diffusion electrode (GDE)	Flow-cell	0.5 M $NaHCO_3$	71 ± 1.1% at -1.1 V vs. RHE	8.58 mA cm^{-2} at -1.1 V vs. RHE	[77]
SnO_2 microsphere	H-cell	0.5 M $KHCO_3$	62.0% at -1.7 V vs. SHE	12.5 mA cm^{-2} at -1.7 V vs. SHE	[78]
SnO_2 nanoparticles (<5 nm)	Flow-cell	1 M KOH	97% at -0.95 V vs. RHE	> 100 mA cm^{-2} after -0.8 V vs. RHE	[79]
SnO_2 chainlike mesoporous structures	H-cell	0.1 M $KHCO_3$	95% at -0.97 V vs. RHE	15.3 mA cm^{-2} at -0.97 V vs. RHE	[80]
Sn/SnS_2	H-cell	0.5 M $NaHCO_3$	84.5% at -1.4 V vs. Ag/AgCl	13.9 mA cm^{-2} at -1.4 V vs. Ag/AgCl	[81]
SnO_2 mesoporous nanosheets	H-cell	0.5 M $NaHCO_3$	87 ± 2 % at -1.6 V vs. Ag/AgCl	45 mA cm^{-2} at -1.6 V vs. Ag/AgCl	[82]
Ag-Sn core–shell	H-cell	0.5 M $NaHCO_3$	~80% at -0.8 V vs. RHE	16 mA cm^{-2} at -0.8 V vs. RHE	[83]
Sn−Cu/SnO_x core/shell	Flow-cell	1M KOH	83.0 ± 1.7 % at -0.93 V vs. RHE	406.7 ± 14.4 mA cm^{-2} at -0.7 V vs. RHE	[84]
Sn(S)/Au	-	0.1 M $KHCO_3$	93% at -0.75 V vs. RHE	55 mA cm^{-2} at -0.75 V vs. RHE	[85]
Bi−Sn/carbon fibres	H-cell	0.5 M $KHCO_3$	96% ± 2% at -1.14 V vs. RHE	45 mA cm^{-2} at -1.14 V vs. RHE	[86]
Bi mesoporous nanosheets	H-cell	0.5 m Na HCO3	~99% at -0.9 V vs. RHE	>17 mA cm^{-2} at -1.0 V vs. RHE	[87]
Bi-based MOF (Bi(btb))	H-cell	0.5 m $KHCO_3$	95(3)% -0.97 V vs.RHE	261(13) A g^{-1} at -1.17 V vs.RHE	[88]
Bi decorated 2D SnO_x nanoflakes	H-cell	0.5 M $KHCO_3$	>90% at -1.27 to -1.47 V vs. RHE	45 mA cm^{-2} at -1.37 V vs. RHE	[89]
Bi/rGO	H-cell	0.1 m $KHCO_3$	98% at -0.8 V vs. RHE	~1.9 mA cm^{-2} at -0.8 V vs. RHE	[90]
Bi nanotubes	H-cell	0.5 M $KHCO_3$	97% at -1.0 V vs RHE	39.4 mA cm^{-2} at -1.1 V vs	[91]
BiO_x@C with enriched oxygen vacancies	H-cell	1 M $KHCO_3$	89.3% at -1.7 V vs. SCE	37.8 mA cm^{-2} at -1.7 V vs. SCE	[92]
Bi-MWCNT-COOH/Cu	H-cell	0.5 M $KHCO_3$	91.9 % at -0.76 V vs. RHE	7.5 mA cm^{-2} at -0.76 V vs. RHE	[93]

Bi ultrathin nanosheets	H-cell	0.1 M $KHCO_3$	86.0% at -1.1 V vs. RHE	16.5 mA cm^{-2} at -1.1 V vs. RHE	[94]
Bi-doped amorphous SnO_x nanoshells	Flow-cell	0.5 m $KHCO_3$	95.8% at -0.88 V vs. RHE	74.6 mA cm^{-2} at -0.88 V vs. RHE	[95]
Bi dendrites with high-index planes	H-cell	0.5 M $KHCO_3$	~89% at -0.74 V vs. RHE	2.7 mA cm^{-2} at -0.74 V vs. RHE	[96]
Bi nanostructures	undivided three-electrode glass cell	0.1 mol L^{-1} $KHCO_3$	86% at -1.8 V vs. Ag/AgCl	24.9 mA cm^{-2} at -1.8 V vs. Ag/AgCl	[97]
Bi nanoparticles / Bi_2O_3 nanosheets with abundant grain boundaries	H-cell	0.5 M $KHCO_3$	~100% at -0.86 V vs. RHE	24.4 mA cm^{-2} at -1.16 V vs. RHE	[98]
Bi nanosheets with electron-rich surface	H-cell	0.1 M $KHCO_3$	97 % at -0.80 V vs. RHE	18 mA cm^{-2} at -1.3 V vs. RHE	[99]
Bi single atoms	H-cell	0.1 M $KHCO_3$	>95% from -0.8 to -1.2 V vs. RHE	12.0 mA cm^{-2} at -1.2 V vs. RHE	[100]
Bismuthene	Flow-cell	1.0 m KOH	~100% at -0.57 and -0.75 V vs. RHE	>300 mA cm^{-2} at -0.95 V vs. RHE	[101]
Bi dendritic structure	high-pressure flow-cell	0.5 M $KHCO_3$	92 ± 4% at -0.82 V vs RHE	95 mA cm^{-2} at -0.82 V vs RHE	[102]
In	H-cell	0.5 M $KHCO_3$	52.7% at -1.9 V vs. Ag/AgCl	27.8 mA cm^{-2} at -2.0 V vs. Ag/AgCl	[103]
Cu-In Dendritic structure	three-electrode setup	0.1 M $KHCO_3$	62% at -1V vs RHE	0.75 mA cm^{-2} at -1V vs RHE	[104]
In doped with S	H-cell	0.5 M $KHCO_3$	93% at -0.98 V vs. RHE	86 mA cm^{-2} at -1.23 V vs. RHE	[105]
In metal–organic framework (MOF)	H-cell	0.5 M $KHCO_3$	88% at -0.669 V vs. RHE	~40 mA cm^{-2} vs. RHE at -1.05 V	[106]
In_2O_3–rGO hybrid	H-cell	0.1 M $KHCO_3$	84.6% at -1.2 V vs. RHE	0.2 mA cm^{-2} at -1.2 V vs. RHE	[107]
In metal electrodes	H-cell	0.5 M K_2SO_4	~90% at -1.7 V vs. SCE	-	[35]
In nanoparticles	three-neck round bottom flasks	0.5 M $KHCO_3$	100% from -1.3 to -1.6 V vs. Ag/AgCl	~7 mA cm^{-2} from -1.5 to -1.7 V vs. Ag/AgCl	[34]

In hierarchical porous catalyst	-	0.1 M $KHCO_3$	~90 % from -1.0 to -1.2 V vs. RHE	67.5 mA cm^{-2} at -1.2 V vs. RHE	[108]
In/In_2O_3 heterostructures	two-chamber cell	0.5 M $KHCO_3$	93% at -1.2 V vs. RHE	50.8 mA cm^{-2} at -1.2 V vs. RHE	[109]
Sn-Pb-Sb alloy	two compartment cell	0.1 M $KHCO_3$	91% at -1.4 V vs. RHE	16 mA cm^{-2} at -1.4 V vs. RHE	[110]
PbS	H-cell	0.1 M $KHCO_3$	88% at -1.08 V vs. RHE	12 mA cm^{-2} at -1.08 V vs. RHE	[111]
Pb modified by amine	H-cell	1 M $KHCO_3$	>80% at -1.29 V vs. RHE	24.0 mA cm^{-2} at -1.29 V vs. RHE	[112]
Sb nanosheets	H-cell	0.5 M $NaHCO_3$	84% at -1.06 V vs. RHE	8 mA cm^{-2} at -1.06 V vs. RHE	[113]
Mesoporous hollow kapok-tubes (MHKTs)	H-cell	0.5 M $KHCO_3$	50% at -1.1 V vs. RHE	8.0 mA cm^{-2} at -1.1 V vs. RHE	[114]
Sn@MHKTs	H-cell	0.5 M $KHCO_3$	95% at -1.0 V vs. RHE	38.1 mA cm^{-2} at -1.1 V vs. RHE	[114]
Bi@MHKTs	H-cell	0.5 M $KHCO_3$	93% at -1.0 V vs. RHE	46.4 mA cm^{-2} at -1.1 V vs. RHE	[114]
Pb@MHKTs	H-cell	0.5 M $KHCO_3$	85% at -1.0 V vs. RHE	17 mA cm^{-2} at -1.1 V vs. RHE	[114]
Cd@MHKTs	H-cell	0.5 M $KHCO_3$	74% at -1.0 V vs. RHE	10.9 mA cm^{-2} at -1.1 V vs. RHE	[114]
PdAg nanospheres	H-cell	0.1 m $KHCO_3$	>80% from -0.1 to -0.35 V vs. RHE	5.3 mA cm^{-2} at -0.35 V vs. RHE	[115]
Pd nanoparticles	two compartment cell	2.8 M $KHCO_3$	88% at -0.35V vs. RHE	3.45 mA cm^{-2} at -0.35V vs. RHE	[66]
PdZn nanoparticles	two compartment cell	0.1 M $KHCO_3$	99.4% at -0.1 V vs. RHE	7.2 A g^{-1}at -0.2 V vs. RHE	[116]
Cu modified by cetyltrimethylammonium bromide (CTAB)	H-cell	0.5 M $KHCO_3$	82% at -0.5V vs. RHE	2.48 mA cm^{-2} at -0.5 V vs. RHE	[117]
Cu fibre felt with rich stepped surface	H-cell	0.1 M $KHCO_3$	71.1 ± 3.1% at -1.1V vs. RHE	~3.5 mA cm^{-2} at -1.1 V vs. RHE	[118]
Pd nanoparticles (3.7nm)	H-cell	1 M $KHCO_3$	~98 % from -0.1 V to -0.2 V	-	[67]

Co partially oxidized atomic layers	H-cell	0.1 M Na_2SO_4	90.1% at -0.85 V vs. SCE	10.59 mA cm^{-2} at -0.85 V vs. SCE	[119]
Pd−Sn Alloy	-	0.5 M $KHCO_3$	99.3% at -0.43V vs. RHE	~2 mA cm^{-2} at -0.43V vs. RHE	[120]
Co_3O_4 ultrathin layers	H-cell	0.1 M KH CO_3	64.3% at -0.88V vs. SCE	0.68 mA cm^{-2} at -0.88 V vs. SCE	[121]

1.3.1 p-block post-transition metal-based electrocatalysts (Sn, Bi, In, Pb, Sb)

Sn, Bi, In, Pb, and Sb are the most widely investigated and promising catalysts for CO_2RR to formate as they have relatively high oxygen affinity and weak hydrogen affinity.[18, 122] The weak hydrogen affinity could help suppress the competing hydrogen evolution reaction. Importantly, high oxygen affinity favours formation of the oxygen-bond intermediates such as *OCHO, that have preferable selectivity toward formate production, whereas the carbon-bond *COOH intermediate would otherwise tend to produce CO. The active site activation of these metallic catalysts via various approaches is the key to achieve aforementioned properties that will be discussed below.

Among them, Sn is the most attractive candidate due to it nontoxicity, abundance in the earth crust and high formate selectivity. Since Hori et al firstly reported that bulk Sn electrodes have good formate selectivity (88 % and 5 mA cm^{-2} at -1.48 V vs NHE) in 1994, the Sn-based electrocatalysts have been extensively studied.[123] However, high overpotentials were required, and the obtained current densities were low. Recent studies show that the nanostructuring of Sn-based catalysts is an effective strategy to overcome those challenges. Luo and co-workers prepared the SnS_2 monolayers in Figure 1.4a and b via a facile Li-

intercalation/exfoliation method and found that the monolayers with atomic-scale thickness (0.59 nm) not only facilitate the *OCHO intermediate, but also promote the subsequent proton-electron transfer for the generation of formate, according to the lower free energy of CO_2 reduction to formic acid (0.38 eV) based on the atomic model of DFT-relaxed SnS_2 monolayer (Figure 1.4c).[71] This ultrathin electrocatalyst is highly durable as there is almost no loss in Faradaic efficiency (> 90 %) and current density (> 45 mA cm^{-2}) during the 80 h test at the potential of 0.8 V vs. RHE (see Figure 1.4d and e). Amal et al synthesized SnO_2 nanoparticles using the industrially adopted flame spray pyrolysis (FSP) method at the feed-rate of 3, 5, and 7 mL min^{-1} and are denoted as FSP-SnO_2-3, FSP-SnO_2-5, and FSP-SnO_2-7, respectively.[72] The hydrogen temperature programmed reduction (H_2-TPR) profiles in Figure 1.4g reveal that the increase in rate during FSP led to a reduction in surface oxygen species. A maximum efficiency of 85 % with a high partial current density of -23.7 mA cm^{-2} at -1.1 V vs. RHE were also observed on FSP-SnO_2-5 (Figure 1.4i). It is interesting to note that the defects arising from oxygen vacancies were more prominent for FSP-SnO_2-5 according to the XPS results in Figure 1.4h. They proposed that the amount of oxygen hole centres (OHC, Sn□O●, where "□" denotes the three Sn-O bond and "●" is the unpaired electron tuned by flame spray conditions) plays a vital role in CO_2 activation and formate production. It should be noted that the most popular Sn-based electrocatalysts are Sn oxides or Sn sulphides. Although the oxides and sulphides were partially reduced to metallic Sn, the catalytic activity with respect to Faradaic conversion efficiency remained stable.[81] Wang et al. reported the SnO_2 nanosheets exhibit increased selectivity and current density during electrolysis at a wide potential range of -0.7 V ~ -1.2 V vs. RHE.[124] They found that the SnO_2 nanosheets were covered by the metallic Sn nanoparticles upon applied potential, and reached a steady state after 3 h electrolysis. The metallic Sn layer becomes a protection for the SnO_2 and meanwhile provides new active sites for formate conversion. Thus, the Faradaic efficiency for formate conversion achieved 80 %,

and above 10 mA cm^{-2} after 24 h durability test at -1.1 V vs RHE in 0.1 M $KHCO_3$, suggesting that the tin oxide catalysts are stable for formate production.

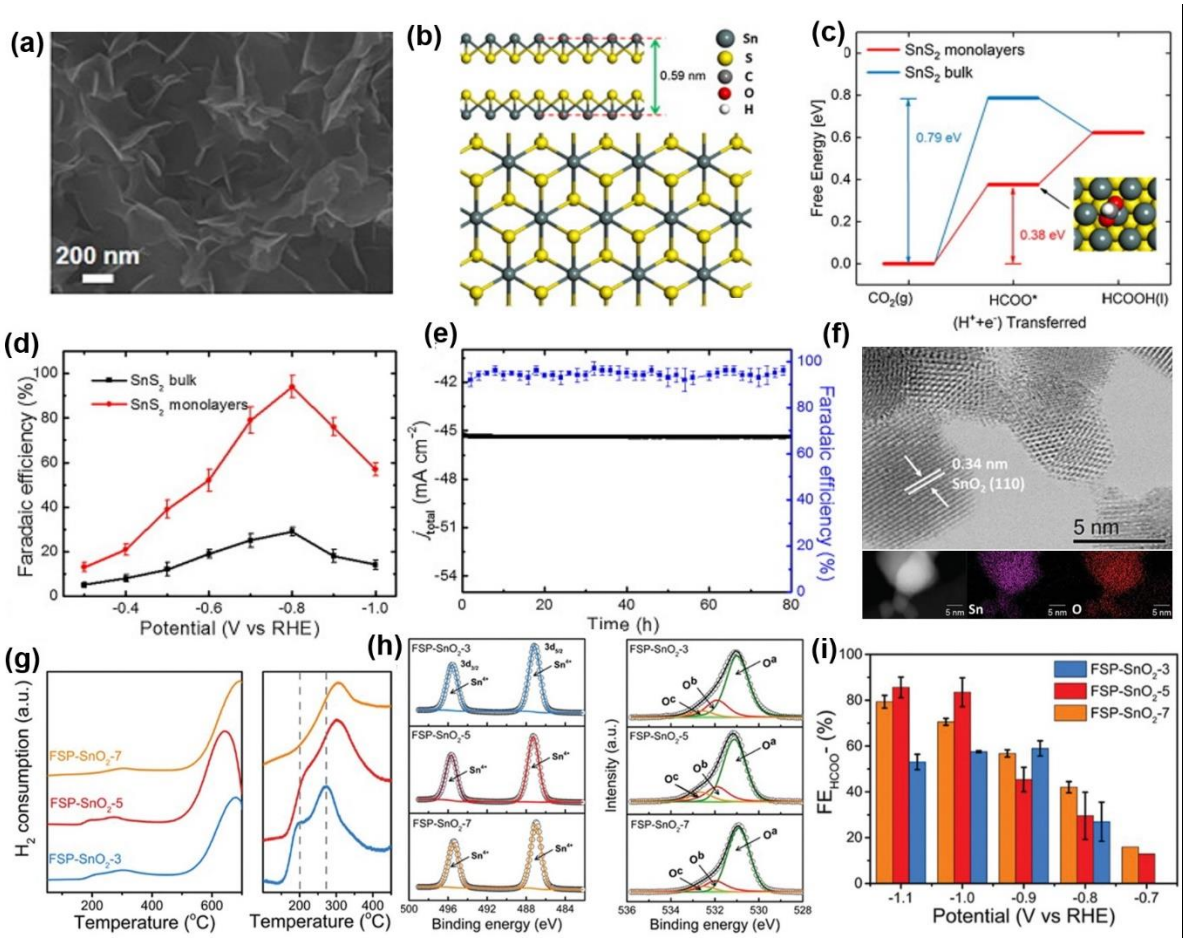

Figure 1.4 Characterizations and performance of Sn-based catalysts for CO_2RR to formate. (a) SEM image of SnS_2 monolayers, (b) Atomic models of DFT-relaxed SnS_2 monolayer (0 0 1) surface, (c) free energy diagrams of CO_2 reduction to HCOOH, (d) $FE_{formate}$ of bulk SnS_2 and SnS_2 monolayers at different potentials in CO_2 saturated 0.1 M $KHCO_3$, (e) long term stability test at the potential of -0.8 V vs RHE. Reproduced with permission.[71] Copyright 2018, Elsevier. (f) HR-TEM imaging and EDX mapping of flame spray pyrolyzed SnO_2 with a precursor feed rate of 5 mL min^{-1} (FSP-SnO_2-5), (g) TPR profiles of FSP-SnO_2-3, FSP-SnO_2-5 and FSP-SnO_2-7, (h) XPS spectra of Sn3d and O1s, (O^a, O^b, O^c refer to peaks of Sn^{4+}-O, adsorbed oxygen and O atoms adjacent to oxygen vacancies, respectively), (i) $FE_{formate}$ of FSP-SnO_2-3, FSP-SnO_2-5 and FSP-SnO_2-7 in CO_2 saturated 0.1 M $KHCO_3$. Reproduced with permission.[72] Copyright 2019, Wiley.

Bi is another low toxicity, inexpensive, and high formate selective catalyst for CO_2 reduction. Since Komatsu et al. demonstrated that bulk Bi has a good selectivity toward formate for the first time in 1995, Bi electrocatalysts with different structures have been investigated.[125] Due to the unstable nature of Bi-based compounds, most of the Bi electrocatalysts are metallic Bi or partially reduced metallic Bi. Nanosheet structures, especially ultrathin nanosheets as two dimensional (2D) catalysts possess the advantages of enhanced surface area, high CO_2 adsorption capacity, rich active sites and facet defects. Bi nanosheets derived from BiOBr,[126] BiOI,[127] and $Bi_2O_2CO_3$,[87] all exhibit excellent formate selectivity. Furthermore, Xu and co-workers prepared a few-layer bismuthene (around 1.28 nm in thickness) by in-situ electrochemical transformation from ultrathin metal-organic layers (see Figure 1.5a and b).[101] The second proton-couple electron transfer for the generation of HCOOH* from OCHO* is the rate determining step due to the largest endothermic (+ 0.12 eV) process in Figure 1.5c. The high formate selectivity (~ 100 % at the potentials of -0.57 and -0.75 V) and large current density (> 300 mA cm^{-2} at -0.95 V) is achievable in a flow-cell setup using 1 M KOH as a result of the high intrinsic activity of atomically thin bismuthene layers (Figure 1.5d and e). Yu et al. compared the CO_2RR performance of Bi nanotubes (Figure 1.5f, diameters: 5-7 nm, wall thickness: ~2 nm) with Bi nanosheets (Figure 1.5 g, thickness: ~2 nm) and found that the Bi nanotubes can maintain high formate efficiency (> 80 %) in a broad potential range of 600 mV (from 0.75 V to 1.35 V vs. RHE) and higher current density (about 50 mA cm^{-2}) at more negative potentials (when more negative than 1.1 V vs RHE) in CO_2-saturated 0.5 M $KHCO_3$, which is superior to the performance of Bi nanosheets (Figure 1.5i and j).[91] The DFT results in Figure 1.5h indicate that the energy barrier for CO_2 reduction to HCOOH decreases with the curvature. Therefore, they provide the explanation that the excellent activity on Bi nanotubes originates from the high CO_2 concentration near the curved

surface coupled with the property that formate intermediates can be strongly adsorbed on the Bi nanotubes.

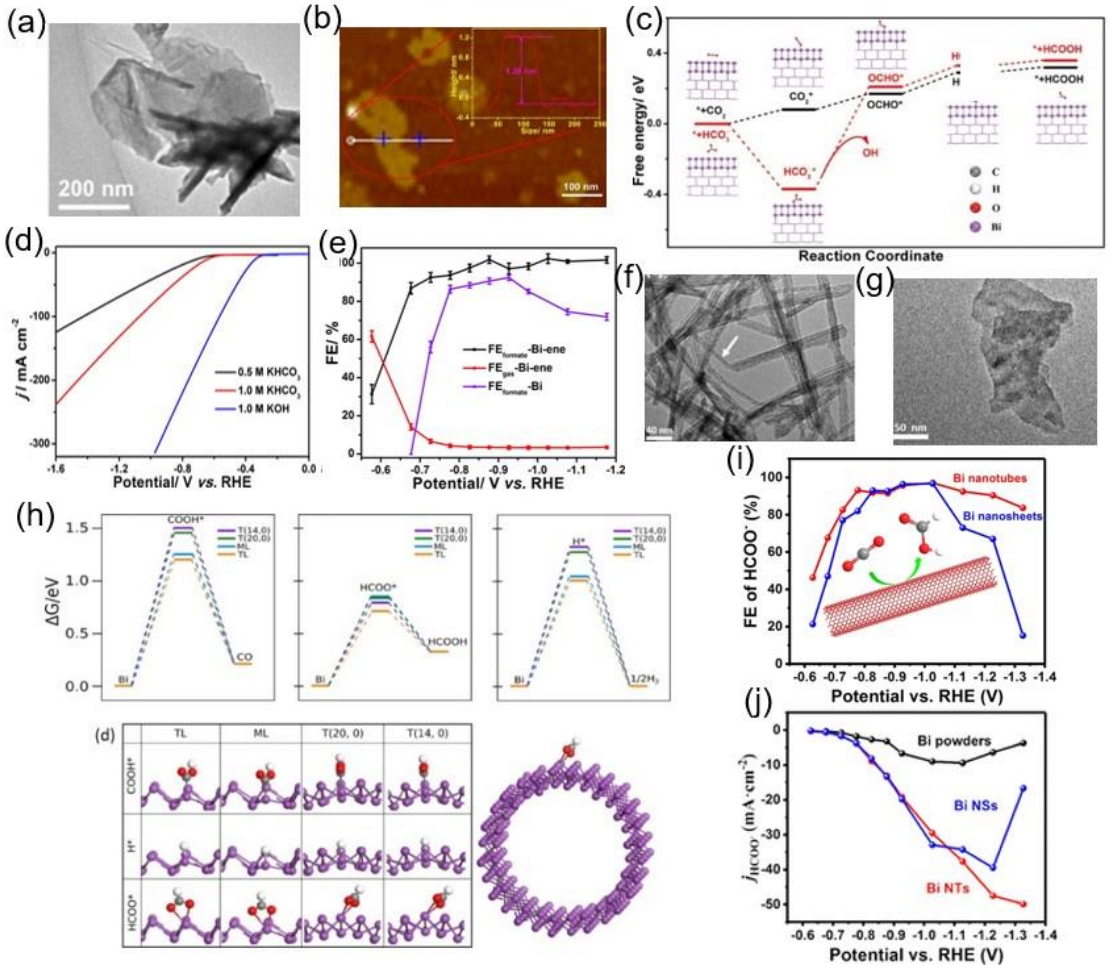

Figure 1.5 Characterizations and performance of Bi-based catalysts for CO_2RR to formate. (a) TEM, and (b) AFM images of bismuthene, (c) Free energy diagrams for HCOOH over bismuthene, (d) LSV curves of bismuthene in different type of electrolytes at a scan rate of 10 mV s^{-1}, (e) FE of formate and gaseous products on bismuthene in CO_2-saturated 0.5 M $KHCO_3$. Reproduced with permission.[101] Copyright 2020, Wiley. TEM images of Bi nanotubes (f) and nanosheets (g), (h) Free-energy landscape for CO, formate, H_2 on (14, 0) tube (T(14, 0)), (20, 0) tube (T(20,0)), monolayer slab (ML), and trilayer slab(TL) (curvature of the surface increases monotonically in the order: ML < T(14, 0) < T(20,0)) and the schematic of COOH*, H*, and HCOO* adsorption sites on T(14, 0), T(20,0), ML, and TL, (i) j_{HCOO^-} and (j) Faradaic efficiency (FE) of Bi NTs, Bi NSs, and Bi powder in CO_2-saturated 0.5 M $KHCO_3$. Reproduced with permission.[91] Copyright 2020, American Chemical Society.

The electronic structure and the electrocatalytic properties of In are similar to that of Sn and Bi. Since Hori and co-workers firstly reported on the bulk In's excellent formate selectivity in 1994, In-related electrocatalysts have been less reported, potentially due to the high cost of In. [123] However, fundamental investigations and exploring strategies to lower the In percentage of content in the electrocatalysts remain of interest. Yang et al. synthesized the In/In oxide heterostructures from the electrochemical reduction of In-MOF (see Figure 1.6a).[109] In this heterostructure, it was proposed that metallic In promoted formate production, whilst In oxide suppressed the competing hydrogen evolution, which leads to outstanding formate conversion Faradaic efficiency of up to 93 % at 50.8 mA cm^{-2} at -1.2 V vs RHE in 0.5 M $KHCO_3$ (Figure 1.6b and c). Single atom electrocatalysts that allow high atomic utilization and possess unique electronic structures are another research direction. Li and co-workers prepared the In single atom electrocatalyst by pyrolysis of $In(AcAc)_3$@ZIF-8.[128] The isolated $In^{\delta+}$-N_4 atomic offers active site rich interfaces for CO_2RR to formate with high efficiency (96 % and 8.87 mA cm^{-2} at -0.65 V vs. RHE) in 0.5 M $KHCO_3$ electrolyte.

The research activity on Pb is significantly less than the above mentioned three metals, due to its high toxicity for humans and the environment. However, there are some excellent studies on Pb-based electrochemical CO_2RR. Yeo et al. prepared the PbS derived Pb (SD-Pb), with wafer structures oriented edge-on, and PbO_x derived Pb (OD-Pb), with contiguous and rounded structures as shown in Figure 1.6d.[111] They discovered that SD-Pb has a distinctly larger current density (~ 12 mA cm^{-2}) and the $FE_{formate}$ reached 88 % at -1.08V vs. RHE (see Figure 1.6e and f), demonstrating that the morphology of Pb cathodes greatly influenced the CO_2RR activity. Tavares and co-workers explored the function of amine for CO_2RR by grafting the 4-aminomethylbenzene (grafting extent: 6.3×10^{-7} mol cm^{-2}) on the surface of Pb electrodes.[112] This amine-modified Pb showed enhanced current density (24.0 mA cm^{-2} at -1.29 V vs. RHE)

and higher Faradaic efficiency toward formate (> 80 %) in 1 M $KHCO_3$ compared to the bare Pb.

Antimony (Sb) is another p-block metal that has been identified as an active catalyst for CO_2RR to formate. Zhang et al activated the bulk Sb metal by cathodically exfoliating bulk Sb into 2D "few-layer" Sb nanosheets (SbNSs) on to the graphene exfoliated from graphite to form graphene-Sb (SbNS-G) (see Figure 1.6 g-i).[113] A maximum Faradaic efficiency of 84 % was obtained at −1.06 V vs. RHE but at a relatively low current density of ~8 mA cm^{-2}.

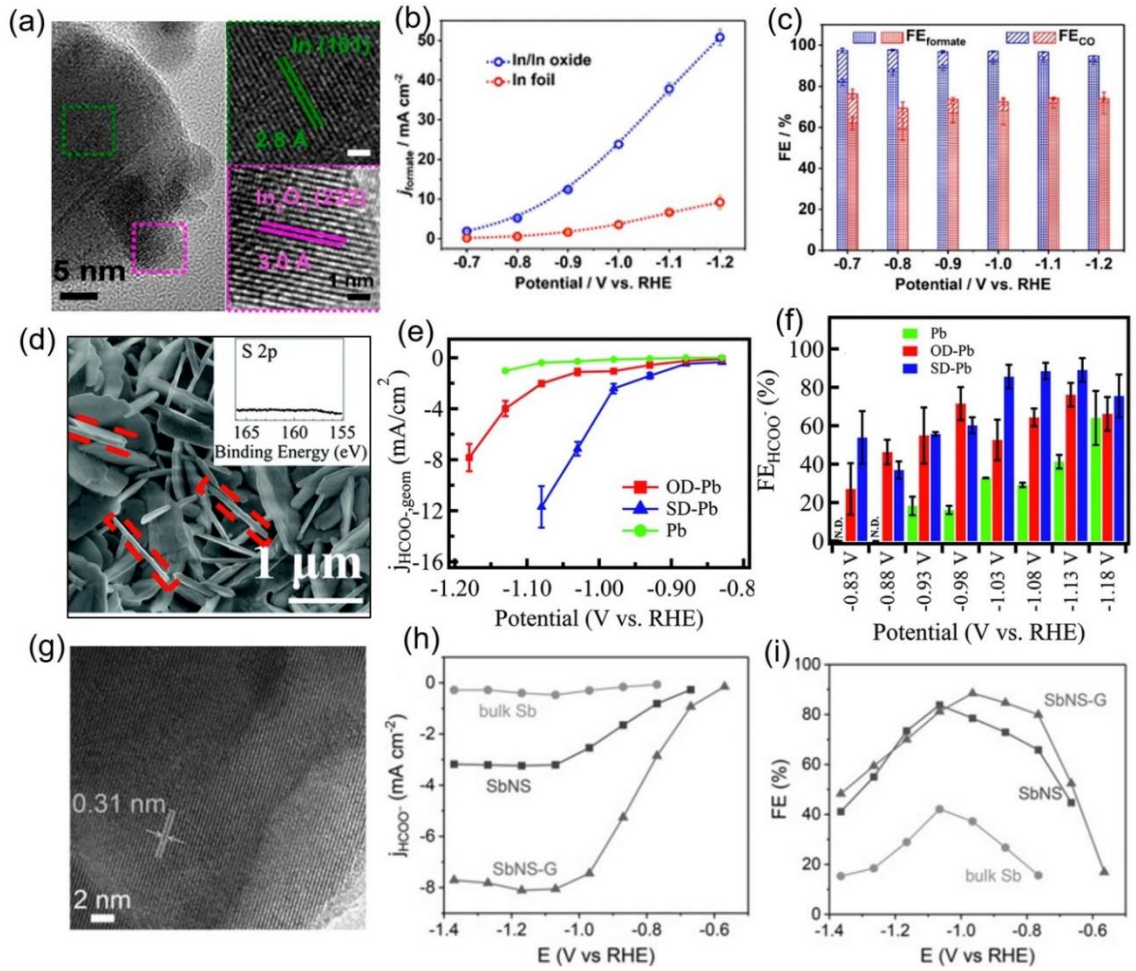

Figure 1.6 Characterization and performance of In, Pb and Sb based catalysts. (a) HRTEM image of the In/In oxide heterostructures, (b) $j_{formate}$ and (c) FEs of formate and CO production for the In foil and In/In oxide heterostructures in CO_2-saturated 0.5 M $KHCO_3$. Reproduced

with permission.[109] Copyright 2020, American Chemical Society. (d) SEM image of PbS derived Pb (SD-Pb) after pre-reduction, (e) $j_{formate}$ and (f) $FE_{formate}$ of polished Pb, PbO_x derived Pb (OD-Pb), PbS derived Pb (SD-Pb) in CO_2-saturated 0.1 M $KHCO_3$. N.D. means 'Not Detected'. Reproduced with permission.[111] Copyright 2019, The Royal Society of Chemistry. (g) HRTEM image of Sb nanosheets, (h) $j_{formate}$ and (i) $FE_{formate}$ of Sb, SbNSs, SbNS-G in CO_2-saturated 0.5 M $NaHCO_3$. Reproduced with permission.[113] Copyright 2017, Wiley.

1.3.2 Transition metal-based electrocatalysts (Pd, Cu, Co)

Copper is a versatile CO_2RR catalyst, and has ability to electro-reduce CO_2 to various products such as CO, HCOOH, CH_4, C_2H_4, C_2H_5OH and C_3H_7OH. The unique property of copper results from its specific electronic structure and the corresponding moderate binding energy for CO* intermediates, which makes it difficult to obtain high selectivity toward a particular product at the low overpotential region. However, by properly regulating catalyst surface structure and the local CO_2RR environments, Faradaic efficiency for formate production can be tuned and promoted. Wang and co-workers modified copper by cetyltrimethylammonium bromide (CTAB).[117] This modification leads to a Tafel slope value of 110 mV dec^{-1} in the mid-overpotential range, indicating that the rate-determining step is the HCOO* desorption. The HCOO* desorption step was found to be greatly improved by Cu-CTAB interaction leading to a high formate Faradaic efficiency of 82 % at -0.5 V vs. RHE (see Figure 1.7b and c). Recently, Zhang et al. designed bimetallic catalysts by incorporating second elements such as Cd, Sb, Pb, and Zn.[129] They found that the formate selectivity can be enhanced in the order of Cu-Cd > Cu-Sb > Cu-Pb > Cu-Zn at a high current density of about 30 mA cm^{-2}

Pd is an attractive metal for CO_2RR to formate, having a relatively low overpotential compared to that of the p-block post-transition metals such as Sn, and Bi. According to Min and Kanan, the outstanding formate efficiency originates from the surface hydride, PdH, which

is the equilibrium state when Pd electrode is held at < 0 V vs. RHE due to its strong H binding.[66] Bao and co-workers further investigated the relationship between phase and selectivity by in-situ X-ray absorption spectroscopy (XAS), in-situ attenuated total reflectance-infrared spectroscopy (ATR-IR), and density-functional theory (DFT) calculations.[67] Their results revealed high potential dependencies of the selectivities of different products (~98 % from -0.1 V to -0.2 V vs RHE) in 1 M $KHCO_3$. The hydrogen can be adsorbed on the Pd surface and form α+β PdH_x@PdH_x (α+β PdH_x is the mixture of α- and β-phases of PdHx core) when above -0.2 V vs. RHE, which facilitates the formation of *OCHO intermediates toward formate production (see Figure 1.7d and e). However, at below -0.5 V, the catalyst surfaces turned to metallic Pd and the β PdH_x @Pd which promotes CO production via the *COOH route. Recently, most Pd-based studies are on Pd containing alloys, such as Pd-Ag,[115] Pd-Cu,[116] and Pd-Sn.[120] These designs overcome the challenges of the Pd catalyst's instability and operation at low current densities, while synergistically promote the merits of Pd low overpotential and high selectivity. The details of alloying strategies will be discussed in the next section.

Cobalt is a transition metal with strong oxygen and hydrogen affinities. These features may suit better for hydrogen evolution reaction, but tailored catalyst structural engineering would create abundant active sites for highly selective CO_2RR to formate. An excellent example is the work by Xie and coworkers of the partially oxidized Co nanosheets (4-atom-thick) synthesized using a ligand-confined growth strategy. The increased electrochemical-active-surface-area of these ultrathin nanosheets is calculated to be 5-fold higher than that of the Co particles.[119] High formate Faradaic efficiency of 90.1 % at - 0.85 V vs. SCE and stable current density (~ 10 mA cm^{-2}) were achieved on this partially oxidized Co 4-atom-thick layer catalyst (see Figure 1.7f-i). They further prepared thick Co_3O_4 nanolayers with a thickness of 1.72 nm

by a fast-heating strategy.[121] These facilely synthesized nanolayers exhibited formate Faradaic efficiency of over 60 % in 20 h due to the nanolayers' rich active sites and high conductivity.

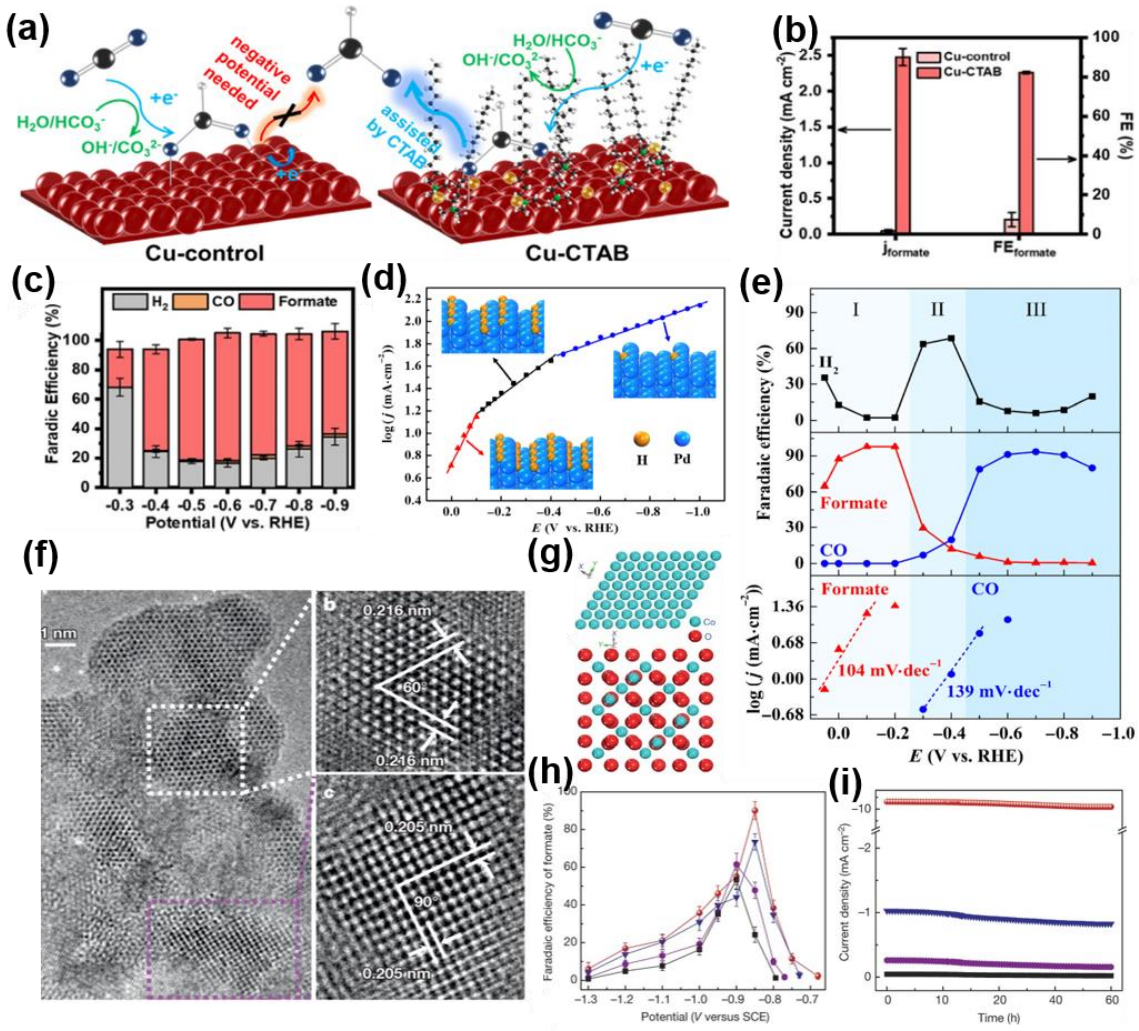

Figure 1.7 Characterization and performance of Cu, Pd, and Co based catalysts. (a) Schematic illustration of the CO_2RR to formate pathways on Cu and Cu-CTAB; (b) Current density and Faradaic efficiency comparison of Cu and Cu-CTAB at -0.5 V vs. RHE in CO_2-saturated 0.5 M $KHCO_3$; (c) Faradaic efficiency of Cu-CTAB at different operating potentials. Reproduced with permission.[117] Copyright 2020 American Chemical Society. (d) Current densities of the 3.7 nm Pd with respect to the potential and the atom configuration of Pd and H at the surface; (e) Faradaic efficiencies for the production of H_2, formate, and CO, with respect to the potential and the Tafel plots for formate and CO in 1 M $KHCO_3$. Reproduced with permission.[67] Copyright 2017 American Chemical Society. (f) High-resolution TEM images of partially

oxidised Co nanolayers; (g) schematic atomic models with distinct atomic configuration corresponding to the hexagonal Co and cubic Co_3O_4; (h) Faradaic efficiencies of formate production at each potential from -1.3 V to -0.7 V vs. SCE in 0.1 M $KHCO_3$ (samples and the corresponding colours: partially oxidized Co 4-atom-thick layers: red; Co 4-atom-thick layers: blue; partially oxidized Co: violet; and bulk Co: black); (i) chronoamperometry results at the potentials in (h) with respect to the maximum Faradaic efficiencies. Reproduced with permission.[119] Copyright 2016 Nature Publishing Group.

1.3.3 Catalyst design strategies

As the CO_2RR to formate is a surface and environment sensitive process involving complex reaction pathways and various intermediate species, it is essential to have a brief discussion about the current prevailing catalyst synthesis strategies. The key strategies from the aspects of morphology regulation, crystal facet tailoring, defect engineering, alloying treatment, surface modification, molecule catalysts and single atom catalysts are summarised in Figure 1.8.

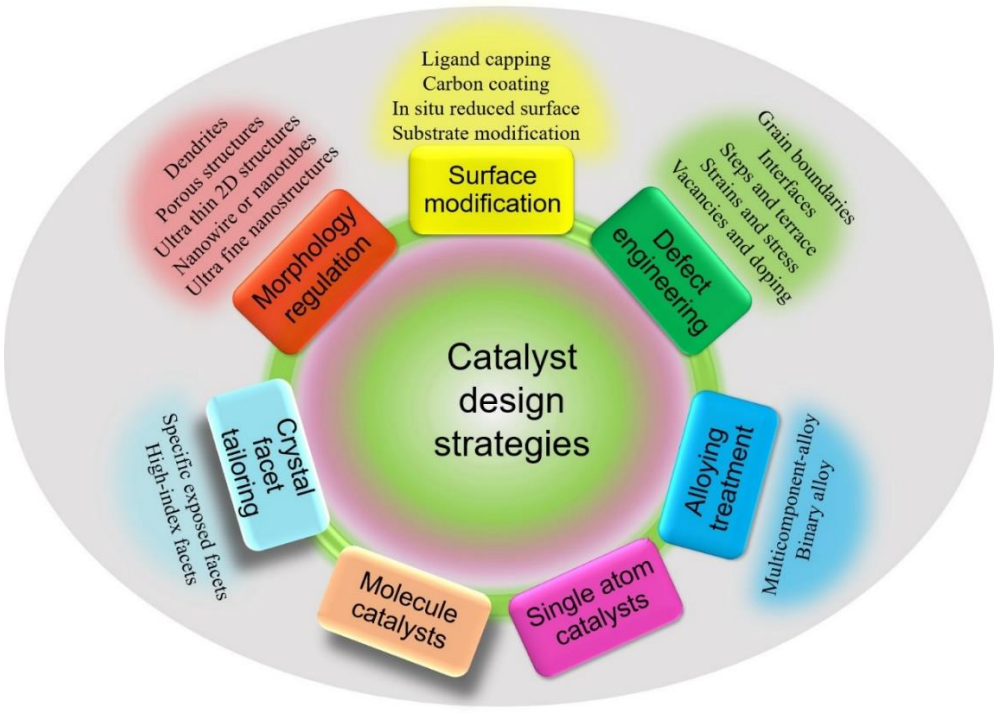

Figure 1.8 Summary of electrocatalyst design strategies for CO_2RR to formate.

Crystal facet is a significant parameter for CO_2RR electrocatalyst design. Tailoring the crystal facet could lead to high formate selectivity, especially for some catalysts whose activity are closely facet-dependent. For a certain catalyst, the specific exposed facets toward CO_2RR products are different due to the varied binding energy for each intermediate. Miller indices (*h*,*k*,*l*) are commonly used in crystal facet study. The nanocrystal catalysts can be classified into two groups: low-index-faceted (h, k, l are all small, or $h + k + l \leq 3$) and high-index faceted (at least one of the Miller indices is greater than 1). The high-index crystalline catalysts have aroused great attention as the energy required for the reaction can be lowered. Min et al. reported a hierarchical Bi dendrite catalyst with high index planes for efficient CO_2 reduction.[96] The good performance (~ 89 % and 2.7 mA cm^{-2} at - 0.74 V vs. RHE) and good durability (~12 h) in 0.5 M $KHCO_3$ can be explained by the DFT results that show the high index planes ((012), (110), and (104)) on dendrites favour the *OCHO intermediates over the *COOH. Sargent and co-workers elucidated the relationship between high-index surfaces and the CO_2RR to formate activities using computational modellings.[130] They then synthesized Pd nanostructures, and experimentally identified that the high index surfaces can improve the catalyst's stability and selectivity.

The morphology of a catalyst can significantly influence the catalysis process as catalysts with different length scales from macroscale to nanoscale or even atomic level could result in substantial variations in catalytic performance. The surface structures such as exposed crystal facets and surface defects are closely related to the morphology and the shape, which could retrospectively influence the mass transfer of reactants and products, hence electrocatalytic performances. Ultrafine nanoparticles are attractive as this morphology promotes the active sites and expose more formate-favoured crystal facets.[131] However, the smallest nanocatalyst does not necessary lead to the best performance. For example , Broekmann et al found that the

best formate selectivity was achieved using 6.5 nm Pd nanoparticles (98 % at 1.5 mA cm^{-2} at -0.1 V vs. RHE) in 0.5 M $NaHCO_3$, instead of the 3.8 nm Pd (86 % at -0.1 V vs. RHE). They proposed that the 6.5 nm Pd has better counterbalancing between CO_2RR and hydrogen evolution reactions.[132]

For the p-block post-transition metal catalysts, layered structures are the preferable morphology. Nanolayers of SnO_2, SnO, SnS, SnS_2, Bi, and Pb, can be facilely prepared by hydrothermal or exfoliation. The layered catalysts not only possess all the advantages of 2D materials in electrochemistry, such as abundant active sites and high conductivity, but also have exposed facets favourable for formate production.[133] There are also other diverse morphologies such as dendrites,[96] nanowires,[134] nanotubes,[91] and mesoporous structures[115] that can promote the formate selectivity. However, such nanostructured morphology could affect the local environments such as the CO_2 concentration and pH, which should be taken into account when designing the catalysts.[65]

Alloying strategies have resulted in the formation of bimetallic catalysts with unique synergetic characteristics that differ from a single metal due to the interaction at the heterometal interfaces. For example, alloys which are combinations of two metals from Sn, Bi, In, and Pb may have favourable performances over those of the single metals alone. Chen et al. have experimentally and theoretically studied the enhancement due to Sn-Bi alloy nanocatalyst in CO_2RR to formate.[86] They found that the interaction between Sn and Bi results in the upshift of the p and d orbitals of Sn electron states, and the electron density from more electronegative O atoms is readily transferred to the p and d orbitals of Sn, which greatly boosts the intermediate toward formate production (96% in $FE_{formate}$ with ~ 55 mA cm^{-2} at −1.1 V vs RHE in 0.5 M $NaHCO_3$). Sun and co-workers prepared the activated carbon supported Pd-Sn alloy nanoparticles via a modified wetting chemistry reduction method.[120] Using a Pd and Sn atomic

composition ratio of 1:1, a high Faradaic efficiency of > 99% toward formic acid was achieved at the low overpotential of -0.26 V with the current density of 2 mA cm^{-2}, where both CO and H_2 evolution were completely suppressed. Their DFT results identified the $HCOO^*$ intermediate-involved pathway is preferable on this Pd-Sn alloy surface. Gunji et al also studied the Pd-based alloys for CO_2RR to formate and formulated a relationship between the formate selectivity and the secondary elements.[116] They found that the secondary elements with relatively small atomic radii, such as Zn and Cu, can help form ideal surfaces for the adsorption of the OCHO intermediates for formate due to the doping of Zn and Cu in the Pd lattice, resulting in a record $FE_{formate}$ of 99.4 % at -0.1 V on Pd-Zn and 65 % at - 0.4 V on Pd-Cu alloy catalysts. Cu-based alloys, such as Cu-Cd and Cu-Sb can promote Cu's selectivity toward formate, according to the systematic study by Zhang et al.[129] They attributed the excellent performance of Cu-Cd (70.5% at -1.05 V vs RHE with the current density of 26.8 mA cm^{-2}) and Cu-Sb (~ 60 % at - 0.95 V vs RHE with the current density of ~ 25 mA cm^{-2}) to the better binding affinity toward $OCHO^*$ instead of H^* at the new interfaces.

Defect engineering has become an increasingly important strategy in tuning the catalysts' intrinsic activities. Defects such as vacancies of anion or cation, grain boundaries and interfaces, doping, steps and terraces, and lattice distortions could alter the electron density near the Fermi level and the orbital hybridization, forming dangling bonds, which could induce more active sites. As listed in Table 1.1 and presented in Figure 1.4e-h, oxygen hole defects on SnO_2 nanoparticles have greatly influenced the CO_2RR performance.[72] The amount of oxygen hole centres tuned by flame spray conditions resulted in CO_2 activation and enhanced formate selectivity (85 % with a high partial current density of -23.7 mA cm^{-2} at -1.1 V vs. RHE). Zeng and co-workers regulated the activity of SnS_2 nanosheets by introducing Ni.[135] The Ni-doped SnS_2 has a defect level below the conduction band and thus narrows the band gap from 2.3 eV

of SnS_2 to 1.9 eV. The decreased work function helps to improve the electron transfer process, thus achieving an efficiency of 80 % at 29.5 mA cm^{-2} and -0.9 V vs. RHE on 5% Ni-SnS in 0.1 M $KHCO_3$.

Surface modification plays a key role in electrocatalysis, as the key steps including CO_2 adsorption, electron transferring, proton transferring, and product desorption all occur at the catalytic interface, and most of the above discussed strategies involve catalyst surface optimization. In addition, some direct surface modification strategies can greatly change the physical or chemical properties. Oxide layer,[136] carbon layer,[137] or hydroxyl layer[76] are all proven to be effective for formate production activity as they can change the adsorption energies and the reaction pathways. In addition, ligands such as CTAB[117] and amine[112] can be grafted on catalysts to tune the selectivity of formate, as those ligands can interact with catalysts and change the rate determining step. As mentioned in Table 1.1 and Figure 1.7a-c, the CTAB ligands can greatly improve the selectivity of Cu catalysts by promoting desorption of HCOO* (Rate Determining Step). However, it should be noted that some ligands on the surface may cause surface blocking, which could suppress the CO_2RR activity or product selectivity.[70] Clean surfaces obtained by in-situ preparation methods are becoming popular since these strategies minimise the contamination or the surface being oxidized when exposed in air. The most commonly used in-situ preparation method is electrochemical transformation during the initial CO_2RR performance test. Wang et al.[84] and Li et al.[127] employed the in-situ reduction strategy to synthesis Bi-based nanostructures and obtained excellent formate selectivity (> 80 %). Bao et al. in-situ reconstructed the Sn/SnO_x interface under the cathodic potentials of CO_2RR on $Sn_{2.7}Cu$ catalysts and obtained an efficiency of 83.0 ± 1.7 % at 404.7 ± 14.4 mA cm^{-2} in 1 M KOH in a flow-cell when cathodic potential was more negative than -0.93 V vs. RHE.[84] According to the DFT results, the binding of *OCHO can be weakened and

the hydrogen evolution can be significantly inhibited at these in-situ formed Sn/SnO_x interfaces, evidently in comparison to the controlled Sn(211) and reduced SnO_2(110) surfaces.

Single atom catalysts gradually aroused interest due to the development of advanced fabrication technology. When dispersed into monodispersed atoms, the electronic structure of the active components can be totally different from the nanostructures or microstructures. In addition, the highly dispersed species reduces the amount of required catalyst, which is particularly beneficial for expensive noble metal-based catalysts. Xie and co-workers synthesized kilogram-scale single-atom $Sn^{\delta+}$ on N-doped graphene by a freeze-vacuum-drying-calcination method.[138] In this catalyst, the atomically dispersed Sn are positively charged. By stabilizing $CO_2^{\cdot-}$* and $HCOO^-$*, the CO_2 activation and protonation can proceed spontaneously according to the results of in-situ Fourier transform infrared spectra and Gibbs free energy, facilitating a formate efficiency of 74.3% with a current density of 11.7 mA cm^{-2}, at -1.6 V vs. SCE in 0.25 M $KHCO_3$. The isolated $In^{\delta+}$-N_4 prepared by pyrolysis of In-based MOF by Shang et al. has larger electrochemical surface area (ECSA) and smaller charge transfer resistance (Rct) compared with In nanoparticles.[128] The high catalytic activity and selectivity (96 % and 8.87 mA cm^{-2} at -0.65 V vs. RHE in 0.5 M $KHCO_3$) might be attributed to the bond-length-shortened $In^{\delta+}$-N_4 sites, according to the results of potential-dependent in-situ XAFS. However, the literature reported selectivity has inconsistencies as the single atom catalysts prepared by different groups resulted in different main products. For example, Zeng et al. anchored the Bi single atoms on carbon black and achieved a formate selectivity of more than 90% at a wide potential range of -0.8 to -1.2 V vs. RHE in 0.1 M $KHCO_3$.[100] However, the Bi-N_4 sites on porous carbon networks prepared by Li et al. obtained a high CO conversion efficiency of up to 97 % at a low overpotential of 0.39 V in 0.1 M $NaHCO_3$, as the *COOH intermediate can be rapidly formed with a low free energy barrier on single-atom Bi-N_4 sites.[139] Further detailed

studies about the intrinsic differences, including local electronic and atom environment, and the corresponding mechanisms are still required.

In summary, the development of formate producing catalysts of both p-block post-transition and transitional metals have achieved great progress in recent years. However, at present, Sn and Bi are still the most promising CO_2RR to formate catalysts due to their low toxicity, high formate selectivity, and excellent stability. This is particularly the case when in comparison to the toxicity of Pb, Sb, and Co, poorly selective Cu, and high cost Pd and In. Significant progress has been made to tune the active sites of catalysts from both the aspects of intrinsic activity and site density via advanced synthetic techniques. Although the two-electron transfer reaction of CO_2RR to formate is relatively simple compared with other multi-carbon CO_2RR products, the effects of catalyst modifications are complex seeing as a slight change could affect the structure and influence the performance. It is unambiguously necessary to divide those influences and formulate a relationship with respect to the modification strategy, the catalyst structure, and the performance. Therefore, precise control of the catalyst structures should be developed to maximise the activity of catalysts.

1.4. Cell design for electrochemical CO_2 reduction to formate

The configuration and design of the CO_2 electrolysers play a key role in the electroreduction performance, particularly in achieving industrially relevant high current densities. The major influencing parameters of cell design are the reactant (CO_2) and product mass transports, the cell resistance, and the kinetics of the catalytic process. Retrospectively, the type of ion-exchange membrane, electrolytes, and reactant feeding modes would be influential.[140-141] Two most commonly employed electrochemical cells are the H-type cell and continuous flow-cell.

The former is widely used for fundamental studies, whilst the latter is relevant and closer to commercial electrolysers designed for industrial CO_2RR.

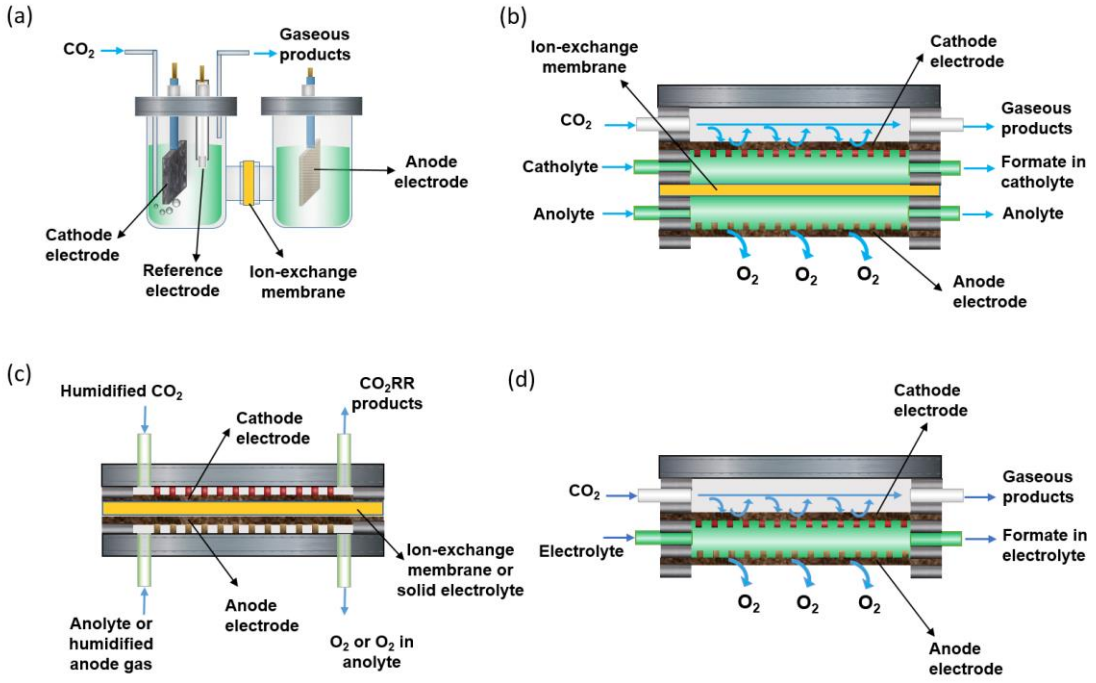

Figure 1.9 Cell configurations for electrochemical CO_2RR to formate. (a) H-cell, (b) standard flow-cell, (c) liquid-catholyte-free flow-cell, and (d) microfluidic flow-cell.

1.4.1 H-cell

The conventional H-cell, or H-type cell (Figure 1.9a) has been widely employed for CO_2 reduction as this design is suitable to study half-cell reactions and convenient to screen suitable electrocatalysts at a laboratory scale. The CO_2-saturated HCO_3^- aqueous solutions are the most commonly used electrolyte as it is a reservoir of carbon source. The CO_2RR product, formate, is present in a liquid-phase and dissolved in the electrolyte. An ion-exchange membrane is usually inserted between cathode and anode chambers to avoid formate product crossover and reoxidation at the anode compartment. There are three main types of ion-exchange membranes:[140] (1) cation exchange membrane (CEM) which favours the transport of cations

such as protons; (2) anion exchange membrane (AEM) driving OH^- or HCO_3^- to the anode; (3) bipolar membrane (BPM) facilitating the exchange of OH^- and H^+ to the anode and cathode, respectively.

The most popular membrane is the CEM, such as the nafion membrane in an H-cell employing bicarbonate electrolyte. However, the CO_2 mass transport issue due to the low CO_2 solubility in the electrolyte limits the enhancement of current density (less than 100 mA cm^{-2}) and has little prospect for industrial application. The large volume of catholyte in the H-cell also makes it difficult to quantify the formate when its concentration in the electrolyte is low. AEM is less commonly used within the H-cell configuration for CO_2RR to formate study, but is popular in flow-cell tests in concentrated alkaline electrolyte. However, the $HCOO^-$ ion might crossover to the anode chamber through the AEM, which should be taken into consideration when quantifying the products. Anolyte and catholyte can be independently chosen with BPM as separator as long as they are not electrochemically active and do not react with CO_2. This type of membrane allows highly caustic anolytes with pH values up to 14 to be employed in an H-cell.

1.4.2 Flow-cell

Depending on the fluid type and the configuration of the cathode chamber, flow-cells can be divided into: standard flow-cell, liquid-catholyte-free flow-cell, and microfluidic flow-cell (see Figure 1.9). The advantages and limitations of different cell types are summarized in Table 1.2. Generally, a flow-cell can partially address the mass transport issue by circularly pumping reactants to the working electrode and timely removal of products away from the chamber, thus obtaining greatly enhanced performance which may meet the high current density and efficiency required by industry. Figure 1.10 compares the literature obtained current densities

for formate production from various catalysts performed in H-cells and flow-cells. The current densities of CO_2RR in H-cell are consistently lower than 100 mA cm^{-2}, whereas those in flow-cell configurations are capable of reaching several hundreds of mA cm^{-2}. Details of different flow cells are described below:

1.4.2.1 Standard flow-cell

The electrolyser with a flowing catholyte is the most common flow-cell employed in electrochemical CO_2RR. The electrocatalysts are usually loaded on a porous gas diffusion layer (GDL) with low mass transfer resistance, large surface area for active species anchoring, and high conductivity. An ion exchange membrane is assembled between catholyte and anolyte to avoid the formate crossover and reoxidation at the anode compartment. Feeding-rate controllable catholytes can be flowed into the cathode chamber using a peristaltic pump. The gaseous CO_2 is flowed through the porous carbon layer with a short diffusion pathway (~50 nm) to reach the surface of catalysts and form abundant triple-phase boundaries (solid catalyst-liquid electrolyte-gaseous CO_2).[27] It is worth noting that the CO_2 gas can be electrochemically reduced at the triple-phase boundaries before dissolving and reacting with the electrolyte, which extends the electrolyte types. For example, alkaline solutions are unsuitable to be applied in a H-cell study as CO_2 can react with OH^- to form carbonate and bicarbonate ions prior to the electroreduction of CO_2. However, in the flow-cell configuration, CO_2 and electrolyte are separated by the gas diffusion electrode, making it possible to realize the high CO_2RR rate at the triple-phase boundaries. It was found that an alkaline electrolyte could create an environment which favours CO_2RR to formate, instead of other hydrocarbon products or H_2. Sargent and co-workers proposed that the hydronium ions can be destabilized in highly concentrated KOH, resulting in lower reaction energy barrier for *OCHO than the *COOH intermediate.[49, 60] In addition, the slow kinetics of water dissociation in alkaline conditions

result in an hydrogen evolution rate that is two orders of magnitude lower than that in acidic or neutral media.[142-143] Moreover, alkaline electrolytes have a much lower solution resistance than bicarbonate electrolyte, thus reducing the cell overpotential. Xia et al compared the current density and the selectivity of Bi_2O_3-C catalysts in KOH electrolyte-involved flow cell and $KHCO_3$ electrolyte-involved H-cell.[144] They found that the current density can be increased from 12.4 mA cm^{-2} in an H-cell to 208 mA cm^{-2} in a flow-cell with retention of formate conversion (92 - 93 %) at -1.1V vs. RHE.

1.4.2.2 Liquid-catholyte-free flow-cell

Another important flow-cell design is the liquid-catholyte-free flow-cell which requires only humid CO_2 gas flowing through the cathode chamber without circulation of liquid catholyte. The zero gap sandwich structure, where the cathode and anode catalysts layers are coated on each side of an ion-exchange membrane, is one of the ideal designs. This configuration has reduced ohmic losses and possibility of poisoning from the electrolyte. This sandwich configuration offers a key advantage of the cell as several cells can readily be stacked for industrial large-scale operation. The ion exchange membrane facilitates ions exchange between the anodic and cathodic compartments with attenuated product crossover. The porous GDL with excellent mechanical strength offers channels to maximise transport of humid CO_2. In addition, the liquid-catholyte-free design affords the possibility of operating the cell at a high temperature. Park et al. used the CO_2RR performance of commercial tin nanoparticles in a catholyte-free full flow-cell.[145] The current density reached 52.9 mA cm^{-2} when the reaction temperature rose to 363 K and a high formate concentration of 41.5 g L^{-1} was obtained at 343 K with high formate Faradaic conversion efficiency (93.3 %) at a voltage of 2.2 V. Solid electrolyte type flow-cell can also be classified in this group since it needs the humid CO_2 as well. Wang and co-workers employed the high formate selectivity (> 90 %) Bi as the catalysts

in a solid state electrolyte ($Cs_xH_{3-x}PW_{12}O_{40}$) -based flow-cell.[146] The formate product was generated via the ionic recombination of crossed ions at the interface between the middle channel of the solid state electrolyte and the membrane, resulting in a stable and continuous generation of 0.1 M HCOOH solution with negligible degradation in selectivity (> 80 %) and activity in 100h. However, it should be noted that the liquid formate or formic acid might flood back into the GDE layer and block the flowing CO_2, which is one of the key challenges in developing durable and stable humid CO_2 fed flow-cell.[147]

1.4.2.3 Microfluidic flow-cell

The microfluidic flow-cell in Figure 1.9d has a thin channel (<1mm) between the anode and cathode that allows for the flowing electrolyte. In this cell, precise control of the channel parameters and the electrolyte flow is critical for sufficient product separation. The compact cell design makes it possible to obtain high CO_2 mass transfer rate and excellent selectivity at a high current density. Moreover, fast screening of optimal catalysts and operating conditions can be achieved in this configuration. Lu and co-workers compared the CO_2RR to formate performance between the microfluidic flow-cell and H-cell using 2D SnO_2 nanosheet catalysts.[148] A current density of 471 mA cm^{-2} and a high Faradaic efficiency of 94.2 % were achieved at -1.13 V vs. RHE in the microfluidic flow-cell, whereas the H-cell only obtained 30 mA cm^{-2} at -1.3 V vs. RHE. In another example, Kenis et al. employed the microfluidic flow-cell in CO_2RR to formic acid using a Sn cathode, and reached high efficiencies (89 % faradaic and 45 % energetic) and current densities of the order of 100 mA cm^{-2}.[149]

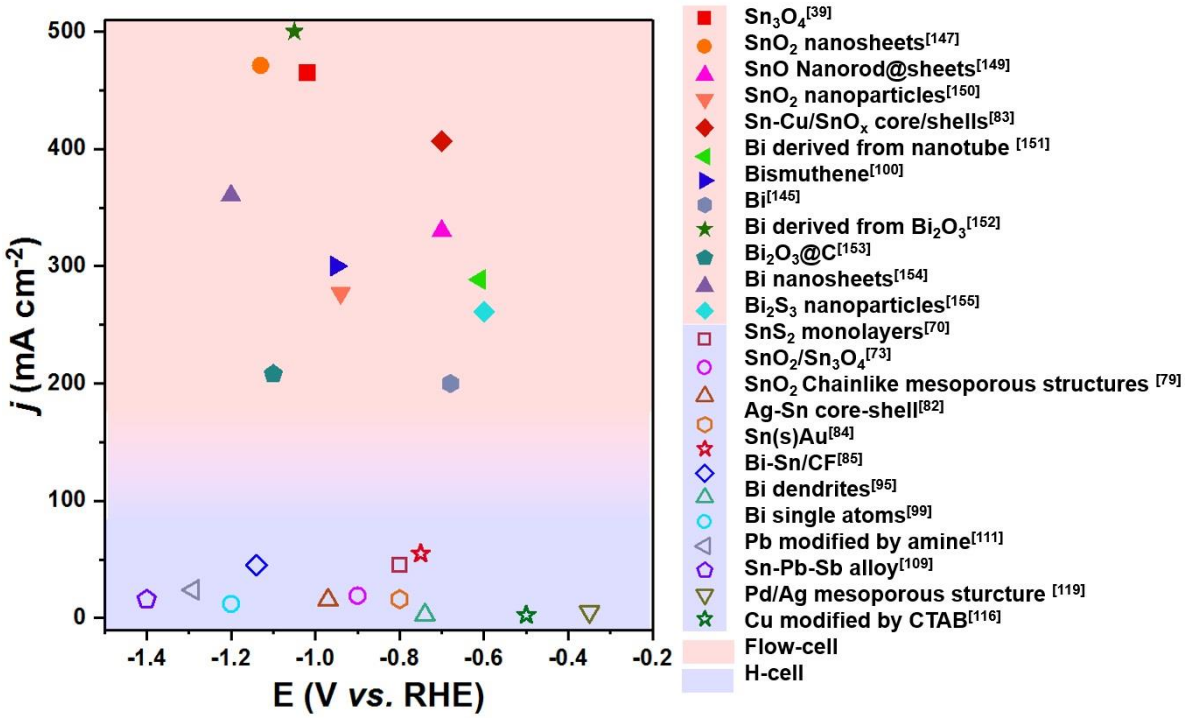

Figure 1.10 Comparison of current densities of CO_2RR to formate based on literature obtained values using various catalysts derived from the H-cell and flow-cell configurations.

Table 1.2 Advantages and limitations of different reactors

Reactor type		Advantages	Drawbacks
H-cell		Easy operation Wide cathode option range Ease of catalyst screening	Poor CO_2 mass transfer Additional resistance loss due to membrane Limitation in detection of trace formate products Limitation for large-scale application
Flow-cell	Standard flow-cell	High CO_2 mass transfer Low cell resistance Wide catholyte range Ease of cell stacking Minimises the pH change effects	Additional resistance loss due to membrane External pump for electrolyte circulation is required Carbonate generated when using neutral or alkaline electrolytes Electrolyte flooding at GDE
	Catholyte-free flow-cell	No liquid catholyte is required High mass transfer of CO_2 Ease of cell stacking Offers durable and stable system	Corrosion of electrode substrates and polymer electrolyte membranes at a high potential Membrane or solid electrolyte is required Liquid formate flooding to GDE
	Microfluidic flow-cell	High mass transfer of CO_2 No membrane is required Less flooding/dry out at cathode Fast catalyst screening	Formate crossover and reoxidation at anode Pressure sensitive

1.4.3 Full cell assemblies

To date, most of the studies on CO_2 reduction is focused on the cathodic half-cell reactions employing a three-electrode system. [157-159] In this system, the potential of the working electrode is obtained with reference to reference electrodes such as Ag/AgCl,[160] calomel,[161] or Hg/HgO

electrode,[162] with a stable, consistent, and large surface area counter electrode that would not limit the reaction at the working electrode. Hence, the applied voltage is the difference between the working electrode and the reference electrode. This half-cell study has been widely employed for catalyst screening and fundamental studies in which the catalysts' activities can be evaluated and readily compared via a convertible reference potential.

A full cell system, commonly using a two-electrode system consisting of an anode and a cathode, is more practical and closely related to commercial industrial cells.[163-164] In a full cell, the CO_2 reduction catalyst is employed at the cathode for the reductive process, and the counterpart can be an oxidative reaction (commonly oxygen evolution reaction), as well as potentially other reactions such as hydrogen[153] and glycerol oxidations[165-166] at the anode. The voltage of the cell refers to the voltage difference between an anode and a cathode. Based on the kinetic overpotentials of CO_2 reduction reaction (CO_2RR) in the cathodic process, and the counterpart anodic process, as well as the cell Ohmic resistance, the cell voltage (E_{cell}) can be calculated from Eqn. (1):[157]

$$E_{cell} = E^0_{cell} + \eta_c + \eta_a + j \cdot R_{ohmic} \qquad (1)$$

where E^0_{cell} corresponds to the reversible voltage (for CO_2RR to formate: 1.34 V), $j \cdot R_{ohmic}$ refers to the voltage loss caused by Ohmic resistance arising from potential sources of resistances such as electrolyte, membrane, electrical wiring connection and gas bubbles. η_c and η_a are the overpotentials of the cathodic CO_2RR and the counterpart anodic half-cell reactions.

There are not many literatures reporting on the full cell for the CO_2RR to formate. Figure 1.11a shows the schematic of a full cell assembly under an electrochemical flow configuration that

was employed by Zhou et al., with key components of Sn-based cathodes (thermal treated Sn NPs at 180 ^{o}C and the native Sn NPs), Pt anode for OER, and Nafion® 212 membrane.[136] This configuration adopts a buffer layer of the liquid phase electrolyte circulating between the cathode and the membrane. In this cell, high formate conversion Faradaic efficiency of ~ 80 % was achieved at -2.0 V on thermal treated Sn NPs (Figure 1.11b). Yang and co-workers assembled a full cell using a tin cathode and IrO_2 anode separated by a centre flow compartment bounded by an anion exchange membrane (Dioxide Materials Sustainion™) at the cathodic compartment, and a cation ion exchange membrane (Nafion® 324) at the anodic compartment (Figure 1.11c).[167] Note that the centre compartment contained a cation ion-exchange resin media to provide conductivity and continuously flowed by deionized water. A maximum $FE_{formate}$ of ~ 90 % was achieved at a single pass flow-rate of 0.5 mL min^{-1}. They experimentally demonstrated the stable operation of cell voltage and product output for 500 h (Figure 1.11d) at 140 mA cm^{-2}. They proposed that the formate crossover through the membrane was substantially reduced by utilizing a Nafion® 324 membrane. Table 1.3 summarizes the literature performance of electrochemical CO_2 reduction to formate in full cells employing various catalysts, cell configurations, and electrolytes. Sn and Bi based catalysts are the most commonly employed CO_2RR catalysts, affording Bi nanostructures that achieve relatively high current densities. Most of the anodes employed high-cost precious metal catalysts such as Ir and Pt.

Table 1.3 CO_2RR to formate performance in full cells comprising various cell configurations, electrolytes and catalysts.

Catalysts	Cell type	Electrolyte	Anode	$FE_{formate}$	j (mA cm^{-2})	Ref.
Bi nanoparticles -C	Flow-cell	0.5 M KCl + 0.45 M $KHCO_3$	Ir-MMO (mixed metal oxide) on Pt	89.5% at 90 mA cm^{-2}	300 mA cm^{-2} at cell voltage of 5.4 V	[168]
Sn cathode	Flow-cell	Sustainion ™ anion membrane electrolyte	IrO_2	~ 90% at the flow rate of 0.5 mL min^{-1}	200 mA cm^{-2} at the cell voltage of ~3.73 V	[167]
Sn nanoparticles	Catholyte - free flow cell	Nafion 115 membrane	Pt gauze	93.3 % at cell voltage of 2.2 V	52.9 mA cm^{-2} at cell voltage of 2.2 V	[145]
Sn	Flow-cell	0.1 M $KHCO_3$	Pt GDE	~80% at cell voltage of 2.0 V	3 mA cm^{-2} at -1.2 V	[136]
Bi derived from Bi_2O_3	Flow cell	Solid state electrolyte	IrO_2-C	97% at cell voltage of 1.51 V	440 mA cm^{-2} at cell voltage of 2.19 V	[153]
SnO_2/CNT	Micro flow cell	1 M KOH	CoO_x/CNT	82 % at cell voltage of 2.5 V	200 mA cm^{-2} at cell voltage of 2.9 V	[169]
Sn	Flow cell	0.45 M $KHCO_3$ + 0.5 M KCl	Ir-MMO on Pt	71.4% at cell voltage of 2.79 V	12.25 mA cm^{-2} at 2.79 V	[170]
Pb powder	Alkaline polymer electrolyte membrane cell	1 M $NaHCO_3$	Pt black	80% at 40 mA cm^{-2}	10 mA cm^{-2} at cell voltage of 2.2 V	[171]

Sn granule cathode	Flow cell	0.45 M $KHCO_3$ + 2 M KCl	316 stainless steel mesh	91% at cell voltage of 2.7 V	60 mA cm^{-2} at cell voltage of 2.7 V	[172]

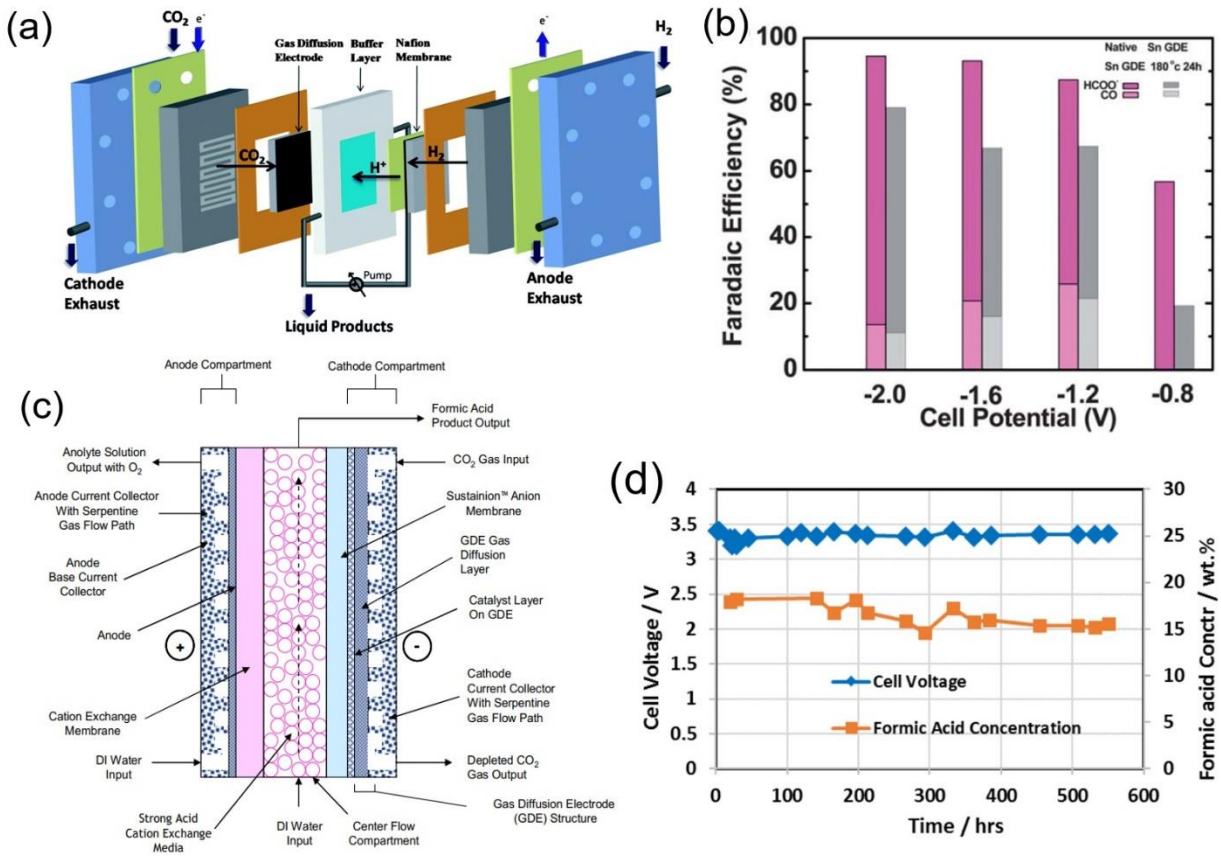

Figure 1.11 Full cell configurations and related performances. (a) Schematic of the full cell for electrochemical CO_2RR to formate. (b) Faradaic efficiencies of formate and CO at different cell voltages in 0.1 M $KHCO_3$ on native Sn GDE and Sn GDE after annealing treatment at 180 °C for 24 h. Reproduced with permission.[136] Copyright 2014, The Royal Society of Chemistry. (c) Design of a three compartment full cell using Sustainion™ anion membrane electrolyte. (d) Cell voltage and formic acid concentrations during 550 h test at a current density of 140 mA cm^{-2}. Reproduced with permission.[167] Copyright 2017, IOP Publishing.

In the full cell assembly studies, the aim is to achieve high current density and high formate selectivity at low cell voltages, and excellent long-term stability. High performance anode and cathode with low overpotentials, under proper cell configurations that operate under low Ohmic resistance should be selected to lower the E_{cell}. The design and preparation of the cathode for CO_2RR to formate have been discussed earlier in Section 1.3. In this section, we will focus on 3 important components: anode design, electrolyte, and membrane used in the full cell assembly.

Firstly, the design and preparation of stable and active catalysts for anodic reactions is important. Oxygen evolution reaction (OER) is a standout anodic process due to the abundance of water, and oxygen is the only product.[173-174] There are many excellent OER catalysts, such as Ru,[175] Ir,[176] Ni-Fe layered double hydroxide (LDH),[177] and Co_3O_4.[178] Li and coworkers developed a continuous reactor employing Sn granule cathode and 316 stainless steel mesh anode for CO_2 reduction to formate.[172] A high formate Faradaic efficiency of 91% was reached at the cell voltage of 2.7 V with a current density of 60 mA cm^{-2} in an electrolyte of 0.45 M $KHCO_3$ and 2 M KCl. Sometimes, the anode may become the limitation for a totally stable performance. Wang et al assembled the microflow cell using the CoO_x/CNT as the anode with the SnO_2/CNT cathode for formate in 1 M KOH electrolyte.[169] The electrolysis process splits CO_2 and H_2O, into formate and O_2 at 1.9 V. The $FE_{formate}$ reaches 82 % at η_{cell} of 1.36 V and $j_{formate}$ of 113 mA cm^{-2}. Both the current density and the $FE_{formate}$ had obvious decay after 35 h stability test at a constant cell voltage of 2.3 V (current density dropped from ~ 50 mA cm^{-2} to ~ 35 mA cm^{-2}; $FE_{formate}$ dropped from ~ 80% to 60%). They attribute the decay mechanism during long-term electrolysis to the consumption of OH^- on the anode side as the gradual pH decrease in the anolyte could worsen the OER kinetics. Díaz-Sainz and co-workers used a dimensionally stable Ir-MMO (mixed metal

oxide) on platinum anode for oxygen evolution in a filter press cell.[168] Using the Bi NPs-C loaded cathode, a $FE_{formate}$ of 89.5 % at 90 mA cm^{-2} can be achieved and the cell can be operated at a high current density of 300 mA cm^{-2} (cell voltage: 5.4 V). However, the high cost of Ir and Pt may limit their practical application. Therefore, development of inexpensive and high performance anode catalysts is necessary to further improve the full cell CO_2 electrolyser performance.

Secondly, the electrolyte choice plays a significant role in the cell performances. The commonly employed electrolytes are the aqueous solutions of bicarbonate and alkalis. The interaction between aqueous electrolyte and catalysts, and the chemical reaction between electrolyte and CO_2 gas, as well as the influence of solution pH, cations, and anions on CO_2RR performance have been discussed in Section 1.2. For full cell electrolysis, the electrolyte conductivity is highly important, as high resistance results in great voltage loss and decrease in energy efficiency in accordance with Eqn 1. Kenis et al studied the electrolyte composition and concentration effects on the electroreduction of CO_2 to CO on a Ag-based cathode by comparing the CO_2RR performance and the electrochemical impedance spectroscopy results obtained from electrolytes such as KOH, KCl, and $KHCO_3$ with different concentrations.[179] They found that the onset potentials of CO_2RR were in the order of KOH (-0.13 V vs RHE) < $KHCO_3$ (-0.46 V vs RHE) < KCl (-0.6 V vs RHE), and the charge transfer resistance and the cell resistance dropped with increases in KOH concentrations from 0.5 M to a 3.0 M KOH. They suggested that the decrease in charge transfer resistance may involve interactions in the electrical double layer, which can either stabilize or destabilize the rate limiting $CO_2^{\cdot -}$ radical. In addition, the electrolyte could also influence the membranes' long term stability. Mustain et al studied the effect of hydroxide and carbonate alkaline media on the ion conductivity of membranes.[180] They observed a decrease

in conductivity that ranged from 27 % to 6 % over a 30-day period, due to the loss of stationary cationic sites according to the Hofmann elimination and nucleophilic displacement mechanisms, which would affect the long term stability of an electrolysis system.

Finally, the membrane employed in the cell can affect the cell voltage and the stability. At present, the most commonly used ion-exchange membranes are cation exchange membrane (CEM), anion exchange membrane (AEM), and bipolar membrane (BPM) as discussed in Section 1.4.1. Proper choice of membranes can greatly lower the overpotential. Smith et al designed a cell using a silver catalyst for CO_2 reduction in a $KHCO_3$ catholyte separated by a BPM from a nickel iron hydroxide oxygen evolution catalyst in a basic anolyte.[181] This strategy decreased the cell voltage by more than 1 V compared to that with conventional use of Pt counter electrode and monopolar membrane (eg. nafion membrane). The ionic conductivity of perfluorosulfonated membrane in a proton exchange membrane (PEM)-electrolyser is 100 $mS \cdot cm^{-1}$ while the carbonated alkaline membrane in a co-electrolysis cell is 7 $mS \cdot cm^{-1}$, according to estimations based on a 50 μm thick membrane by Durst et al.[157]

1.5 Thesis aim and structures

1.5.1 Thesis Aim

As detailed in the above comprehensive literature review, electrochemical CO_2 reduction is a promising approach to alleviate CO_2 accumulation in the atmosphere through conversion to valuable chemical feedstocks such as formate. An ideal CO_2 electrolyser to formate should possess criteria such as enhanced kinetics at a low overpotential, high partial current density, excellent

formate selectivity and ability to operate with high durability and stability. However, there are fundamental and applied challenges to be addressed to achieve ideal electrolysers.

The major goal of this thesis is to systematically study the CO_2RR to formate from the aspects of catalyst structure designs, electrolyte effects, to cell optimization, which may lead to improvements in the operating potential window, current densities, conversion efficiencies, and stability. This thesis involved the development of several high-performing and selective catalysts for formate production, including mesoporous Pd, SnS nanosheets, and Bi nanoparticles. Since various dimensional nanostructured catalysts have been synthesized, it remains unclear as to the influence of structures such as 1D nanotubes and 3D mesoporous toward the mass transport, localised pH, and formate selectivity. Understanding of such influences would provide insights into designing an optimal architecture and dimension for the synthesized catalysts. The electrolyte effects such as the use of KOH in CO_2RR to formate remains not as widely investigated, and detailed understanding is essential as the highly conductive electrolyte is one of the most promising candidates for practical application. As most of the reported studies are half-cell studies, the understanding of full cell systems by combining the CO_2RR cathode and anode is rather limited. Hence, the development of suitable oxygen evolution catalysts to be coupled to the highly active formate producing cathode is essential toward this goal.

1.5.2 Thesis Structure

Chapter 2 presents the synthesis of a novel hierarchical 1D-3D catalyst structure by loading mesoporous Pd with an average pore size of ~ 10 nm and wall thickness of ~ 4 nm onto highly ordered TiO_2 nanotube arrays via pulse electrodeposition. Electrochemical CO_2 reductions

achieved a CO_2-to-formate Faradaic conversion efficiency of 88 ± 2 % under optimal conditions. Importantly, the product selectivity is found to depend significantly on the tube length, highlighting the influence of mass transport limitations of CO_2. This work offers vital insight into practical considerations in designing efficient catalyst-support interfaces with an optimal hierarchical geometry, which must optimise mass transport as well as electrochemical kinetics.

Chapter 3 describes strategies to overcome the challenges of low operation current density and inefficiencies in mass transfer through employment of a flow cell configuration with the use of a low cost and highly selective SnS nanosheets for CO_2RR to formate. Under these conditions, a dramatic influence of electrolyte alkalinity in widening potential window for CO_2 electroreduction was observed. The optimized SnS catalyst operated in 1 M KOH achieved a maximum formate Faradaic efficiency of 88 ± 2 % at -1.3 V *vs.* RHE with a current density of ~ 120 mA cm^{-2}. Alkaline electrolyte was found to suppress hydrogen evolution across all potentials, which is particularly dominant at the less negative potentials, as well as CO evolution at more negative potentials. This in turn widens the potential window for formate conversion (> 70 % across -0.5 to -1.5 V *vs.* RHE). A comparative study of the SnO_x counterpart, indicates sulfur also acts to suppress hydrogen evolution, although electrolyte alkalinity results in a greater suppression.

Chapter 4 addresses the issue of anode activity, as it is one of the most critical factors that might limit the electrolysis performance. Oxygen evolution reaction with the release of oxygen is a common anodic process for the operation of electrolysers. Stable and active oxygen evolution catalysts would be important for the long term durability of a CO_2 electrolyser. Therefore, a strategy is introduced which involves a facile approach to the synthesis of ultrathin iron

oxyhydroxide nanosheets for anodic OER via cyclic voltammetry (CV) potential modulations on thermally treated iron foil. By controlling the number of CV cycles, potential ranges and duration, as well as the employed electrolytes, the size of the ultrathin nanosheets can be tuned and low overpotentials can be obtained for OER. This 2D material also provides a platform for further performance enhancement via integration of species such as nickel onto the ultrathin nanosheet structure. The incorporation of Ni resulted in a much lower onset potential and higher current density.

In Chapter 5, a full cell mimicking a single cell CO_2 electrolyser has been assembled by coupling the highly active Bi nanoparticle loaded carbon paper cathode, to the earth-abundant NiFe LDH-Ni foam anode. Based on the flow cell design, high formate Faradaic efficiency and current density were achieved with low cell voltages. A maximum formate Faradaic efficiency of 90.2 ± 1.7% at a relatively low cell voltage of 2.12 V, and high current density of 155 mA cm^{-2} at the cell voltage of 2.36 V were achieved in this full cell system. The rate determining step of CO_2RR to formate is the one-electron transfer step to form the *OCHO intermediates according to the Tafel slope of 127.6 eV dev^{-1}. The formate Faradaic efficiency remained at above 85% after 10 h at 2.12 V, demonstrating the promising commercial prospect of this design.

Finally, Chapter 6 concludes on the results on electrochemical CO_2 reduction to formate production derived from this PhD thesis, and offers perspectives for future research.

Chapter 2 Hierarchical architectures of mesoporous Pd on highly ordered TiO_2 nanotube arrays for electrochemical CO_2 reduction

This chapter has been adapted, with the publisher's permission, from the article entitled 'Hierarchical architectures of mesoporous Pd on highly ordered TiO_2 nanotube arrays for electrochemical CO_2 reduction' published in the Journal of Materials Chemistry A.

Citation: Zou et al., Journal of Materials Chemistry A, 2020, 8, 8041-8048.

DOI: https://doi.org/10.1039/D0TA02077J

Jinshuo Zou,[a] Muhammad Iqbal,[b,c] Amruthalakshmi Vijayakumar,[a] Caiyun Wang,[a] Douglas R. Macfarlane,[d] Yusuke Yamauchi,[b] Chong-Yong Lee,*[a] Gordon G. Wallace*[a]

[a] ARC Centre of Excellence for Electromaterials Science, Intelligent Polymer Research Institute, AIIM, Innovation Campus, University of Wollongong, Wollongong, NSW 2500, Australia.

[b] School of Chemical Engineering, Faculty of Engineering, Architecture and Information Technology (EAIT), University of Queensland, Brisbane, QLD 4072, Australia.

[c] National Institute for Materials Science, International Center for Materials Nanoarchitectonics, 1-1 Namiki, Tsukuba, Ibaraki 305-0044, Japan.

[d] School of Chemistry, Monash University, Clayton, VIC 3800, Australia.

* Corresponding author

Author statement:

The study in this chapter was conceptual, experimentally designed and written by Jinshuo Zou. All experiments including material preparations, characterizations, electrochemical studies and the data analysis presented in this chapter were performed by Jinshuo Zou. Dr. Chong-Yong Lee and Prof. Gordon G. Wallace supervised the study, and assisted in the conception, experimental design and revisions of manuscript. Prof. Yusuke Yamauchi and Dr. Muhammad Iqbal contributed in their expertise in mesoporous Pd, scientific discussions and manuscript's revision. Amruthalakshmi Vijayakumar, Dr. Caiyun Wang and Prof. Douglas R. Macfarlane revised the manuscript and contributed to scientific discussions.

2.1 Abstract

The understanding of the influence of hierarchically nanostructured architectures as support materials for catalysts loading, is critical toward development of efficient electrocatalytic interfaces. The knowledge on mass transport limitation of reactants within such catalyst-support structures remains elusive. Herein, we performed systematic investigation through a novel hierarchical 1D-3D structure by loading mesoporous Pd with an average pore size of ~ 10 nm and wall thickness of ~ 4 nm onto highly ordered TiO_2 nanotube arrays via pulse electrodeposition. Electrochemical CO_2 reductions achieved a CO_2-to-formate Faradaic conversion efficiency of 88 ± 2 % under optimal conditions. Importantly, the product selectivity is found to depend significantly on the tube length, highlighting the influence of mass transport limitations of CO_2. This work offers vital insight into practical consideration in designing efficient catalyst-support

interfaces with an optimal hierarchically geometry, that must optimise mass transport as well as electrochemical kinetics.

2.2 Introduction

World energy consumption that heavily relies upon fossil fuel resources has resulted in the continuous release of anthropogenic CO_2 into the atmosphere.[182-183] Electrochemical CO_2 reduction technology, along with CO_2 capture, powerable by renewables, could recycle the CO_2 by converting it into valuable fuels and chemical feedstocks, creating a carbon neutral energy loop. This has created intense interest in the CO_2 reduction reaction (CO_2RR) and the electrocatalysts that can support it. Nanostructuring of electrocatalysts of various dimensions and hierarchical structures decreases the required overpotential for CO_2RR, and/or enhances the selectivity of carbon-based products over hydrogen evolution.[184-185] It is increasingly evidenced that the reactant concentration gradients between the nanostructured electrode surface and bulk solution play an essential role in influencing the product selectivity, and contribute to the intrinsic complexity of the electrocatalytic CO_2 reduction processes.[186-188]

Another avenue of significant interest is in designing optimal and efficient hierarchically nanostructured catalyst-support structures, which can provide large surface area with abundant active sites, as well as suppress the aggregation of active electrocatalyst particles.[82] The combination of a 3D mesoporous catalyst and a 1D nanotubular structure is a highly desirable hierarchical design in this regard. Mesoporous-based catalysts are known to exhibit excellent electrocatalytic performance,[189-191] and TiO_2 nanotubular arrays (TNTAs) are arguably among the most investigated hierarchical structures.[192-194] For example, nanoporous gold loaded onto

TNTAs by controlled dewetting-dealloying showed enhanced photocatalytic H_2 generation performance.[195] Metal catalysts have been loaded on TNTAs for various functional applications,[196-198] it is however remained a challenge to form mesoporous catalysts on a 1D hierarchical structure with a high level of precise control. Issues such as weak interfacial binding compatibility, and the inhomogeneous deposition of mesoporous catalysts onto the 1D nanotubular structure needed to be overcome.

Palladium (Pd) can electrocatalytically convert CO_2 to formate at very low overpotentials via the HCOO* reaction pathway.[66, 199-201] However, the low barrier toward the formation of the palladium hydride (PdH_x) makes hydrogen evolution reaction (HER) a strong competing reaction.[202] Pd is known to exhibit a strong size, morphological structure, and applied cathodic potential dependence on the CO_2RR performance.[16-21] Klinkova et. al. experimentally and theoretically identified that high index surfaces of Pd can facilitate the formation of $HCOO^*$, while low index surfaces favour the formation of CO^*.[130] Gao et al. found that the main products, which is either formate or CO, are tuned by varying the applied potential.[199] In this regard, a mesoporous structure of Pd that encompasses nanosized catalytic sites is of strong interest.

Mesoporous Pd was prepared by a facile and scalable electrodeposition method. The presence of micelles as template allows self-assembly reduction to Pd, followed by template removal which permit direct mesoporous Pd deposited on the electrode.[203-204] Support materials is also critical to allow successful growth of electrodeposited mesoporous Pd. Commonly employed atomically flat gold surface would possesses challenge for materials evaluation as gold is known as CO_2 electroreduction catalysts. Inert material such as TiO_2 would be ideal, particular hierarchical structures such as nanotubes facilitating enhanced loading of catalyst. Herein, we report the

successful synthesis of a hierarchical architecture of mesoporous Pd on TiO_2 nanotube arrays (mPd/TNTAs) for the first time. Such structures are investigated for electrochemical CO_2 reduction, with comparison being made to non-mesoporous structure. Furthermore, taking advantage of highly ordered aligned TiO_2 nanotube arrays with controllable thicknesses, as well as a simplicity of CO_2 electroreduction products in the case of Pd: liquid phase formate and gas-phase hydrogen; we examine the influence of both mesoporous and nanotubular structures, as well as local concentration changes on the CO_2RR Faradaic conversion efficiency.

2.3 Experimental Section/Methods

2.3.1 Materials and electrode preparation.

Titanium foil (99.7%, Sigma Aldrich), ethanol (Chem-Supply), acetone (Chem-Supply), glycerol (Chem-Supply), ethylene glycol (Chem-Supply), ammonium fluoride (Sigma Aldrich), palladium (II) chloride (99%, Sigma Aldrich), pluronic P123 (average Mn ~ 5800, Sigma Aldrich) were used directly without further purification. Mili-Q system deionized water (18.2 MΩ·cm at 25 °C) was used to prepare all solutions. Carbon dioxide (CO_2, 99.99%) cylinder was purchased from BOC.

Synthesis of 1D-TNTAs and compact TiO_2: Titanium foil was cut into 1×1 cm^2 sheet with a neck of 0.5×1 cm^2, subject to ultrasonic cleaning successively in acetone, ethanol and distilled water, followed by drying under N_2 stream. For TiO_2 nanotubes of 1-3 μm, anodization was performed in the electrolyte containing 0.5 wt % of NH_4F, 10 wt % of H_2O and 90 wt % of glycerol. The longer TiO_2 nanotubes of 6-20 μm was obtained in electrolyte contains 0.35 wt % NH_4F, 2 vol % H_2O and 98 % of ethylene glycol. Various lengths of TNTAs were obtained by altering the

anodization duration, at a fix potential of 50 V using a Voltcraft power supply (VSP 2653). Compact layer of TiO_2 was obtained by anodization in the above-mentioned ethylene glycol containing electrolyte, at 10 V for 30 min. The anodized foils were washed in ethanol and annealed at 450 ^oC for 1 h to obtain crystalline TNTAs or compact TiO_2.

Synthesis of mPd /TNTAs, mPd/compact TiO_2, and Pd/TNTAs: The electrodeposition of mesoporous Pd was conducted at room temperature by using a CHI650 potentiostat. A single compartment electrochemical cell was employed with Pt mesh as a counter electrode, Ag/AgCl (3M NaCl) as a reference electrode, and the TNTAs as a working electrode. Before electrodeposition, the TNTAs were ultrasonicated for 1 min in the aqueous electrolyte containing 2.5 wt % Pluronic P123 and 40 mM $PdCl_2$. The Pd was obtained by either pulse deposition or non-pulse method at 0 V (vs. Ag/AgCl). In the pulse deposition, the square-wave voltage was applied to the TNTAs with the pulse width of 30 s. The same electrodeposition procedure was applied to obtain mPd/compact TiO_2. For the synthesis of Pd/TNTAs, electrodeposition was performed in the 40 mM $PdCl_2$ aqueous solution at 0 V (*vs.* Ag/AgCl).

Synthesis of mesoporous Pd on carbon paper: The mesoporous Pd was deposited on carbon paper using the same electrodeposition method as described earlier on TNTAs. The deposition time was 2 min.

2.3.2 Materials characterization

XRD patterns of the mPd/TNTAs, Pd/TNTAs, and TNTAs were collected on a GBC MMA diffractometer with Cu K_α radiation at a scan rate of 2^o min^{-1}. The surface morphologies of the samples were recorded on a scanning electron microscope (SEM) of JEOL JSM-7500FA. The X-

ray photoelectron spectroscopy (XPS) measurements were performed on the VG Multilab 2000 (VG Inc.) photoelectron spectrometer with the monochromatic Al K_α radiation under vacuum at 2 $\times 10^{-6}$ Pa. The Fourier Transform Infrared Spectroscopy (FTIR) were collected on a PerkinElmer FT-IR Spectrometer Frontier instrument with the scan number of 16 for each sample.

2.3.3 Electrochemical characterization

All the measurements were carried out on CHI650 potentiostat at room temperature, in an H-cell separated by cation exchange membrane (Nafion 115). Before use, the Nafion membrane was pretreated by soaking in a sequence of 5 wt% of H_2O_2, pure water, 1 M H_2SO_4, pure water at the temperature of 80 ^oC. The Pt mesh was used as the counter electrode. All the potentials were measured against Ag/AgCl reference electrode (3.0 M NaCl). The foil with 1 cm^2 active geometry area was used as working electrode. Before the electrolysis, the CO_2 gas was introduced into the cathodic chamber at a flow rate of 20 mL min^{-1} for 20 min to obtain a CO_2 saturated electrolyte. CVs were performed at a scan rate of 50 mV s^{-1} over a window of 0 to -1.5 V *vs.* Ag/AgCl.

2.3.4 Products analysis

The liquid products were analysed on a 400 MHz NMR spectrometer (Bruker Avance). The 1D ^1H spectra were measured with water suppression.[205] 1-propanesulfonic acid 3-(trimethylsilyl) sodium (DSS)(99.7%, Sigma Aldrich) was used as internal standard solution. A 0.5 mL of product-containing electrolyte, 0.1 mL of DSS, and 0.1 mL of D_2O (99.9%, Cambridge Isotope Lab) was added and mixed in the NMR tube for the analysis. The gaseous products were analysed by gas chromatography (GC) (8610C, SRI Instruments) equipped with a flame ionization detector (FID)

for CO, CH_4, C_2H_4, C_2H_6 and a thermal conductivity detector (TCD) for H_2, CO, CH_4, C_2H_4, C_2H_6 and CO_2.

2.3.5 The active surface area measurements

To measure the active surface area of the working electrodes, cyclic voltammograms were scanned in a 0.5 M H_2SO_4 solution from 0 to 1.5 V vs. Ag/AgCl at the scan rate of 50 mV s^{-1}. The active surface area was calculated by the oxide reduction charge at the range of 0.2 to 0.8 V vs. Ag/AgCl with the assumption that the Pd surface is smooth and the conversion factor for the oxide monolayer reduction is 420 μC cm^{-2} according to the model of Kadirgan for the oxide monolayer on a smooth Pd surface.[203, 206]

2.3.6 pH effects of electrolyte on the current density and the formate efficiency

To investigate the effect of pH, we tested the CO_2 reduction performance in electrolytes with different initial pH values (6.8, 9.2, and 12.1). The electrolytes were obtained by adding certain amount of NaOH into 0.5 M $NaHCO_3$. The current density vs. time curves were recorded and the formate efficiency were calculated.

2.4 Results and discussion

2.4.1 Growth of mesoporous Pd

Figure 2.1 illustrates the procedure to synthesize 3D mesoporous Pd layer on TiO_2 nanotube arrays (mPd/TNTAs). The annealed TNTAs were immersed in an electrodeposition bath containing 2.5

wt % Pluronic P123 (its concentration is beyond the critical micelle concentration, CMC) and 40 mM $PdCl_2$. To ensure the electrolyte homogenously diffuses into the inner and outer layers of tubes, a short 1 min ultrasonication was applied. The mesostructured Pd layer was grown on TiO_2 nanotube arrays by performing electrodeposition at 0.0 V (*vs.* Ag/AgCl). Finally, micelles were removed by immersing the electrodeposited Pd layer-TNTAs in water for 24 h as followed the protocol reported elsewhere.[203] Further details on the experimental procedure can be referred to the experimental section and Figure 2.2.

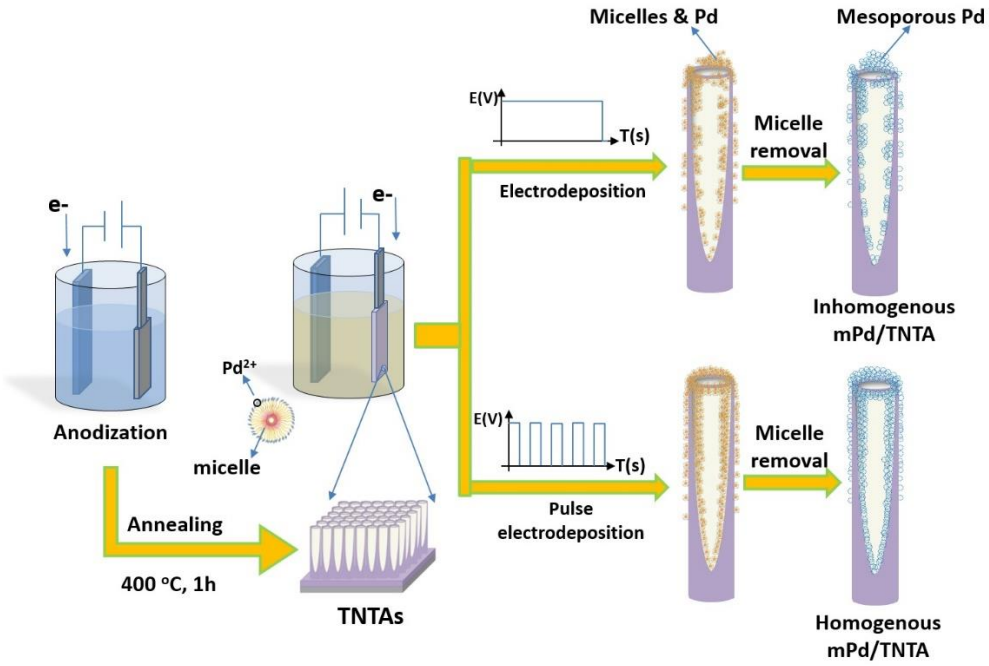

Figure 2.1 Schematic procedure for the electrochemical deposition of mesoporous Pd onto TiO_2 nanotube arrays (mPd/TNTAs).

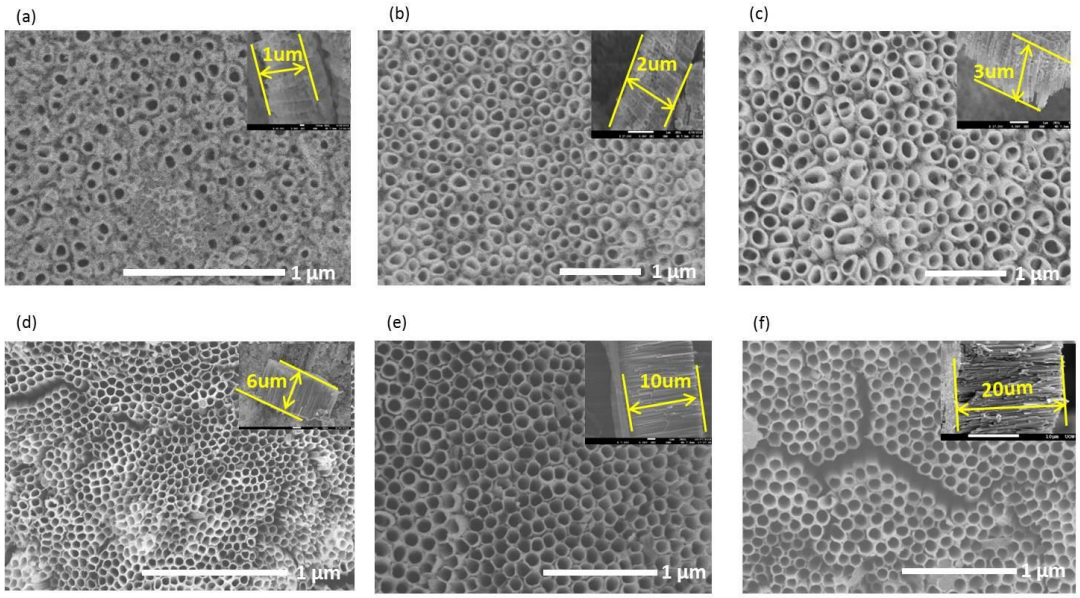

Figure 2.2 SEM images of TiO_2 nanotube arrays of different tube lengths: (a) 1 µm, (b) 2 µm, (c) 3 µm, (d) 6 µm, (e) 10 µm, (f) 20 µm.

To successfully grow mesoporous Pd structures, relatively high Pd^{2+} and micelle concentrations were required, beyond the CMC.[203, 207] However, the local concentration change during the deposition process may affect the quality of mesoporous layer. Especially, 1D nanotubearray architecture could restrict the supply of micelle protected Pd^{2+} to its inner and outer layers, resulting in an inhomogeneous distribution of the mesoporous Pd layer (Figure 2.1, 2.3a-b). To compensate for this local concentration change issue, instead of a constant voltage during deposition, a square-wave voltage pulse was applied with a pulse width of 30 s of rest potential between pulses, which allows the Pd^{2+} ions to migrate toward the TNTAs during the rest time.[208] Via this strategy, a homogenously distributed mesoporous Pd layer on TNTAs was evidenced (Figure 2.3c-d, and 2.4).

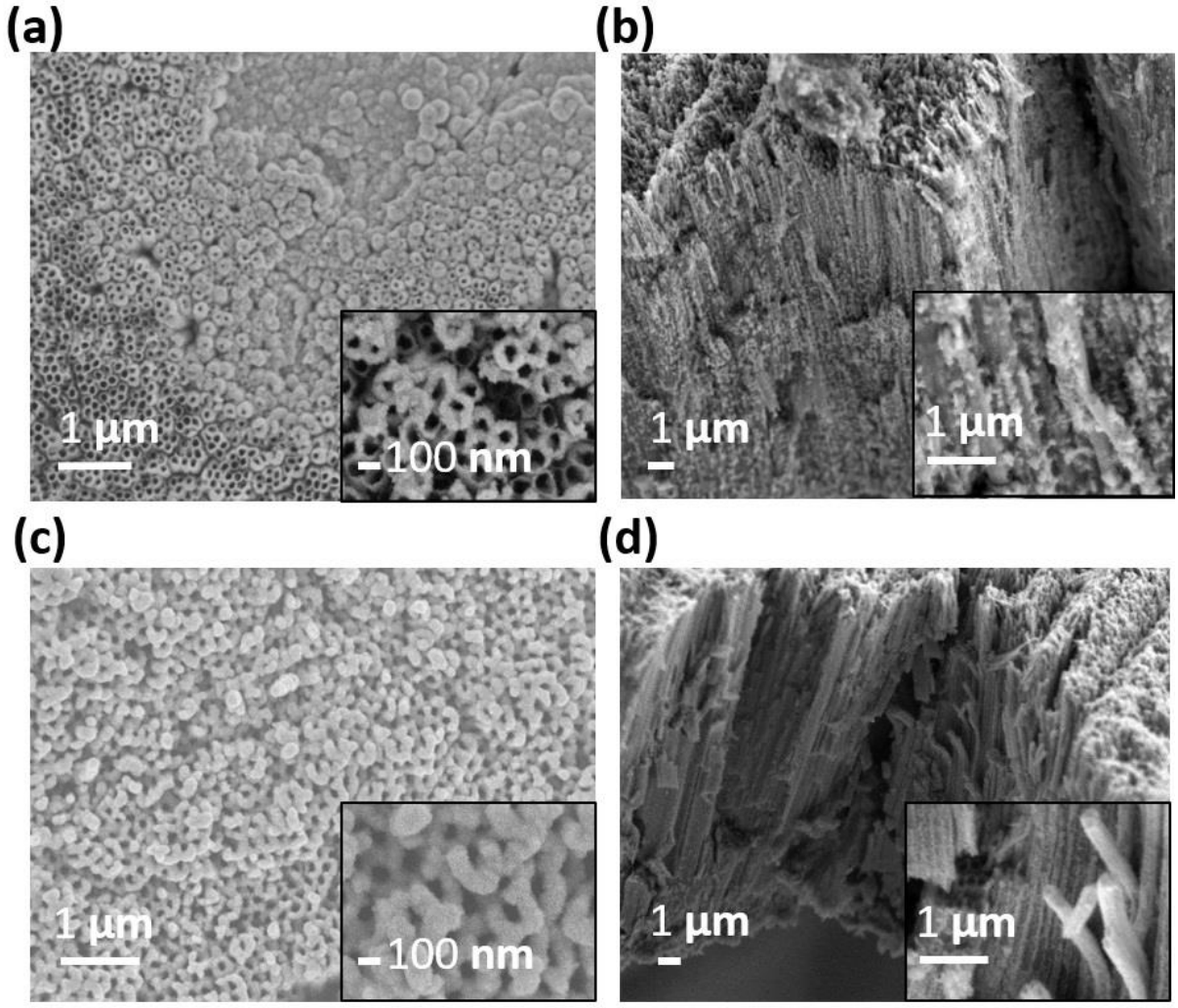

Figure 2.3 Comparison of SEM images of mPd/TNTA prepared without (a, b) and with (c, d) pulse-electrodeposition of 2 min. (a) and (c) are the top views; (b) and (d) are the cross-sectional views. Insets in each figure are the enlarged views. The TNTAs tube length is ~ 20 µm.

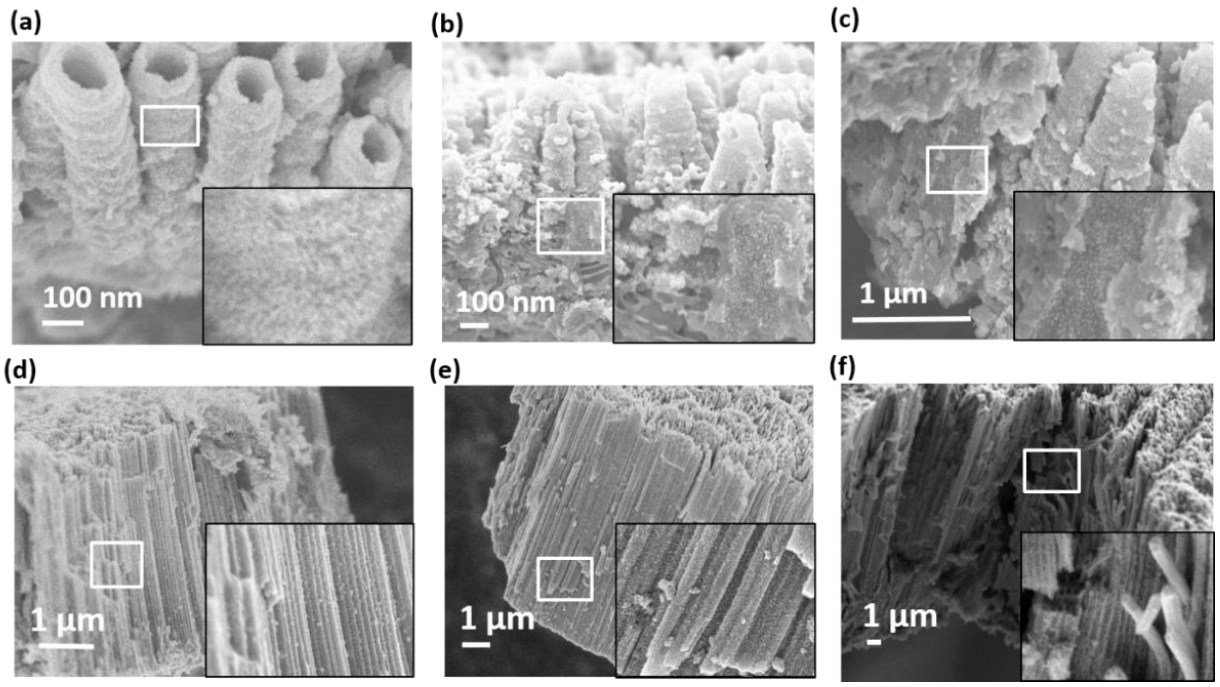

Figure 2.4 SEM images of mPd/TNTAs with different tube lengths: (a) 1µm, (b) 2 µm, (c) 3 µm, (d) 6 µm, (e) 10 µm, (f) 20 µm.

Layers with a pulsed-electrodeposition time of 1, 2, 3 and 5 min were synthesized as shown in Figure 2.5. The 2 min deposition duration was found to be optimal to achieve a uniform mesoporous layer. A shorter duration of 1 min deposition resulted in a thin layer of inhomogenous coverage, wheareas 3 min started to cover some of the tube openings. A longer 5 min deposition produced a thick mesoPd layer almost completely blocking the tube openings. Such surface morphology is not ideal for electrocatalysis, as the reactants should be readily accessible and interacting with the whole active catalyst, including inner and outer surface of the tubes. Unless otherwise stated, the mPd/TNTAs prepared in this study were based on the 2 min pulsed electrodeposition. Detailed examination indicates the mesoporous structure produced has an average pore size of ~ 10 nm, and a pore wall thickness of ~ 4 nm (Figure 2.6). TEM image in the

inset of Figure 2.6c shows evidenced coverage of mesoporous Pd on TiO_2 nanotubes, and HRTEM shows the crystallinity of the obtained Pd and the difference in contrast highlights the porous nature of the mesoporous Pd film.

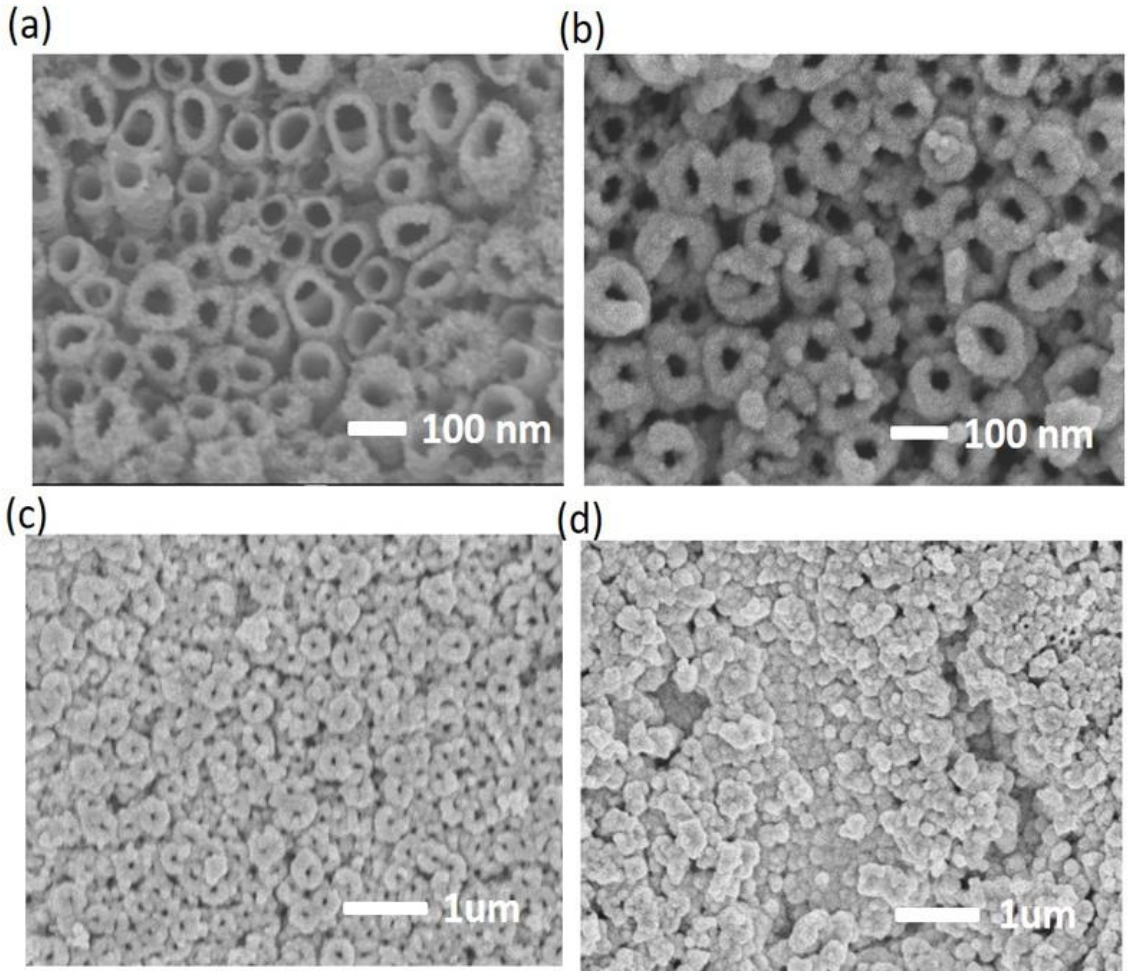

Figure 2.5 SEM images of mPd/TNTA samples with different electrodeposition time: (a) 1 min, (b) 2 min, (c) 3 min, (d) 5min.

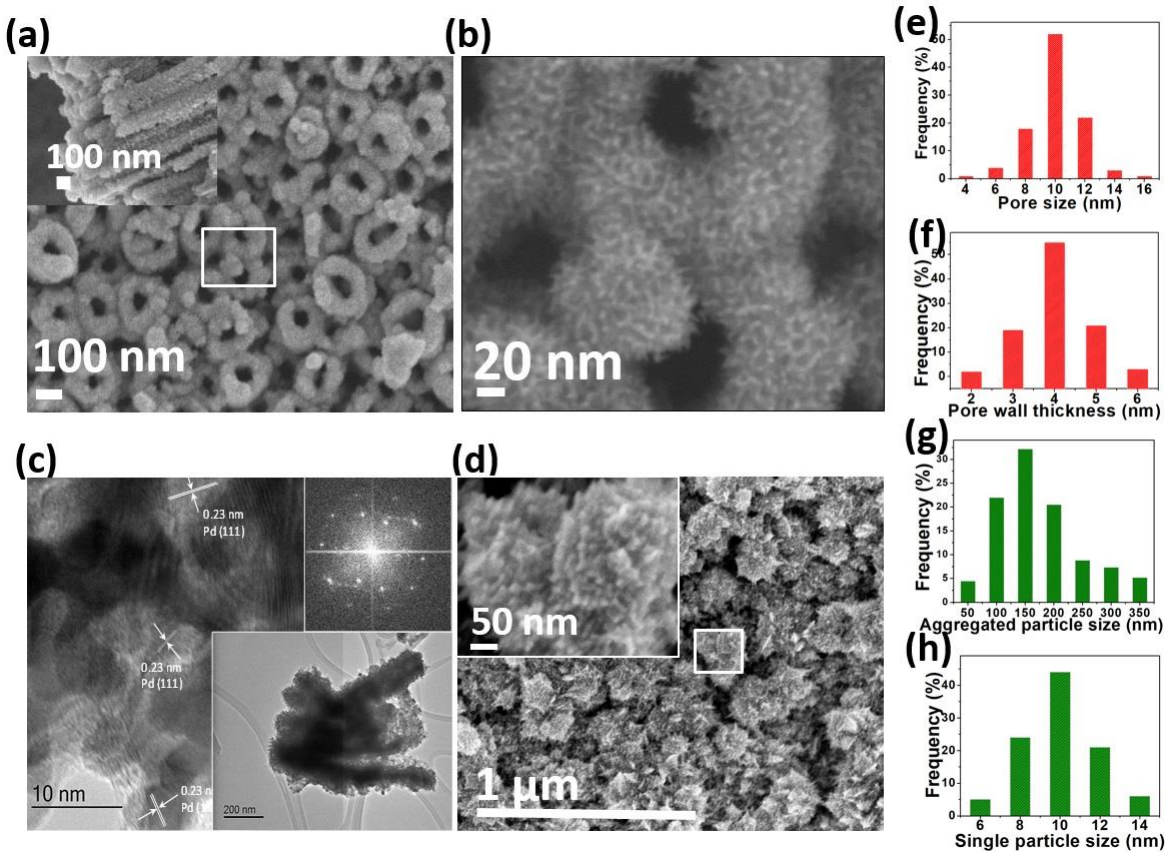

Figure 2.6 Morphology and size distribution of mPd/TNTAs and Pd/TNTAs. SEM (a,b) and TEM (c) images of mPd/TNTAs, and (d) SEM images of Pd/TNTAs. Histograms showing distribution of the obtained pore size (e) and pore wall thickness (f) of meso Pd on mPd/TNTAs; distribution of the aggregated Pd particle sizes (g); and the distribution of single Pd particle sizes (h) on the aggregated large particles of Pd/TNTAs. Inset in (a) is the cross-sectional view of mPd/TNTAs. (b) is the enlarged of selected square zones shown in (a). Top and bottom insets in (c) are the SAED pattern and the lower resolution TEM image, respectively. Inset in (d) is the higher magnification of the selected square zones.

Comparison was made with non-mesoporous Pd layer on TiO_2 nanotubes (Pd/TNTAs) without a mesoporous structure, which was deposited from a micelle-free electrolyte (Figure 2.6d).

It was found that the Pd aggregated and covered the tube openings instead of growing on the inner and outer surfaces of the nanotubes. The pulsed electrodeposition current of Pd/TNTAs was larger than that of the mPd/TNTAs (Figure 2.7), indicating the higher electrodeposition rate in the micelle-free electrolyte. This high deposition rate could result in rapid aggregation of Pd at the tube openings. In contrast, in mPd/TNTAs case, the electrodeposition structure and kinetics are controlled by the P123 micelles, which template the reduction of Pd^{2+} at the tube interface to form a well-distributed mesoporous layer. Note that the micelles of P123 can be easily removed by immersing in water for 24 h and then followed by water rinsing. This micelles removal procedure was followed other reports,[203, 209] and confirmed by Fourier Transform Infrared Spectroscopy (FTIR) measurements (Figure 2.8).

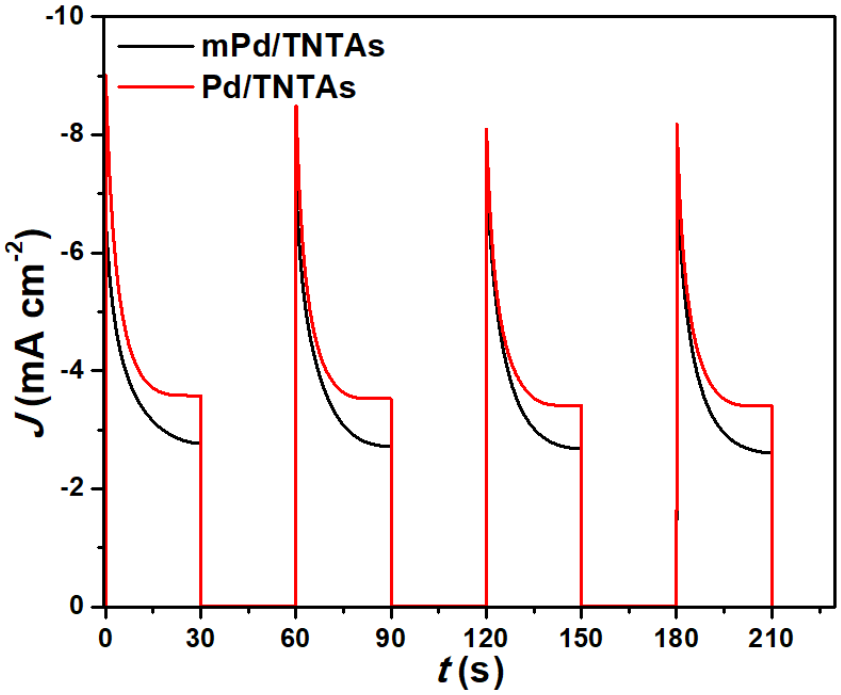

Figure 2.7 Current -time curves of mPd/TNTAs and Pd/TNTAs during the electrodeposition.

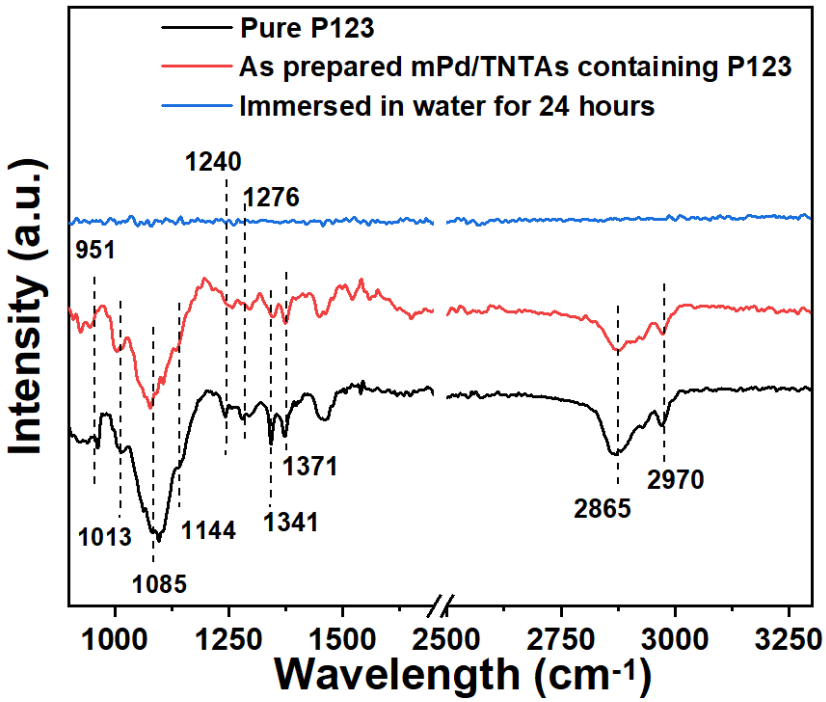

Figure 2.8. FTIR of pure P123, as prepared mPd/TNTAs containing P123 micelles, and after immersing in water for 24 h.

We examined X-ray diffraction (XRD) pattern of synthesized samples: TNTAs, mPd/TNTAs, and Pd/TNTAs (Figure 2.9a). The diffraction peaks of TNTAs can be assigned to Ti (JCPDS Card No. 65-6231) and anatase TiO_2 (JCPDS Card No. 21-1272), respectively, indicating that the TiO_2 nanotubes were in anatase phase. The peaks of Pd/TNTAs and mPd/TNTAs at 40.18°, 46.72°, and 68.16° can be ascribed to Pd (JCPDS Card No. 05−0681). This is further validated by X-ray photoelectron spectroscopy (XPS) measurement (Figure 2.9b) of two main characteristic peaks of Pd(0) at the position of 335.1 and 340.4 eV. Peaks at 336.1 and 341.3 eV can be assigned to Pd (PdO_x) intermediates. Peaks at 337.1 and 342.4 eV are corresponding to PdO, whilst 338.2 and 343.4 eV can be attributed to Pd^{2+}.[210]

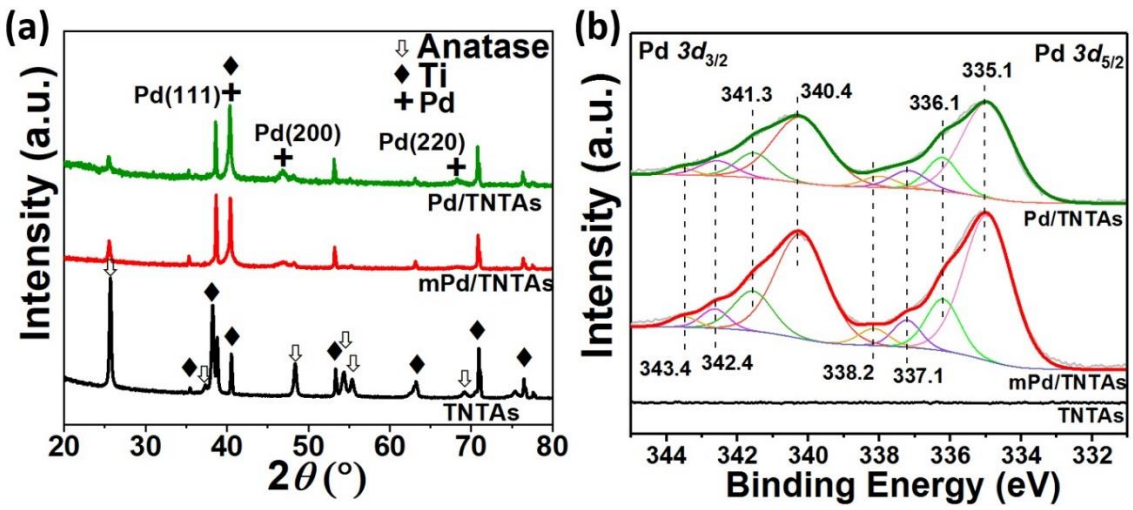

Figure 2.9 XRD patterns (a) and XPS spectra (b) of TNTAs, mPd/TNTAs, and Pd/TNTAs samples.

2.4.2 CO_2 reduction performance

The CO_2 electroreduction performance was examined in a three-electrode system in a H-cell separated by a cation exchange membrane (Nafion 115). The gaseous and liquid products were analyzed by gas chromatography (GC) and nuclear magnetic resonance (NMR) spectra, respectively. Details of the analysis methods can be found in the supporting information (Figure 2.10). The data were reported with each experiment performed in triplicate, with average values included standard deviations.

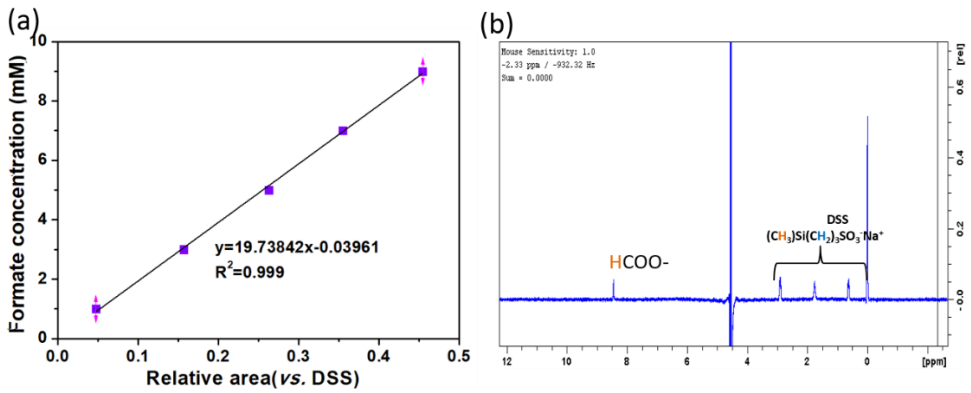

Figure 2.10 (a) the linear relationship between the formate concentration and the relative area (vs. DSS); (b) the 1H-NMR spectrum for formate. The single peak at 8.44 ppm coresponding to the H in formate and the peak at 0.00 ppm represents the internal standard DSS.

The relative areas were calculated based on the equation:

$$Relative\ area(Formate) = Peak\ area\ at\ 8.44\ ppm / Peak\ area\ at\ 0.00\ ppm$$

In the examined potential region of -0.5 to 0 V *vs.* RHE (Figure 2.11, 12), the detected liquid product was formate, and hydrogen was a gas-phase by-product. There is a strong dependency of formate Faradaic conversion efficiency with respect to the applied cathodic potentials. As for mPd/TNTAs (Figure 2.11a), the formate Faradaic conversion efficiency of ~ 88 ± 2 % at -0.1 V, but decreased to 72 ± 2% at -0.3 V, and further dropped to only 17 ± 4 % at -0.5 V. The Pd/TNTAs exhibited a similar trend, with the highest Faradaic conversion efficiency of 35 ± 7 % at -0.1 V. This was about 2.4 time lower than that of mPd/TNTAs. Overall, formate Faradaic conversion efficiencies of mPd/TNTAs were much higher than that of the non-mesoporous Pd/TNTAs evidencing the merits of the mesoporous structure. The mesoporous Pd was in a foam shape having an average pore wall thickness of 4 nm; in contrast, the Pd deposition unassisted by micelles resulted in large Pd particles (Figure 2.6d) with an average diameter of 150 nm covering the TiO_2

nanotubes (Figure 2.6g). Pd/TNTAs consisted of aggregations of small particles (~ 10 nm, Figure 2.6h) forming a rather dense layer. Gao et al. reported the size effect on Pd toward CO_2 electroduction selectivity, where they found that Pd particles with the size of 3.7 nm had the highest corner and edge site ratio that drives the formation of the HCOO*.[201] This is fully consistent with our finding with a smaller size mesoporous structure having a much better CO_2 electroreduction performance.

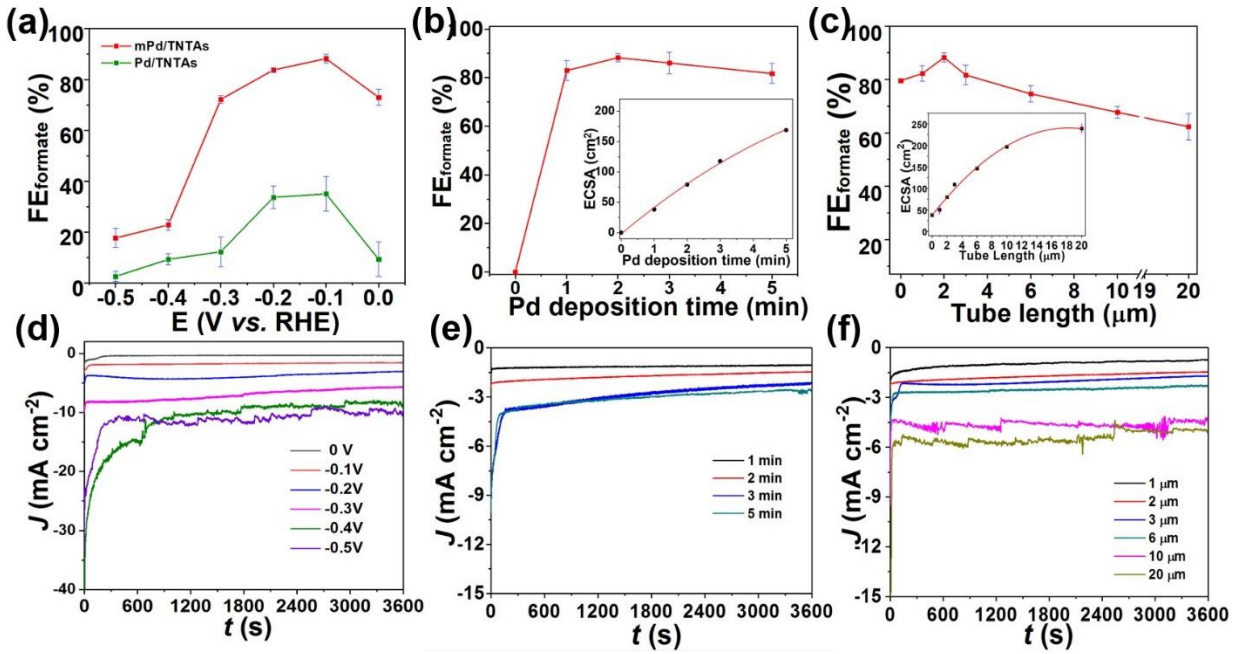

Figure 2.11 Performance of mPd/TNTAs. Comparison of formate Faradaic conversion efficiencies of mPd/TNTAs and Pd/TNTAs as a function of applied potential (a), formate Faradaic conversion efficiencies of mPd/TNTAs with different mPd loading time (b) and different length of the TiO_2 nanotube arrays of mPd/TNTAs (c). Insets in (b) and (c) are the corresponding active surface area of the mesoporous Pd films at different deposition times and lengths of TiO_2 nanotube arrays, respectively. (a, b) based on TNTAs of 2 μm; (a, c) mPd loading time of 2 min, and (b, c) at -0.1 V vs. RHE. (d) Current density-time curves of mPd/TNTAs at the potential range of 0 to -0.5 V vs. RHE. Current density-time curves of mPd/TNTAs with (e) different Pd layer thicknesses and

TiO_2 (f) nanotube lengths, with an applied potential of -0.10 V vs. RHE. All experiments were performed in 0.5 M $NaHCO_3$ solution under constant purging of CO_2 (20 mL min^{-1}) for 1 h.

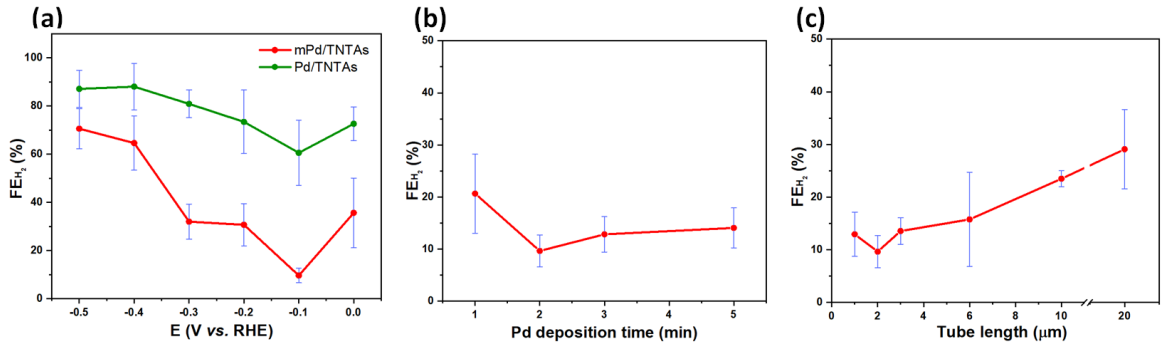

Figure 2.12 Faradaic efficiency of H_2. Comparison of H_2 faradaic conversion efficiencies of mPd/TNTAs and Pd/TNTAs as a function of applied potential (a), H_2 faradaic conversion efficiencies of mPd/TNTAs with different mPd loading time (b) and different length of the TiO_2 nanotube arrays of mPd/TNTAs (c). (a, b) based on TNTAs of 2 μm; (a, c) mPd loading time of 2 min, and (b, c) at -0.1 V vs. RHE. All experiments were performed in 0.5 M $NaHCO_3$ aqueous solution under constant purging of CO_2 (20 mL min^{-1}) for 1 h.

An examination of the Tafel plot of the mPd/TNTAs (Figure 2.13a) with a slope of 145 mV dec^{-1} from -0.05 to -0.1 V vs. RHE is similar to other reported values,[66, 211] suggesting absorbed hydrogen as a rate-limiting chemical reaction in an electrohydrogenation mechanism. The second high overpotential region exhibited a slope of 426 mV dec^{-1} which is postulated as a result of saturation of absorbed hydrogen and mass transport limitations.[201] The long term CO_2RR stability of the mPd/ TNTAs of 2 μm (Figure 2.13b) indicates a 72 % current density retention at ~ 2 mA cm^{-2} with formate Faradaic conversion efficiency of 84 % after 4 h electrolysis, and the mesoporous Pd structure remained intact. The drop in performance could be attributed to CO poisoning which generates as an intermediate species during CO_2 electroreduction.[66, 130, 212] The XRD and the XPS spectra of the mPd/TNTAs after performing 4h CO_2 electroreduction suggest

that the crystalline phase and the surface oxidation state of Pd species remained unchanged. The Pd mesoporous structure in this work exhibiting CO_2 to formate Faradaic conversion efficiency of 88 % is showing comparable value to those reported in literatures (Table 2.1). Noted that to examine the influence of support materials, we further perform electrodeposition of mesoporous Pd on carbon paper, and found that this support materials is highly unstable as the mesoporous Pd peeled-off and exhibit significant drop in current density (Figure 2.14) highlighting the advantage of TNTAs as hierarchical support materials.

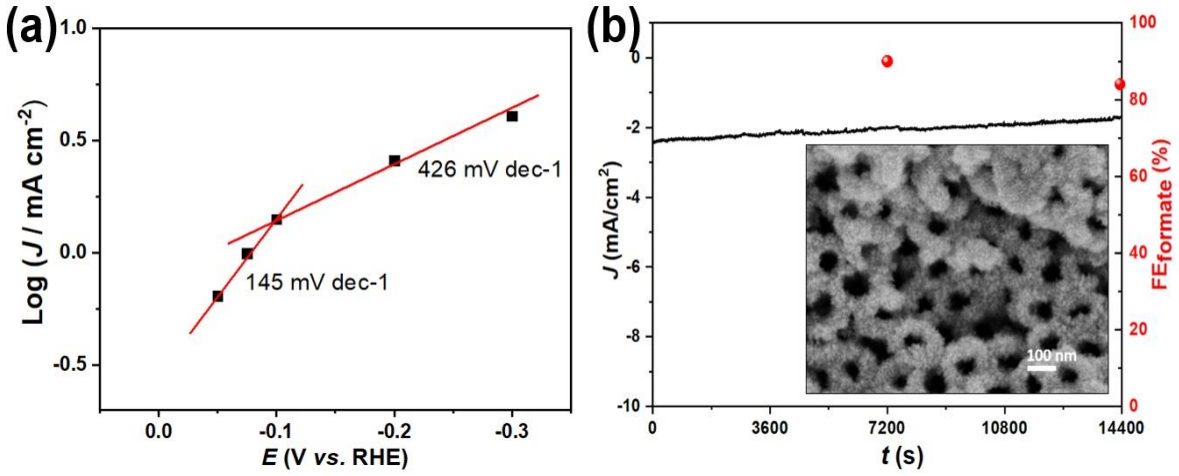

Figure 2.13 (a) Tafel plot of the mPd/TNTAs at the potentials between 0 to -0.3 V vs. RHE. (b) The long term CO_2RR stability test of the mPd/TNTAs samples performed at - 0.10 V vs. RHE. Inset showing the SEM of mPd/TNTAs after the 4 h electrochemical CO_2RR.

It is important to note that, as described earlier, a 2 min electrodeposition was found to be optimal in achieving homogeneous coverage of mesoporous palladium. The sample prepared under this condition is also found exhibit an optimum formate Faradaic conversion efficiency (Figure 2.11b), which is supported by the controlled potential electrolysis data (Figure 2.13b). A

control experiment with TNTAs alone (refer to 0 min of Pd deposition time) only detected the H_2 product, suggesting that TiO_2 nanotubes were inert toward CO_2 electroreduction.

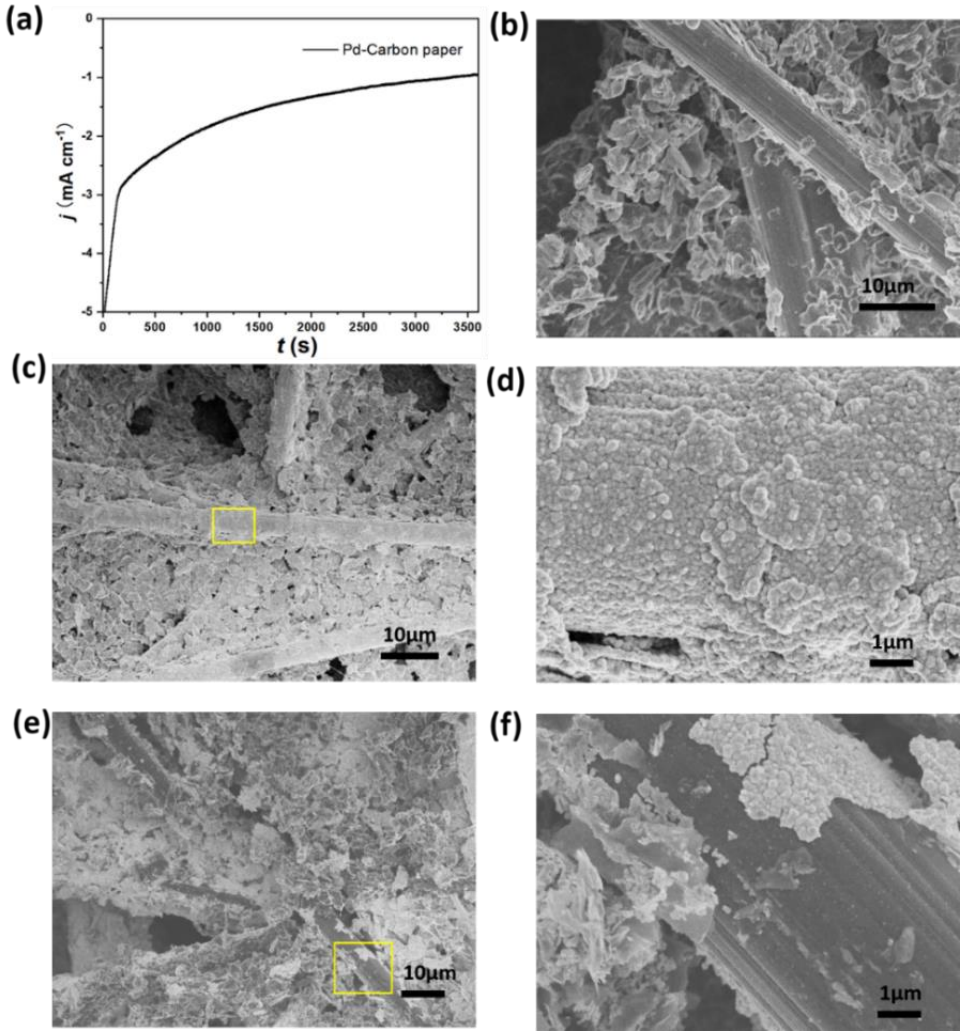

Figure 2.14 Current density-time curve and SEM images of mesoporous Pd on carbon paper. (a) Current density vs. time of mesoporous Pd on carbon paper. SEM image of (b) carbon paper, (c-d) mesoporous Pd on carbon paper before test, and (e-f) after test. (d) and (f) are the enlarged areas in the selected areas in (c) and (e), respectively. The CO_2RR performace test were conducted in CO_2 saturated $NaHCO_3$ (0.5M) aqueous solution under constant purging of CO_2 (20 mL min^{-1}) for 1 h. The mesoporous Pd on carbon paper was electrodeposited for 2 min.

Table 2.1 Summary of Pd-based catalysts for CO_2 electroreduction with formate product.

Sample	Structure	Electrolyte	Potential (V vs. RHE)	Faradaic efficiency (%)	Reference
Pd nanoparticles	~5 nm Pd nanoparticles on carbon particles	2.8 M $KHCO_3$	-0.05 V ~ -0.25 V	Formate: 86 to 94 %	Min and Kanan[66]
Pd nanoparticles	3.7 nm nanoparticles	1 M $KHCO_3$	-0.1 V ~ -0.2 V	Formate: ~98 %	Gao et al.[67]
Boron-doped Pd	4.1± 0.5 nm	0.1 M $KHCO_3$	-0.5 V	Formate: 70%	Jiang et al.[213]
Pd nanoparticles	~ 4.2 nm Pd nanoparticles	0.5 M $NaHCO_3$	-0.15 V	Formate: 71%	Takashima et al.[212]
Pd@TiO_2/ Carbon Nanohorns	Pd nanoparticles (1.5 nm) shielded within the TiO_2 phase	0.5 M $NaClO_4$	~ -0.2 V vs. RHE	Formate: ~95% in the initial 5 min, 40% after 1 h	Melchionna et al.[214]
RuO_2 + TiO_2	RuO_2:TiO_2=35:65 (mole percent)	0.05M H_2SO_4 (pH = 12)	-0.9 V vs. Hg_2SO_4	Formate: ~2%	Bandi et al.[215]
RuO_2 + MoO_2 + TiO_2	RuO_2:MoO_2:TiO_2= 25:30:45 (mole percent)	0.05M H_2SO_4 (pH = 12)	-0.9 V vs. Hg_2SO_4	Formate: <1%	Bandi et al.[215]
RuO_2 + Co_3O_4 + SnO_2 + TiO_2	RuO_2:Co_3O_4:SnO_2: TiO_2= 20:10:8:62 (mole percent)	0.05M H_2SO_4 (pH = 12)	-0.9 V vs. Hg_2SO_4	Formate: 18%	Bandi et al.[215]
mPd/TNTAs	MesoporousPd-TiO_2 nanotube hierarchical structures	0.5 M $NaHCO_3$	-0.1 V	Formate: 88%	This work

The active surface area plot in the inset of Figure 2.11c shows an almost linear increase of Pd loading corresponding to the increase in the tube length up to 10 μm. Excessively long tubes of 20 μm resulted in much more difficult access of electrolyte to the outer as well as inner layer of the bottom level of tubes, which makes the active surface area gradually decrease. Taking this into account, we examined the CO_2 electroreduction performance of various TNTA tube lengths.[216] The highest formate Faradaic conversion efficiency of 88 ± 2% at -0.1 V vs. RHE was obtained using TNTAs of 2 μm (Figure 2.11c). Longer tubes increased the Pd loading (Figure 2. 15b), as well as current density during the controlled potential electrolysis (Figure 2.11f), but this trend did not translate into formate Faradaic conversion efficiency. Instead, with the increase of tube length, the conversion to H_2 became gradually dominant. As a control experiment, a compact layer of TiO_2 on Ti foil was used (refer to 0 μm tube length in Figure 2.11c). Under the equivalent Pd deposition time, it had lesser Pd loading compared to the tubular TiO_2, indicating that the TiO_2 nanotube arrays with enhanced specific surface area can significantly improve the Pd loading. The samples with tube length of 1 μm showed slightly lower efficiency as a result of the poorer nanotubular morphology (Figure 2.2a) with some anodization initiation layers remaining.

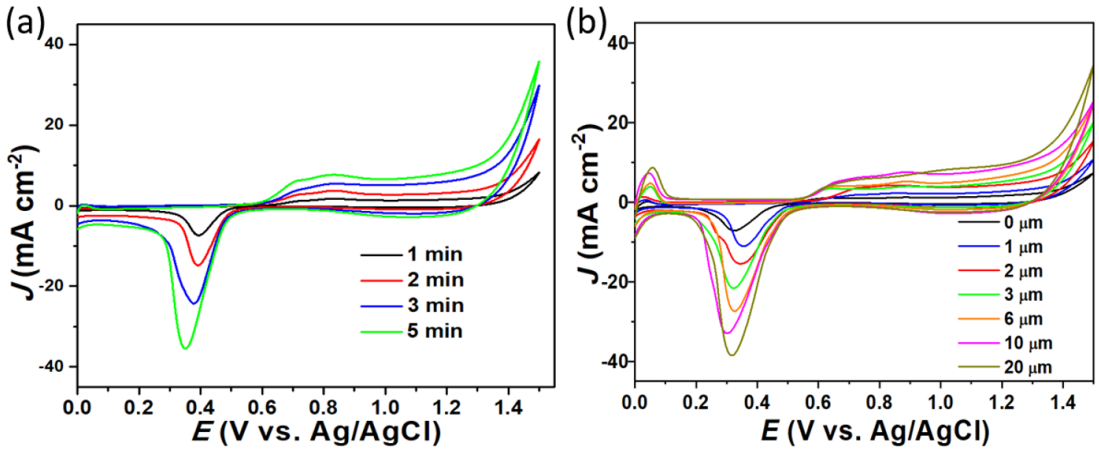

Figure 2.15 CV for the calculation of active surface area. CV measurements of (a) mPd-TNTAs (2 μm) with different Pd deposition time; (b) mPd-TNTAs with different TNTAs lengths, the loading time in (b) is 2 min. All the measurements were performed in 0.5 M H_2SO_4.2.4.3 Tube length effects on performance

Our results suggest a systematic influence of TiO_2 tube lengths on the electrocatalytic activity of mesoporous Pd, as summarised in the plot of partial current densities of CO_2RR and H_2 evolution reaction (HER) (Figure 2.16a). For further discussion, we categorized the reaction zones into three regions: CO_2RR dominated, CO_2RR & HER mixed, and HER & non-active regions, according to the distance between the tube openings and the tube ends (Figure 2.16b). The plots of Figures 2.16a and 2.16b were based on the experimental data presented in Figure 2.11. This result underlying competition between the two reactants: dissolved CO_2 that is externally supplied to the electrolyte, and protons that are abundant in the electrolyte. Note that the concentration of CO_2 in aqueous electrolyte under ambient conditions is low, e.g. C_{CO_2} = 0.033 M.[37] At the CO_2RR active zone near the tube openings, fresh CO_2-saturated electrolyte readily reaches the Pd

surface to be electroreduced to formate continuously. In this case, the applied potential governs the products formation from the CO_2 electroreduction.

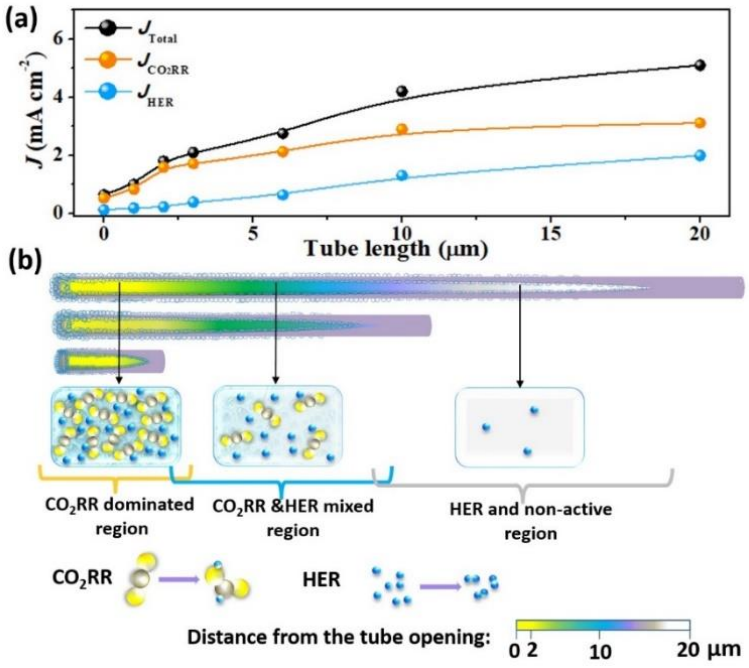

Figure 2.16 Summary of the total current density J_{Total}, partial current density of formate J_{CO2RR} and J_{HER} (a); schematic of the tube length effect on the dominated reaction (b).

However, when the tube length is in excess of ~ 3 μm, the slow mass transport of CO_2 (diffusion coefficient of CO_2 , DCO_2 = 0.0016 mm^2 s^{-1})[140, 217] results in less CO_2 reaching the inner and outer parts of the longer tubes. It was previously found the accessibility of proton to be optimal for TiO_2 tube length of 10 μm for photoeletrochemical water splitting, indicating an aqueous electrolyte can penetrate efficiently to this tube length.[218-219] Therefore, the lack of continuous CO_2 supply to compensate for the consumed CO_2, as well as the competition from proton, in this CO_2RR & HER mixed region result in a gradual drop of formate Faradaic conversion efficiency. The electroreduction processes in this region is expected to be more

complicated than that of the CO_2RR dominated region due to the mass transport limitation. During these processes, local pH change in the tubes may also influence the electrocatalytic performance.[50, 220-221] The consumption of CO_2 and protons result in increased local pH within the inner and outer layers of the nanotubes. Smith and coworkers demonstrated the influence of local pH changes with the length of copper nanowires increasing alkalinity thus influencing the generated products.[188] The one-dimensional nanostructured architecture is known could affect the mass transport properties of the diffuse species.[193, 222-223] In our case, the compact and well-aligned highly ordered TiO_2 nanotube arrays with increasing length create a region of depleted CO_2 concentration. This would have predominant effect along with the local pH change. To verify the impact of local pH toward formate conversion efficiency, we examined CO_2 electroreduction performance in 0.5 M $NaHCO_3$ electrolytes of different pH at the potential of -0.1 V vs.RHE (Figure 2.17). At initial pH=9.2 and pH=12.1, the formate conversion efficiency dropped to 41 % and 3 %, respectively (note that at pH 6.8, formate conversion Faradaic efficiency = 88 %), indicating alkalinity decreases the CO_2 to formate conversion efficiency.

At the longer lengths of TiO_2 nanotubes (e.g. > 10 μm), under ambient conditions, even aqueous electrolyte have difficulty in accessing the inner part of the tubes (as shown in active surface area curve of Figure 2.11c). Consequently, limited electrocatalytic reaction takes place, and hence we categorise this as a non-active region. It is noticeable that for the long tubes, substantial gas bubbles are generated from the proton reduction. These bubbles may be released from as well as adsorbed onto the surface of the Pd which decreases the contact of dissolved CO_2 molecules with the Pd active sites, which may result in gradual expansion of non-active region as the experiment progressed. Our examination of a model hierarchical structure consisting of highly

ordered TiO_2 nanotube arrays, implies differences in the mass transport properties of reactants, CO_2 and proton, could result in tuneable product selectivity by simply varying the lengths of the TiO_2 nanotubes. This strategy could be extended to control products from other CO_2 reduction electrocatalysts, such as Ag for CO production, which may realise the variation of syngas ration of H_2 and CO.

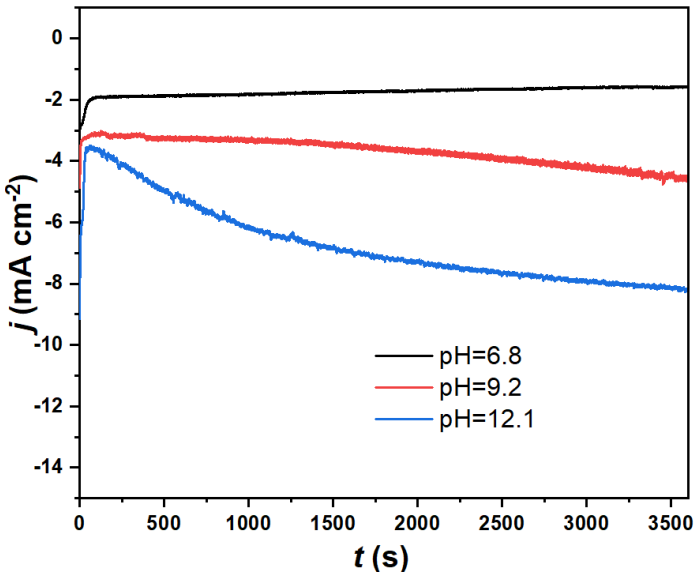

Figure 2.17 Current density-time curves of mPd/TNTAs with different initial pH. All experiments were performed in 0.5 M $NaHCO_3$ aqueous solution under constant purging of CO_2 (20 mL min^{-1}) for 1 h using the mPd/TNTAs of 2 min mesoporous Pd loading and TiO_2 tubes of 2 µm.

2.5 Conclusions

A hierarchical structure consisting of mesoporous Pd homogeneously covering TiO_2 nanotube arrays favours the formate conversion in comparison to a non-mesoporous counterpart. This work reveals that the advantageous features of both 3D meso and 1D tubular structures can only be realised by considering the types and availability of reactants, as well as competing reactions participating in catalytic conversion processes. Unlike other catalytic reactions such as water

oxidation, proton reduction or methanol oxidation where the targeted reactants are abundant, the low solubility of CO_2 only allows a short tube length to be an effective region for CO_2 conversion. Tuning the mass transport limitation of reactants within catalyst/hierarchical support structure offers an efficient way of tuning product selectivity. As hierarchical features are one of the most investigated and promising scalable strategies for wide-range of catalytic reactions, this work offers key insights toward designing catalytic-support interfaces to achieve efficient electrocatalytic conversion of targeted products.

2.6 Acknowledgements

J.Z. and C.Y.L thank the University of Wollongong for the awards of postgraduate scholarship and VC Fellowship, respectively. Funding from the Australian Research Council Centre of Excellence Scheme (CE140100012) is gratefully acknowledged. The authors would like to thank Australian National Fabrication Facility-Materials Node (ANFF) and University of Wollongong Electron Microscopy Centre for equipment use.

Chapter 3 Boosting formate production from CO_2 at high current densities over a wide electrochemical potential window on a SnS catalyst

This chapter has been adapted, with the publisher's permission, from the article entitled 'Boosting formate production from CO_2 at high current densities over a wide electrochemical potential window on a SnS catalyst' published in Advanced Science.

Citation: Zou et al., Advanced Science, 2021, 2004521.

DOI: https://doi.org/10.1002/advs.202004521

Jinshuo Zou, Chong-Yong Lee* and Gordon G. Wallace*

ARC Centre of Excellence for Electromaterials Science, Intelligent Polymer Research Institute, AIIM, Innovation Campus, University of Wollongong, Wollongong, NSW 2500, Australia.
* Corresponding author

Keywords: Tin sulphide, alkaline, CO_2 reduction, flow-cell, formate

Author statement:

The study in this chapter was conceptual, experimentally designed and written by Jinshuo Zou. All experiments including material preparations, characterizations, electrochemical studies and the data analysis presented in this chapter were performed by Jinshuo Zou. Dr. Chong-Yong Lee and Prof. Gordon G. Wallace supervised the study, and assisted in the conception, experimental design and revisions of manuscript.

3.1 Abstract

The flow-cell design offers prospect for transition to commercial-relevant high current density CO_2 electrolysis. However, it remains to understand the fundamental interplay between the catalyst, and the electrolyte in such configuration toward CO_2 reduction performance. Herein, the dramatic influence of electrolyte alkalinity in widening potential window for CO_2 electroreduction in a flow-cell system based on SnS nanosheets is reported. The optimized SnS catalyst operated in 1 M KOH achieves a maximum formate Faradaic efficiency of 88 ± 2 % at -1.3 V *vs.* RHE with the current density of ~ 120 mA cm^{-2}. Alkaline electrolyte is found suppressing the hydrogen evolution across all potentials which is particularly dominant at the less negative potentials, as well as CO evolution at more negative potentials. This in turn widens the potential window for formate conversion (> 70% across -0.5 to -1.5 V *vs.* RHE). A comparative study to SnO*x* counterpart indicates sulfur also acts to suppress hydrogen evolution, although electrolyte alkalinity resulting in a greater suppression. The boosting of the electrochemical potential window, along with high current densities in SnS derived catalytic system offers a highly attractive and promising route toward industrial-relevant electrocatalytic production of formate from CO_2.

3.2 Introduction

The burning of fossil-fuels as energy sources to support increasingly demanding industries and household activities over the past decades has resulted in the alarming level of anthropogenic CO_2 gas in the atmosphere.[224-226] Electrochemical reduction of CO_2 offers a viable clean energy technology to mitigate CO_2 by converting this greenhouse gas to valuable chemical feedstocks.[44, 227-228] Among the liquid products, formic acid or formate has been found wide-ranging

applications in chemical industries for production of household products,[23, 27] as well as offering promise as a safe liquid-phase chemical for hydrogen storage and conversion.[229-231] In comparison to other formate producing CO_2 electrocatalysts, such as Bi,[86] In,[232] Pb,[233] and Pd,[200] the low cost, eco-friendly and nontoxic characteristics of tin make it an outstanding and promising catalyst candidate for CO_2 reduction to formate.[31, 234-235]

To overcome the intrinsically poor electrocatalytic CO_2 reduction performance of a bulk Sn with a large overpotential and low current density, various material engineering strategies have been applied. This includes nanostructuring of Sn to structures such as metallic Sn quantum sheets,[236] coralline structured SnO_x,[237] SnO_2 porous nanowires,[134] ultra-small SnO,[238] and SnS_2 nanosheets[81], that promotes surface area and active sites toward selective formate production. In addition to alloying or doping with metals such as Cu,[239] Ag,[83] Pd,[240] Ni,[135] positive synergetic impact of doping of a non-metallic element such as sulfur[85] or nitrogen[241] is another attractive approach toward enhancing formate production. From experimental and density functional theory results, sulfur was found played a role in stabilising the *OCHO intermediate, weakening the interaction between CO and electrode, and therefore favouring the formation of formate.[81, 85, 242-243] However, there are still limitations with respect to generally low operating current density, as well as the narrow electrochemical potential window available to ensure high formate Faradaic efficiency.

Recent studies suggest that the use of a flow-cell capable of supplying gaseous CO_2 from the backside of a gas diffusion electrode (GDE) to react with the electrocatalyst, overcomes the limitation of poor CO_2 solubility (0.034 M) in an aqueous solution when employing a laboratory H-cell configuration.[77, 244] Flow-cells have recently been employed for electrochemical CO_2

reduction reaction (CO_2RR) to overcome the low current densities by reducing the mass transfer issue that exists in the H-cell system, as the tri-phasic solid/liquid/gas interfaces maximise the interaction between the catalysts and the reactants.[140] In this configuration, the selectivity of a catalyst can be tuned by employing an alkaline KOH or NaOH electrolyte. For example, Dinh et. al. reported improved ethylene selectivity to 70% via KOH-mediated CO_2 electrocatalysis on a copper catalyst.[245] Irtem et al.[77] applied the flow-cell using Sn based catalyst which obtain formate conversion Faradaic efficiency as high as 71% for 6 h, though the current density was low (8.58 mA cm^{-2} at -1.1 V *vs.* RHE). Liang et al.[79] improved the total current density (147 mA cm^{-2} at -0.95 V *vs.* RHE) and tuned the selectivity of hydrocarbon and oxygenate (C_2H_5OH) by changing the electrolyte (KOH *vs.* $KHCO_3$) on ultra-small SnO_2 nanoparticles. This system shows formate Faradaic conversion efficiency of ~ 75% with a narrow potential window of around -0.73 V *vs.* RHE.

It is desirable if the non-noble metallic catalyst such as Sn is able to be developed to achieve the high formate conversion efficiency, as well as operability over a wide range of potential window for electrochemical CO_2 reduction. Boosting the cathodic potential window offers an advantage of the flexibility in coupling to anodic reactions. This in turn will allow full-cell CO_2 electrolyser operable at a wider operation potential range. In this study, we synthesized and optimised tin-based catalyst, SnS nanosheets, to be an efficient electrocatalyst for formate production. This followed by rationally investigating conditions that allows operation at a wide potential window, as well as promoting the SnS electrocatalyst long term stability. We also examined mechanistic aspects of the role of alkalinity in widening the electrochemical potential window.

3.3 Experimental Section/Methods

3.3.1 Electrode preparation

Tin (II) chloride (99%, Sigma Aldrich), ethylene glycol (Chem-Supply), thiourea (99%, Sigma Aldrich), gas diffusion layer (Sigracet 39 BC, FuelCellStore), Carbon dioxide (CO_2, 99.99%), hydrogen (H_2, 99.99%) and Ar cylinders were purchased from BOC.

Catalyst preparation: 1 mmol of $SnCl_2$ and 2 mmol of thiourea were dissolved in 35 mL of ethylene glycol and stirred for 1h to obtain a homogeneous solution. The solution was then transferred to autoclave (50 mL). The autoclave was kept at 140 ^oC, 160 ^oC, 180 ^oC and 200 ^oC for 12 h. After cooling down to room temperature, the precipitates were collected and washedby centrifuging with ethanol for 5 times and dried to get the tin sulphide particles. The particles were exfoliated to nanosheets by ultrasonicating in isopropanol to obtain a homogenous SnS catalyst suspension (25 mg mL^{-1}).

Working electrode preparation: 400 µL of SnS catalyst suspension, 460 µL of isopropanol, 100 µL of DI water, and 40 uL of nafion solution (15%) were ultrasonically mixed for 30 min to form a homogenous catalyst ink. The diferrent volumes of catalyst ink were air-brushed on the gas diffusion layers (GDL) and dried at 50 ^oC overnight to serve as SnS/GDL working electrodes.

3.3.2 Characterization:

XRD patterns of the tin sulphide based samples were collected on a PANalytical Empyrean diffractometer with Cu K_α radiation at a scan rate of 2 ^{o} min^{-1}. The surface morphologies of the

samples were recorded on a scanning electron microscope (SEM) of JEOL JSM-7500FA. Transmission electron microscopy (TEM) was carried out on a JEOL JEM-2100F microscope. The X-ray photoelectron spectroscopy (XPS) measurements were performed on the VG Multilab 2000 (VG Inc.) photoelectron spectrometer with the monochromatic Al K_α radiation under vacuum at 2×10^{-6} Pa. Raman analysis was performed with a Raman spectrometer of HORIBA Scientific with the laser line of 633 nm and the accumulations of 50.

3.3.3 Electrochemical characterization:

All the measurements were carried out on a CHI660D potentiostat at room temperature, in a home-made flow-cell separated by a cation exchange membrane (Nafion 115) in the neutral electrolyte and anion exchange membrane (Fumasep FAB-PK-130, FuelCellStore) in the alkaline electrolyte. HgO electrode and nickel mesh were used as the reference and counter electrodes, respectively when employing alkaline electrolyte. Ag/AgCl (3 M NaCl) electrode and Pt mesh were used as the reference and counter electrodes, respectively when employing neutral electrolyte (0.5 M $KHCO_3$). The CO_2 gas was introduced into the cathodic chamber at a flow rate of 20 mL min^{-1} and the electrolyte was pumped by a peristaltic pump (BT100-2J, Thermoline) at the flow rate of 17.5 mL min^{-1}. All test were conducted without IR-compensation.

3.3.4 Product analysis:

The gaseous products were analysed by a gas chromatography (GC) (8610C, SRI Instruments) equipped with both flame ionization detector (FID) and thermal conductivity detector (TCD). CO, CH_4, C_2H_4, C_2H_6 were detected by the FID and H_2, CO, CH_4, C_2H_4, C_2H_6 and CO_2 were detected

by TCD. The analysis of liquid products were carried out on a 400 MHz NMR spectrometer (Bruker Avance). The 1D ^{1}H spectra were measured with water suppression. 1-propanesulfonic acid 3-(trimethylsilyl) sodium (DSS) was used as internal standard solution. A 0.5 mL of product-containing electrolyte, 0.1 mL of DSS (99.7%, Sigma Aldrich), and 0.1 mL of D_2O (99.9%, Cambridge Isotope Lab) was added in the NMR tube and mixed by ultrasonication before NMR analysis.

3.3.5 Electrochemically active surface area (ECSA) measurement

The electrochemically active surface area (ECSA) of SnS was obtained using cyclic voltammetry over the potential window of -0.5 to -0.7 V in the electrolyte of 1 M KOH. The C_{dl} was estimated by plotting the Δj (j_a-j_c) at 0.6V against the scan rate. The specific capacitance (20–60 μF cm^{-2}) of 40 μF cm^{-2} was used to calculate the ECSA:[246]

$$ECSA = C_{dl}/40\ \mu F \cdot cm^{-2}$$

3.4 Results and Discussion

3.4.1 Preparation and characterization of SnS / gas diffusion layer (SnS/GDL)

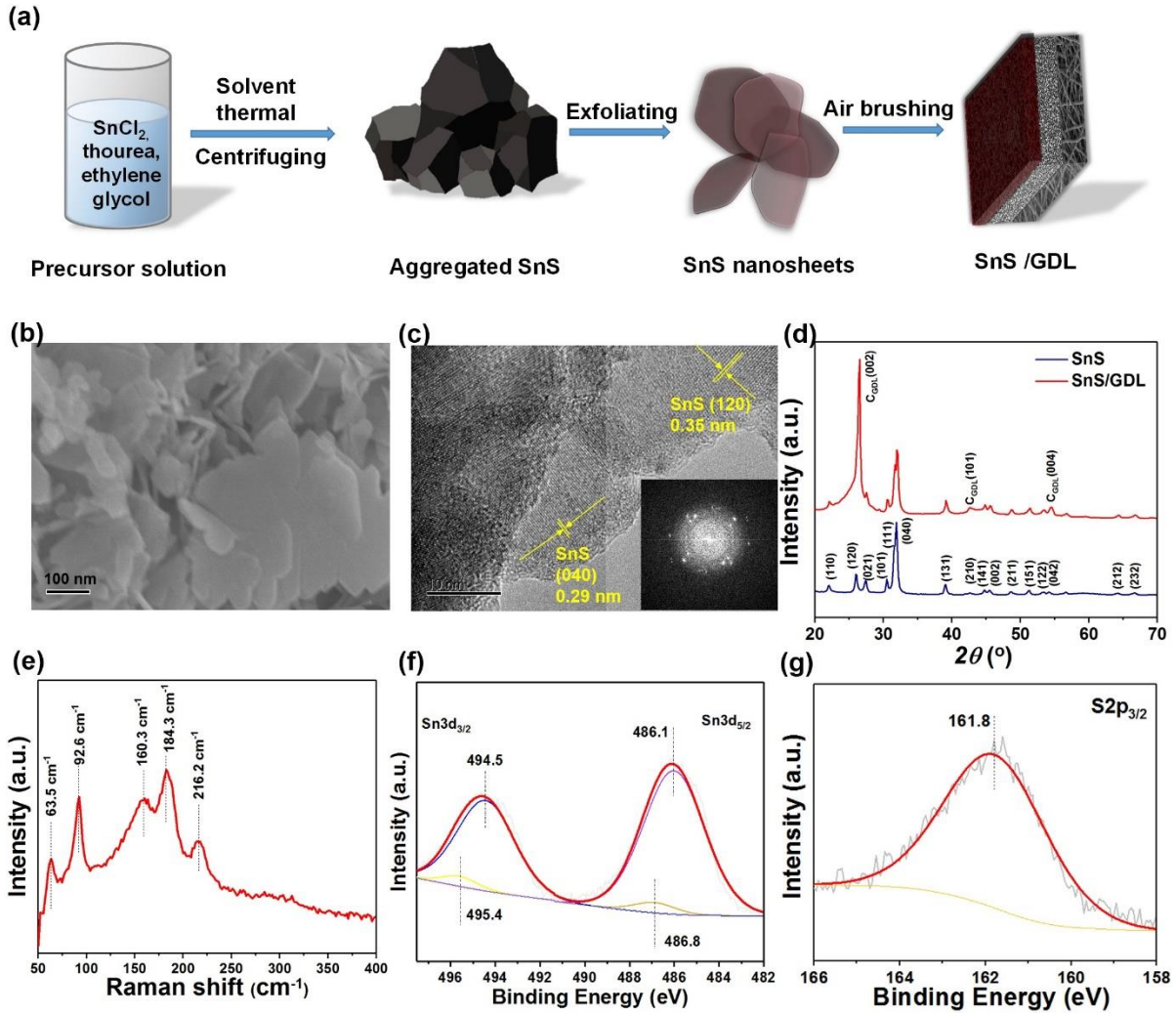

Figure 3.1 Preparation and characterization of SnS-based samples. (a) The schematic diagram on the steps to fabricate SnS/GDL; SEM (b) and TEM (c) image of SnS, with inset in c is the corresponding Fast Fourier Transform (FFT) image taken from the TEM image; (d) XRD patterns of SnS and SnS/GDL, (e) Raman spe spectrum of SnS/GDL, and (f, g) XPS spectra of Sn and S elements on SnS/GDL.

Figure 3.1a schematically illustrates the preparation of the SnS catalyst loaded on a gas diffusion layer (GDL). The SnS was firstly formed by a modified solvothermal method by treating the precursors $SnCl_2$ and thiourea in the solvent of ethylene glycol at the temperatures between 140 ^oC and 200 ^oC for 12 h. After washing several times by centrifuging in ethanol, the bulk SnS was exfoliated by ultrasonication for 1 h in isopropanol to obtain a homogenous SnS nanosheet suspension.[247] Then the ink containing SnS nanosheets, isopropanol and nafion solution was air-brushed on a commercially available carbon paper-based GDL (Sigracet 39 BC) with the catalyst loading of 0 to 2 mg cm^{-2} and dried at 50 ^oC overnight. More experimental details are described in the experimental section. The XRD patterns and the SEM images of the catalysts synthesized at different temperatures are shown in Figures 3.1b, 3.1d, 3.2, and 3.3. As presented in Figure 3.4 and 3.5, it was found the SnS catalyst obtained at solvothermal temperature of 180 ^oC, with the SnS loading of 1 mg cm^{-2} to be the optimal conditions. Therefore, unless otherwise stated, all the characterization and performance results are based upon the SnS/GDL samples prepared under the above conditions.

The SEM images in Figures 3.1b and 3. 3 reveal the synthesized SnS nanosheets with sheet sizes of 0.1 to 1 μm and a thickness of 10 ± 2 nm. The lattice structure of SnS was further characterized by TEM (Figure 3.1c). The SnS lattice fringes with d-spacing of 0.35 nm and 0.29 nm are from SnS (120) and SnS (040), respectively. The XRD patterns of SnS and SnS/GDL confirming the crystalline phase of SnS with predominant diffraction peaks in Figure 3.1d at 22.0^o, 27.4^o, 30.5^o, 31.9^o, 39.0^o are originated from orthorhombic SnS crystal facets (JCPDS 39-0354), which is in agreement with the d-spacing in Figure 3.1c. The Raman spectroscopy spectrum of the SnS/GDL recorded at the wavelength of 50 - 400 cm^{-1} is presented in Figure 3.1e. Raman modes at 63.5, 92.6, 160.3, 184.3, 216.2 cm^{-1} are consistent with the signature optical phonons modes of

SnS.[248-249] The peaks at 184.3 and 216.2 cm^{-1} represent the longitudinal optical A_g (LO) modes, whereas 92.6 cm^{-1} belongs to the transverse optical A_g (TO) mode. The mode at 63.5 cm^{-1} is assigned to the combination of A_g and B_{2g} of SnS while the mode at 160.3 cm^{-1} can be attributed to B_{2g} of SnS phase. Importantly, there is no SnS_2 or Sn_2S_3 associated peaks that are expected to be at around 312 cm^{-1} and 308 cm^{-1}, suggesting that the obtained tin sulphide is a pure SnS phase. Composition and valence state analyses were conducted by XPS spectrum of Sn 3d (Figure 3.1f). There are two main peaks at 486.1 eV and 494.5 eV corresponding to $Sn3d_{5/2}$ and $Sn3d_{3/2}$.[250-251] The XPS fittings of small peaks at 486.8 eV and 495.4 eV represent the Sn^{4+}, potentially attributed to natural oxidation of Sn^{2+} in air. The $Sp_{3/2}$ peak at 161.8 eV in Figure 3.1g corresponds to S^{2-} species attached to Sn^{2+}.[250]

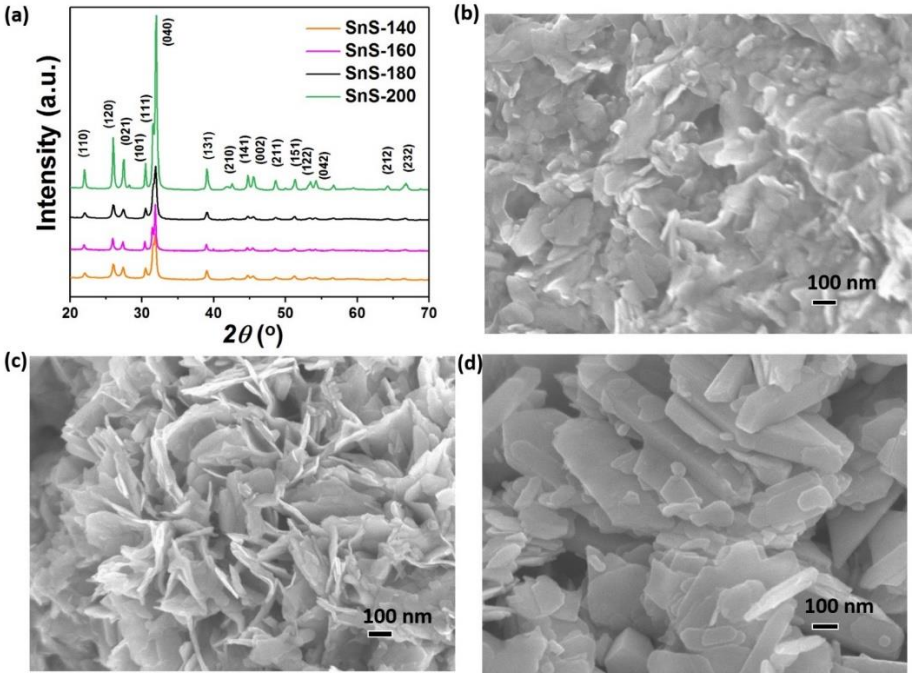

Figure 3.2 Characterization of SnS catalysts obtained at different solvothermal synthesis temperatures from 140 to 200 ºC. XRD patterns (a), SEM images of SnS heated at (b) 140 ºC (SnS-140), (c) 160 ºC (SnS-160), and (d) 200 ºC (SnS-200).

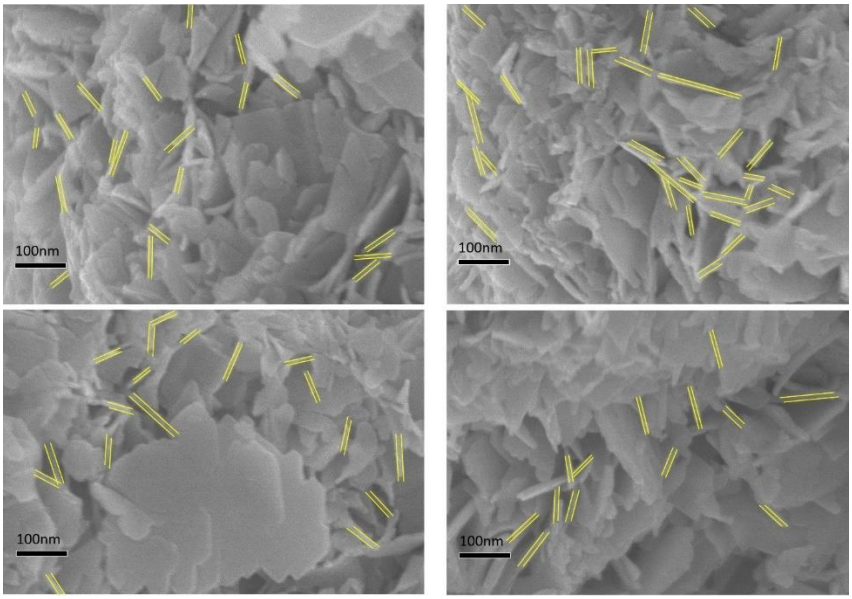

Figure 3.3 SEM images of SnS nanosheets. The parallel yellow lines marked the layer thicknesses.

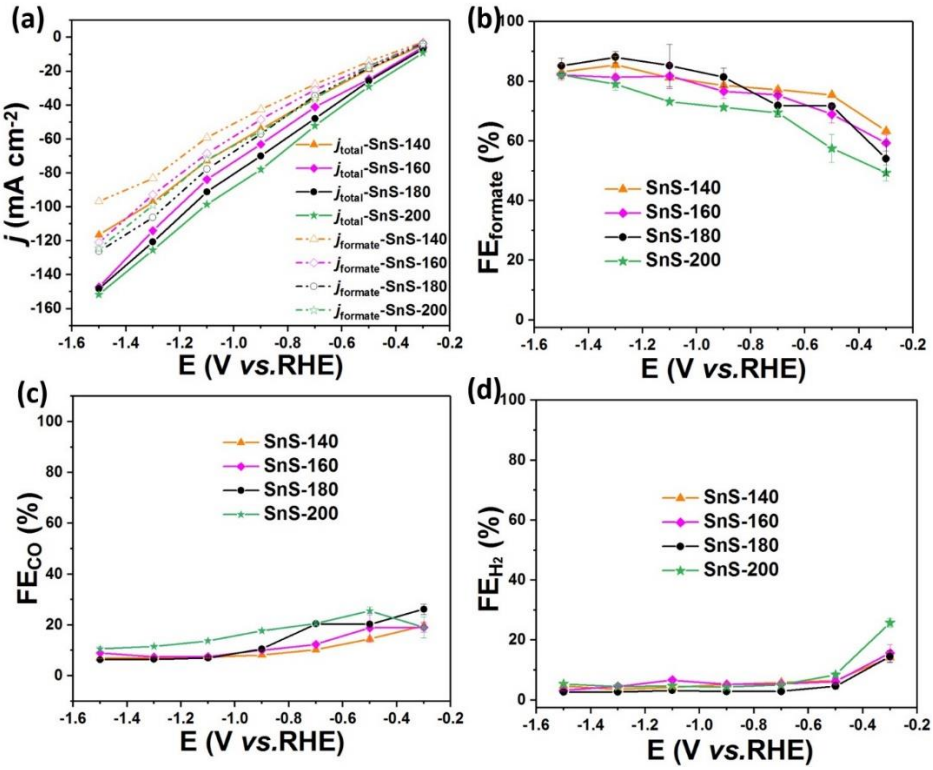

Figure 3.4 Performance of SnS synthesis at differrent temperatures. Steady-state current density (a), Faradic efficiencies toward formate (b), CO (c) and H_2 (d) productions from CO_2

electroreduction in 1 M KOH. The error bars represent the standard deviations of three independent measurements of the samples.

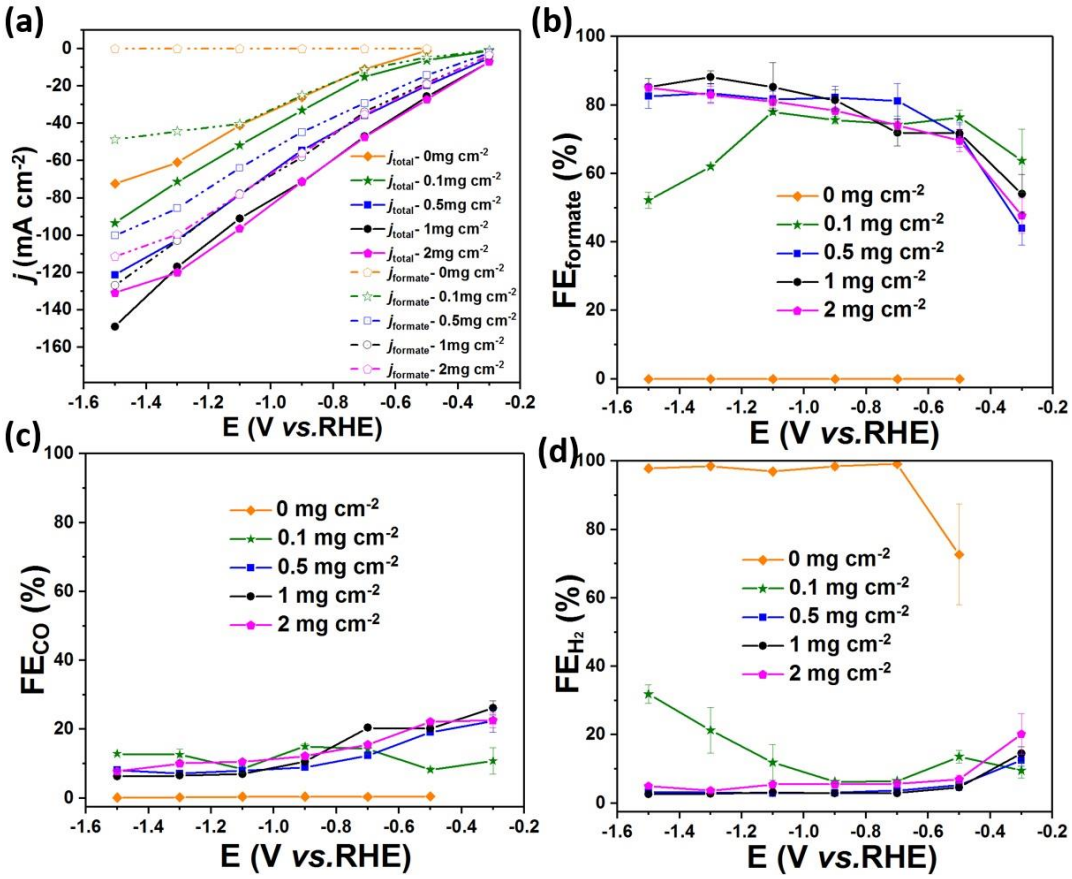

Figure 3.5 Performance of SnS synthesized at 180 ^{o}C with different catalyst loading. Steady-state current density (a), Faradic efficiencies toward formate (b), CO (c) and H_2 (d) productions from CO_2 electroreduction in 1 M KOH. The error bars represent the standard deviations of three independent measurement of the sample.

3.4.2 CO_2 electroreduction performance

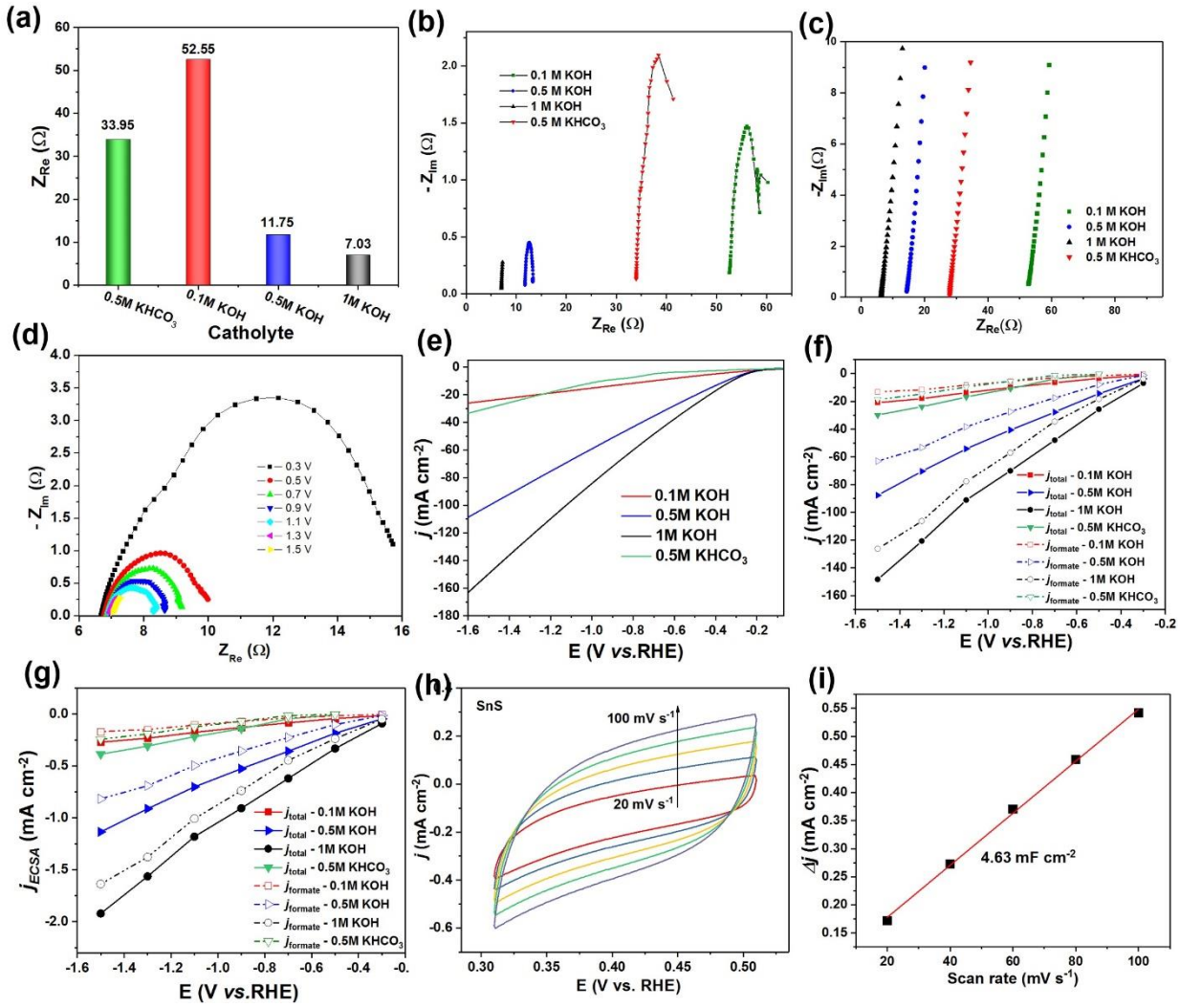

Figure 3.6 Electrochemical characterization of SnS/GDL samples. (a) Ohmic resistance of SnS/GDL samples in different electrolytes obtained from the Nyquist impedance plots in (b) with the electrode potential of -1.5 V vs. RHE; Nyquist impedance plots of SnS/GDL sample at open circuit potentials (c) and at different potentials from -0.3 to -1.5 V vs. RHE (d) in the catholyte of 1 M KOH. All the Nyquist impedance plots were obtained in frequency range from 1 to 100 mHz with 30 mV amplitude. (e) Linear Sweep Voltammetry (LSV) curves of SnS/GDL samples performed in different electrolytes at 10 mV s^{-1}. (f) Steady-state current density of SnS/GDL samples in different electrolytes, solid symbols represent the total current density (j_{total}) while

empty symbols represent the partial current density of formate ($j_{formate}$). (g) ECSA normalized steady-state current density of SnS/GDL sample at different potentials from -0.3 to -1.5 V vs. RHE. (h) CV curves of SnS, obtained at the non-Faradaic capacitance current range at the scan rates of 20, 40, 60, 80, and 100 mV s^{-1} in the electrolyte of 1 M KOH for ECSA calculation of SnS/GDL. (i) plot of the Δj - Scan rate derived from CV curves in (h). The CO_2RR performance tests were conducted in a three-electrode flow electrochemical cell (Figure 3.6a), a photograph of the experimental setup is shown in Figure 3.7a. The synthesized SnS was homogenously loaded on the GDL consisting of a microporous carbon layer on a macroporous carbon fiber layer to serve as the working electrode (Figure 3.8). In this tri-phasic solid/liquid/gas system, the CO_2 gas flowed through the carbon layers to reach the SnS catalyst at a flow rate of 20 mL min^{-1}. The catholyte and anolyte were circulated into the corresponding compartments at a flow rate of 17.5 mL min^{-1}.

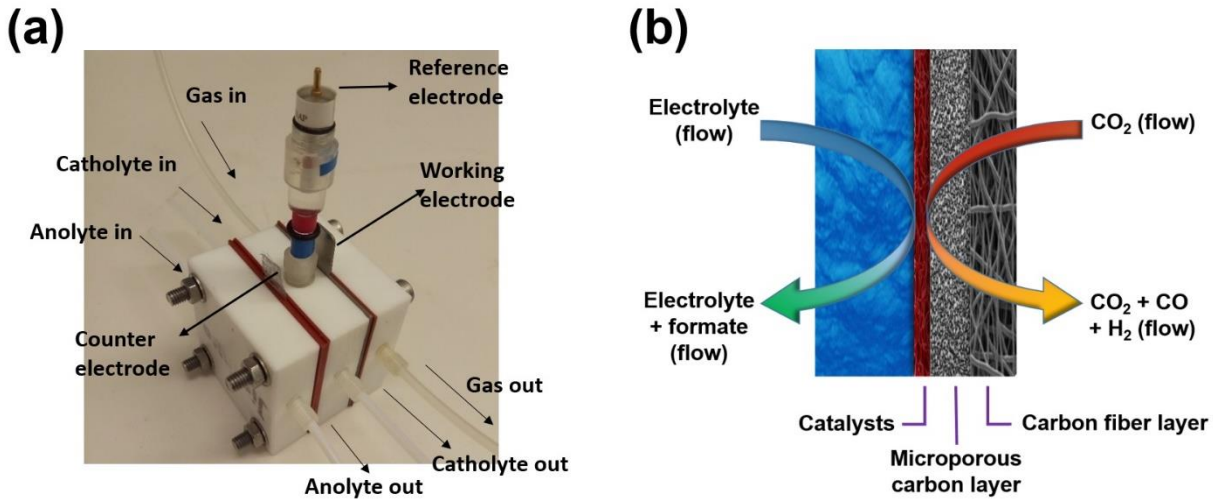

Figure 3.7 (a) The photograph of a flow-cell for CO_2 electroreduction employed in this study, (b) Schematic of the cathodic part of flow-cell configuration.

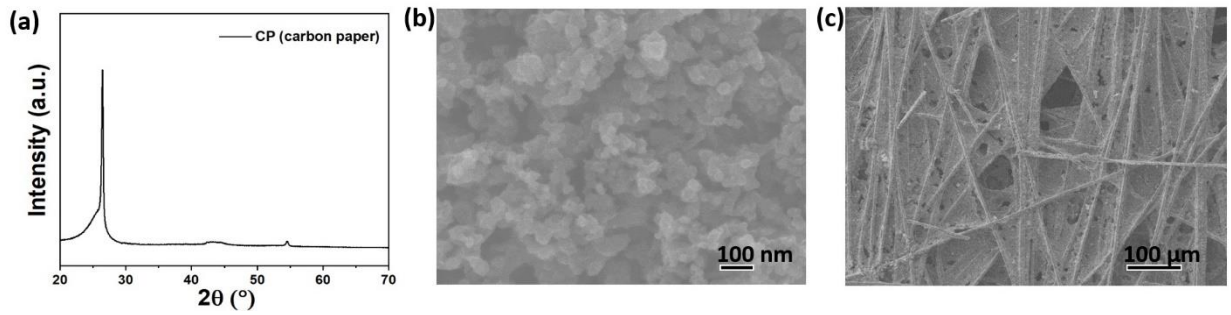

Figure 3.8 Characterization of the gas diffusion layer (GDL). (a) XRD pattern and (b, c) SEM images. The SEM image in (b) is the carbon based mesoporous layer side and the SEM image in (c) is the carbon fibre layer side.

We investigated CO_2 electroreduction using the SnS/GDL with different electrolytes: 0.5 M $KHCO_3$ and KOH with concentrations from 0.1 M to 1.0 M. As shown in the linear sweep voltammogram (LSV) curves in Figure 3.6e, the current densities increased significantly with the use of more concentrated KOH electrolyte, which is largely attributed to the drop of ohmic resistance from 52.6 Ω (0.1 M KOH) to 7.0 Ω (1 M KOH) (Figures 3.6a and 6b), meanwhile solution resistance of 0.5 M $KHCO_3$ is 33.9 Ω. Noted that an identical trend of ohmic resistance was observed at -1.5 V vs. RHE and under the open circuit voltage (see Figure 3.6c). In addition to the ohmic resistance information, potential-dependent Nyquist impedance plots offer valuable information on the charge-transfer resistance that reflecting the electrocatalytic activity. The impedance plots at a low frequency region for SnS/GDL in Figure 3.6d reveals the drop in charge transfer resistance (smaller semicircles) with the increase of applied cathodic potentials from -0.3 to -0.5 V vs. RHE, correlated well with the enhancement in electrocatalytic current. Likewise, greater driving force at more negative applied potentials (-0.5 to -1.5 V) results in lower charge-transfer resistances.

Controlled potential electrolysis (CPE) experiments were performed at fixed potentials of between - 0.3 and -1.5 V *vs.* RHE (Figure 3.9 and 3.10). The gaseous products from CPE experiments, CO and H_2, were quantified by gas chromatography (GC), whereas formate (a liquid product) was determined using nuclear magnetic resonance (NMR). The plots of total current density (j_{total}) and the partial current density of formate ($j_{formate}$) based on geometrical surface area are presented in Figure 3.6f and 3.9, showing an almost linear increment with increased cathodic potentials. The j_{total} and $j_{formate}$ were normalised by electrochemical surface area (ECSA) (Figure 3.6g-i) employing the ECSA value of 115.75 cm^2. As is consistent with Figure 3.6e, increased KOH concentration shows higher current densities. j_{total} in 1 M KOH is ~7.1 and ~1.7 times larger than that in 0.1 M and 0.5 M KOH, whereas $j_{formate}$ in 1 M KOH is ~9.7 and ~2.0 times of that in 0.1 M and 0.5 M KOH at -1.5 V. In 0.5 M $KHCO_3$, the j_{total} and $j_{formate}$ are relatively low, almost at the same level of those in 0.1 M KOH.

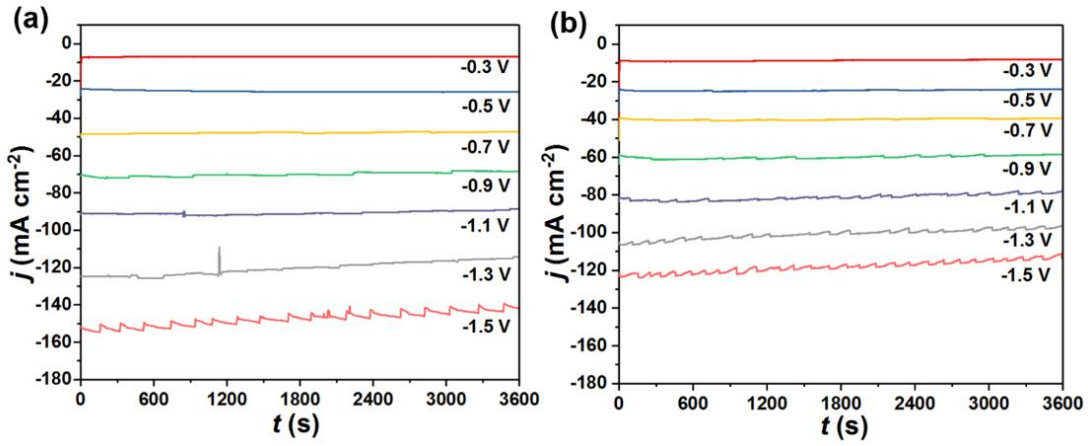

Figure 3. 9 Amperometric i-t curves of (a) SnS and (b) SnO_x at applied potentials from -0.3 to -1.5 V vs. RHE.

CPE Data in Figures 3.10 and 3.11 shows that 1 M KOH electrolyte corresponds to highest CO_2 to formate conversion Faradaic efficiency ($FE_{formate}$) across the applied potentials in comparison to other electrolytes. In this electrolyte, even at the potential of -0.3 V *vs.* RHE, which is considered as a relatively positive potential for Sn-based electrocatalysts, a $FE_{formate}$ of 54.1 ± 6% can be reached. The maximum $FE_{formate}$ of 88 ± 2% was obtained at -1.3 V *vs.* RHE. Maximum $FE_{formate}$ was also observed at this potential for other KOH electrolytes: 0.5 M KOH (75.7 ± 2%) and 0.1 M KOH (64.5 ± 2%). In addition to the maximum $FE_{formate}$ as commonly reported as a figure of merits for CO_2 reduction benchmark efficiencies, an interesting feature observed from this study is a wide potential range was achieved with efficiency over 70 % from -0.5 to -1.5 V *vs.* RHE. This performance to our best knowledge has not been reported before for any SnS-based catalysts for CO_2 electroreduction to formate.

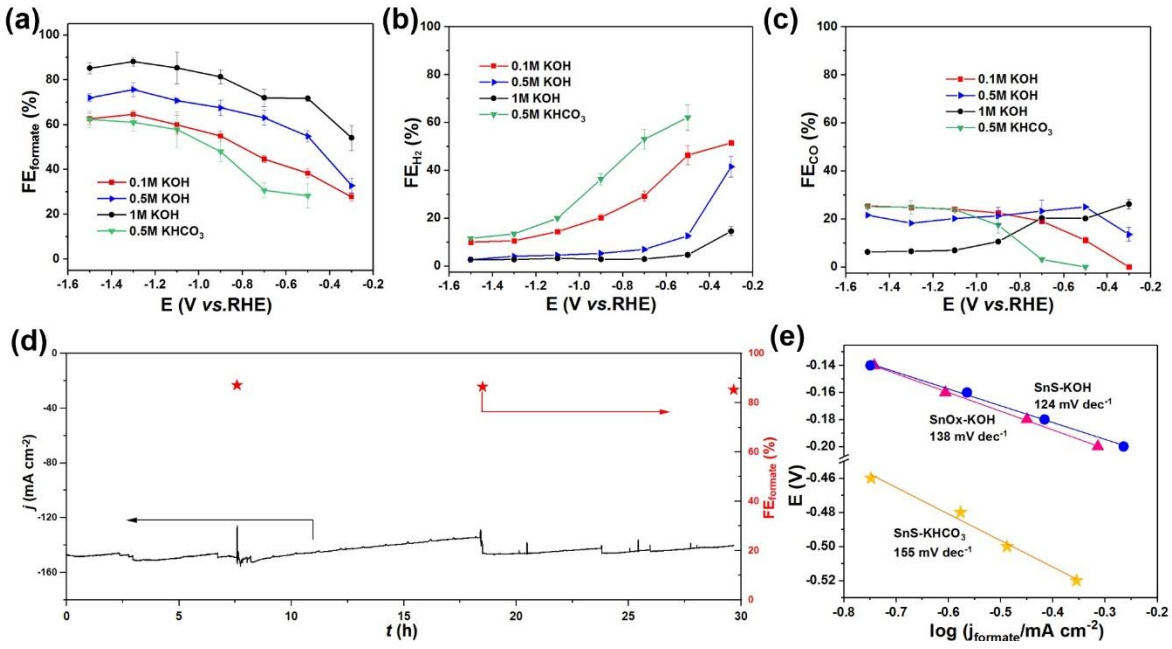

Figure 3.10 Electrochemical performance. (a, b, c) Faradic efficiencies toward formate, H_2 and CO obtained in 0.5 M $KHCO_3$, 0.1 M KOH, 0.5 M KOH, 1 M KOH. The error bars represent the

standard deviations of three independent measurement of the sample. (d) Stability test of SnS/GDL at -1.5 V vs. RHE. The experiments were conducted in the catholyte of 1.5 L of 1 M KOH. (e) Tafel plots of SnS and SnOx catalysts in 1 M KOH electrolyte and SnS in 0.5 M $KHCO_3$ electrolyte.

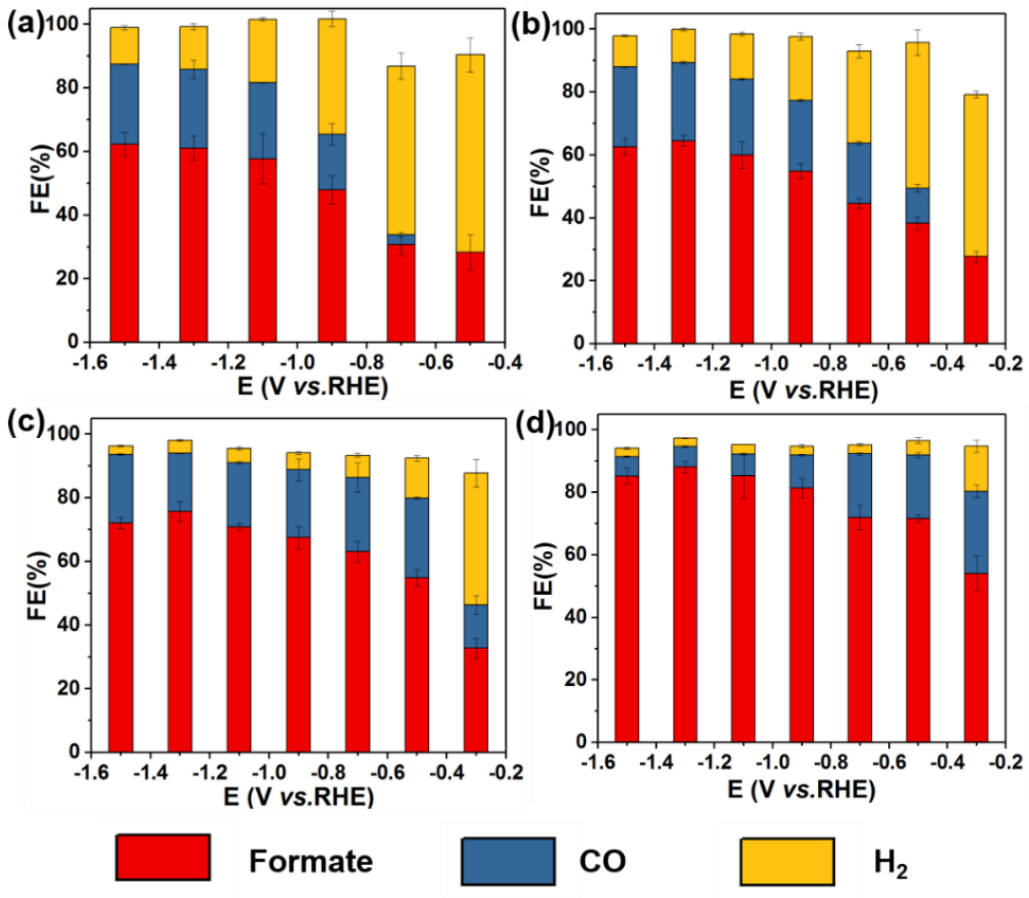

Figure 3.11 Performance of SnS/GDL in different electrolytes. Total Faradic efficiency obtained in 0.5 M $KHCO_3$ (a), 0.1 M KOH (b), 0.5 M KOH (c), 1 M KOH (d). The error bars represent the standard deviations of three independent measurements of the samples.

To shed some light on factors contributing to the Faradaic conversion efficiencies, H_2 and CO are plotted in Figures 3.10b and 3.10c, respectively. FE_{H2} was found to be dominant at the less negative potentials, -0.3 V to -0.9 V, especially in 0.5 M $KHCO_3$. The use of KOH, with increased

concentrations from 0.1 M to 1.0 M, drastically suppresses the H_2 production, eg. FE_{H2} dropping from 46.3 ± 4% (in 0.1 M KOH) to 4.6 ± 1% (in 1.0 M KOH) FE_{H2} at -0.5 V *vs.* RHE. To further understand the suppression of hydrogen evolution of SnS during CO_2 reduction, a control experiment was performed to compare the partial current density of H_2, j_{H2}, under the flow of CO_2 and Ar gases in 1 M KOH electrolyte (Figure 3.12). In Ar atmosphere, hydrogen gas (eg. j_{H2} = ~ 90 mA cm^{-2} at -1.5 V vs. RHE) with unity Faradaic efficiency was detected. In CO_2 atmosphere, both CO_2 reduction and hydrogen evolution occur with j_{H2} significantly suppressed across a wide potential range (eg. j_{H2} < ~ 4 mA cm^{-2} from -0.3 to -1.5 V vs. RHE). This result highlights the significant of CO_2 as a reactant competing with protons in the electrolyte. Although both the formation of formate and hydrogen need protons, the formate production is a preferable pathway under CO_2 atmosphere. Across all the electrolytes, the CO by-product contributes less than 30 % Faradaic conversion efficiency. At more negative potentials from -0.9 V to -1.5 V, it is found CO was suppressed to ~7 % in 1.0 M KOH. Hence, we proposed that the suppressions of both H_2 and CO by-products have contributed to an overall wider operational potential range. The Tafel slopes for SnS in both 1 M KOH and 0.5 M $KHCO_3$ (see Figure 3.10e) are close to the theoretical value of 118 mV dev^{-1}, indicating the one electron transfer forming CO_2^- intermediates is the rate determining step (RDS).[69] Comparatively, SnS in KOH (124 mV dev^{-1}) has improved kinetics as it exhibits a lower Tafel slope than that in $KHCO_3$ (155 mV dev^{-1}).

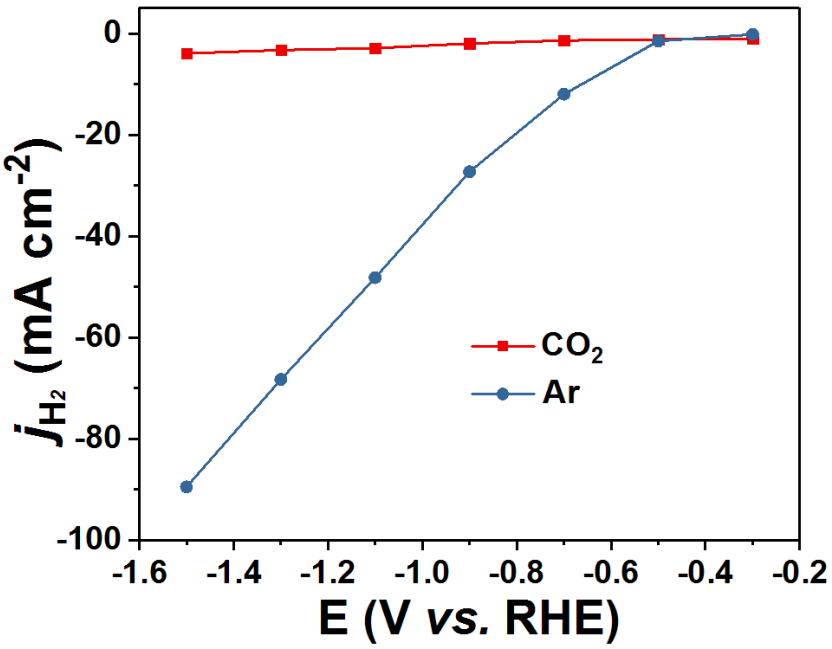

Figure 3.12 Partial current density of H_2, j_{H2}, with purging of CO_2 and Ar gas in 1 M KOH electrolyte.

It should be noted that we also performed CO_2RR in 2 M KOH, however, SnS nanosheets were unstable as they gradually dissolved over time in this highly concentrated alkaline, evidently from the dropped in current from CPE study (Figure 3.13). Noted also control experiment performed on the employed bare GDL, did not exhibit CO_2 reduction products such as CO and formate, except H_2, as a result of proton reduction reaction. The stability test of SnS/GDL was conducted in 1.5 L of 1 M KOH catholyte for 30 h (Figure 3.10d). Noted that this large volume of electrolyte reservoir was employed as it was found the electrolyte volume can affect the current density as the carbonate or bicarbonate formed during the CO_2 gas purging can reduce the current density and a large volume of KOH electrolyte could help to mitigate this effect (see discussion in Figure 3.16). After a 30 h test, the current density remained at 140.3 mA cm^{-2}, only dropped 4%.

The $FE_{formate}$ decreased from 87% to 85%, indicating the excellent stability of CO_2 reduction to formate. To evaluate catalyst stability during electrolysis, we performed structural and composition characterization of samples after 1 h and 30 h CO_2 electroreduction, respectively. The XRD, SEM and XPS results are shown in Figure 3.14. After 1 h electrolysis, the nanosheets structure remained and the SnS was a dominant phase. However, after 30 h electrolysis, the surface morphology indicated aggregation of nanosheets with metallic Sn becoming the dominant phase. Such phase transition during electrolysis whereby some SnS is reduced to metallic Sn is consistent with the literature reports. [71, 85] As the current density and formate selectivity remained relatively stable, suggesting that catalyst active sites are not significantly affected by the alteration in the surface morphology and phase transition within the performed experimental time-scale.

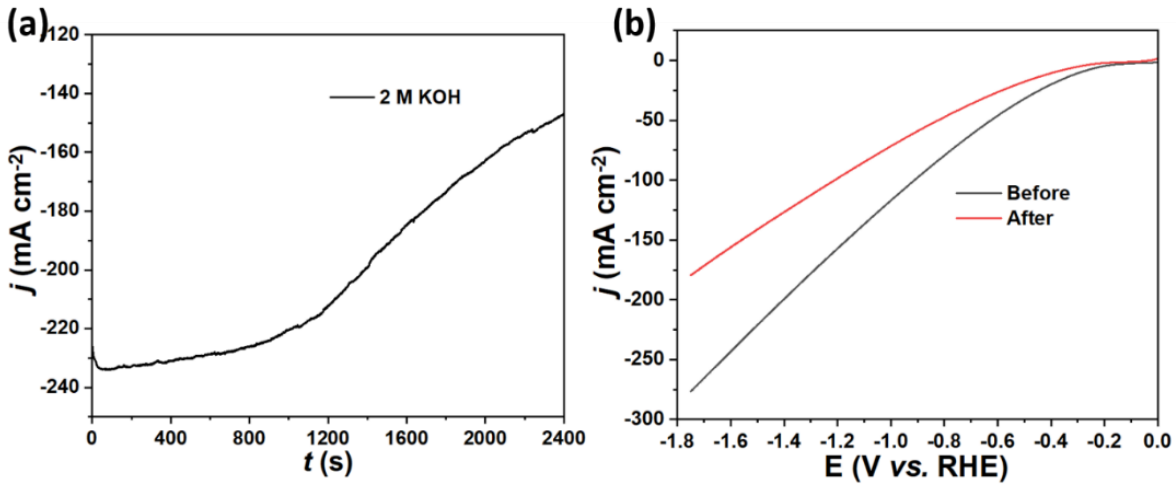

Figure 3.13 Performance of SnS/GDL in 2 M KOH. (a) j-t curve of CO_2 electroreduction on a SnS/GDL at -1.5 V vs. RHE, (b) LSV curves of SnS/GDL before and after 2400 s test at -1.5 V vs. RHE.

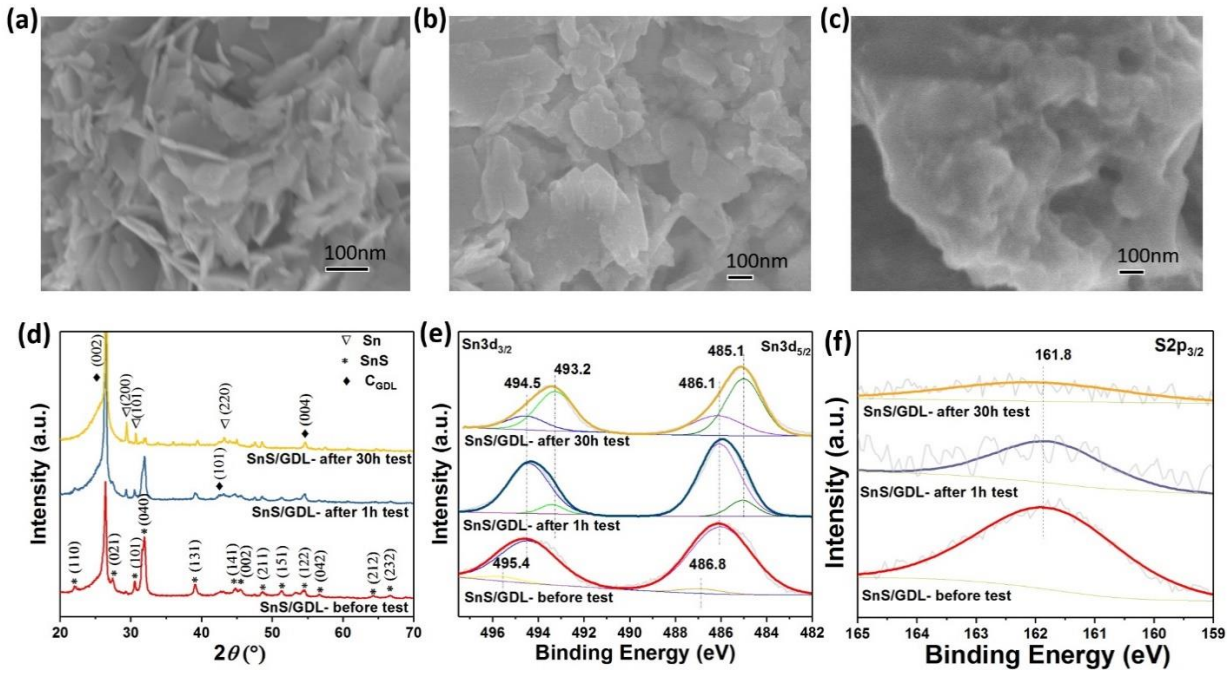

Figure 3.14 Characterization of SnS/GDL before and after performance test. SEM images of (a) SnS/GDL before performance test, (b) SnS/GDL after 1 h performance test, (c) SnS/GDL after 30 h performance test, (d) XRD patterns of SnS/GDL before and after performance test, (e, f) XPS spectra of Sn and S elements of SnS/GDL before and after performance test.

A detailed performance comparison between this work and other published Sn-based electrocatalysts for CO_2 reduction to formate is presented in Figure 3.15and Table 3. 1.[71, 77, 79, 81-82, 134, 137, 236-238, 252-255]. The potential window across - 0.5 V to - 1.5 V with $FE_{formate}$ over 70 % obtained from this work is clearly broader than literature studies that typically display ‘‘volcano shape’’ characteristic. Li et al.[81] reported SnS_2 nanosheets that having a potential window of -0.4 V to -0.8 V, but having a low current density (< 20 mA cm^{-2}). In contrast, although ultra-small SnO_2 reported by Liang et al.[79] has a high current density of 147 mA cm^{-2} at -0.95 V *vs.* RHE, the $FE_{formate}$ - E curve shows a narrow operating potential window. Other tailored catalysts such as Sn quantum sheets/Graphene,[236] SnO_2 nanosheets on carbon cloth,[82] SnS_2 monolayer,[71] and

electrodeposited Sn[77] have either low current density or narrow operating potential window. It is important to note that all studies in literatures are based on the H-cell configuration, except ultra-small SnO_2[79] and electrodeposited Sn.[77] This work outperforms in achieving both high current density and high Faradaic efficiency for formate over a broad potential window. The three-phase boundary, namely gaseous CO_2, liquid KOH, and solid phase of SnS catalysts in this flow-cell configuration promoting high current density, as well as allowing alkalinity impact to take place in suppressing competitive H_2 and CO evolutions.

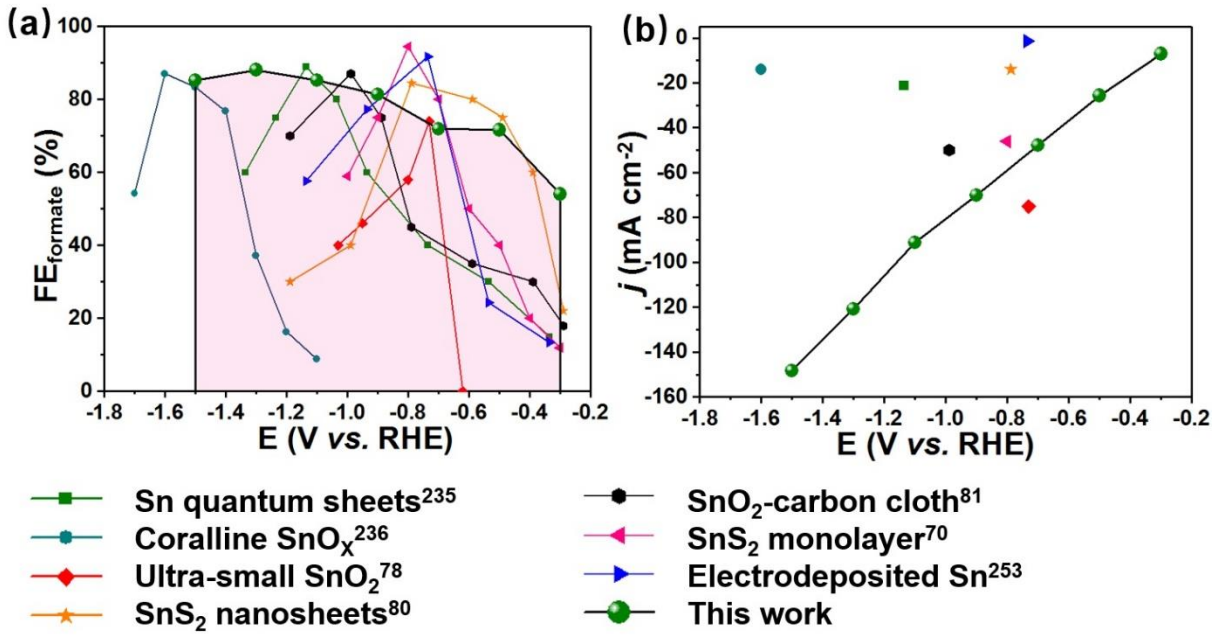

Figure 3.15 Summary of comparison between the reported Sn-based catalyst and the current work for electrochemical CO_2 reduction. (a) $FE_{formate}$ as a function of applied cathodic potentials, and (b) The obtained current densities at the maximum $FE_{formate}$ as a function of applied cathodic potentials. The potentials were converted to RHE scale based on the equations: E (vs. RHE) = E (vs. Ag/AgCl) + 0.0591 * pH + 0.21 and E (vs. RHE) = E (vs. SCE) + 0.0591 * pH + 0.24. It was

assumed that the pH values of CO_2 - saturated 0.1 M and 0.5 M $NaHCO_3$ /$KHCO_3$ aqueous solution were 6.8 and 7.2, respectively.

Table 3. 1 Performance of Sn-based electrocatalysts for CO_2 reduction to formate.

Electrocatalyst	Electrolyte	Setup	Products	Formate FEmax	j at the potential of FE_{max}	Ref
Sn quantum sheets	0.1 M $NaHCO_3$	H-cell	$HCOO^-$	89% (-1.134V vs. RHE)	21.1 mA cm^{-2}	[236]
Sn-CF1000	0.1 M $KHCO_3$	H-cell	$HCOO^-$ & CO	65% (-0.8V vs. RHE)	11 $mAcm^{-2}$	[137]
SnOx	0.5 M $KHCO_3$	H-cell	$HCOO^-$	87.1% (-1.6V vs SHE)	14.0 $mAcm^{-2}$	[237]
SnO_2 Wire in Tube	0.1 M $KHCO_3$	H-cell	$HCOO^-$ & CO	~70%(-1.29V vs RHE)	12 mA cm^{-2}	[252]
SnO_2 Porous Nanowires	0.1 M KH CO_3	H-cell	$HCOO^-$ & CO	78% (−1.0 V vs. RHE)	10 mA cm^{-2}	[134]
Ultra-small SnO_2	1 M KOH	Flow-cell	$HCOO^-$, C_2H_4, C_2H_5OH, CH_3COOH, n-C_3H_7OH	74% (−0.73 V vs. RHE)	~75 mA cm^{-2}	[79]
Ultra Small SnO Nanoparticles	0.5 M $KHCO_3$	H-cell	$HCOO^-$ & CO	68% (−0.73 V vs. RHE)	20 mA cm^{-2}	[238]
Sn-GDE	0.5 M $NaHCO_3$	Flow-cell	$HCOO^-$ & CO	71% (−1.1V vs. RHE)	8.58 mA cm^{-2}	[77]
SnS_2/rGO	0.5 M $NaHCO_3$	H-cell	$HCOO^-$ & CO	84.5 (-0.788V vs. RHE)	~13.9 m A cm^{-2}	[81]

Nano SnO_2	0.1 M $NaHCO_3$	H-cell	$HCOO^-$ & CO	86.2% (−1.134V vs. RHE)	5.4 mA cm^{-2}	[253]
SnO_2 nanosheets on carbon cloth	0.5 M $KHCO_3$	H-cell	$HCOO^-$ & CO	87±2 % (-0.988V vs. RHE)	~50 mA cm^{-2}	[82]
SnS_2 monolayer	0.1 M $KHCO_3$	H-cell	$HCOO^-$ & CO	94 ± 5% (-0.8V vs. RHE)	~46 mA cm^{-2}	[71]
Electrodeposited Sn	0.1 M $KHCO_3$	H-cell	0.1 M KHCO3	91.7% (−0.734V vs. RHE)	0.9–1.4 mA c m^{-2}	[254]
SnS/GDL	1 M KOH	Flow-cell	$HCOO^-$ & CO	88.10±1.87 % (-1.3V vs. RHE)	120.63 mA cm^{-2}	This work

Note: The potentials were converted to RHE scale based on the equations: E (vs. RHE) = E (vs. Ag/AgCl) + 0.0591 * pH + 0.21 and E (vs. RHE) = E (vs. SCE) + 0.0591 * pH + 0.24. It was assumed that the pH values of CO_2-saturated 0.1 M or 0.5 M $NaHCO_3$ or $KHCO_3$ aqueous solution is 6.8 and 7.2, respectively.

3.4.3 Understanding the impact of catholyte volume toward current stability

To understand the impact of volume of KOH electrolyte reservoir on current stability, CO_2RR performance was studied by replacing fresh batches of 1 M KOH catholyte with increasing volumes from 10 mL to 100 mL after consecutive 1 h study on the same SnS/GDL sample. In a small 10 mL KOH reservoir, the current density was found to decrease by 29% from 150 to 106 mA cm^{-2}. In contrast, a high current stability was achieved with only 4% drop from an initial current when 100 mL KOH was employed. From Figure 3.16a, it is important to note that the current density recovered to initial current of ~ 150 mA cm^{-2} when a fresh catholyte was introduced,

suggesting the current deactivation is a reversible process. Another important observation is despite the dropped in current densities, the impact on Faradaic conversion efficiencies of CO_2 reduction products is negligible (Figure 3.16c).

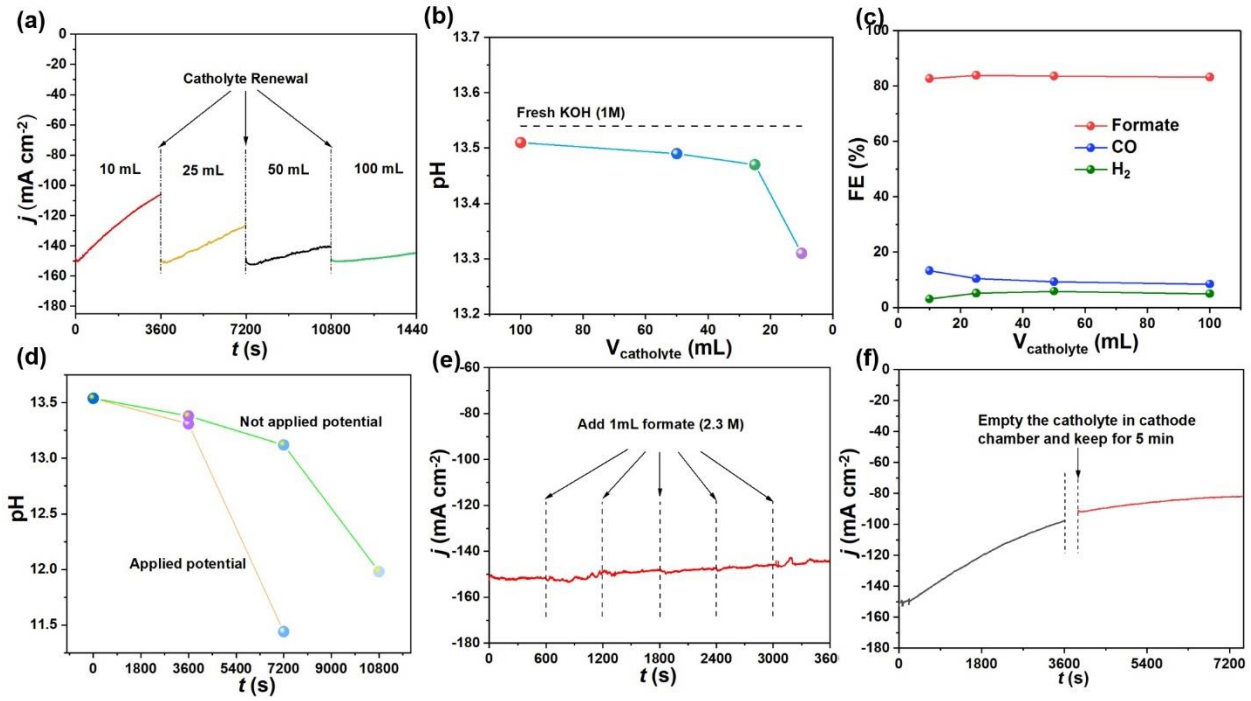

Figure 3.16 Electrolyte volume, products and pH effects on performance. (a) j-t curves of SnS/GDL sample with different catholyte volumes. The experiments were conducted at the potential of -1.5 V vs. RHE. (b) The pH values of the catholyte after one hour test in a. (c) Faradic efficiencies toward formate, CO, and H_2 productions from CO_2 electroreduction performed on SnS/GDL samples with different catholyte volumes. (d) The plot of pH change in catholyte chamber (10 mL KOH) as a function of time with continues CO_2 gas purging with (-1.5 V vs. RHE) or without applied potential. (e) Formate effect on the current density. The j-t curve with consecutively adding 1 mL of 2.3 M formate into the catholyte every 10 min. The experiment was conducted on a SnS/GDL working electrode in 50 mL of catholyte (1 M KOH) at the potential of -1.5 V vs. RHE. (f) CO effect on the current density. The experiment was conducted on a SnS/GDL working electrode in 10 mL of catholyte (1 M KOH) at -1.5 V vs. RHE.

We further investigated the sources that causes the drop in current density. Since formate is the main product, it may be adsorbed on SnS and make the catalyst deactivated. To examine this possibility, we intentionally added 1 mL of 2.3 M formate in 50 mL catholyte every 10 min (Figure 3.16e). Each addition of 1 mL formate solution provides equivalent amount of formate generated over 1 h electrocatalysis in 1M KOH at -1.5 V *vs.* RHE. However, there is a negligible change in the current density, indicating formate does not affect the current density. The second possibility might be the gaseous product, CO, adsorbed on the electrode surface, as reported in other catalyst such as Pd.[256] We employed the method reported by Kanan and co-workers to investigate potential CO effect. [66] The 1 M KOH in cathodic chamber was emptied after 1 h electrocatalysis, and kept for 5 min to ensure any adsorbed CO on SnS electrocatalyst was readily purged and removed by the continuous flow of CO_2. In the subsequent 1 h electrocatalysis using the same electrolyte, the current density was not recovered but continuously dropped (Figure 3.16f). We ruled out CO as the cause of deactivation since the gas-phase CO would have been purged and removed, and current density would have returned to the initial value if CO causes the deactivation.

We then investigated the final possible reason, the formation of carbonate or bicarbonate, which leads to pH change during the CO_2 electrolysis. The continuously CO_2 was purging at 20 mL min^{-1} through the backside of GDE to the SnS catalyst for electroreduction process. Some CO_2 will concurrently react with the strongly alkaline 1.0 M KOH to form carbonate or bicarbonate.[79, 140, 257] The carbonate species formation process consumed KOH and generated water as a by-product, which reduces OH^- concentration resulting in the pH change. This is in good agreement with the variations in pH after 1 h experiments in relation to the catholyte volumes (Figure 3.16b). The catholyte of 10 mL has the largest pH decreased from 13.55 to 13.30, which is corresponding to

the drop in OH^- concentration from 0.355 M to 0.199 M, consequently resulting in the significant drop in current density as shown in Figure 3.16a. We performed a control experiment by continuously purging CO_2 into the 1 M KOH without applied electrochemical potential (Figure 3.16d). The observed drop in pH value over the time further confirmed the reaction of CO_2 with KOH to form carbonate or bicarbonate that influencing the electrolyte property. This justified the employment of 1.5 L of 1.0 M KOH in the long term stability test of SnS/GDL, ensuring the buffered OH^- concentration (Figure 3.10d).

3.4.4 The role of sulfur in the CO_2RR of SnS

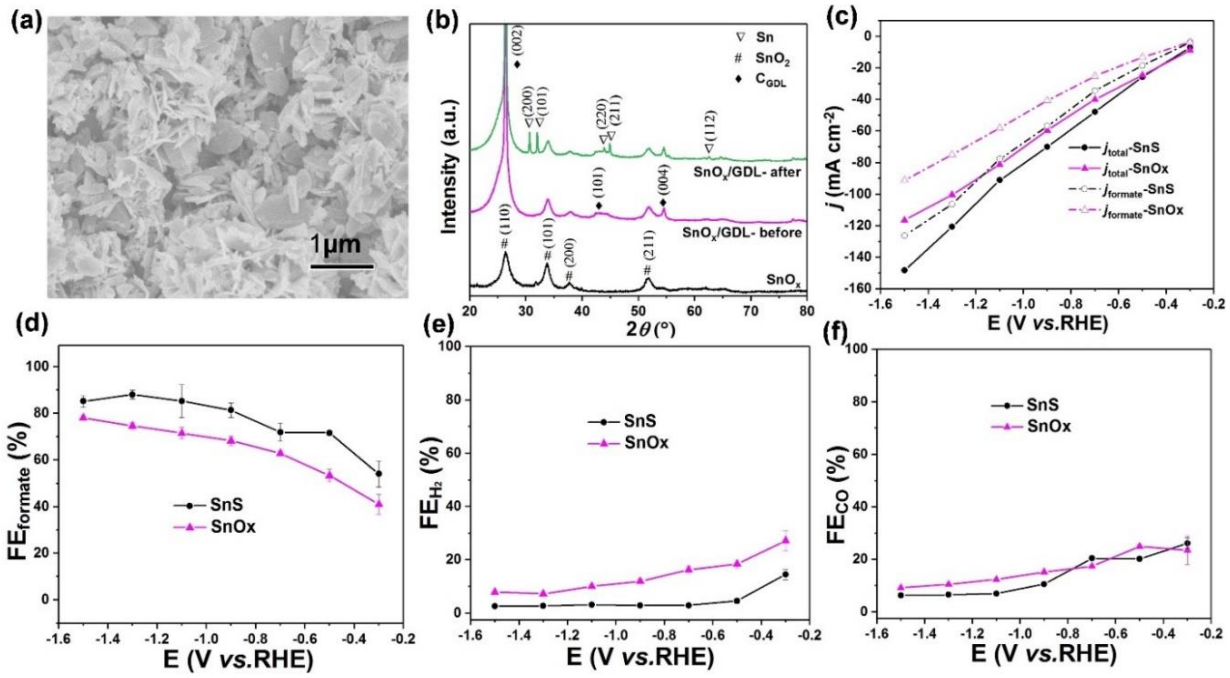

Figure 3.17 Effects of sulfur element in SnS catalyst. (a) A SEM image of SnOx/GDL. (b) XRD patterns of SnOx, SnOx/GDL-before test, and SnOx/GDL-after test. (c) Steady-state current density of SnOx/GDL and SnS/GDL samples, solid symbols represent the total current density

(j_{total}) while empty symbols represent the partial current density of formate ($j_{formate}$). (d, e, f) Faradic efficiencies toward formate, H_2 and CO on SnO*x*/GDL and SnS/GDL samples. All the performance tests were conducted in the electrolyte of 1 M KOH. The error bars represent the standard deviations of three independent measurement of the sample.

It was reported that the incorporation of sulfur on Sn either as major, or adventitious additive as a doping element could enhance the CO_2 electroreduction performance as it may help stabilise the intermediate *OCHO intermediate,[81] weaken the interaction between CO and electrode,[242] and/or increase the catalysis sites by introducing atom distortion.[85] To understand the role of sulfur in this alkaline system toward CO_2RR performance, the sulfur element in the synthesized SnS was removed by thermal treatment in an oven at 500 ^oC for 2 h in air. As shown in SEM image in Figure 3.17a and Figure 3.18a and b, the obtained tin oxide (SnO_x) retained the nanosheet morphology. XRD spectra in Figure 3.17b and 3. 18c displays characteristic peaks of SnO_2 at (110), (101), (200) and (211), consistent with tetragonal rutile phase of SnO_2 (JCPDS 21-1250). Raman modes of SnOx in Figure 3.18d further indicate the oxide phase of SnO_2. The SnO*x* was subsequently air-brushed on a GDL with the loading of 1 mg cm^{-2}. In comparison to SnS catalyst, the SnO_x exhibits lower steady state current densities (Figure 3.17c), as well as ~ 10 % smaller $FE_{formate}$ than that of SnS (Figure 3.17d). As shown in Figure 3.17e, in comparison to SnO*x*, the lower FE_{H2} in SnS suggests sulfur acts to suppress hydrogen evolution. To identify the influence of alkaline electrolyte on SnOx, the performance of SnOx in 1 M KOH and 0.5 M $KHCO_3$ electrolytes were compared in Figure 3.19. Both the selectivity and the current density can be greatly improved by alkaline electrolyte. However, SnS catalyst shows greater performance enhancement in comparison to SnO_X (see Figure 3.11).

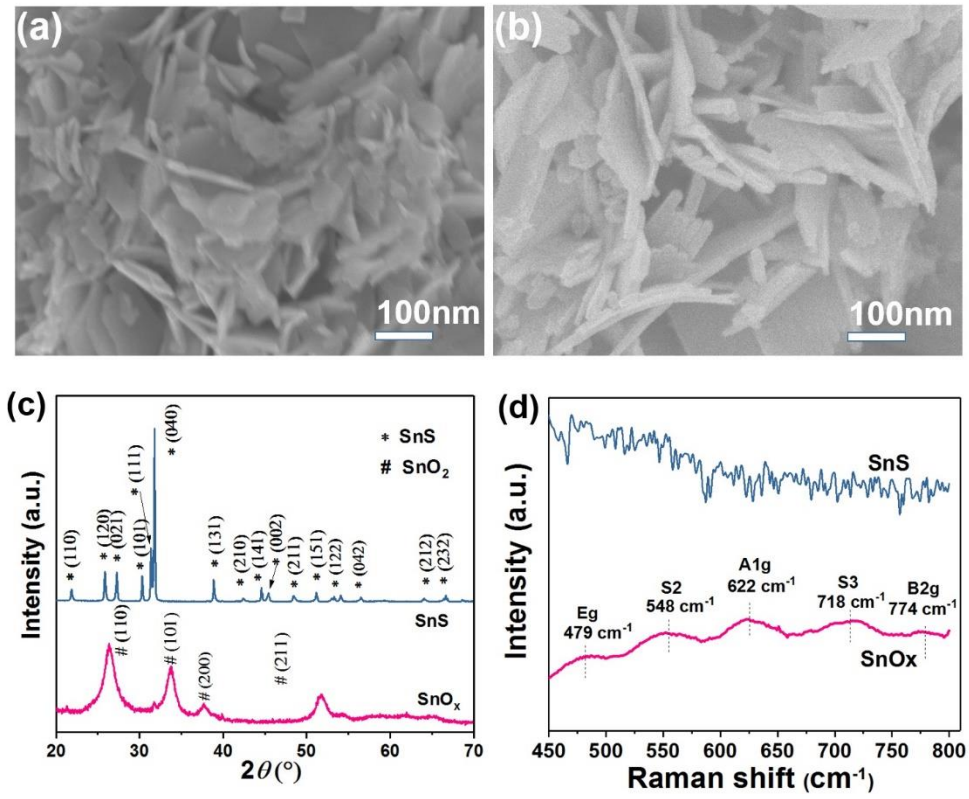

Figure 3.18 SEM images of (a) SnS and (b) SnO_x samples. (c)XRD patterns and (d) Raman spectra of SnS and SnO_x. The peaks at 497, 548, 622, 718, and 774 cm^{-1} are the Raman modes of SnO_2 [102].

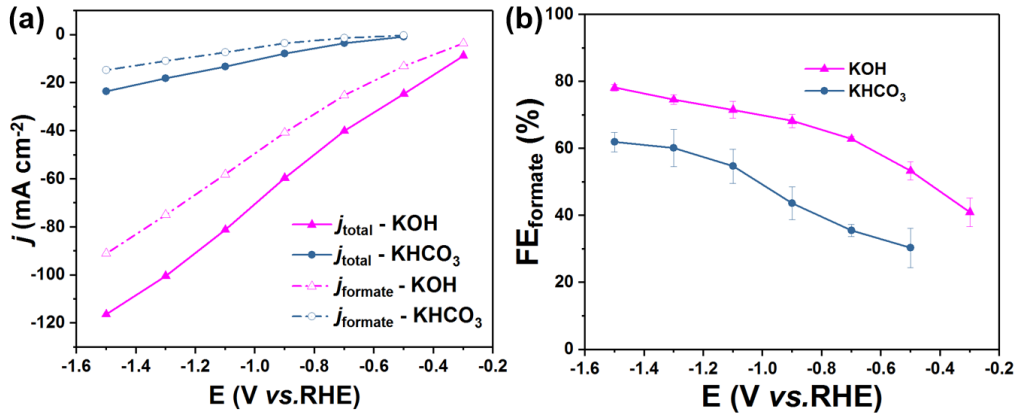

Figure 3.19 Performance comparison in KOH and $KHCO_3$. (a) Steady-state current density of SnO_x/GDL in 1 M KOH and 0.5 M $KHCO_3$, solid symbols represent the total current density (j_{total})

while empty symbols represent the partial current density of formate ($j_{formate}$). (b) formate Faradic efficiency of SnO_x/GDL in 1 M KOH and 0.5 M $KHCO_3$.

The Tafel plots of SnS and SnOx in KOH (Figure 3.10e) are 124 and 138 mV dev^{-1}, respectively. The slightly lower Tafel slope of SnS illustrates that sulfur may promote the formation of absorbed *CO_2 (the rate determining step) by offering faster kinetics, which facilitates the formate production. The suppression of hydrogen evolution can be explained by the mechanism reported by Wang et al..[105] Sulfur elements can suppress hydrogen evolution by activation of water and the formed hydrogen species preferred to react with adsorbed CO_2 to form formate intermediate instead of following the hydrogen evolution pathway. Comparatively, Sn peaks at (200), (101), (220), (211) and (112) were seen after 1 h CO_2 electroreduction for SnO_2 (Figure 3.17b), indicating oxide phase is less stable and readily reduced to metallic Sn in tetragonal phase (JCPDS 04-0673).

3.4.5 Proposed mechanism of alkaline enhancement

There are three competing reactions in SnS-based electrochemical CO_2 reduction, namely formate, H_2 and CO evolutions. The plausible pathways are summarized in Figure 3.20. Our discussion emphasizes on how alkalinity influences the dynamic of those competing reactions, which contributes positively in broadening the potential window for formate production as we observed from our experimental data. As schematically illustrated in Figure 3.20a, the rate determining step for the formate generation is the transfer of an electron to the surface adsorbed *CO_2 radical anion (step 1), follow by the protonation (step 2).[27, 255] After the reduction of the *OCHO intermediate (step 3), the formate can readily release as a product (step 4). In this study, the concentration of

protons is low (~$10^{-13.55}$ M) in 1 M KOH electrolyte and thus the protons needed in each pathway is expected to be derived from the Volmer reaction (step 9): $* + H_2O + e^- \rightarrow *H_{ads} + OH^-$, where * is the adsorption site.[142, 258]

There are two dominant competitive products, H_2 and CO, which could influence the formate conversion efficiency. From the obtained CO_2 electroreduction performance data presented in Figures 3.10b and 3.10c, the competing reactions can be divided into two regions: (1) H_2 evolution competing dominated region occurred at a less negative potential range (~ -0.3 to -0.9 V *vs.* RHE), and (2) CO evolution competing dominated region at a more negative potential range (~ -0.9 to -1.5 V *vs.* RHE). In the H_2 competing dominated region, after the Volmer reaction, the hydrogen was generated either following the Tafel (step 10)： $2 *H_{ads} \rightarrow H_2 + 2 *$ or Heyrovsky (step 11)： $*H_{ads} + H_2O + e^- \rightarrow * + H_2 + OH^-$ steps.[258] It is worth noting that although less significant H_2 competition at -0.9 V to -1.5 V, it still accounts for ~ 10 to 25 % suppression of hydrogen evolution reaction (see Figure 3.10b) in 1 M KOH in comparison to 0.5 M $KHCO_3$ which understates the critical impact of hydrogen suppression across whole potential range. In an alkaline electrolyte, multiple reaction steps, and the slower kinetics of water dissociation result in about two orders of magnitude lower hydrogen evolution activity than that in acidic or neutral medium.[142-143] Therefore, as is consistent with our experimental data in Figures 3.10a and 3.10b, increasing electrolyte alkalinity (eg. KOH of 0.1 M to 1.0 M) successfully suppresses hydrogen evolution, which favours formate production.

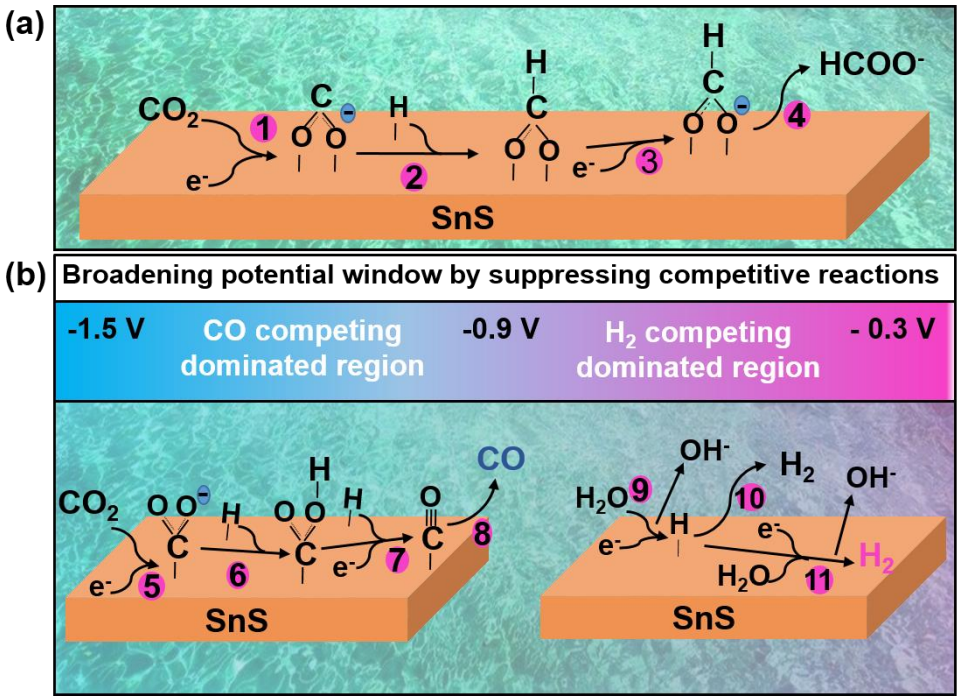

Figure 3.20 The diagrams proposed mechanistic aspects of electrochemical CO_2 reduction to (a) formate, and (b) H_2 and CO on SnS/GDL in alkaline KOH electrolyte.

In the CO competing dominated region, it is well documented that carbon atom in adsorbed $*CO_2^-$ radical anion is bonded to the catalyst surface (step 5) and protonation process occurs at the oxygen atom (step 6). The CO can be generated by further protonation on the *COOH intermediate (steps 7 and 8). The selectivity of CO_2RR is determined by the active energy barrier for the formation of *OCHO (intermediate to formate) and *COOH (intermediate to CO).[27, 50] According to Gabardo et al.,[49, 60] highly concentrated KOH can destabilize hydronium ions, which makes the reaction energy barrier for the *COOH intermediate much higher than that of *OCHO. Thus, increasing alkalinity makes formate production process more favourable. The suppression of CO and H_2 at both competing regions broadens the electrochemical potential window for formate production from CO_2.

3.5 Conclusions

We have demonstrated the unexpected significant broadening of an electrochemical potential window for CO_2 reduction to formate on a SnS catalyst at high current densities using an alkaline electrolyte in a flow-cell configuration. A wide potential window of -0.5 V to -1.5 V *vs.* RHE with $FE_{formate}$ over 70 % was achieved in 1 M KOH. The maximum $FE_{formate}$ of 88 ± 2 % was obtained at -1.3 V *vs.* RHE and the current density can reach ~ 148 mA cm^{-2} at -1.5 V. Based on the experimental data, it is evidenced that the suppression of H_2 competing reaction in KOH medium occurred across the whole potential range, though more predominant at the less negative potentials. This is in addition to CO suppression at a more negative potential resulting in a widening of overall potential windows for formate production. A control experiment study indicated sulfur in SnS acts to suppress H_2 generation as in comparison to SnO_x. To ensure the long-term current stability of the electrolysis reaction in KOH solution, we demonstrated the importance of buffering hydroxide concentration, which otherwise diminishes due to chemical reactions between KOH and CO_2 to form carbonate or bicarbonate species. This study offers insights into the essence of integrating a suitable catalyst, cell design, and electrolyte toward achieved desirable CO_2 electroreduction performance with features such as high formate conversion efficiencies at high current densities over a wide potential window. The outstanding performance obtained in this work may be extendable to other catalysts for formate conversion, which brings it closer to translational research of industrial relevant high yield formate production from CO_2.

3.6 Acknowledgements

J. Z. thanks the University of Wollongong for the postgraduate scholarship. Funding from the Australian Research Council Centre of Excellence Scheme (CE 140100012) is gratefully acknowledged. We thank Gemeng Liang and Patricia Hayes for their assistance in the XRD and Raman Spectroscopy experiments respectively. The authors would also like to thank Australian National Fabrication Facility-Materials Node (ANFF) and UOW Electron Microscopy Centre for equipment use.

Chapter 4 Facile electrochemical synthesis of ultrathin iron oxyhydroxide nanosheets for oxygen evolution reaction

This chapter has been adapted, with the publisher's permission, from the article entiled 'Facile electrochemical synthesis of ultrathin iron oxyhydroxide nanosheets for oxygen evolution reaction' published in Chemical Communications.

Citation: Zou et al., Chemical Communication, 55, 8808-8881.

DOI: https://doi.org/10.1039/C9CC02941A

Jinshuo Zou,[a] Germanas Peleckis,[b] Chong-Yong Lee[*a] and Gordon G. Wallace[a]

[a] ARC Centre of Excellence for Electromaterials Science, Intelligent Polymer Research Institute, AIIM, Innovation Campus, University of Wollongong, Wollongong, NSW 2500, Australia

[b] Institute for Superconducting and Electronic Materials, AIIM, Innovation Campus, University of Wollongong, Wollongong, NSW 2500, Australia

[*] Corresponding author

Author statement:

The study in this chapter was conceptual, experimentally designed and written by Jinshuo Zou. All experiments including material preparations, characterizations, electrochemical studies and the data analysis presented in this chapter were performed by Jinshuo Zou. Dr. Chong-Yong Lee and Prof. Gordon G. Wallace supervised the study, and assisted in the conception, experimental design

and revisions of manuscript. Dr. Germanas Peleckis assisted in obtained XRD data, and revised the manuscript.

4.1 Abstract

We propose a facile approach to synthesis of ultrathin iron oxyhydroxide nanosheets for use in catalysing the electrochemical oxygen evolution reaction. This two dimensional material lowering the overpotential, and provides a platform for further performance enhancement via integration of species such as nickel onto the ultrathin nanosheet structure.

4.2 Introduction

The oxygen evolution reaction (OER) is a kinetically sluggish and thermodynamically uphill anodic half-reaction, involving a four proton coupled electron transfer process to form an O-O bond.[259-260] In water based electrolysers, improving efficiency of this process is of utmost importance as it can severely constrain H_2 production at the cathode, contributing to increased operating costs.[261-262] Metallic catalysts such as Ir,[263] Ru,[264] Ni,[265] Co,[266] and Fe,[267] including metal oxides,[268] sulfides,[269] hydroxides,[270] phosphides,[271] chalcogenides,[272] have been widely used to catalyse the OER. The low-cost and earth-abundant Fe and its derivatives are attractive electrode materials for OER due to their excellent stability and low water oxidation overpotential.[273-274]

The production of electrocatalysts as ultrathin nanosheet structures has the potential to promote OER activity. Two-dimensional (2D) materials resulting in an enhanced surface area and abundance of active sites, facilitate mass transport of reactants and products during

electrocatalysis.[275-278] The hierarchical 2D materials also offer favourable structure for incorporation of a secondary metal such as Co and/or Ni to provide synergetic effect in promoting electrocatalytic performance.[279-280] In search of low cost and abundant electrocatalysts, iron based nanosheet structure could provide beneficial features for water oxidation electrocatalysis.[281] In recent years, the preparation of 2D iron based nanosheets has attracted significant interest. Wan and coworkers introduced ethylene glycol-mediated process to allow self-assembly of flower-like iron oxide nanosheet structures.[282] Jin et al. used metal ion-intervened hydrothermal and annealing methods to prepare ultrathin iron oxide nanosheets, though the synthesis procedure is laborious.[283] Another approach involves simple thermal annealing in air or mixed gas to grow iron oxide nanosheets.[284-286] However, this method is highly sensitive to the pre-conditioning of iron foils and annealing conditions, affecting homogeneous growth of nanosheets. Therefore, an approach allowing a greater control of formation of ultrathin iron-based nanosheets with desirable electrocatalytic properties for OER is highly desirable. Electrochemical potentiostatic method is one of such strategy allowing formation of oxyhydroxide films of metals such as Fe, Ni and Co in aqueous alkaline solution.[287-290] In particularly, strategy in promoting and controlling the formation of ultrathin iron oxyhydroxide nanosheets that would be beneficial for OER activity is of interest.

Herein, we report a facile and highly reproducible method to prepare ultrathin iron oxyhydroxide nanosheets via cyclic voltammetry (CV) potential modulations on thermally pretreated iron foils. The size and the thickness of the iron oxyhydroxide nanosheets can be tuned by controlling the number of CV cycles, range of potentials, duration, and variation of electrolytes used. Ultrathin iron oxyhydroxide nanosheets with thicknesses of ~ 10 nm exhibited a current

density of 10 mA cm^{-2} at an overpotential of 0.428 V and a low Tafel plot slope of 44 mV dec^{-1}. The large surface area of such ultrathin iron oxyhydroxide nanosheets also offered opportunities for tuning electrocatalytic performance by incorporation of other suitable catalyst, such as Ni. By further loading Ni species onto the ultrathin iron oxyhydroxide nanosheets, the current density was increased to 42 mA cm^{-2} at the same overpotential, indicating that iron oxyhydroxide nanosheets can act as an excellent 2D support for achieving synergies effect of bimetallic catalysis.

4.3 Experimental Section/Methods

4.3.1 Electrode preparation

Iron foil (thickness: 0.25 mm, 99.5%, Advent Research Materials), potassium hydroxide (90%, Sigma Aldrich), Nickel (II) sulfate hexahydrate (98%, Sigma Aldrich), ethanol (ChemSupply), acetone (ChemSupply). All materials and chemicals were used as received without further purifications. Mili-Q system deionized water was used to prepare all solutions.

Iron foil pre-treatment: Iron foils were cut into 1 × 1 cm^2 sheets with a neck of 0.5 × 1 cm^2, cleaned and ultrasonicated in acetone, ethanol, and distilled water, before being dried by purging under N_2 stream. Cleaned iron foil sheets were then annealed in air for 1 h at 400 ^oC and naturally cooled down, before further use (Fe-400).

Synthesis of Fe-400-nC: Electrochemical synthesis of iron oxyhydroxide nanosheets was performed on the annealed iron foil (Fe-400) as a working electrode, a platinum mesh as a counter electrode, and a double-frit Ag/AgCl (3 M NaCl) as a reference electrode, using a CH Instrument 650 potentiostat. Designated cyclic voltammetric (CV) cycles were applied to the annealed iron

foils in 1 M KOH, unless otherwise stated. CVs were performed at 50 mV s^{-1} over a potential window of 0 to -1.5 V vs. Ag/AgCl except for a study of potential effect from 0 to -1.0 V. Samples obtained using this procedure are denoted as follows: Fe-400-nC, where "400" corresponds to the heat treatment temperature in degrees Celcius and ''n'' corresponds to the number of CV cycles.

Synthesis of Fe-nC: Multiple CV method as described for Fe-400-nC samples, except the working electrode was a cleaned iron foil without thermal annealing.

Ni deposition: Ni was deposited onto the Fe-400-nC by electrodeposition in a solution of 0.01 M $NiSO_4$ and 0.2 M sodium citrate at -1.0 V vs. Ag/AgCl (3M NaCl) for either 1, 5, or 10 min.

4.3.2 Characterization

A field-emission Scanning Electron Microscope (JEOL JSM-7500FA) was used to examine the surface morphology of the samples. X-ray diffraction (XRD) analysis was performed on PANalytical Empyrean XRD apparatus at a scan rate of 2^o min^{-1}. X-ray photoelectron spectra (XPS) were collected by illuminating the samples with a non-monochromatic X-ray source (Omnivac) using Al K_α (1486.6 eV) radiation and photoemission collected by an SES2002 analyser (Scienta). The working pressure in the analysis chamber during XPS measurements was typically ~4.5 x 10^{-9} mBar, with a base pressure of 9 x 10^{-10} mBar. XPS spectra were calibrated by referencing the primary C1s peak to 284.5 eV in accordance to the literature data.

4.3.3 Electrochemically active surface area (ECSA) study

The ECSA study of iron materials were estimated based on the electrochemical double-layer capacitance (C_{dl}) examined by using CV method as the C_{dl} is proportional to the ECSA. The CV curves were taken in the non-faradaic current potential region (0 to 0.1 V vs. Ag/AgCl). The C_{dl} was measured by plotting the $\Delta j/2$ and scan rate, where $\Delta j = j_a - j_c$. j_a and j_c are the anodic and cathodic current densities at 0.05 V vs. Ag/AgCl. ECSA was calculated by the equation:

$$\text{ECSA} = \underline{C}_{dl} / C_{s,}$$

where C_s value was 0.040 mF cm^{-2}, assuming that the electrode in KOH was atomically smooth.

4.3.4 Performance test and kinetic study

The performance tests were carried out using the same setup as described in the electrochemical synthesis part, employing 1.0 M KOH. The measured potentials vs. Ag/AgCl were converted to the reversible hydrogen electrode (RHE) scale according to the following Nernst equation: $E_{RHE} = E_{Ag/AgCl} + 0.0591 \times pH + 0.1976$ V. The linear sweep voltammetry (LSV) measurements and kinetic studies were conducted at a 5 mV s^{-1}. Tafel plot was obtained in 1.0 M KOH electrolyte at 5 mV s^{-1}. Tafel equation, $\eta = a + b \log (j)$, in which "a" is the Tafel constant, "b" is the Tafel slope, and "j" is the current density, was employed to obtain linear fit and relevant Tafel slopes.

4.3.5 Thickness statistics for the nanosheets

The statistic value of nanosheet lateral sizes and thicknesses were obtained by the edges of the nanosheets marked in the SEM images. Some of the edges might be broadened because of the

charging effect. Therefore, only sharp edges visible in the SEM images were included in the evaluation.

4.4 Results and discussion

4.4.1 Growth of ultrathin iron oxyhydroxide nanosheets

Ultrathin iron oxyhydroxide nanosheets were grown on an iron foil substrate (99.5 % purity) utilizing a two-step process (Figure 4.1a). Firstly, the annealing of a pre-cleaned iron foil to form a thin mixed iron oxide layer (Fe-400) on the iron substrate at 400 ^{o}C, that follow by the growth of iron oxyhydroxide nanosheets by CV in 1.0 M KOH solution. Here we denote our samples as Fe-400-nC, where "400" refers to heat treatment temperature in degrees Celcius, while "nC" refers to the number of CV cycles.

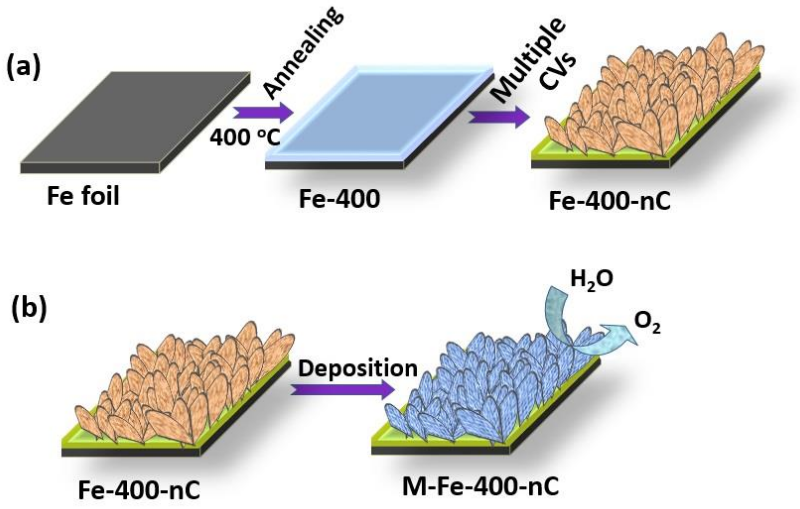

Figure 4.1 Schematic diagrams of iron oxyhydroxide nanosheet based materials. A two-step approach to grow Fe-400-nC with heat treatment followed by multiple CVs to grow nanosheets

(a); second metal deposition process, M means the metallic species deposition process on the nanosheets (b).

The surface morphologies of the ultrathin iron oxyhydroxide nanosheet samples, prepared under various conditions, were analysed using Scanning Electron Microscopy (SEM). A flat and smooth surface was observed for the pre-cleaned iron foil sample (Figure 4.2a). Upon thermal annealing of a bare iron foil at 400 ^{o}C in air for 1h, a layer of iron oxide with a thickness of ~ 200 nm was formed (Figure 4.2b). Figure 4.3b shows the successive 9 CVs on the pre-treated annealed iron foil in 1 M KOH electrolyte. In alkaline solution, iron with oxidation states of 2^{+} and 3^{+} were reduced when exposed to sufficiently negative reductive potentials.[287, 289] As can be seen in Figure 4.3b and Figure 4.2c and 2d, at reduction potentials more negative than - 1.2 V, the characteristic peak corresponding to the nucleation and growth of amorphous Fe occurred and the subsequent CVs cycling showed enhanced capacitive currents for both oxidative and reductive peaks. The SEM image in the inset of Figure 4.3b showed the Fe-400-9C nanosheets with an average diameter of 600 ± 200 nm and an average thickness of 10 ± 2 nm (Figure 4.4 and Table 4.1). Further increase in the number of CV cycles from 10 to 20 cycles resulted in progressive decrease of peak currents (Figure 4.3d). This suggests the reorganisation of previously grown nanosheets, and the nanosheets became thicker. The electrochemically active surface area (ECSA) for Fe-400-9C is calculated to be 19.69 m^2 g^{-1}, higher than that for Fe-400-1C (14.66 m^2 g^{-1}) and Fe-400-20C (3.95 m^2 g^{-1}) (Figures. 4.5 and 4.6). Therefore, it is concluded that CV cycles could alter the number of active sites of the samples.

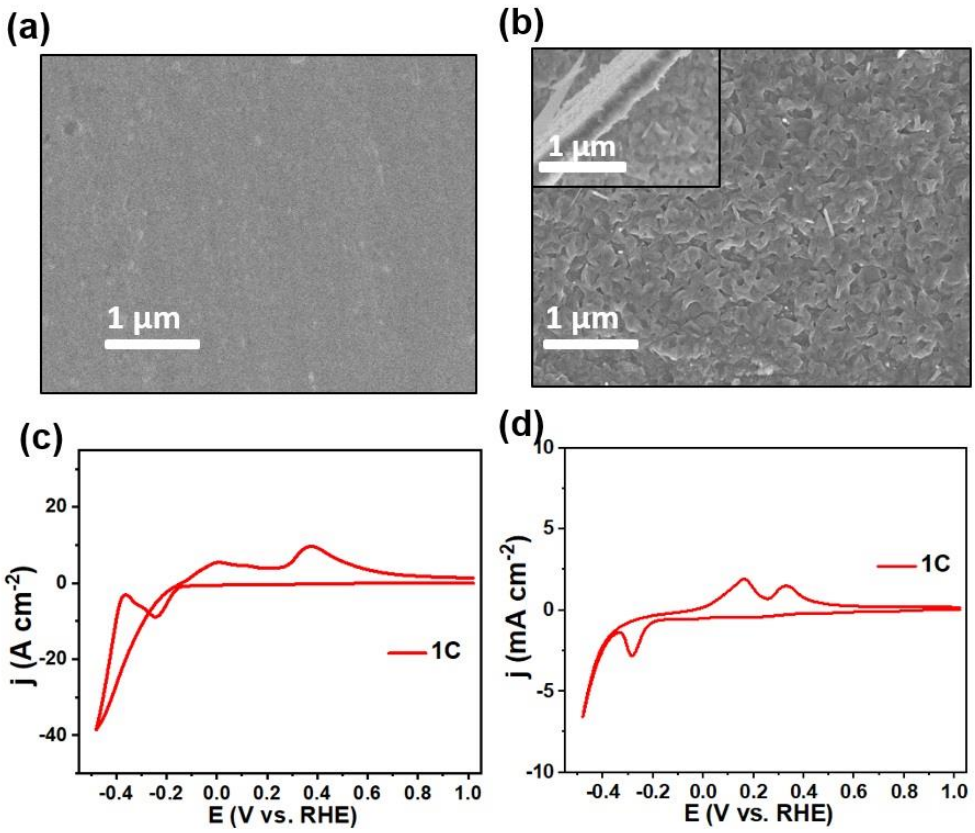

Figure 4.2 SEM images of (a) clean bare Fe foil without further treatment and (b) Fe foil heat-treated at 400 ºC for 1 h (Fe-400).The inset shows the cross sectional oxide layer of Fe-400; CVs for the first cycles of annealed iron foil (c) and bare iron foil (d).

Table 4.1 Sizes of nanosheets grown under different conditions

Samples	Growth conditions	Thickness(nm)	Diameter / lateral size (nm)
Fe-400-1C	-1.5 V - 0 V, 1 M KOH	6 ± 2	400 ± 100
Fe-400 -9C	-1.5 V - 0 V, 1 M KOH	10 ± 2	600 ± 200
Fe-400 -20C	-1.5 V - 0 V, 1 M KOH	15 ± 2	800 ± 200
Fe-9C	-1.5 V - 0 V, 1 M KOH	20 ± 2	250 ± 50
Fe-400 -9C	-1.0 V - 0V, 1 M KOH	N/A	N/A
Fe-400 -9C	-1.5 V - 0 V, 0.1 M KOH	5 ± 2	200 ± 100
Fe-400 -9C	-1.5 V - 0 V, 10 M KOH	45 ± 5	1500 ± 500

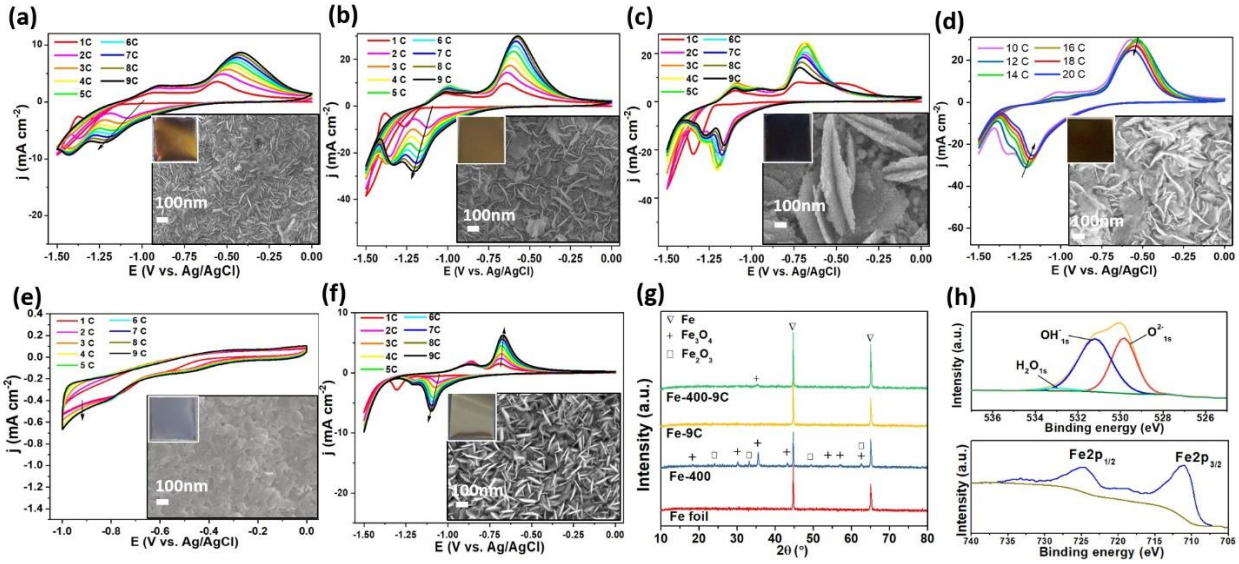

Figure 4.3 Growth and characterization of iron oxyhydroxide nanosheets. The growth of iron oxyhydroxide nanosheets under 9 CVs cycles from 0 to -1.5 V vs. Ag/AgCl on annealed iron foil performed in 0.1 M KOH (a), 1.0 M KOH (b) and 10.0 M KOH (c); and annealed iron foil from 10th to 20th cycle in 1.0 M KOH (d). Control experiments with CVs of annealed iron foil performed in 1.0 M KOH, with a narrower reductive potential up to -1.0 V (e) and a non-annealed iron foil (f); (g) X-ray diffraction patterns for the Fe foil, Fe-400, Fe-400-9C, Fe-9C; (h) X-ray photoelectron spectra of O1s and Fe2p for Fe-400-9C sample. The insets in (a-f) are their corresponding SEM and optical images of the synthesized amorphous iron oxyhydroxide nanosheet structures at the maximum number of cycles shown in their respective CV voltammograms.

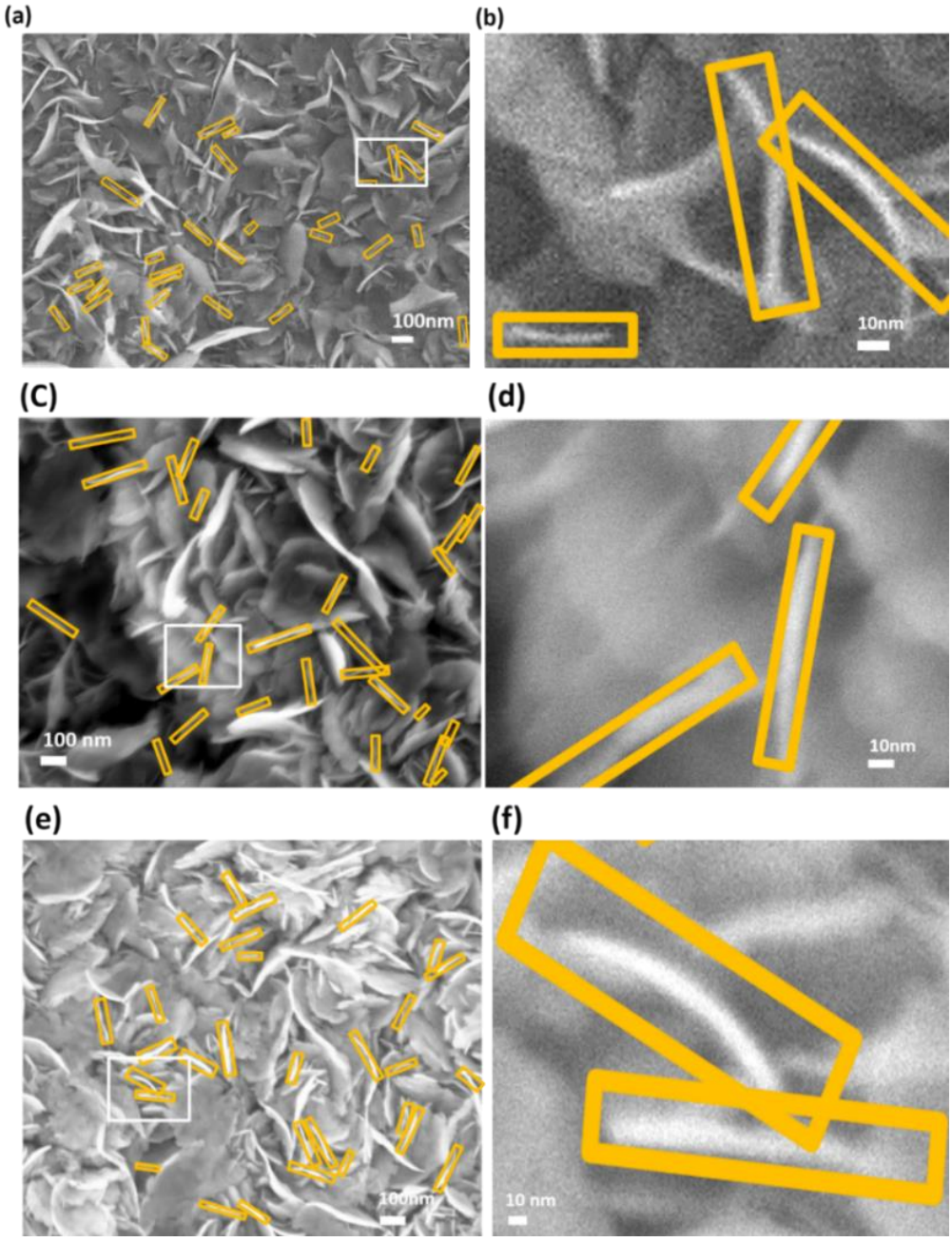

Figure 4.4 SEM images of the iron oxyhydroxide nanosheets. Fe-400-1C (a) Fe-400-9C (c) and Fe-400-20C (e); (b), (d), and (f) are the enlarged image of the selected regions in (a) (c) and (e), respectively.

When the negative potential was restricted to -1.0 V, no nanosheet growth occurred, as indicated by the CVs and SEM images in Figure 4.3e. Therefore, sufficiently negative reductive potential is necessary to drive the reduction of FeO_x toward the formation of ultrathin nanosheets. We performed another control experiment, where CV was performed on an iron foil not exposed to heat treatment and is denoted as Fe-nC. The obtained iron oxyhydroxide nanosheets were thicker (20 ± 2 nm) and smaller in diameter (250 ± 50 nm) (Figure 4.7) as compared to nanosheets grown on a thermally pre-treated iron foil substrate. The increment in the peak currents (Figure 4.3f and Figure 4.2d), which were 5 times lower than those for the nanosheets grown on thermally pre-treated substrate, indicated the essential role of underlying iron oxides in promoting the growth of iron oxyhydroxide nanosheets. To understand the growth mechanism of iron oxyhydroxide nanosheets, we examined the effect of KOH concentration. Figure 4.3a and 4.3c illustrated the CVs of the pre-treated iron foil in 0.1 M and 10 M KOH solutions. When compared to the CVs obtained in 1.0 M KOH solution (Figure 4.3b), a low KOH concentration (0.1 M) results in slower growth rate as reflected by a low current density. In 10 M KOH, a high hydroxide concentration and conductivity resulting in higher nanosheet growth rate. The current density reached a maximum at the 3rd cycle before the decay of current occured, suggesting that the iron oxyhydroxide nanosheets would quickly increase in thickness from the 4th cycle. After 9 CVs, the nanosheets were thicker (45 ± 5 nm) (Figure 4.8). This phenomenon is similar to the growth of nanosheets in 1M KOH in Figure 4.3b and 4.3d, but the decrease starts as early as the 3rd cycle, instead of the 9th cycle. Therefore, it is evident that concentration of KOH plays a key role in controlling the surface morphologies and growth rates of nanosheets.

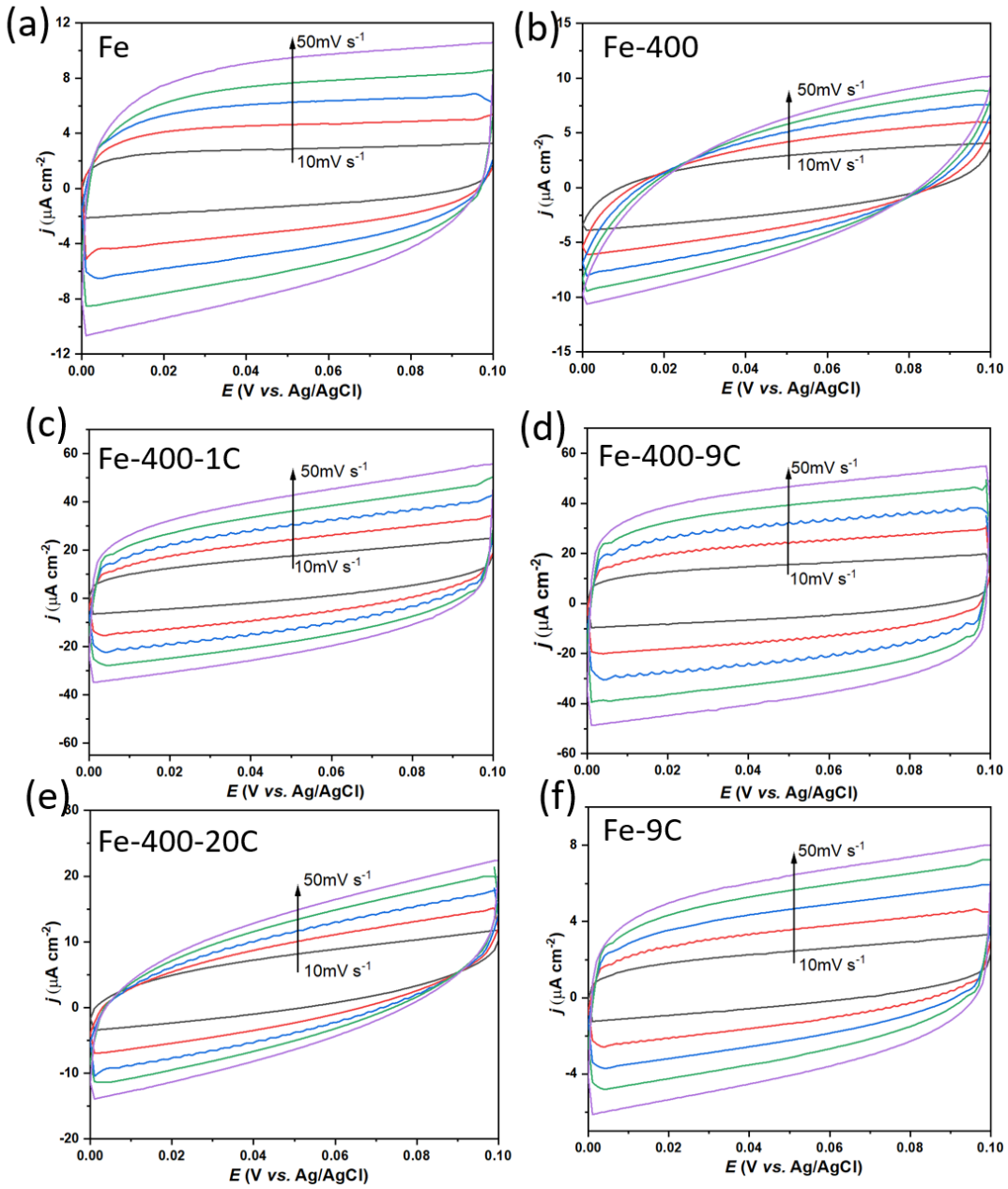

Figure 4.5 CV curves of Fe (a), Fe-400 (b), Fe-400-1C (c), Fe-400-9C (d), Fe-400-20C (e), Fe-9C (f) for ECSA calculation performed at various scan rates in a 1.0 M KOH solution.

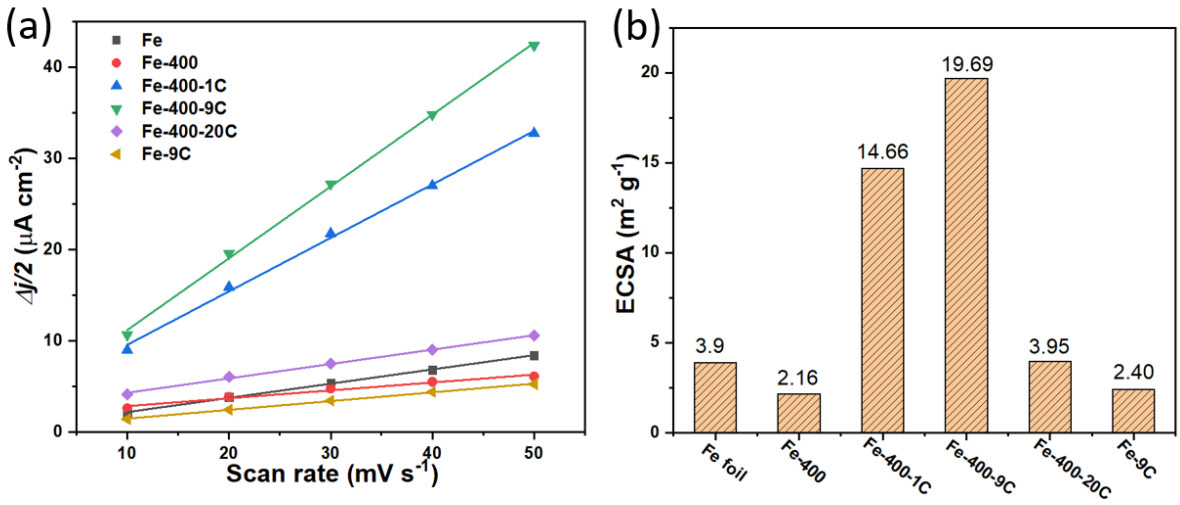

Figure 4.6 The plots of (a) Δj/2 as a function of scan rate and (b) calculated ECSA for various iron-based samples. The ECSA was calculated by the equation: ECSA = C_{dl} / C_s, where C_s value was 0.040 mF cm^{-2} and the C_{dl} is the slope of Δj/2-Scan rate assuming that the electrode in KOH was atomically smooth.

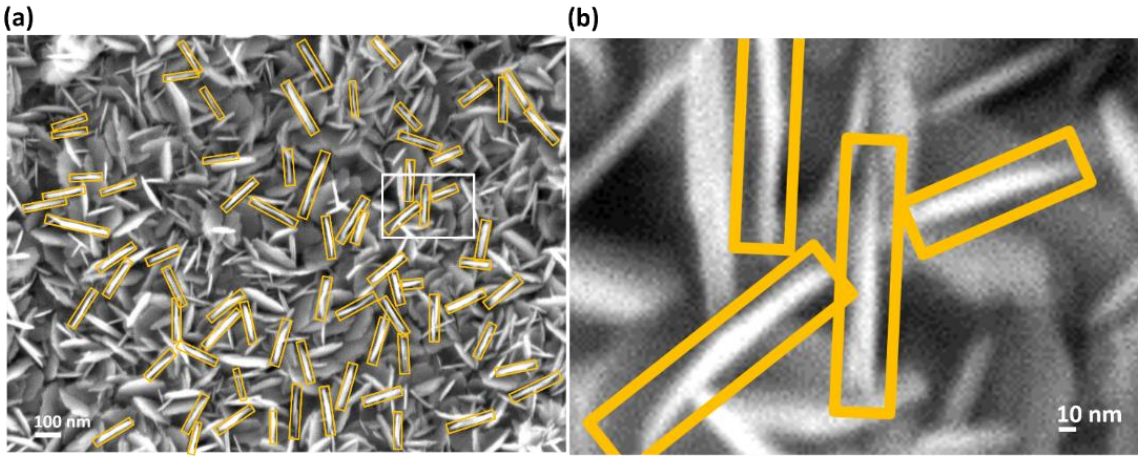

Figure 4.7 SEM images of the Fe-9C (a) and the enlarged image of the selected region (b).

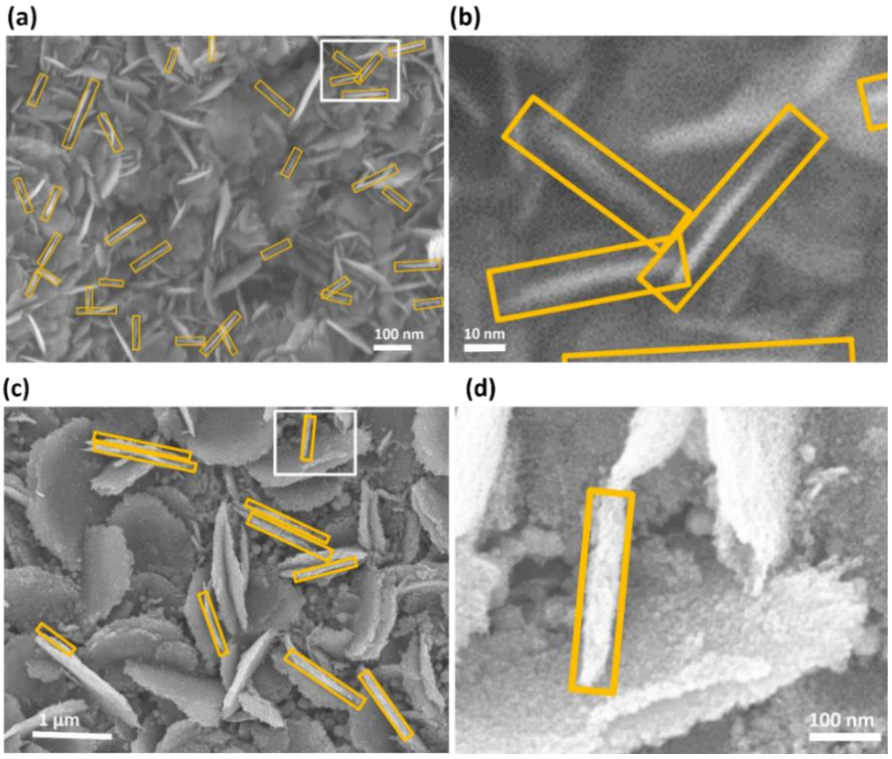

Figure 4.8 Electrolyte concentration effects on the nanosheet growth. SEM images of the Fe-400-9C grown in 0.1 M KOH (a) and 10 M KOH (c); (b) and (d) are the enlarged image of the selected regions in (a) and (c), respectively.

X-ray diffraction (XRD) patterns (Figure 4.3g) indicate two dominant peaks of α-Fe (PDF Card-04-014-0164) for all samples originating from the Fe foil substrate. The Fe-400 sample annealed at 400 ^{o}C has a clearly identified oxide layer consisting of Fe_3O_4 (PDF Card-04-005-4307) and Fe_2O_3 (PDF Card-01-085-0599). As can be seen in Figure 4.3g, after 9 CV cycles (Fe-400-9C) the peak intensity of Fe_3O_4 has been dramatically reduced, while peaks characterisic to α-Fe originating from the substrate remained unchanged. No other crystalline peaks could be observed, indicating that the amorphisation of iron oxyhydroxide nanosheets was succesfully achieved. As expected, X-ray diffraction of a control sample, i.e. non-annealed Fe-9C, resulted in

the observation of α-Fe diffraction peaks only. The electronic states at the surface of Fe-400-9C sample was further analysed by the X-ray photoelectron spectroscopy (XPS) as shown in Figure 4.3h. Peaks at 711 eV and 725 eV are associated with $Fe2p_{1/2}$ and $Fe2p_{1/2}$.[291] Three peaks for O1s spectrum were clearly identified: O^{2-} (529.836 eV), OH^- (531.194 eV), and water (533.008 eV) suggesting the presence of oxides, hydroxides, and moisture on the surface of the nanosheets. All the above characterisation results were in an agreement with literature data for iron oxyhydroxide.[30, 292-293]

4.4.2 OER performance of ultrathin iron oxyhydroxide nanosheets

The electrocatalytic OER performance of iron foil, Fe-400, Fe-nC, and Fe-400-nC samples were examined in 1.0 M KOH (Figure 4.9a). All the experiments were recorded in a standard three-electrode setup as described in detail in the ESI. All the potentials were converted to the reversible hydrogen electrode (RHE) scale. The onset potential of bare Fe foil was 1.65 V. The iron oxyhydroxide nanosheets, fabricated by thermal treatment followed by CVs, showed lower onset potential. Among the Fe-400-nC samples, Fe-400-9C exhibits the lowest onset potential of 1.61V vs.RHE (inset in Figure 4.9a). Increasing the number of cycles during CVs to 9 improved the OER activity. However, a further increase in the number of cycles (e.g. 10 and 20 cycles) resulted in a decreased OER activity, which is in a good agreement with the drop of the number of active sites as indicated by ECSA analysis (Figures 4.5 and 4.6). Comparetively, although Fe-9C (without thermal annealing step) posseses nanosheet structure, it showed a similar onset potential as compared to that for the bare Fe foil. This indicated that the smaller and thicker nanosheets formed on the surface of Fe-9C were not as active as the thin and large nanosheets formed in Fe-400-9C. This can be attributed to the 2D ultrathin nanosheets having 1) a large number of active

sites (ECSA: 19.69 m^2 g^{-1}) for OER resulting from the higher specific surface area and 2) promoting faster mass transfer and electron transport, which is consistent with the thickness-dependent properties of 2D materials.[294] It is noticeable that the Fe-400 exhibited significantly lower OER performance. Such a low OER activity can be explained by the semiconducting nature of the crystalline Fe_3O_4 & Fe_2O_3 layer formed and the low ECSA (2.06 m^2 g^{-1}).

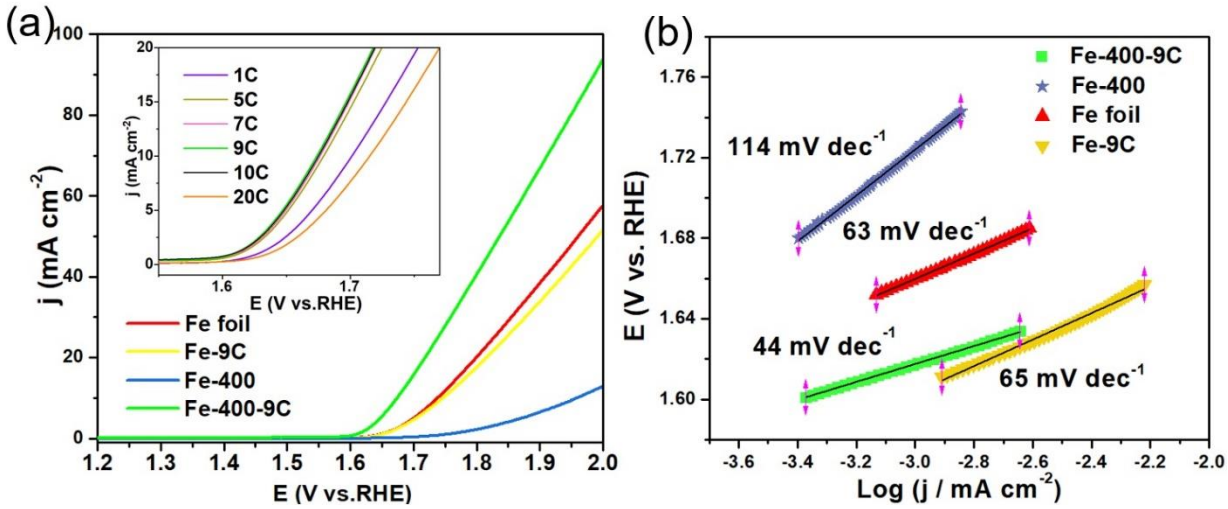

Figure 4.9 Electrochemical OER performances of various samples. (a) Linear sweep voltametries (LSVs) of Fe foil, Fe-400, Fe-400-9C, and Fe-9C. The inset shows the LSV of Fe-400-n (n = 1, 5, 7, 9, 10, 20)C samples; (b) Tafel plots of OER catalyzed by Fe foil, Fe-400, Fe-400-9C, and Fe-9C samples. All the measurements were performed at 5 mV s^{-1} in 1.0 M of KOH aqueous solution without IR compensation.

The OER kinetics of the samples were further assesed by the Tafel plots. Ultrathin iron oxyhydroxide nanosheet layer had a much lower slope than the crystalline iron oxide and foil (Figure 4.9b). The slope for Fe-400-9C was 44 mV dec^{-1}, being the lowest among the four samples measured. The Fe-400 had a relatively large slope (65 mV dec^{-1}) as compared to that for Fe foil. It should be noted that the Tafel slope of 114 mV dec^{-1} for Fe-400 was much higher, consistent

with the OER performance ilustrated in Figure 4.9a. The stability of the obtained ultrathin iron oxyhydroxide in 1.0 M KOH solution (Figure 4.10 and the inset in Figure 4.11) was also examined. At an overpotential of 0.428 V, the current density of the initial ~ 10 mA cm^{-1} was relatively stable with 80% of the initial current retained after 10 h. Comparision of the OER performance with other non-nanosheets iron oxyhydroxide structures is shown in Table 4.2, where ultrathin iron oxyhydroxide nanosheets in this work exhibiting a lower overpotential.

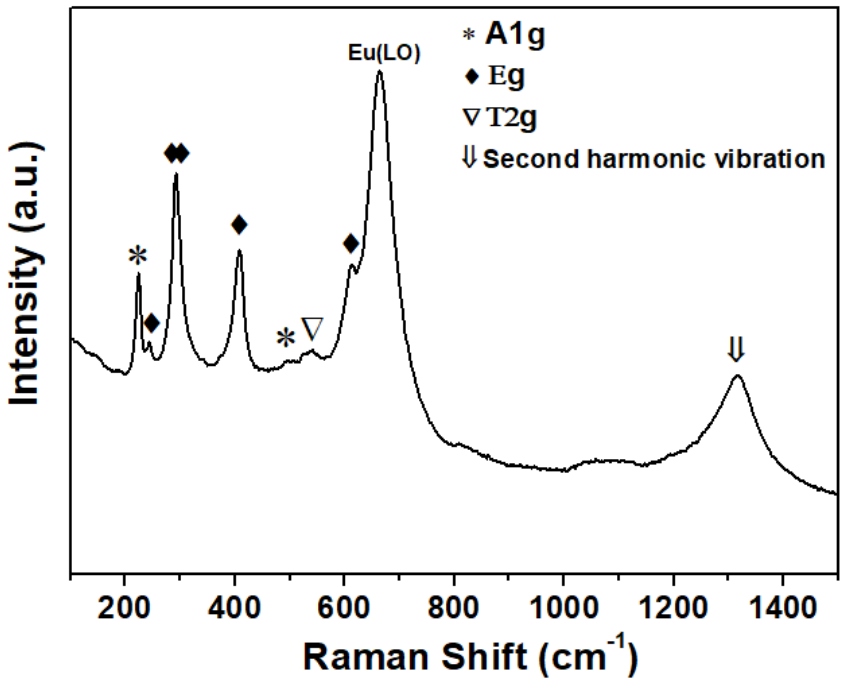

Figure 4.10 Raman spectrum of Fe-400-9C sample.

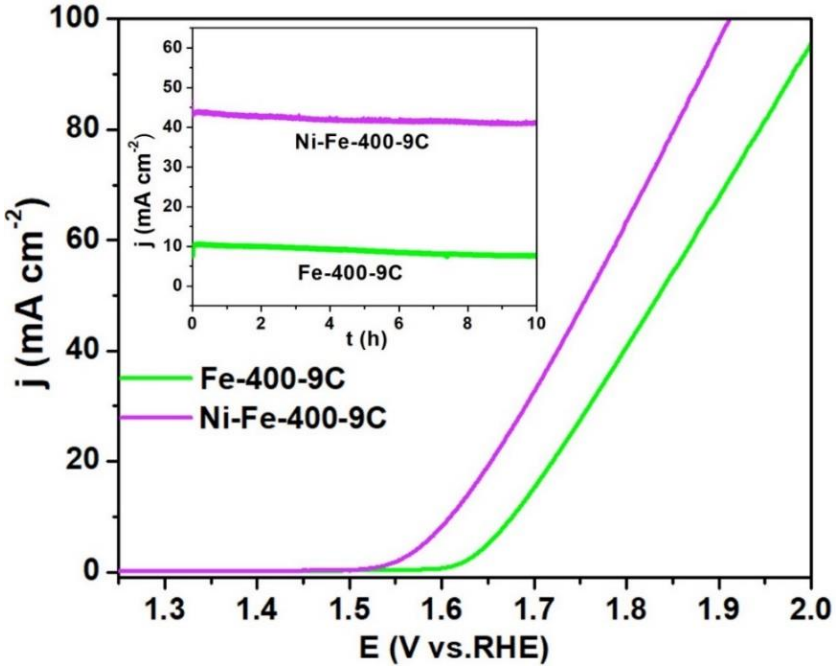

Figure 4.11 The comparison of LSVs between Fe-400-9C and Ni-Fe-400-9C. The inset is the chronoamperometric test of Fe-400-9C with a fixed overpotential of 0.428 V. For LSVs, all the measurements were conducted at a scan rate of 5 mV s^{-1} in 1.0 M of KOH aqueous solution without IR compensation.

Table 4.2 OER performance of iron oxyhydroxides obtained by different methods

Synthesis method	Required overpotential to reach j=10 mA cm^{-2}	References
Chemical bath deposition method	> 0.55 V	[295]
Bath deposition method	0.49-0.56 V	[296]
Solution method	0.58 V	[297]
Hydrothermal method	0.53 V	[298]
Thermal treatment & CV cycling	0.43 V	This work

4.4.3 OER performance of Ni-deposited ultrathin iron oxyhydroxide nanosheets

The ultrathin iron oxyhydroxide nanosheets with large surface area and excellent stability offer great potential for tuning electrocatalytic performance, by incorporation of a secondary metallic catalyst (Figure 4.1b). Ni was deposited onto the amorphous nanosheets by electrodeposition from a solution containing 0.01 M $NiSO_4$ and 0.2 M sodium citrate at -1.0 V vs. Ag/AgCl. Ni can be uniformly loaded onto the nanosheets in this weakly alkaline electrolyte (Figure. 4.13). The Fe-400-9C sample with the Ni loading time of 5 min showed the best performace as compared to samples with loading times of 1 min or 10 min (Figure 4.14). The 5 min electrodeposition estimated from accumulated charge resulting in Ni loading of ~ 0.7 μmol cm^{-2}. The presence of Ni lowered the onset potential to 1.52 V vs. RHE (Figure 4.11) corresponding to overpotential of 0.274 V. In comparison to Fe-400-9C sample, a Ni-Fe-400-9C sample exhibited a much higher current density (42 mA cm^{-2}) at the overpotential of 0.428 V. It shows enhanced performance than Ni-Fe and Ni-Fe-9C, further demonstrated the beneficial feature of an ultrathin iron oxyhydroxide nanosheet structure.

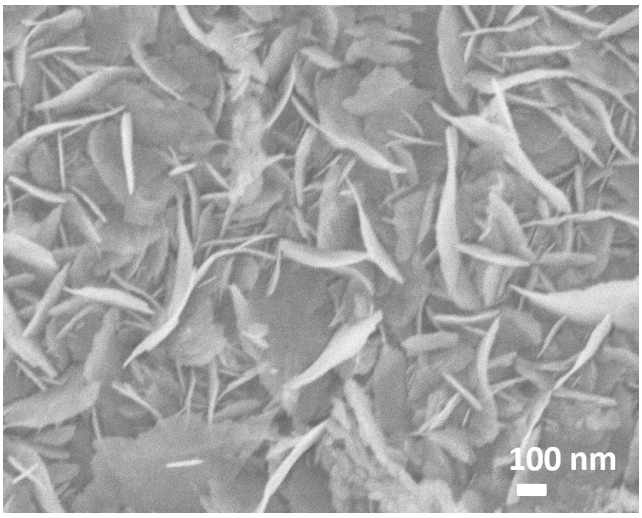

Figure 4.12 SEM image of the Fe-400-9C after the stability test.

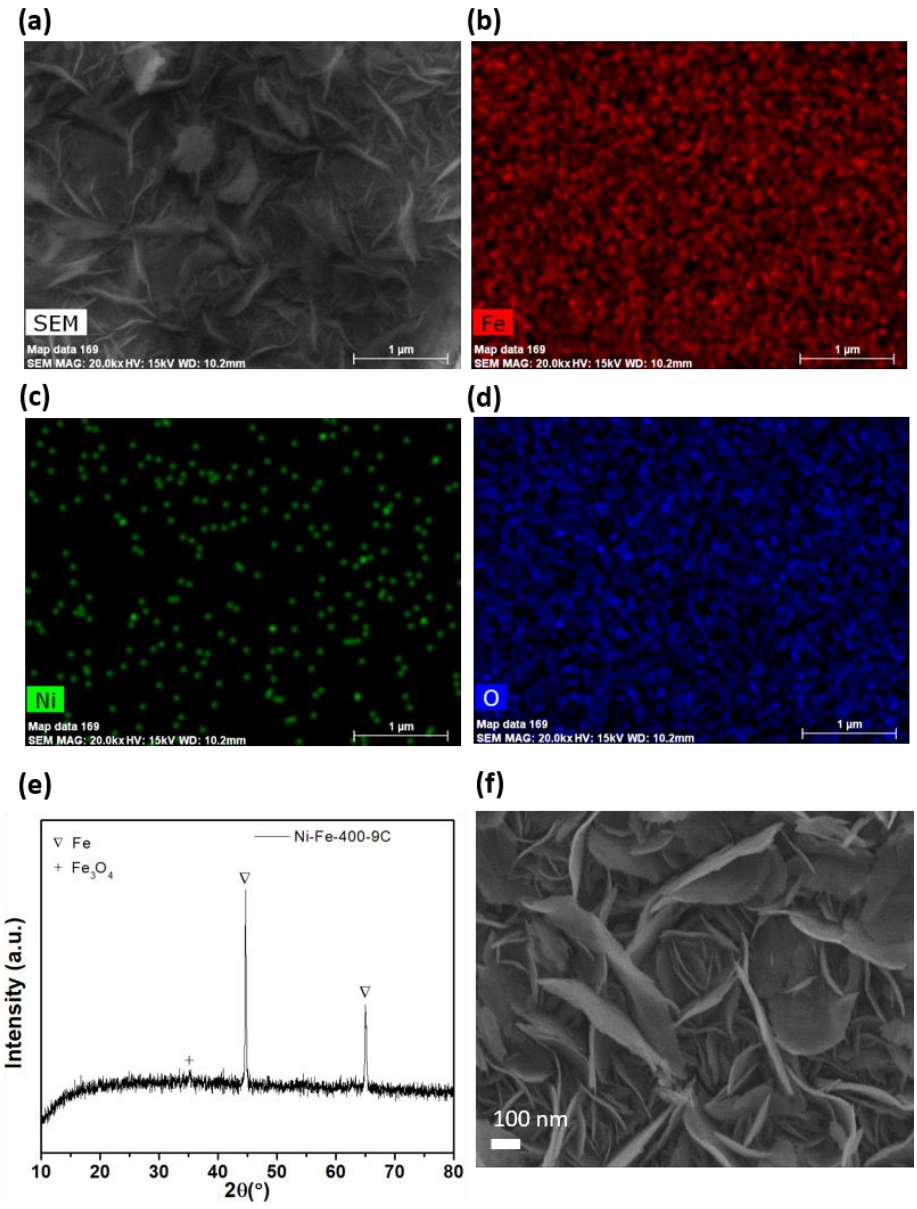

Figure 4.13 Elemental mapping images of Ni-Fe-400-9C (a), (b), (c), (d); XRD pattern of Ni-Fe-400-9C (e), and SEM image of the Ni-Fe-400-9C after the 10 h stability test (f).

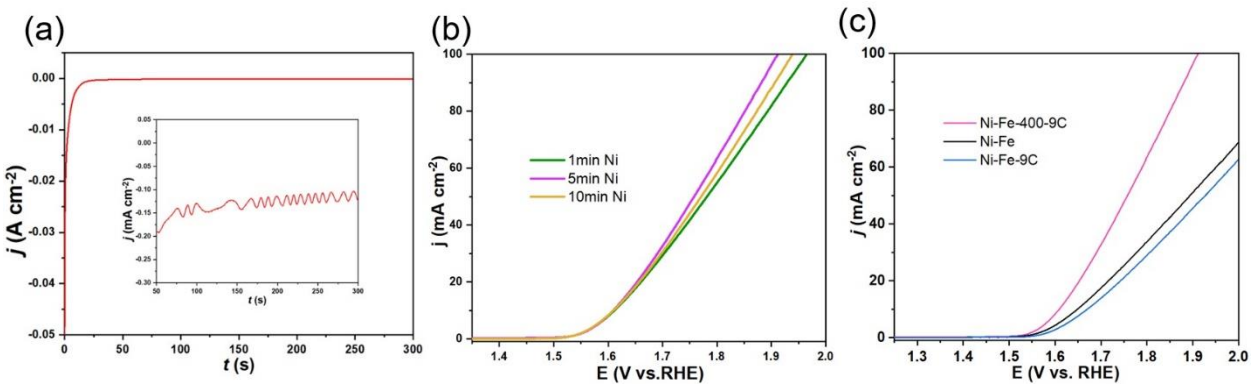

Figure 4.14 (a) Current time profile of Ni loading of the Ni-Fe-400-9C sample. The inset is the enlarged curve from 50 to 300 s. (b) Linear sweep voltammetry (LSV) of Ni-Fe-400-9C samples with different Ni loading time. All the measurements were conducted at a scan rate of 5 mV s^{-1} in 1.0 M of KOH aqueous solutions. (c) The OER performance comparison of Ni-Fe-400-9C, Ni-Fe, and Ni-Fe-9C.

4.5 Conclusions

In summary, facile preparation of ultrathin iron oxyhydroxide nanosheets is achieved by cycling the potential using a thermally annealed iron foil electrode. Optimization of various conditions such as thermal annealing, hydroxide concentration, and negative potential limits is necessary for successful growth of the ultrathin nanosheets. The resulting ultrathin 2D structures exhibited an abundancy of active sites and lowered the OER overpotentials. Furthermore, Ni loaded iron oxyhydroxide nanosheets showed even lower onset potential and higher current density, suggesting that the incorporation of secondary active species into the 2D structure is a feasible strategy for designing electrocatalysts with enhanced performance.

4.6 Acknowledgements

J.Z. and C.Y.L. thanks University of Wollongong for the postgraduate scholarship and VC fellowship, respectively. Funding from the Australian Research Council Centre of Excellence Scheme (CE140100012) is gratefully acknowledged. The authors would like to thank University of Wollongong Electron Microscopy Centre for equipment use. This work, in part, was performed within the materials node of the Australian National Fabrication Facility, an entity established under the National Collaborative Research Infrastructure Strategy to provide nano and microfabrication facilities to Australian researchers.

Chapter 5 A non-noble metal catalyst-based electrolyser for efficient CO_2-to-formate conversion

This chapter has been adapted, with the publisher's permission, from the article entitled 'A non-noble metal catalyst-based electrolyser for efficient CO_2-to-formate conversion'

Citation: Zou et al., *ACS Sustainable Chem. Eng.* 2021.

DOI: https://doi.org/10.1021/acssuschemeng.1c06295

Jinshuo Zou, Chong-Yong Lee and Gordon G. Wallace**

ARC Centre of Excellence for Electromaterials Science, Intelligent Polymer Research Institute, AIIM, Innovation Campus, University of Wollongong, Wollongong, NSW 2500, Australia.
E-mail: cylee@uow.edu.au; gwallace@uow.edu.au

* Corresponding author

Keywords: Full cell, CO_2 reduction, formate, Bi nanoparticles, NiFe layered double hydroxide

Author statement:

The study in this chapter was conceptual, experimentally designed and written by Jinshuo Zou. All experiments including material preparations, characterizations, electrochemical studies and the data analysis presented in this chapter were performed by Jinshuo Zou. Dr. Chong-Yong Lee and Prof. Gordon G. Wallace supervised the study, and assisted in the conception, experimental design and revisions of manuscript.

5.1 Abstract

Electrochemical CO_2 reduction offers a promising approach to alleviate environmental and climate impacts attributed to increasing atmospheric CO_2. Intensive research work has been performed over the years on catalysts, membranes and other associated components related to the development of CO_2 electrolysers. Herein, we assembled a full cell comprised of a Bi nanoparticles (NPs) based cathode for reducing CO_2 to formate, and the earth-abundant NiFe layered double hydroxide (LDH) based anode for oxygen evolution. The electrolyte used was 1 M KOH and an anion exchange membrane separator was employed. A formate conversion Faradaic efficiency ($FE_{formate}$) of 90 ± 2 % was obtained at the cell voltage of 2.12 V. This full cell system operating at 2.12 V was found to perform well over 10 h, as the $FE_{formate}$ remained above 85 % with ~ 82 % retention of current. This is amongst the best performing CO_2-to-formate conversion systems based on all non-precious metal catalysts. The low water oxidation overpotential of NiFe LDH, coupled with the highly efficient Bi NPs CO_2 reduction catalyst, as well as the use of KOH electrolyte operated under flow cell configuration that maximises the reactant/product mass transfer, all contribute to this high-performance electrolyser.

5.2 Introduction

The over-reliance and intensive consumption of fossil fuels in order to meet industry and household energy demands over the past decades has contributed to recent historically high 421 ppm atmospheric CO_2.[12] As an alternative of being released to the atmosphere, the transformation of CO_2 to value-added chemical products and fuels is highly desirable.[299] The electrochemical route to such reductive processes powered by renewable energy sources such as solar and wind

offers the potential to close the carbon cycle disrupted by human activity. Formate is a promising CO_2 reduction product due to the wide use in energy, pharmaceutical, rubber, leather, textile, and agricultural industries.[21-23] An efficient and robust formate conversion CO_2 electrolyser should have features such as operation at lower voltages at high partial current densities, excellent formate conversion selectivity and stability.[300] The use of appropriate catalysts in both the anodic and cathodic compartments, preferably based on low cost non-noble metals, plays a critical role in achieving this goal.

For catalyst screening and to obtain an understanding of their reaction mechanisms, cathodic half-cell reactions in three electrode configurations are commonly employed. Applied voltage is the difference between the working electrode and the reference electrode, hence offering convertible reference potentials that facilitate comparison between experimental data. In a full electrochemical cell, cathodic compartment contains a CO_2 electroreduction catalyst, with the counterpart catalyst involving an anodic oxidation process, commonly water oxidation. Taking into account the kinetic overpotentials of CO_2 reduction reaction (CO_2RR), and oxygen evolution reaction (OER), as well as the overall Ohmic resistance, the cell voltage (E_{cell}) of such systems can be calculated from Eqn. (1): [157]

$$E_{cell} = E^0_{cell} + \eta_c + \eta_a + j \cdot R_{ohmic} \quad (1)$$

Where E^0_{cell} corresponds to the reversible voltage, $j \cdot R_{ohmic}$ refers to the voltage loss caused by Ohmic resistances such as electrolyte resistance, membrane resistance, and connection resistance. η_c and η_a are the overpotentials of the cathodic CO_2RR and anodic OER half-cell reactions. Efficient anodic and cathodic catalysts hold the key in lowering the anodic and cathodic reactions

overpotentials, respectively. This along with an optimised cell configuration with low Ohmic resistances should be employed to lower the E_{cell}.

Numerous metals, particularly Sn, Bi, In, Pd, Cu, and Co have been investigated as electrocatalysts for formate production from CO_2 reduction.[27] Among them, Bi has been proven to be a promising catalyst due to its low toxicity, low cost, and high formate selectivity. Since Komatsu et al. reported bulk Bi exhibited good selectivity toward formate production for the first time in 1995,[125] Bi has been synthesized in various nanostructured morphologies such as nanosheets,[87] nanotubes[91] and nanoparticles[131] to overcome the intrinsically poor electrocatalytic CO_2 reduction performance of bulk Bi. Xu and co-workers prepared a few-layer bismuthene (thickness: around 1.28 nm) by in situ electrochemical transformation from ultrathin metal-organic layers.[101] The high intrinsic activity of atomically thin bismuthene layer was proposed contributing in high formate selectivity (~100%) at high current density (>300 mA cm^{-2}) at -0.95V under a flow-cell configuration. Wu et al prepared a hybrid structure containing Bi nanoparticles on graphene using a hydrothermal method with the addition of hydrazine hydrate and aqueous ammonia.[301] The synergetic metal-support interaction is proposed to contribute to the high formate conversion Faradaic efficiency of 92.7% at -0.97 V vs RHE at ~20 mA cm^{-2}

Bi-based cathodes have been employed in full cell CO_2 reduction studies. Fan and co-workers reported an all-solid-state electrochemical CO_2RR system for formate generation, employing *n*-butyl lithium - treated Bi (nBuLi-Bi) cathode and IrO_2-C anode separated by a porous solid electrolyte layer [153]. The cell exhibited a high current density of ~450 mA cm^{-2} at a cell voltage of 2.19 V. Díaz-Sainz et al synthesized the carbon-supported Bi NPs as the cathode, Ir-mixed metal oxide on platinum as an anode, and assembled a filter-press full cell.[168] Although the Faradaic

efficiency of formate conversion reached 89.5 % at a current density of 90 mA cm^{-2}, it requires a relatively high voltage of 3.1 V. It should be noted that the above examples of Bi-cathodes involves coupling to precious metals such Ir and platinum for the water oxidation reaction. Preferably, low-cost non-precious metal anodic catalysts should be employed as this would facilitate the large-scale deployment of CO_2 electrolysers.

Herein, we synthesized Bi nanoparticles (Bi NPs) with an average size of 13 ± 3 nm as an active catalyst for CO_2 reduction, and the earth-abundant NiFe LDH on Ni foam as an anode for water oxidation. The cathode and anode were assembled in an electrochemical flow cell using an anion exchange membrane and 1 M KOH electrolyte. We first examined the intrinsic activity of individual anodic and cathodic catalysts through half-cell studies. Then, we studied the performance of the full-cell assembly.

5.3 Experimental section/methods

5.3.1 Electrode preparation

Bismuth(III) nitrate pentahydrate ($Bi(NO_3)_3 \cdot 5H_2O$, 98 %, Sigma Aldrich), Sodium borohydride ($NaBH_4$, 99 %, Sigma Aldrich), ethylene glycol (Chem-Supply), urea (≥98 %, Sigma Aldrich), gas diffusion layer (Sigracet 39 BC, FuelCellStore), Iron(III) nitrate nonahydrate ($Fe(NO_3)_3 \cdot 9H_2O$, 99.95 %, Sigma Aldrich), Nickel(II) nitrate hexahydrate($Ni(NO_3)_2 \cdot 6H_2O$, ≥98.5 %, Sigma Aldrich), Ni foam (98 %, Lizhiyuan Co. Ltd), Carbon dioxide (CO_2, 99.99 %), hydrogen (H_2, 99.99 %) and Ar cylinders were purchased from BOC.

Cathode preparation: The Bi NPs nanoparticles were prepared by $NaBH_4$ reducing method. Typically, 1 mmol $Bi(NO_3)_3 \cdot 5H_2O$ was added to 80 mL ethylene glycol. After 30 min of stirring and subsequent ultrasonic treatment for 1 h, the $Bi(NO_3)_3 \cdot 5H_2O$ can be fully dissolved in ethylene glycol. Then 200 mg of $NaBH_4$ was added directly and stirred intensively. The Bi^{3+} can be fully reduced to Bi nanoparticles after 2 min stirring. Afterward, the black nanoparticle suspensions was vibrated for 10 min and ultrasonicated for another 1 h to shatter the large Bi clusters assembled by Bi nanoparticles during the crystallization process. Finally, the Bi NPs were washed by centrifuging in ethanol and dried in vacuum oven at room temperature.

To make a catalyst ink, 10 mg of Bi NPs catalyst, 860 µL of isopropanol, 100 µL of DI water, and 40 uL of nafion solution (15%) were ultrasonically mixed for 30 min to form a homogenous catalyst ink. Then the catalyst ink was air-brushed on the gas diffusion layers (GDL) and dried at 50 ^oC overnight to serve as Bi NPs/GDL working electrodes.

Anode preparation: The NiFe LDH/Ni foam was prepared by hydrothermal method. Typically, the nickel foam was pre-cleaned in 2 M HCl solution under sonication for 5 min and followed by washing with water and ethanol. Then 0.5 mmol of $Fe(NO_3)_3 \cdot 9H_2O$, 1.5 mmol of $Ni(NO_3)_2 \cdot 6H_2O$, and 10 mmol of urea were added to 35 mL of deionized water and stirred to form a uniform solution. Subsequently, the pre-treated Ni foam was immersed in the above solution in an autoclave (50 mL). The autoclave was kept at 150 ^oC for 12 h. Finally, the obtained NiFe LDH/Ni foam was washed in ethanol and water before drying in a vacuum oven at room temperature.

5.3.2 Characterization:

XRD patterns of the Bi NPs/GDL and NiFe LDH/Ni foam were collected at a scan rate of 2 ^{o} min^{-1} on a PANalytical Empyrean diffractometer with Cu K_{α} radiation (λ=1.54056 Å). The transmission electron microscopy (TEM) analysis of Bi NPs was carried out on a JEOL JEM-2100F microscope at an acceleration voltage of 200 kV. The surface morphology of NiFe LDH/Ni foam was recorded on a scanning electron microscope (SEM) of JEOL JSM-7500FA. The X-ray photoelectron spectroscopy (XPS) measurements were performed on the Nexsa surface analysis system (ThermoFisher SCIENTIFIC) photoelectron spectrometer using the monochromatic Al K_{α} X-ray as the excitation source under the vacuum of 1×10^{-8} Pa. Fourier transform infrared (FTIR) characterizations for NiFe LDH were performed on a Spotlight 400 FTIR Imaging System (PerkinElmer).

5.3.3 Electrochemical characterization:

All the measurements were carried out on a CHI660D potentiostat at room temperature, in a home-made flow-cell separated by anion exchange membrane (Fumasep FAB-PK-130, FuelCellStore) in the alkaline electrolyte. A solution of 1 M KOH was employed as the catholyte (200 mL) and anolyte (20 mL), pumped to the cathode and anode chambers respectively by a peristaltic pump (BT100-2J, Thermoline) at the flow rate of 17.5 mL min^{-1}. The CO_2 gas was introduced into the cathodic chamber at a flow rate of 20 mL min^{-1}. For three electrode system test, HgO electrode was used as the reference. All potentials and voltages were manually compensated using the resistances obtained from electrochemical impedance spectroscopy measurements.

5.3.4 Product analysis:

The gaseous products were analysed by a gas chromatography (GC) (8610C, SRI Instruments) equipped with both flame ionization detector (FID) and thermal conductivity detector (TCD). CO, CH_4, C_2H_4, and C_2H_6 can be analysed by the FID signal and H_2, CO, CH_4, C_2H_4, C_2H_6 and CO_2 can be detected by TCD signal. The Peak 454 software was used to do data processing. The analysis of formate were carried out on a 400 MHz NMR spectrometer (Bruker Avance) by 1D ^1H spectra. 1-propanesulfonic acid 3-(trimethylsilyl) sodium (DSS) was used as internal standard solution. A 0.5 mL of product-containing electrolyte, 0.1 mL of DSS (99.7%, Sigma Aldrich), and 0.1 mL of D_2O (99.9%, Cambridge Isotope Lab) was added in the NMR tube and mixed by ultrasonication before NMR analysis.

5.3.5 Electrochemically active surface area (ECSA) measurement

The electrochemically active surface area (ECSA) of Bi NPs/GDL and NiFe LDH/Ni foam were obtained using cyclic voltammetry at the non-Faradaic region in the electrolyte of 1 M KOH. The double-layer capacitance was estimated by plotting the Δj (j_a-j_c) at proper potentials against the scan rate. The specific capacitance (20–60 μF cm^{-2}) was used to calculate the ECSA:[246]

$$ECSA = C_{dl}/C_s \cdot cm^{-2}$$

Where C_{dl} is the double-layer capacitance and C_s is the specific capacitance.

5.4 Results and discussion

5.4.1 Characterization of Bi NPs/GDL cathode

As described in the experimental section, $NaBH_4$ reduction in ethylene glycol was used to form Bi NPs (Figure 5.1a). Vibration and ultrasonication resulted in a suspension of uniform Bi nanoparticles. After centrifugation Bi nanoparticles with average size of 13 ± 3 nm were obtained. A catalyst ink with homogeneously mixed Bi NPs, isopropanol and nafion solution was air-brushed on a commercially available carbon paper-based gas diffusion layer (GDL, Sigracet 39BC) with a catalyst loading of 1 mg cm^{-2}. This was dried at 50 ^{o}C overnight. The lattice fringe spacing obtained from TEM (shown in Figure 5.1b) of 0.33 nm corresponds to (012) of metallic Bi. The XRD patterns of the Bi NPs, Bi NPs/GDL, and GDL are shown in Figure 5.2a and Figure 5.1c. The main diffraction peaks of (012), (104), (110), (202), (024) can be indexed to the R-3m rhombohedral phase (JCPDS card No. 05-0519) without any other impurity phases. The present of metallic bismuth is evident from the Bi 4f peaks at 156.9 eV (Bi $4f_{5/2}$) and 162.3 eV (Bi $4f_{7/2}$) from X-ray photoelectron spectra (Figure 5.2b). In addition, two strong binding energy peaks at 158.8 eV (Bi $4f_{5/2}$) and 164.1 eV (Bi $4f_{7/2}$) correspond to Bi^{3+}, suggesting that the oxidative nature of Bi NPs on the cathode surface. This phenomenon can be explained by the oxidation of the surface Bi NPs due to exposure to air consistent with literature reports.[302-305]

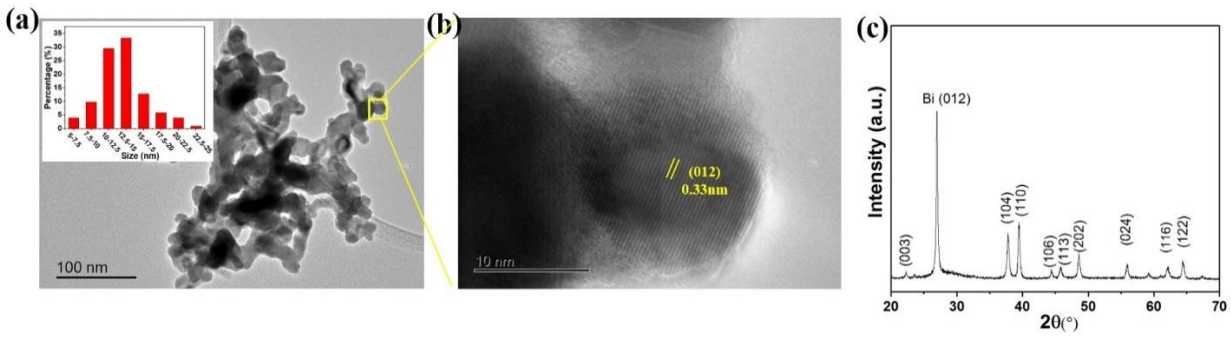

Figure 5.1 Characterization of Bi nanoparticles. (a) and (b) TEM images, (c) XRD patterns.

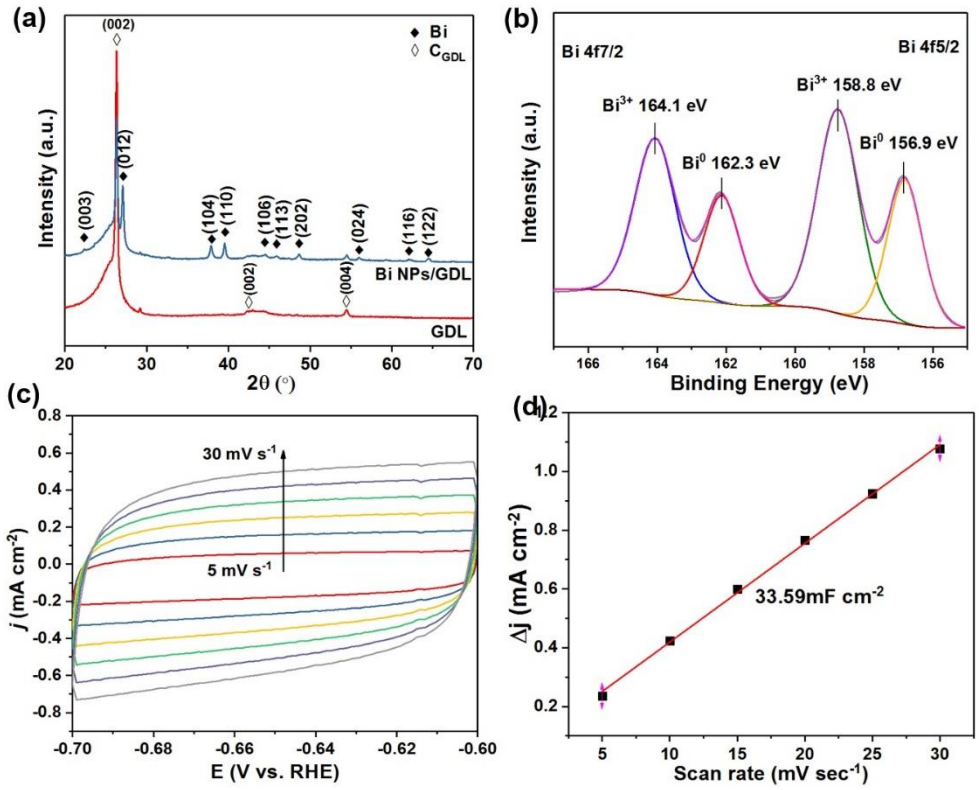

Figure 5.2 Characterization of Bi NPs/GDL and GDL. (a) XRD pattern of Bi NPs/GDL and GDL; (b) XPS spectra of Bi4f.of Bi NPs/GDL, (c) Cyclic voltammetry (CV) curves for ECSA test obtained in 1 M KOH at various scan rates. (d) Plot of the Δj vs. scan rate derived from CV curves in (c).

The electrochemical CO_2 reduction half-cell studies were conducted in a three-electrode flow cell as previously employed.[306] The gas diffusion layer (GDL) with the gas phase CO_2 in three phase interface (liquid electrolyte-solid catalyst-gaseous CO_2) at the cathode enables high current density electrolysis.[306] The cathode and anode chambers are separated by an anion exchange membrane (Fumasep FAB-PK-130, FuelCellStore). The Bi NPs/ GDL serves as a working electrode. The HgO electrode and nickel mesh were used as the reference, and counter electrodes, respectively. The CO_2 gas flows through the mesoporous carbon layers in the GDL to reach the Bi NPs catalyst at a flow rate of 20 mL min^{-1}. As shown in the linear sweep voltammogram (LSV) curves in Figure 5.3a, the current density increases quickly at more negative applied potentials, and reaches 250 mA cm^{-2} at -0.7 V vs RHE. The electrochemical surface area (ECSA) of the Bi NPs/GDL were determined by cyclic voltammetry performed at the non-Faradaic potential region from 0.3 to 0.4 V vs RHE (Figure 5.2c and d). The ECSA value is calculated to be 33.59 mF cm^{-2}, which is high compared with that of other Bi electrodes reported in the literature (less than 20 mF cm^{-2}).[90, 94, 307] The small sizes of Bi NPs which results in more exposed electrochemically active sites may contribute to the enhanced ECSA obtained here.

Controlled potential electrolysis (CPE) experiments were performed in the potential window between -0.29 and -0.59 V vs RHE. The formate product disolved in catholyte was detected and quantified by nuclear magnetic resonance (NMR). The gaseous CO and H_2 byproducts were analysed by gas chromatography which is connected to the gas outlet of the cell. The current density (Figure 5.3b) increased with higher cathodic potential and reached a maximum value of 155 mA cm^{-2}. The current density remained stable over 1 h constant cathodic potential, except at -0.59 V vs RHE a gradual drop was observed after 2500 s. The $FE_{formate}$ at -0.29 V is 55.8 ± 5.8 %

as the hydrogen evolution reaction (HER) is competing at this relatively low overpotential (Figure 5.3c). The $FE_{formate}$ reached > 80% when cathodic potential shifted to -0.39 V, with an optimal 91.9 ± 3.6 % at -0.44 V. However, at -0.59 V, the $FE_{formate}$ decreases to 72.4 ± 1.9 % as a result of increase in the HER partial current density (FE_{H2} : 18.7 ± 6.5 %). This can be explained by the detachment of Bi species from carbon GDL as the Bi peaks in XRD pattern becomes weak and the measured ECSA decreases to 19.50 mF cm^{-2} as shown in Figure 5.4. Previous studies proposed the two-electron CO_2 electroreduction to formate for bismuth catalysts follows the below reaction steps[91, 94]:

$$CO_2 + {}^* \rightarrow CO_2{}^* \qquad (2)$$

$$CO_2{}^* + e^- \rightarrow CO_2{}^{*-} \qquad (3)$$

$$CO_2{}^{*-} + H^+ + e^- \rightarrow HCOO^{*-} \qquad (4)$$

$$HCOO^{*-} \rightarrow HCOO^- + {}^* \qquad (5)$$

Where * indicates the active site at which a species can adsorb. The first step involves adsorption of the CO_2 molecule on the catalyst active site (eq. 2), followed by one electron transfer to the adsorbed CO_2 to form the $CO_2{}^{*-}$ intermediate (eq. 3). Subsequently, proton-couped one electron transfer results in adsorbed formate (eq. 4). The formed formate is then desorbed from the catalyst surface (eq. 5). The Tafel slope obtained from Figure 5.3d for Bi NPs/GDL is 127.6 mV dec^{-1}, which is close to the theoretical value of 118 mV dec^{-1} for a one electron transfer process, suggesting that the rate determining step (RDS) for the CO_2RR is $CO_2{}^{*-}$ formation (eq. 3).[91, 111, 205, 308]

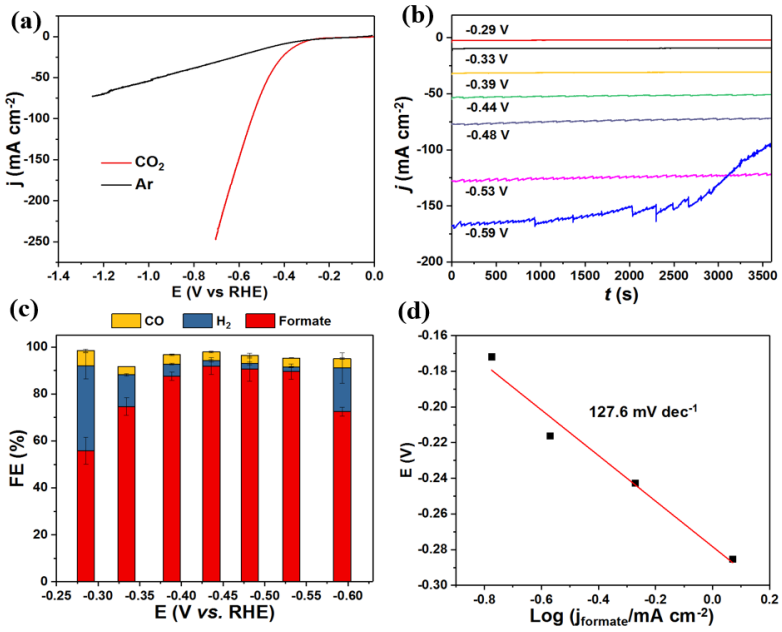

Figure 5.3 Electrochemical characterization and performance of Bi NPs. (a) LSV of Bi NPs/GDL performed under the flow of CO_2 and Ar gases, respectively (b) i-t curves for performance test in a three-electrode system, (c) Faradaic efficiencies of CO, H_2 and formate at different potentials vs RHE, (d) Tafel plot of Bi catalysts. All experiments were conducted in the catholyte of 1 M KOH, and all potentials were IR compensated. The error bars in c represent the standard deviations of three independent measurement of the samples.

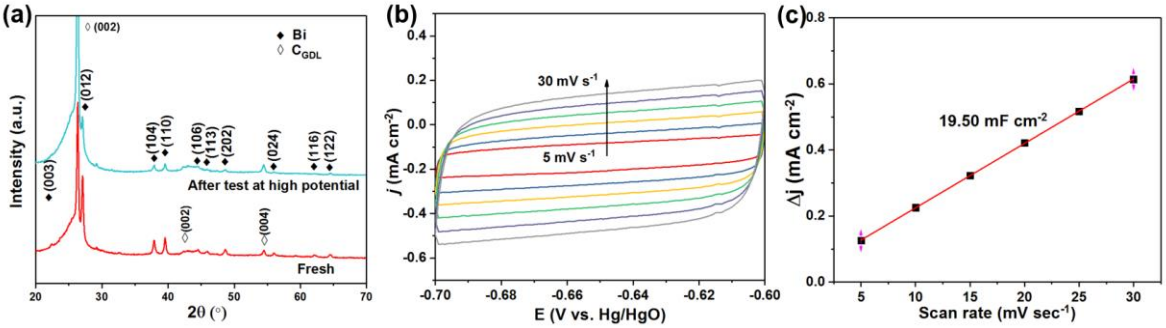

Figure 5.4 Characterization of Bi NPs/GDL after performance test at -0.59 V vs RHE. (a) Comparison of XRD patterns of fresh Bi NPs/GDL and that after performance test at -0.59 V vs. RHE for 10 h, (b) CV curves obtained in 1 M KOH at various scan rates for ECSA calculation of

the Bi NPs/GDL after cathodic half-cell stability test at -0.59 V vs RHE For 10 h. (c) Plot of the Δj vs. scan rate derived from CV curves in (b).

5.4.2 Characterization of NiFe LDH on Ni foam

The NiFe LDH was grown on a Ni foam substrate via a facile hydrothermal method. The Ni foam pretreated by acid was immersed in a solution containing $Ni(NO_3)_2 \cdot 6H_2O$, $Fe(NO_3)_3 \cdot 9H_2O$, and urea in an autoclave, followed by thermal treatment at 150 ^oC for 12 h. Here, the urea was employed as the hydrolysis agents to release carbonate during pyrolysis to promote the formation of LDH with high crystallinity.[309-311] The SEM images of the NiFe LDH in Figure 5.5a and 5b reveal the LDH exists as nanosheets uniformly assembled on the Ni foam. The XRD peaks (Figure 5.5c) at 11.3^o, 22.8^o, 33.5^o, 34.4^o, 38.6^o, 59.7^o and 60.9^o are consistent with the characteristic (003), (006), (110), (012), (015), (110), and (113) of NiFe LDH (JCPDS card No. 40-0215), respectively, confirm the formation of crystalized LDH on the Ni foam substrate. The peaks of Fourier transform infrared spectra at 714 and 514 cm^{-1} (Figure 5.5d), are attributed to the vibrations of metal-oxygen bonds in the LDH, are consistent with generally reported results.[312-313] The Ni2p and Fe2p XPS spectra (Figure 5.5eand 5.5f) indicated the Ni and Fe are mainly in the chemical oxidative state of Ni^{2+} and Fe^{3+}.[314-315]

The ECSA of NiFe LDH/Ni foam and Ni foam were determined using the double-layer capacitance from CV curves at different scan rates in Figure 5.5g-i. The C_{dl} of NiFe LDH/Ni foam (25.3 mF cm^{-2}) is about 3.4 times of that for Ni foam (7.42 mF cm^{-2}), suggesting that the LDH nanosheets significantly improve the electrochemical active area. A lower onset potential (1.45 V vs RHE) in LSV (Figure 5.6a) and Tafel slope (79 mV dec^{-1}, Figure 5.6b) from the Tafel plot of

NiFe LDH/Ni foam indicated that NiFe LDH/Ni foam is significantly more active for oxygen evolution reaction, than the Ni foam substrate. A comparable study of the stability for NiFe LDH/Ni foam and Ni foam was conducted by chronoamperometry at a fixed potential of 1.6 V vs RHE (Figure 5.6c). The unattenuated current density (~109 mA cm^{-2}) after 10 h and the almost unchanged crystalline and morphology further identify the stability of NiFe LDH/Ni foam over this time period. Therefore, the NiFe LDH/Ni foam was employed for the subsequent full cell assembly.

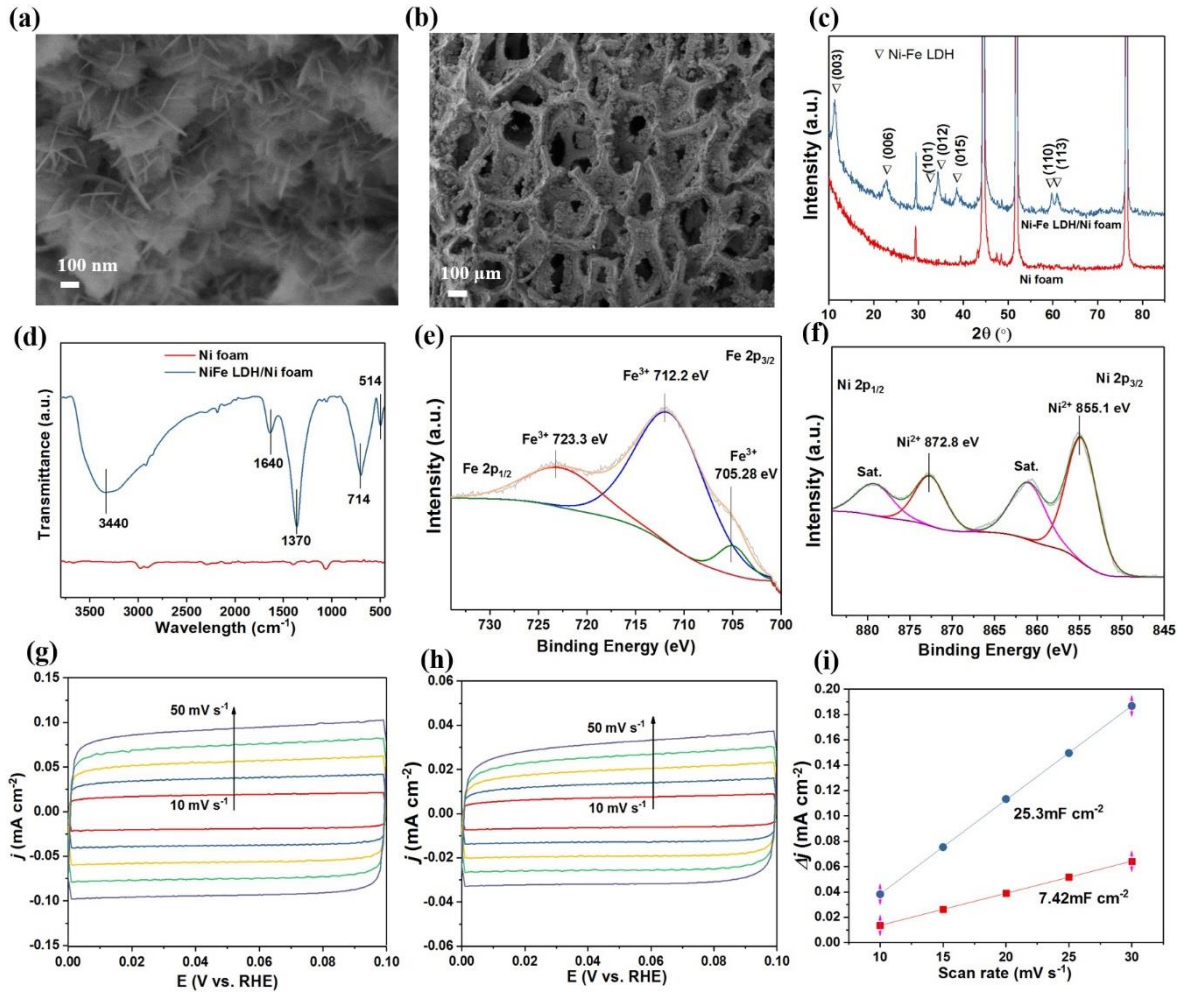

Figure 5.5 Characterization of Ni-Fe LDH/Ni foam and Ni foam. SEM of Ni-Fe LDH on Ni foam

at high (a) and low (b) magnifications; (c) The XRD patterns of Ni-Fe LDH/Ni foam and Ni foam; (d) FTIR of NiFe LDH/Ni foam and Ni foam, XPS spectra and corresponding fitting spectra of Fe 2p (e) and Ni 2p (f) of the Ni-Fe LDH/ Ni foam sample. CV curves obtained for ECSA calculation of NiFe LDH/Ni foam (g) and Ni foam (h) performed in 1 M KOH at various scan rates; (i) Plots of the Δj vs. scan rate derived from CV curves in (g) and (h).

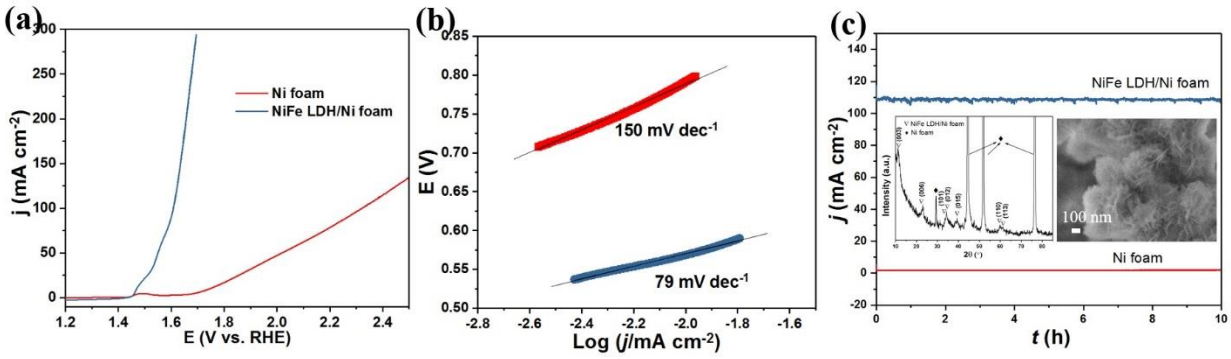

Figure 5.6 OER performance of Ni-Fe LDH/Ni foam and Ni foam. (a) LSV curves, (b) Tafel plots, and (c) long term stability test. The insets in (c) are XRD pattern and the SEM image of the NiFe LDH/Ni foam after 10 h stability test

5.4.3 Full cell performance

The electrochemical flow cell employed the Bi NPs/GDL and the NiFe LDH/Ni foam as a cathode and an anode, respectively (Figure 5.7a). The internal configuration of the cell is similar to the three-electrode half-cell flow cell system except in the absence of HgO reference electrode. In the cathodic chamber, three phase interface (liquid electrolyte-solid catalyst-gaseous CO_2) formed on the Bi catalysts that facilitate CO_2 reduction, and the liquid-phase formate product was transported

with the 1 M KOH catholyte. In the anodic chamber, O_2 bubbles were generated on NiFe LDH/Ni foam.

Using the full cell, CO_2 reduction to formate commenced at a cell voltage of 1.76 V, where HER is dominant with a hydrogen conversion efficiency of 89 ± 4 % in Figure 5.7c. With the increment in cell voltage, the formate became the main product where $FE_{formate}$ is > 80 % at 1.98 V. The maximum $FE_{formate}$ (90 ± 2 %) was achieved at a cell voltage of 2.12 V with a current density of 55 mA cm^{-2}. At 2.36 V, the current density initially reached 160 mA cm^{-2}. Current density dropped to ~ 149 mA cm^{-2} after 1 h electrolysis with the $FE_{formate}$ decreasing to 74 ± 9 % due to the competition with the hydrogen evolution reaction. This phenomenon is consistent with the performance at -0.59 V vs RHE in the three-electrode system as discussed in section 5.3.1. The previously reported results for electrochemical CO_2 reduction to formate in full cells employing various catalysts, cell configurations, and electrolytes are summerized in Table 5.1. Sn and Bi based catalysts are the commonly employed CO_2RR catalysts, with Bi nanostructures performing at high current densities. Lee and co-workers used a platinum gauze as an anode in a catholyte-free flow cell and obtained a high formate conversion efficiency of 93.3 % at the cell voltage of 2.2 V.[145] Other examples of precious metals as anodes including the use of IrO_2-C (97% in $FE_{formate}$ with ~100 mA cm^{-2} at 1.51V)[153] and Ir-mixed metal oxide (89.5% in $FE_{formate}$ with 90 mA cm^{-2} at 3.1 V).[168] However, the high cost of precious metals Ir and Pt would be an obstacle with respect to the economics of CO_2 electrolysers.Compared with these aqueous full cells listed in Table 5.1, this work employing the non-precious metal based anodic catalysts exhibits excellent performance of 92 % formate conversion efficiency with current density of ~55 mA cm^{-2} at 2.12 V).

The long-term performance of this full cell was examined at 2.12 V for 10h (Figure 7d). The $FE_{formate}$ remained above 80 % after 10 h. XRD, XPS and electrochemical characterizations of the cathode after 10 h electrolysis (Figure 5.8) suggest there is no catalyst phase transition during the electrolysis, and the C_{dl} still remained at 26.83 mF cm^{-2}, indicating the cathode is chemically stable at the cell voltage of 2.12 V. At 2.23 V, the current density dropped from 110 to 84 mA cm^{-2}, and the $FE_{formate}$ dropped from 91% to 78% (Figure 5.9). Although there is a drop in the current density, it is relatively stable compared to other full cell CO_2 electrolysis systems for formate production, particularly in retaining high Faradaic conversion efficiency. For example, Wang and co-workers tested the long-term stability of an electrolytic cell with SnO_2/CNT as the cathode and CoO_x/CNT as the anode at a constant voltage of 2.3 V in KOH electrolyte.[169] The current density dropped from about 50 mA cm^{-2} to 40 mA cm^{-2} and the $FE_{formate}$ dropped from >80 % to ~ 65 % in 10 h. Park et al tested the stability of full cell using Sn NP-based cathode and Pt anode in 1 M KOH. The current density keeps at about 34 mA cm^{-2}, but the $FE_{formate}$ dropped from about 70 % to 60 % in 10 h.

Electrolyte effects also plays an important role in full cell electrolysis performance. Irabien and coworkers used the 0.5 M KCl+0.45 M $KHCO_3$ electrolyte, with an Ir-based anode coupled to a Sn plate cathode.[170] The current density and $FE_{formate}$ only reached 12.25 mA cm^{-2} and 71.4% at 2.79 V. Valdez et al employed a Pb-based cathode and a Pt black anode to perform a full cell test in 1 M $NaHCO_3$ electrolyte, achieving low current density of 10 mA cm^{-2} at 2.7 V.[171] In comparison, the use of the alkaline electrolyte helps improve current density and formate efficiency.[169, 316-317] For example, Wang et al employed 1 M KOH with a SnO_2/CNT cathode and a CoO_x/CNT anode for the full cell test, and obtained a high current density of 200 mA cm^{-2} at 2.9

V.[169] Therefore, the formate production process is more favourable in alkaline compared to the use of a bicarbonate-based near neutral electrolyte.

The high $FE_{formate}$ can be attributed to the active Bi CO_2RR catalyst, facilitated by a highly conductive KOH electrolyte. This in combination with the flow cell configuration, as well as the active OER NiFe LDH anodic catalyst, ensured the high current densities were achieved at relatively low cell voltages. To understand voltage-current performance of the full cell system (Figure 5.7b), we combined the LSV curves from individual anodic (Figure 5.3a) and cathodic (Figure 5.6a) half-cell studies in a single plot, as shown in Figure 5.7e. This facilitates the calculation of the cell voltage required to achieve the corresponding current density in a full cell. We determined the cathodic and anodic voltages that achieved the same cathodic and anodic current densities (but with different polarity) respectively, based on the experimentally obtained current density, at a specific applied voltage shown in Figure 5.7b. The corresponding potentials are defined as E^c and E^a, shown in Table 5.2. The potential differences between E^c and E^a determined and calculated from two half-cells are stated in Figure 5.7e, exhibiting comparable value to the experimentally applied voltages (Figure 5.7b), as plotted in Figure 5.10. The reversible cell voltage (E^o_{cell} = 1.34 V) is largely attributed to anodic water oxidation reaction (E^a_{eq} = 1.23 V vs. RHE), in compare to CO_2 to formate reduction reaction (E^c_{eq} = 0.12 V vs. RHE). The corresponding E^c, E^a, η_c, and η_a at each current density were calculated and listed in Table 5.2. The relatively low overpotentials from highly active NiFe OER and Ni NPs CO_2RR catalysts resulted in favorable operating cell voltages. This result represents among the best performing formate conversion CO_2 electrolyser employing non-precious metal catalysts inclusive of a nanostructured Bi-cathode.

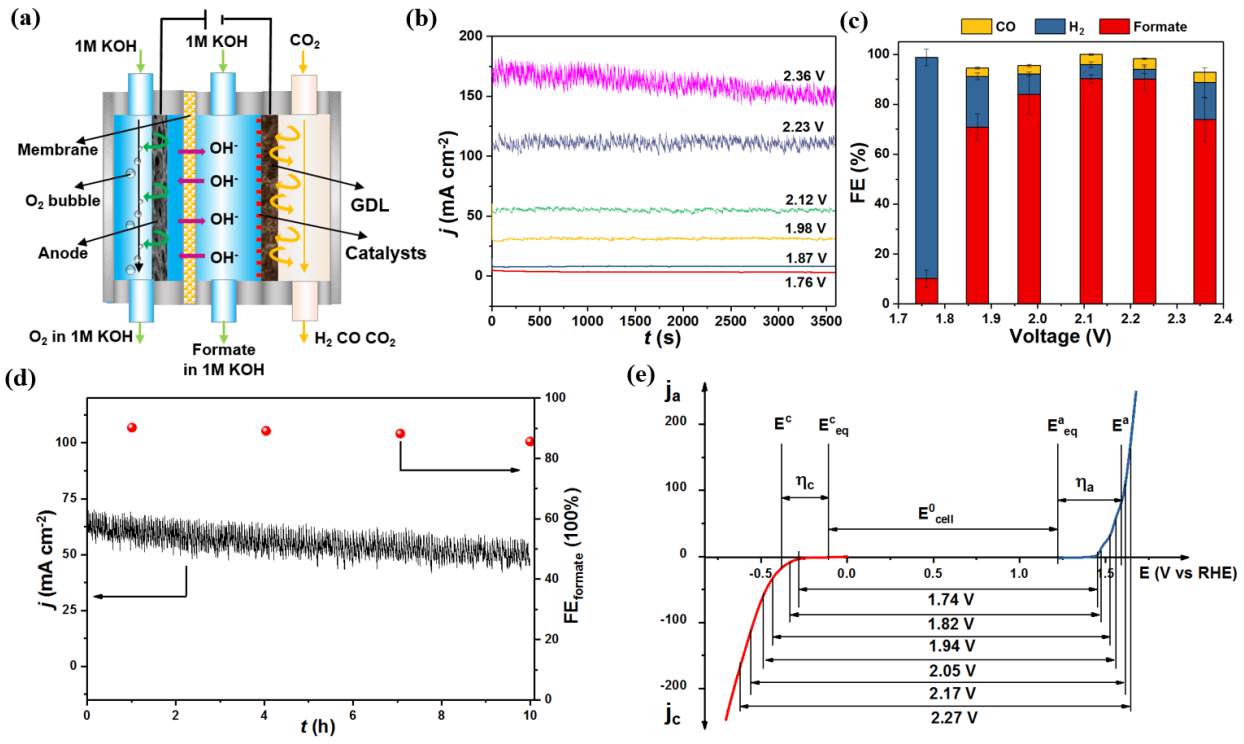

Figure 5.7 Full cell schematic and performance. (a) Schematic of the full cell. The i-t curves (b) of full-cell test consists of Bi NPs/GDL and the NiFe LDH/Ni foam performed at different cell voltages in 1.0 M KOH, and the corresponding Faradaic efficiencies of CO, H_2 and formate (c) at different cell voltages. (d) Long term stability test for 10 h operation in full cell at 2.12 V in 1.0 M KOH. (e) The plot of combined LSVs at half cathodic (red curve) and anodic (blue curve) compartments.

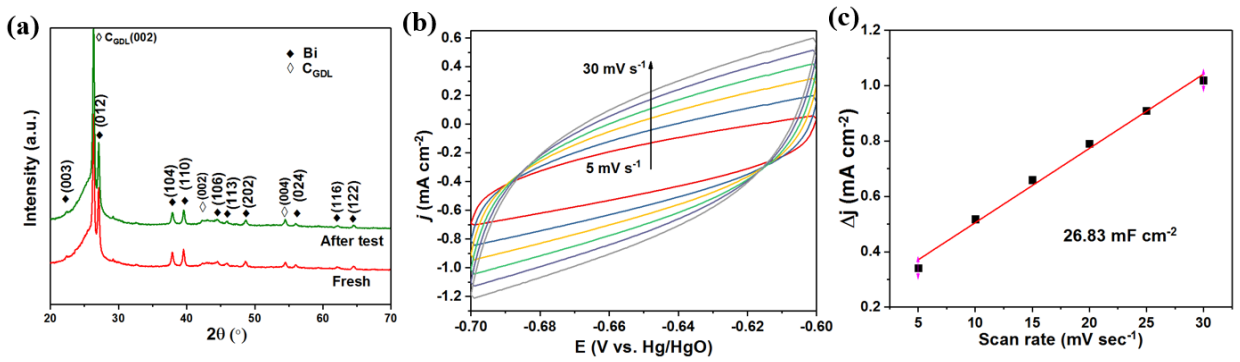

Figure 5.8 Characterization of Bi NPs/GDL after long term stability test. (a) XRD patterns of the fresh Bi NPs/GDL and that after long term full cell stability test at 2.12 V (10 h), (b) CV curves obtained in 1 M KOH at various scan rates for ECSA calculation of the Bi NPs/GDL after long term stability test at 2.12 V. (c) Plot of the Δj vs. scan rate derived from CV curves in (b).

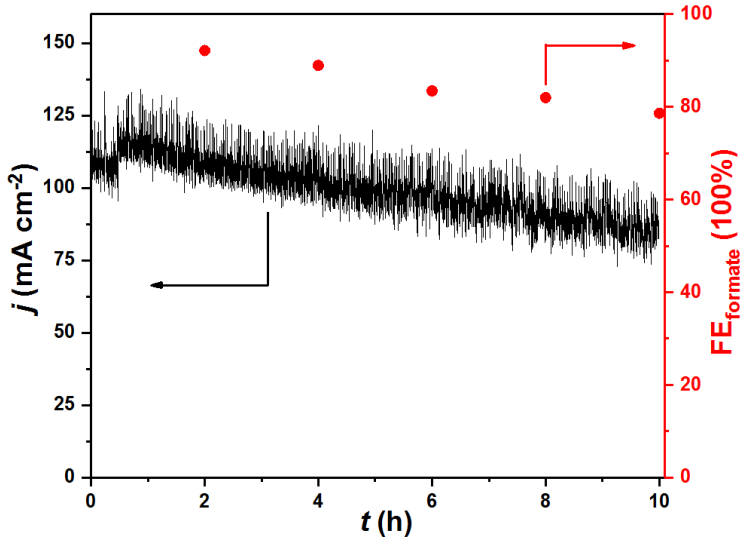

Figure 5.9 Long term stability test for 10 h electrolysis performed at 2.23 V in 1.0 M KOH, based on full cell consisted of a NiFe LDH/Ni foam anode and a Bi-NPs cathode.

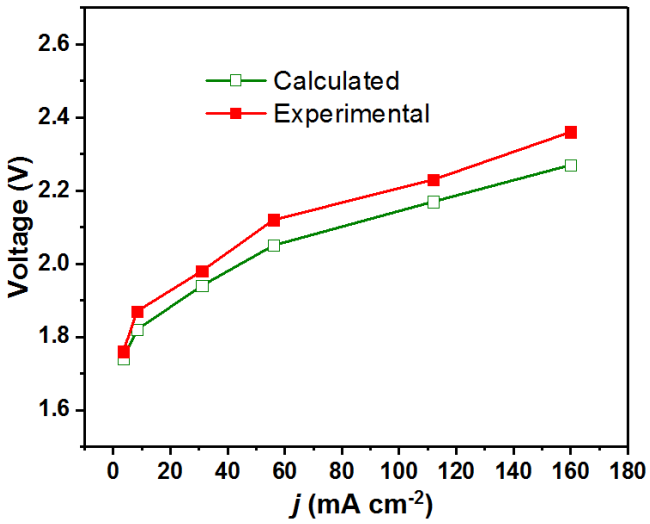

Figure 5.10 The plot of full-cell voltages applied experimentally in comparison to that calculated from half-cell studies as a function of current density.

Table 5.1 Summary of electrochemical CO_2 reduction to formate performance in full cells.

Cathode	Anode	Cell type	Electrolyte	$FE_{formate}$	*j* (mA cm^{-2})	Ref.
Bi nanoparticles-C	Ir-MMO (mixed metal oxide) on platinum	Flow-cell	0.5 M KCl + 0.45 M $KHCO_3$	89.5% at 90 mA cm^{-2}	300 mA cm^{-2} at cell voltage of 5.4 V	[168]
Sn nanoparticles	Pt gauze	Catholyte-free flow cell	Nafion 115 membrane	93.3 % at cell voltage of 2.2 V	52.9 mA cm^{-2} at cell voltage of 2.2V	[145]
Bi derived from Bi_2O_3	IrO_2-C	Flow cell	Solid state electrolyte	97% at cell voltage of 1.51V	440 mA cm^{-2} at cell voltage of 2.19V	[153]

SnO_2/CNT	CoO_x/CNT	Micro flow cell	1 M KOH	82 % at cell voltage of 2.5 V	200 mA cm^{-2} at cell voltage of 2.9V	[169]
Sn plate	Ir-MMO (mixed metal oxide) on platinum	Flow cell	0.45 M $KHCO_3$ + 0.5 M KCl	71.4% at cell voltage of 2.79 V	12.25 mA cm^{-2} at 2.79V	[170]
Pb powder	Pt black	Alkaline polymer electrolyte membrane cell	1 M $NaHCO_3$	80% at 40 mA cm^{-2}	10 mA cm^{-2} at cell voltage of 2.2V	[171]
Sn granule cathode	316 stainless steel mesh	Flow cell	0.45 M $KHCO_3$ + 2 M KCl	91% at cell voltage of 2.7V	60 mA cm^{-2} at cell voltage of 2.7V	[172]
Bi NPs/GDL	NiFe LDH/Ni foam	Flow cell	1 M KOH	92% at cell voltage of 2.12 V	155 mA cm^{-2} at cell voltage of 2.36 V	This work

Table 5.2 Calculated E^c, E^a, η_c and η_a at each calculated cell voltage in Figure 5.7e.

Calculated cell voltage	j (mA cm^{-2})	E^c (V vs. RHE)	E^a (V vs. RHE)	η_c (V)	η_a (V)
1.74	3.5	-0.28	1.46	0.16	0.23
1.81	8.3	-0.34	1.47	0.22	0.24
1.94	31	-0.43	1.52	0.31	0.29
2.05	58	-0.48	1.57	0.36	0.34
2.17	112	-0.56	1.61	0.44	0.38

2.26	160	-0.62	1.64	0.5	0.41

5.5 Conclusions

A Bi NPs-based cathode and an earth-abundant NiFe LDH-based anode have been used to assemble a full cell system for highly efficient CO_2 electroreduction to formate. The use of Bi NPs provides a high formate Faradaic efficiency of 90 ± 2% at a relatively low cell voltage of 2.12 V. The use of a flow cell employing the highly conductive KOH electrolyte and the active NiFe LDH-based anode made it possible to achieve a high current density of 155 mA cm^{-2} at a cell voltage of 2.36 V. After 10 h electrolysis, the formate Faradaic efficiency remained above 85% at a constant cell voltage of 2.12 V. The stability of Bi NPs cathode for operation at higher current densities and voltages may be further improved by the use of binder consists of mixture of nafion and poly(tetrafluoroethylene).[318] This work demonstrated the employ of all non-precious metal-based catalysts facilitate to development of CO_2 electrolyser that exhibited high performance formate conversion efficiencies. The use of a highly conductive KOH and the flow cell configuration also contributed to this performance.

5.6 Acknowledgements

J. Z. thanks the University of Wollongong for the postgraduate scholarship. C.-Y. L acknowledged the UOW's AIIM for gold investigator funding. Funding from the Australian Research Council Centre of Excellence Scheme (CE 140100012) is gratefully acknowledged. The authors would also like to thank Australian National Fabrication Facility-Materials Node (ANFF) and UOW Electron Microscopy Centre for equipment use.

Chapter 6 Conclusions and perspective

6.1 Conclusions

This thesis aims at achieving understanding of the CO_2RR to formate reaction from the aspects of catalyst design, mass transport and electrolyte effects, to the investigation of full-cells by coupling the cathode to a suitable anode. Three types of cathodes have been designed and prepared, namely: mesoporous Pd on TiO_2 nanotube arrays, SnS nanosheets on GDE, and Bi NPs on GDE for the cathodic half-cell reaction of CO_2 reduction to formate. Two types of anodes were synthesised: ultrathin amorphous iron oxyhydroxide nanosheets and NiFe layered double hydroxide on Ni foam for the anodic half-cell oxygen evolution reaction. All the prepared cathodes showed high formate selectivity at relatively low overpotentials and excellent stabilities with respect to current density and Faradaic efficiency. Systematic studies from this thesis revealed that factors such as catalyst structure, electrolyte, anode type, and cell design are all essential for CO_2RR to formate performance improvement.

A novel hierarchical structure of 3 dimensional (3D) mesoporous Pd containing structures on highly ordered 1 dimensional (1D) TiO_2 nanotubes was synthesized successfully via electrodeposition to investigate the effects of catalyst structure (Chapter 2). The results revealed that the use of nanosized Pd in the mesoporous structure promoted electrocatalysis by lowering the overpotential. Importantly, this study determined the impact of the nanotubular structure in 3 zones: (1) CO_2RR dominated, (2) CO_2RR and hydrogen evolution reaction (HER) mixed region, and (3) HER & non-active regions. In the non-active region, limited proton and CO_2 accessibility resulted in negligible CO_2RR and HER reactions. This implies that

differences in the mass transfer properties of reactants, CO_2 and proton, can result in tunable formate selectivity by simply varying the length of the TiO_2 nanotubes. Since hierarchical features are one of the most investigated strategies for a wide-range of catalytic reactions, this finding has far-reaching impact by offering key insights toward designing catalytic-support interfaces to achieve efficient electrocatalytic conversion.

In Chapter 3, SnS nanosheet catalysts prepared by the solvent thermal method were spray-coated on gas diffusion electrodes, and operated in a flow-cell system employing KOH electrolyte. CO_2 reduction to formate could be achieved at high current densities of > 100 mA cm^{-2}, and Faradaic efficiencies of over 70% over -0.5 to -1.5 V (max at ~ 88%) were obtained. The attractive unique feature of a wide electrochemical potential window coupled with high densities was achieved. The alkaline electrolyte suppresses hydrogen evolution over the applied potential range, which is particularly dominant at the less negative potential. In addition, CO evolution was suppressed at a more negative potential, resulting in a broad operating potential window for formate production. The flow-cell design also offers prospects for translation to commercially-relevant high current density electrolysis with optimised reactant and product mass transfers at the tri-phasic solid/liquid/gas interfaces.

To develop a high performance anodic catalyst, ultrathin amorphous iron oxyhydroxide nanosheets were prepared using cyclic voltammetry (CV) to condition thermally pretreated iron foils. The optimized conditions to form amorphous ultrathin iron oxyhydroxide nanosheets for oxygen evolution were 9 CV cycles over the potential range of -1.5 V to 0 V vs Ag/AgCl in 1 M KOH. The electrodeposition of Ni species onto nanosheets resulted in a lower onset potential and higher current density, demonstrating

that designing 2D nanostructured electrocatalyst is a feasible strategy for oxygen evolution reaction at the anode.

Finally, a highly active Bi NP-based cathode and earth-abundant NiFe LDH-based anode were successfully assembled in a two-electrode flow-cell electrolyser system. The rate determining step of CO_2RR to formate was found to be the one-electron transfer step to form the *OCHO intermediates, in accordance to the Tafel slope of 127.6 eV dec^{-1}. Faradaic efficiency of formate ($FE_{formate}$) reached 90 ± 2 % at the cell voltage of 2.12 V, and a maximum current density of 155 mA cm^{-2} was achieved at the cell voltage of 2.36 V. The low overpotentials from anodic and cathodic catalysts, the flow cell configuration, as well as the highly ion-conductive aqueous KOH electrolyte contributed to this performance. Moreover, using a full cell system, the $FE_{formate}$ was maintained above 85 % over 10 h. This study demonstrated the excellent performance of an all-non-precious metal-based catalyst full-cell CO_2 electrolyser in a flow cell configuration.

6.2 Perspective and future works

This thesis addressed the issues of CO_2 electroreduction to formate with respect to development in catalysts design and synthesis; resulting in an enhanced mechanistic understanding of this reaction. Cell designs have been optimized to move toward commercial relevant full cell systems. However, there are still some challenges that need to be overcome to achieve high CO_2 electroreduction to formate performance. For example, notice has been taken of the influence of reactant mass transfer issue on the mesoPd/TiO_2 nanotube cathode (Chapter 2), however, theoretical stimulation or in-situ spectrum evidence could further illustrate such effects. The formation of bicarbonate or carbonate from the chemical reaction between KOH electrolyte and

the CO_2 gas would undermine cell long term stability. The internal resistance in the full cell should be minimized to obtain high performance. Therefore, it is proposed that further development of electrochemical CO_2RR to formate should focus on areas as discussed below.

Theoretical studies are essential to deepen the mechanistic understanding for electrochemical CO_2 reduction. This thesis experimentally investigated the influence of alkaline electrolyte on formate selectivity (Chapter 3). However, theoretical results to support the alkaline suppression of H_2 at a less negative potential and CO at a more negative potential would be beneficial. Density functional theory (DFT) calculation could be employed to not only understand the binding energies of reaction intermediates and the associated activation energies, but also reveal the effects of electrolytes and the applied potentials.[319-321] Predictions on reaction pathways, the rate determining steps, and key parameters such as overpotential and selectivity could be made. This would help to establish relationship between the electrolyte pH and the reaction pathways, and propose a plausible alkaline enhancement mechanism.

Another research challenge is to build a suitable model for the study of mass transfer influence on one-dimensional materials, as touched on in Chapter 2. Although it was observed that the mass transfer from the mesoporous Pd loaded one-dimensional TiO_2 nanotube cathodes could be tuned by varying the length of the tubes, theoretical stimulations of the surface CO_2 concentration and the interfacial pH during electrocatalysis would assist in understanding the relationship between the tube length and the reactant/product mass transport. For example, Smith et al simulated the surface CO_2 concentration and the Cu cathode surface pH as a function of buffer electrolyte concentration and current density based on the Nernst−Planck equation.[186] Their computational

data greatly assisted in evaluating the mass transfer effects that have significant impacts on the catalysts' performance such as selectivity and faradaic conversion efficiency.

In-situ/operando measurements have been widely applied to track the changes in catalyst structure, electronic states, chemical states, surface species, and the spin states with temporal resolution. These advancements enable the real-time illustration of the structural reconstruction of catalysts, and identify the surface adsorbed intermediates, which assist in proposing the mechanistic pathways. For example, in-situ optical techniques such as Fourier-transform infrared spectroscopy (FTIR), Raman and UV-Vis could detect the species adsorbed at the catalysts surface, and identify the intermediates during CO_2RR.[322] Recently, in-situ surface enhanced infrared absorption spectroscopy (SEIRAS) has been used for the near-surface concentration gradients of reactants, such as CO_2 and protons during electrolysis in neutral pH electrolytes.[323-324] If this technique can be applied to study the mesoporous Pd-TiO_2 system, more evidence on the reactant/product mass transport could be revealed. Other useful techniques, including in-situ X-ray diffraction (XRD) in identifying the crystal structure changes, X-ray absorption spectroscopy (XAS) to provide atomic-level electronic states and coordination environments, and [324] in-situ High-resolution transmission electron microscopy (HRTEM) to monitor the morphology change and the phase transformation at the atomic scale could be applied. The above techniques could be applied in investigating the SnS nanosheets and the Bi nanoparticles, to provide direct information about the catalyst stability with respect to the electronic state, and structure during prolonged electrolysis.

Thirdly, the stability of the cathode is crucial to improve the long term electrolysis performance, as most of the stability tests at present are performed for a rather short period (eg.

less than 100 h). Catalyst decomposition in the electrolyte, and detachment from the support under applied voltages could be the reason for the decrease of $j_{formate}$ and $FE_{formate}$ during electrolysis. The properties of GDL surface, such as hydrophilic/hydrophobic is important for flow cells, as an hydrophilic surface at the catalyst layer improves electrolyte interface contact, and the CO_2 gas prefers an hydrophobic surface as optimal channels to introduce and dissipate gas which prevent electrolyte flooding. Therefore, a GDL with suitable hydrophilic/ hydrophobic properties is necessary in flow cells to achieve excellent long-term stability. Burdyny et al reported that flooding was induced by the applied high potential needed to drive the CO_2RR, and has promoted the HER and accelerated the wetting of initially hydrophobic GDL.[325] Therefore, in addition to improving catalyst activity, modifying GDL configurations by stabilizing the hydrophobic surface is essential for cathode improvement.

In Chapter 3, alkaline KOH electrolyte was found to improve the formate selectivity, and enhanced the electrolysis current density. However, the reactions between CO_2 and the alkaline KOH electrolyte forming carbonate or bicarbonate resulted in a drop in pH, thus affecting the stability with respect to the current density and the formate Faradaic efficiency. One of the strategies to mitigate this issue is by using acidic electrolytes. Recently, Li and coworkers conducted CO_2 electrolysis on copper catalyst in a strong acid electrolyte. They performed electrolysis in 1 M H_3PO_4 + 3 M KCl electrolyte, and achieved high current density (1.2 A cm^{-2}) with faradaic efficiency of 50 % for CO_2 conversion to multi-carbon products (ethylene, ethanol, and 1-propanol) using a Cu catalyst.[326] Hence the use of acidic electrolyte may also be a strategy worth considering for CO_2 to formate conversion. However, it should be noted that the selected formate producing catalysts should be highly stable in acidic media, which remains a challenge.

Last but not the least, a proper reactor design is required for high performance electrochemical CO_2 reduction to formate. The work in this thesis employed a flow cell to enhance mass transports of reactant and product, hence achieving high current densities and high formate selectivities at low overpotentials. In addition to a highly active cathode, an efficient anode is essential to lower the overall cell voltage when assembled in a full cell. In Chapter 5, NiFe layered double hydroxide was employed as a low-cost catalyst for OER. However, the overpotential of NiFe LDH, which is operated in alkaline electrolyte, could be further improved by structural and electronic modifications. If an acidic electrolyte is employed, expensive noble metal-based catalysts such as Ir, Ru, and Pt maybe more suitable as OER catalysts. Therefore, more active and stable low cost OER catalysts should be developed and examined to lower the cell voltage in their designated type of electrolytes.

The ion-exchange membrane should also be optimized to lower the internal cell resistance. To obtain highly conductive membranes, the fraction of ion-exchange resin must be in excess of 50-70 wt. %.[327-329] However, this high ion-exchange resin fraction may lead to high swelling and poor mechanical stability. Therefore, the newly developed membranes should not only possess properties such as high transport number of counter-ions, low diffusion coefficient of salt, high selective permeability for specific ions, but also mechanical and chemical stability. The studies in this thesis work show that the employment of highly conductive KOH electrolyte (Chapters 4 and 5) successfully reduced the cell ohmic resistance. Reducing the spacing between membrane and the electrodes could further minimize the cell resistance, hence improving the electrolyser performance.

References

[1] J. Artz, T. E. Müller, K. Thenert, J. Kleinekorte, R. Meys, A. Sternberg, A. Bardow, W. Leitner, *Chem. Rev.* **2018**, *118*, 434.

[2] Q.-W. Song, Z.-H. Zhou, L.-N. He, *Green Chem.* **2017**, *19*, 3707.

[3] G. Fiorani, W. Guo, A. W. Kleij, *Green Chem.* **2015**, *17*, 1375.

[4] J. Song, J. Liu, W. Zhao, Y. Chen, H. Xiao, X. Shi, Y. Liu, X. Chen, *Ind. Eng. Chem. Res.* **2018**, *57*, 4941.

[5] J. N. Gonzales, M. M. Matson, S. Atsumi, *Biochemistry* **2018**, *58*, 1470.

[6] J. Jin, J. Yu, D. Guo, C. Cui, W. Ho, *Small* **2015**, *11*, 5262.

[7] B. Tahir, M. Tahir, N. A. S. Amin, *Appl. Surf. Sci.* **2017**, *419*, 875.

[8] W.-H. Wang, Y. Himeda, J. T. Muckerman, G. F. Manbeck, E. Fujita, *Chem. Rev.* **2015**, *115*, 12936.

[9] I. Ledezma-Yanez, E. P. Gallent, M. T. M. Koper, F. Calle-Vallejo, *Catal. Today* **2016**, *262*, 90.

[10] J.-H. Kim, D. H. Youn, *Chem. Phys. Lett.* **2018**, *704*, 27.

[11] H.-K. Lim, H. Kim, *Molecules* **2017**, *22*, 536.

[12] R. R. Bhosale, *Greenh. Gases* **2020**, *10*, 703.

[13] J. Huang, Y. Fu, Y. Zhao, J. Zhang, S. Li, S. Li, G. Li, Z. Chen, Y. Sun, *Chem. Eng. J.* **2021**, *404*, 127067.

[14] S. Xu, E. A. Carter, *Chem. Rev.* **2018**, *119*, 6631.

[15] Z. Ni, H. Liang, Z. Yi, R. Guo, C. Liu, Y. Liu, H. Sun, X. Liu, *Coordin. Chem. Rev.* **2021**, *441*, 213983.

[16] J. Qiao, Y. Liu, F. Hong, J. Zhang, *Chem. Soc. Rev.* **2014**, *43*, 631.

[17] C. S. Le Duff, M. J. Lawrence, P. Rodriguez, *Angew. Chem.* **2017**, *129*, 13099.

[18] A. Vasileff, C. Xu, Y. Jiao, Y. Zheng, S.-Z. Qiao, *Chem* **2018**, *4*, 1809.

[19] Y. Wu, Z. Jiang, X. Lu, Y. Liang, H. Wang, *Nature* **2019**, *575*, 639.

[20] https://www.mordorintelligence.com/industry-reports/formic-acid-market.

[21] S. C. Ricke, D. K. Dittoe, K. E. Richardson, *Front. Vet. Sci.* **2020**, *7*.

[22] D. Luise, F. Correa, P. Bosi, P. Trevisi, *Animals* **2020**, *10*, 887.

[23] J. Ross, *Appl. Catal.* **1986**, *27*, 403.

[24] J. S. Yoo, R. Christensen, T. Vegge, J. K. Nørskov, F. Studt, *ChemSusChem* **2016**, *9*, 358.

[25] Z. Ma, U. Legrand, E. Pahija, J. R. Tavares, D. C. Boffito, *Ind. Eng. Chem. Res.* **2020**.

[26] Y. Zhou, X. Zhu, B. Zhang, D.-D. Ye, R. Chen, Q. Liao, *Int. J. Hydrogen Energy* **2020**, *45*, 29235.

[27] N. Han, P. Ding, L. He, Y. Li, Y. Li, *Adv. Energy Mater.* **2019**, 1902338.

[28] T.-C. Chou, C.-C. Chang, H.-L. Yu, W.-Y. Yu, C.-L. Dong, J.-J. s. Velasco-Vélez, C.-H. Chuang, L.-C. Chen, J.-F. Lee, J.-M. Chen, *J. Am. Chem. Soc.* **2020**, *142*, 2857.

[29] Z. Chen, M.-R. Gao, N. Duan, J. Zhang, Y.-Q. Zhang, T. Fan, J. Zhang, Y. Dong, J. Li, Q. Liu, *Appl. Catal. B: Environ.* **2020**, *277*, 119252.

[30] J. T. Feaster, C. Shi, E. R. Cave, T. Hatsukade, D. N. Abram, K. P. Kuhl, C. Hahn, J. K. Nørskov, T. F. Jaramillo, *ACS Catal.* **2017**, *7*, 4822.

[31] S. Zhao, S. Li, T. Guo, S. Zhang, J. Wang, Y. Wu, Y. Chen, *Nano-Micro Lett.* **2019**, *11*, 62.

[32] M. F. Baruch, J. E. Pander III, J. L. White, A. B. Bocarsly, *ACS Catal.* **2015**, *5*, 3148.

[33] J. E. Pander III, M. F. Baruch, A. B. Bocarsly, *ACS Catal.* **2016**, *6*, 7824.

[34] J. L. White, A. B. Bocarsly, *J. Electrochem. Soc.* **2016**, *163*, H410.

[35] Z. M. Detweiler, J. L. White, S. L. Bernasek, A. B. Bocarsly, *Langmuir* **2014**, *30*, 7593.

[36] R. Kortlever, J. Shen, K. J. P. Schouten, F. Calle-Vallejo, M. T. Koper, *J. Phys. Chem. Lett.* **2015**, *6*, 4073.

[37] Z. Sun, T. Ma, H. Tao, Q. Fan, B. Han, *Chem* **2017**, *3*, 560.

[38] X. Zhang, S.-X. Guo, K. A. Gandionco, A. M. Bond, J. Zhang, *Mater. Today Adv.* **2020**, *7*, 100074.

[39] L.-X. Liu, Y. Zhou, Y.-C. Chang, J.-R. Zhang, L.-P. Jiang, W. Zhu, Y. Lin, *Nano Energy* **2020**, *77*, 105296.

[40] Z. Chen, X. Zhang, M. Jiao, K. Mou, X. Zhang, L. Liu, *Adv. Energy Mater.* **2020**, *10*, 1903664.

[41] X. Li, W. Bi, M. Chen, Y. Sun, H. Ju, W. Yan, J. Zhu, X. Wu, W. Chu, C. Wu, *J. Am. Chem. Soc.* **2017**, *139*, 14889.

[42] C. Zhang, S. Yang, J. Wu, M. Liu, S. Yazdi, M. Ren, J. Sha, J. Zhong, K. Nie, A. S. Jalilov, *Adv. Energy Mater.* **2018**, *8*, 1703487.

[43] M. Yamamoto, T. Yoshida, N. Yamamoto, H. Yoshida, S. Yagi, *e-J. Surf. Sci. Nanotechnol.* **2014**, *12*, 299.

[44] A. Bagger, W. Ju, A. S. Varela, P. Strasser, J. Rossmeisl, *ACS Catal.* **2019**, *9*, 7894.

[45] R. P. Jansonius, L. M. Reid, C. N. Virca, C. P. Berlinguette, *ACS Energy Lett.* **2019**, *4*, 980.

[46] C. W. Lee, K. D. Yang, D. H. Nam, J. H. Jang, N. H. Cho, S. W. Im, K. T. Nam, *Adv. Mater.* **2018**, *30*, 1704717.

[47] Y. Ji, J. K. Nørskov, K. Chan, *J. Phys. Chem. C* **2019**, *123*, 4256.

[48] F. Calle-Vallejo, M. T. Koper, ACS Publications, 2017.

[49] A. Seifitokaldani, C. M. Gabardo, T. Burdyny, C.-T. Dinh, J. P. Edwards, M. G. Kibria, O. S. Bushuyev, S. O. Kelley, D. Sinton, E. H. Sargent, *J. Am. Chem. Soc.* **2018**, *140*, 3833.

[50] P. Bumroongsakulsawat, G. Kelsall, *Electrochim. Acta* **2014**, *141*, 216.

[51] A. S. Malkani, J. Anibal, B. Xu, *ACS Catal.* **2020**, *10*, 14871.

[52] S. Ringe, E. L. Clark, J. Resasco, A. Walton, B. Seger, A. T. Bell, K. Chan, *Energy Environ. Sci.* **2019**, *12*, 3001.

[53] M. R. Singh, Y. Kwon, Y. Lum, J. W. Ager III, A. T. Bell, *J. Am. Chem. Soc.* **2016**, *138*, 13006.

[54] C. X. Zhao, Y. F. Bu, W. Gao, Q. Jiang, *J. Phys. Chem. C* **2017**, *121*, 19767.

[55] J. Wu, F. G. Risalvato, F.-S. Ke, P. Pellechia, X.-D. Zhou, *J. Electrochem. Soc.* **2012**, *159*, F353.

[56] Y. Hori, A. Murata, R. Takahashi, *J. Chem. Soc., Faraday Trans. 1* **1989**, *85*, 2309.

[57] Y. Yoon, A. S. Hall, Y. Surendranath, *Angew. Chem. In. Ed.* **2016**, *55*, 15282.

[58] S. Zhu, B. Jiang, W.-B. Cai, M. Shao, *J. Am. Chem. Soc.* **2017**, *139*, 15664.

[59] S. Nitopi, E. Bertheussen, S. B. Scott, X. Liu, A. K. Engstfeld, S. Horch, B. Seger, I. E. Stephens, K. Chan, C. Hahn, *Chem. Rev.* **2019**, *119*, 7610.

[60] C. M. Gabardo, A. Seifitokaldani, J. P. Edwards, C.-T. Dinh, T. Burdyny, M. G. Kibria, C. P. O'Brien, E. H. Sargent, D. Sinton, *Energy Environ. Sci.* **2018**, *11*, 2531.

[61] H.-Y. Kim, I. Choi, S. H. Ahn, S. J. Hwang, S. J. Yoo, J. Han, J. Kim, H. Park, J. H. Jang, S.-K. Kim, *Int. J. Hydrogen Energy* **2014**, *39*, 16506.

[62] D. Gao, F. Scholten, B. Roldan Cuenya, *ACS Catal.* **2017**, *7*, 5112.

[63] S. H. Yoon, G. Piao, H. Park, N. O. Elbashir, D. S. Han, *Appl. Surf. Sci.* **2020**, *532*, 147459.

[64] A. S. Varela, W. Ju, T. Reier, P. Strasser, *ACS Catal.* **2016**, *6*, 2136.

[65] J. Zou, M. Iqbal, A. Vijayakumar, C. Wang, D. R. Macfarlane, Y. Yamauchi, C.-Y. Lee, G. G. Wallace, *J. Mater. Chem. A* **2020**, *8*, 8041.

[66] X. Min, M. W. Kanan, *J. Am. Chem. Soc.* **2015**, *137*, 4701.

[67] D. Gao, H. Zhou, F. Cai, D. Wang, Y. Hu, B. Jiang, W.-B. Cai, X. Chen, R. Si, F. Yang, *Nano Research* **2017**, *10*, 2181.

[68] C. Chen, J. F. K. Kotyk, S. W. Sheehan, *Chem* **2018**, *4*, 2571.

[69] Y. i. Hori, in *Modern aspects of electrochemistry*, Springer, 2008, 89.

[70] W. Choi, Y. J. Hwang, *J. Mater. Chem. A* **2020**.

[71] J. He, X. Liu, H. Liu, Z. Zhao, Y. Ding, J. Luo, *J. Catal.* **2018**, *364*, 125.

[72] R. Daiyan, E. C. Lovell, N. M. Bedford, W. H. Saputera, K. H. Wu, S. Lim, J. Horlyck, Y. H. Ng, X. Lu, R. Amal, *Adv. Sci.* **2019**, *6*, 1900678.

[73] H. Cheng, S. Liu, J. Zhang, T. Zhou, N. Zhang, X.-s. Zheng, W. Chu, Z. Hu, C. Wu, Y. Xie, *Nano Letters* **2020**, *20*, 6097.

[74] J. Wu, Y. Xie, S. Du, Z. Ren, P. Yu, X. Wang, G. Wang, H. Fu, *Science China Materials* **2020**, *63*, 2314.

[75] J. Huang, X. Guo, Y. Wei, Q. Hu, X. Yu, L. Wang, *J. CO_2 Util.* **2019**, *33*, 166.

[76] W. Deng, L. Zhang, L. Li, S. Chen, C. Hu, Z.-J. Zhao, T. Wang, J. Gong, *J. Am. Chem. Soc.* **2019**, *141*, 2911.

[77] E. Irtem, T. Andreu, A. Parra, M. Hernández-Alonso, S. García-Rodríguez, J. Riesco-García, G. Penelas-Pérez, J. Morante, *J. Mater. Chem. A* **2016**, *4*, 13582.

[78] Y. Fu, Y. Li, X. Zhang, Y. Liu, J. Qiao, J. Zhang, D. P. Wilkinson, *Appl. Energ.* **2016**, *175*, 536.

[79] C. Liang, B. Kim, S. Yang, Y. Liu, C. F. Woellner, Z. Li, R. Vajtai, W. Yang, J. Wu, P. J. Kenis, *J. Mater. Chem. A* **2018**, *6*, 10313.

[80] K. Bejtka, J. Zeng, A. Sacco, M. Castellino, S. Hernández, M. A. Farkhondehfal, U. Savino, S. Ansaloni, C. F. Pirri, A. Chiodoni, *ACS Appl. Energ. Mater.* **2019**, *2*, 3081.

[81] F. Li, L. Chen, M. Xue, T. Williams, Y. Zhang, D. R. MacFarlane, J. Zhang, *Nano Energy* **2017**, *31*, 270.

[82] F. Li, L. Chen, G. P. Knowles, D. R. MacFarlane, J. Zhang, *Angew. Chem. In. Ed.* **2017**, *56*, 505.

[83] W. Luc, C. Collins, S. Wang, H. Xin, K. He, Y. Kang, F. Jiao, *J. Am. Chem. Soc.* **2017**, *139*, 1885.

[84] K. Ye, Z. Zhou, J. Shao, L. Lin, D. Gao, N. Ta, R. Si, G. Wang, X. Bao, *Angew. Chem. In. Ed.* **2020**, *59*, 4814.

[85] X. Zheng, P. De Luna, F. P. G. de Arquer, B. Zhang, N. Becknell, M. B. Ross, Y. Li, M. N. Banis, Y. Li, M. Liu, *Joule* **2017**, *1*, 794.

[86] G. Wen, D. U. Lee, B. Ren, F. M. Hassan, G. Jiang, Z. P. Cano, J. Gostick, E. Croiset, Z. Bai, L. Yang, *Adv. Energy Mater.* **2018**, *8*, 1802427.

[87] H. Yang, N. Han, J. Deng, J. Wu, Y. Wang, Y. Hu, P. Ding, Y. Li, Y. Li, J. Lu, *Adv. Energy Mater.* **2018**, *8*, 1801536.

[88] P. Lamagni, M. Miola, J. Catalano, M. S. Hvid, M. A. H. Mamakhel, M. Christensen, M. R. Madsen, H. S. Jeppesen, X. M. Hu, K. Daasbjerg, *Adv. Funct. Mater.* **2020**, *30*, 1910408.

[89] T. Yuan, Z. Hu, Y. Zhao, J. Fang, J. Lv, Q. Zhang, Z. Zhuang, L. Gu, S. Hu, *Nano Letters* **2020**, *20*, 2916.

[90] Y. X. Duan, K. H. Liu, Q. Zhang, J. M. Yan, Q. Jiang, *Small Methods* **2020**, *4*, 1900846.

[91] K. Fan, Y. Jia, Y. Ji, P. Kuang, B. Zhu, X. Liu, J. Yu, *ACS Catal.* **2019**, *10*, 358.

[92] X.-H. Zhao, Q.-S. Chen, D.-H. Zhuo, J. Lu, Z.-N. Xu, C.-M. Wang, J.-X. Tang, S.-G. Sun, G.-C. Guo, *Electrochim. Acta* **2021**, *367*, 137478.

[93] Q. Li, X. Zhang, X. Zhou, Q. Li, H. Wang, J. Yi, Y. Liu, J. Zhang, *J. CO_2 Util.* **2020**, *37*, 106.

[94] W. Zhang, Y. Hu, L. Ma, G. Zhu, P. Zhao, X. Xue, R. Chen, S. Yang, J. Ma, J. Liu, *Nano energy* **2018**, *53*, 808.

[95] Q. Yang, Q. Wu, Y. Liu, S. Luo, X. Wu, X. Zhao, H. Zou, B. Long, W. Chen, Y. Liao, *Adv. Mater.* **2020**, *32*, 2002822.

[96] J. H. Koh, D. H. Won, T. Eom, N.-K. Kim, K. D. Jung, H. Kim, Y. J. Hwang, B. K. Min, *ACS Catal.* **2017**, *7*, 5071.

[97] J. Bei, R. Zhang, Z. Chen, W. Lv, W. Wang, *Int. J. Electrochem. Sci* **2017**, *12*, 2365.

[98] L. Li, D.-K. Ma, F. Qi, W. Chen, S. Huang, *Electrochim. Acta* **2019**, *298*, 580.

[99] M. Zhao, Y. Gu, W. Gao, P. Cui, H. Tang, X. Wei, H. Zhu, G. Li, S. Yan, X. Zhang, *Appl. Catal. B: Environ.* **2020**, *266*, 118625.

[100] X. Yang, Y. Chen, L. Qin, X. Wu, Y. Wu, T. Yan, Z. Geng, J. Zeng, *ChemSusChem* **2020**, *13*, 6307.

[101] C. Cao, D. D. Ma, J. F. Gu, X. Xie, G. Zeng, X. Li, S. G. Han, Q. L. Zhu, X. T. Wu, Q. Xu, *Angew. Chem.* **2020**, *132*, 15124.

[102] M. Fan, S. Prabhudev, S. Garbarino, J. Qiao, G. A. Botton, D. A. Harrington, A. C. Tavares, D. Guay, *Appl. Catal. B: Environ.* **2020**, 119031.

[103] B. Bohlen, D. Wastl, J. Radomski, V. Sieber, L. Vieira, *Electrochem. Commun.* **2020**, *110*, 106597.

[104] Z. B. Hoffman, T. S. Gray, K. B. Moraveck, T. B. Gunnoe, G. Zangari, *ACS Catal.* **2017**, *7*, 5381.

[105] W. Ma, S. Xie, X.-G. Zhang, F. Sun, J. Kang, Z. Jiang, Q. Zhang, D.-Y. Wu, Y. Wang, *Nat. Commun.* **2019**, *10*, 1.

[106] S.-Z. Hou, X.-D. Zhang, W.-W. Yuan, Y.-X. Li, Z.-Y. Gu, *Inorg. Chem.* **2020**, *59*, 11298.

[107] Z. Zhang, F. Ahmad, W. Zhao, W. Yan, W. Zhang, H. Huang, C. Ma, J. Zeng, *Nano letters* **2019**, *19*, 4029.

[108] W. Luo, W. Xie, M. Li, J. Zhang, A. Züttel, *J. Mater. Chem. A* **2019**, *7*, 4505.

[109] W. Yang, Y. Zhao, S. Chen, W. Ren, X. Chen, C. Jia, Z. Su, Y. Wang, C. Zhao, *Inorg. Chem.* **2020**, *59*, 12437.

[110] S. Rasul, A. Pugnant, H. Xiang, J.-M. Fontmorin, H. Y. Eileen, *J. CO_2 Util.* **2019**, *32*, 1.

[111] J. E. Pander, J. W. J. Lum, B. S. Yeo, *J. Mater. Chem. A* **2019**, *7*, 4093.

[112] N. Zouaoui, B. D. Ossonon, M. Fan, D. Mayilukila, S. Garbarino, G. de Silveira, G. A. Botton, D. Guay, A. C. Tavares, *J. Mater. Chem. A* **2019**, *7*, 11272.

[113] F. Li, M. Xue, J. Li, X. Ma, L. Chen, X. Zhang, D. R. MacFarlane, J. Zhang, *Angew. Chem.* **2017**, *129*, 14910.

[114] J. Huang, X. Guo, X. Huang, L. Wang, *Electrochim. Acta* **2019**, *325*, 134923.

[115] Y. Zhou, R. Zhou, X. Zhu, N. Han, B. Song, T. Liu, G. Hu, Y. Li, J. Lu, Y. Li, *Adv. Mater.* **2020**, *32*, 2000992.

[116] T. Gunji, H. Ochiai, T. Ohira, Y. Liu, Y. Nakajima, F. Matsumoto, *Chem. Mater.* **2020**, *32*, 6855.

[117] Z. Tao, Z. Wu, Y. Wu, H. Wang, *ACS Catal.* **2020**, *10*, 9271.

[118] S. Shen, J. He, X. Peng, W. Xi, L. Zhang, D. Xi, L. Wang, X. Liu, J. Luo, *J. Mater. Chem. A* **2018**, *6*, 18960.

[119] S. Gao, Y. Lin, X. Jiao, Y. Sun, Q. Luo, W. Zhang, D. Li, J. Yang, Y. Xie, *Nature* **2016**, *529*, 68.

[120] X. Bai, W. Chen, C. Zhao, S. Li, Y. Song, R. Ge, W. Wei, Y. Sun, *Angew. Chem.* **2017**, *129*, 12387.

[121] S. Gao, X. Jiao, Z. Sun, W. Zhang, Y. Sun, C. Wang, Q. Hu, X. Zu, F. Yang, S. Yang, *Angew. Chem. In. Ed.* **2016**, *55*, 698.

[122] Z. Yang, F. E. Oropeza, K. H. Zhang, *APL Mater.* **2020**, *8*, 060901.

[123] Y. Hori, H. Wakebe, T. Tsukamoto, O. Koga, *Electrochim. Acta* **1994**, *39*, 1833.

[124] X. Li, S. Dou, J. Wang, X. Wang, *Chem.– Asian J.* **2020**, *15*, 1558.

[125] S. Komatsu, T. Yanagihara, Y. Hiraga, M. Tanaka, A. Kunugi, *Denki Kagaku oyobi Kogyo Butsuri Kagaku* **1995**, *63*, 217.

[126] F. P. García de Arquer, O. S. Bushuyev, P. De Luna, C. T. Dinh, A. Seifitokaldani, M. I. Saidaminov, C. S. Tan, L. N. Quan, A. Proppe, M. G. Kibria, *Adv. Mater.* **2018**, *30*, 1802858.

[127] N. Han, Y. Wang, H. Yang, J. Deng, J. Wu, Y. Li, Y. Li, *Nat. Commun.* **2018**, *9*, 1.

[128] H. Shang, T. Wang, J. Pei, Z. Jiang, D. Zhou, Y. Wang, H. Li, J. Dong, Z. Zhuang, W. Chen, *Angew. Chem. In. Ed.* **2020**, *59*, 22465.

[129] V. S. S. Mosali, X. Zhang, Y. Zhang, T. Gengenbach, S.-X. Guo, G. Puxty, M. D. Horne, A. M. Bond, J. Zhang, *ACS Sustain. Chem. Eng.* **2019**, *7*, 19453.

[130] A. Klinkova, P. De Luna, C.-T. Dinh, O. Voznyy, E. M. Larin, E. Kumacheva, E. H. Sargent, *ACS Catal.* **2016**, *6*, 8115.

[131] D. Wu, X. Wang, X.-Z. Fu, J.-L. Luo, *Appl. Catal. B: Environ.*, *284*, 119723.

[132] M. Rahaman, A. Dutta, P. Broekmann, *ChemSusChem* **2017**, *10*, 1733.

[133] H. Chen, J. Chen, J. Si, Y. Hou, Q. Zheng, B. Yang, Z. Li, L. Gao, L. Lei, Z. Wen, *Chem. Sci.* **2020**, *11*, 3952.

[134] B. Kumar, V. Atla, J. P. Brian, S. Kumari, T. Q. Nguyen, M. Sunkara, J. M. Spurgeon, *Angew. Chem. In. Ed.* **2017**, *56*, 3645.

[135] A. Zhang, R. He, H. Li, Y. Chen, T. Kong, K. Li, H. Ju, J. Zhu, W. Zhu, J. Zeng, *Angew. Chem.* **2018**, *130*, 11120.

[136] J. Wu, F. G. Risalvato, S. Ma, X.-D. Zhou, *J. Mater. Chem. A* **2014**, *2*, 1647.

[137] Y. Zhao, J. Liang, C. Wang, J. Ma, G. G. Wallace, *Adv. Energy Mater.* **2018**, *8*, 1702524.

[138] X. Zu, X. Li, W. Liu, Y. Sun, J. Xu, T. Yao, W. Yan, S. Gao, C. Wang, S. Wei, *Adv. Mater.* **2019**, *31*, 1808135.

[139] E. Zhang, T. Wang, K. Yu, J. Liu, W. Chen, A. Li, H. Rong, R. Lin, S. Ji, X. Zheng, *J. Am. Chem. Soc.* **2019**, *141*, 16569.

[140] D. M. Weekes, D. A. Salvatore, A. Reyes, A. Huang, C. P. Berlinguette, *Accounts Chem. Res.* **2018**, *51*, 910.

[141] S. Garg, M. Li, A. Z. Weber, L. Ge, L. Li, V. Rudolph, G. Wang, T. E. Rufford, *J. Mater. Chem. A* **2020**, *8*, 1511.

[142] C. Hu, L. Zhang, J. Gong, *Energy Environ. Sci.* **2019**, *12*, 2620.

[143] R. Subbaraman, D. Tripkovic, D. Strmcnik, K.-C. Chang, M. Uchimura, A. P. Paulikas, V. Stamenkovic, N. M. Markovic, *Science* **2011**, *334*, 1256.

[144] P. Deng, F. Yang, Z. Wang, S. Chen, Y. Zhou, S. Zaman, B. Y. Xia, *Angew. Chem. In. Ed.* **2020**, *59*, 10807.

[145] W. Lee, Y. E. Kim, M. H. Youn, S. K. Jeong, K. T. Park, *Angew. Chem. In. Ed.* **2018**, *57*, 6883.

[146] C. Xia, P. Zhu, Q. Jiang, Y. Pan, W. Liang, E. Stavitski, H. N. Alshareef, H. Wang, *Nat. Energy* **2019**, *4*, 776.

[147] O. G. Sánchez, Y. Y. Birdja, M. Bulut, J. Vaes, T. Breugelmans, D. Pant, *Curr. Opin. Green Sustain. Chem.* **2019**, *16*, 47.

[148] J. Li, J. Jiao, H. Zhang, P. Zhu, H. Ma, C. Chen, H. Xiao, Q. Lu, *ACS Sustain. Chem. Eng.* **2020**, *8*, 4975.

[149] D. T. Whipple, E. C. Finke, P. J. Kenis, *Electrochem. Solid-State Lett.* **2010**, *13*, B109.

[150] Y. Qian, Y. Liu, H. Tang, B.-L. Lin, *J. CO_2 Util.* **2020**, *42*, 101287.

[151] S. Sen, S. M. Brown, M. Leonard, F. R. Brushett, *J. Appl. Electrochem.* **2019**, *49*, 917.

[152] Q. Gong, P. Ding, M. Xu, X. Zhu, M. Wang, J. Deng, Q. Ma, N. Han, Y. Zhu, J. Lu, *Nat. Commun.* **2019**, *10*, 1.

[153] L. Fan, C. Xia, P. Zhu, Y. Lu, H. Wang, *Nat. Commun.* **2020**, *11*, 1.

[154] K. Subramanian, K. Asokan, D. Jeevarathinam, M. Chandrasekaran, *J. Appl. Electrochem.* **2007**, *37*, 255.

[155] L. Yi, J. Chen, P. Shao, J. Huang, X. Peng, J. Li, G. Wang, C. Zhang, Z. Wen, *Angew. Chem.* **2020**, *132*, 20287.

[156] P. Ding, J. Zhang, N. Han, Y. Zhou, L. Jia, Y. Li, *J. Mater. Chem. A* **2020**, *8*, 12385.

[157] J. Durst, A. Rudnev, A. Dutta, Y. Fu, J. Herranz, V. Kaliginedi, A. Kuzume, A. A. Permyakova, Y. Paratcha, P. Broekmann, *CHIMIA International Journal for Chemistry* **2015**, *69*, 769.

[158] J. Shi, F. Shi, N. Song, J.-X. Liu, X.-K. Yang, Y.-J. Jia, Z.-W. Xiao, P. Du, *J. Power Sources* **2014**, *259*, 50.

[159] V. Singh, H. Muroyama, T. Matsui, K. Eguchi, *Electrochemistry* **2014**, *82*, 839.

[160] T. Ohmori, A. Nakayama, H. Mametsuka, E. Suzuki, *J. Electroanal. Chem.* **2001**, *514*, 51.

[161] R.-G. Ciocarlan, N. Hoeven, E. Irtem, V. Van Acker, M. Mertens, E. M. Seftel, T. Breugelmans, P. Cool, *J. CO_2 Util.* **2020**, *36*, 177.

[162] S. D. Giri, S. M. Mahajani, A. Suresh, A. Sarkar, *Mater. Res. Bull.* **2020**, *123*, 110702.

[163] T. Liu, M. Li, C. Jiao, M. Hassan, X. Bo, M. Zhou, H.-L. Wang, *J. Mater. Chem. A* **2017**, *5*, 9377.

[164] H. Shi, H. Liang, F. Ming, Z. Wang, *Angew. Chem.* **2017**, *129*, 588.

[165] L. Klaas, M. Modibedi, M. Mathe, H. Su, L. Khotseng, *Catalysts* **2020**, *10*, 968.

[166] J. Qi, L. Xin, D. J. Chadderdon, Y. Qiu, Y. Jiang, N. Benipal, C. Liang, W. Li, *Appl. Catal. B: Environ.* **2014**, *154*, 360.

[167] H. Yang, J. J. Kaczur, S. D. Sajjad, R. I. Masel, *ECS Trans.* **2017**, *77*, 1425.

[168] G. Díaz-Sainz, M. Alvarez-Guerra, J. Solla-Gullón, L. García-Cruz, V. Montiel, A. Irabien, *J. CO_2 Util.* **2019**, *34*, 12.

[169] X. Lu, Y. Wu, X. Yuan, L. Huang, Z. Wu, J. Xuan, Y. Wang, H. Wang, *ACS Energy Lett.* **2018**, *3*, 2527.

[170] M. Alvarez-Guerra, A. Del Castillo, A. Irabien, *Chem. Eng. Res. Des.* **2014**, *92*, 692.

[171] S. Narayanan, B. Haines, J. Soler, T. Valdez, *J. Electrochem. Soc.* **2010**, *158*, A167.

[172] H. Li, C. Oloman, *J. Appl. Electrochem.* **2007**, *37*, 1107.

[173] J. Yu, Q. Cao, Y. Li, X. Long, S. Yang, J. K. Clark, M. Nakabayashi, N. Shibata, J.-J. Delaunay, *ACS Catal.* **2019**, *9*, 1605.

[174] J. Yu, Z. Wang, J. Wang, W. Zhong, M. Ju, R. Cai, C. Qiu, X. Long, S. Yang, *ChemSusChem* **2020**, *13*, 5273.

[175] Y. Hu, G. Luo, L. Wang, X. Liu, Y. Qu, Y. Zhou, F. Zhou, Z. Li, Y. Li, T. Yao, *Adv. Energy Mater.* **2021**, *11*, 2002816.

[176] D. Böhm, M. Beetz, M. Schuster, K. Peters, A. G. Hufnagel, M. Döblinger, B. Böller, T. Bein, D. Fattakhova - Rohlfing, *Adv. Funct. Mater.* **2020**, *30*, 1906670.

[177] S. Dresp, T. N. Thanh, M. Klingenhof, S. Brückner, P. Hauke, P. Strasser, *Energy Environ. Sci.* **2020**, *13*, 1725.

[178] J. Rosen, G. S. Hutchings, F. Jiao, *J. Am. Chem. Soc.* **2013**, *135*, 4516.

[179] S. Verma, X. Lu, S. Ma, R. I. Masel, P. J. Kenis, *Phys. Chem. Chem. Phys.* **2016**, *18*, 7075.

[180] J. A. Vega, C. Chartier, W. E. Mustain, *J. Power Sources* **2010**, *195*, 7176.

[181] D. A. Vermaas, W. A. Smith, *ACS Energy Lett.* **2016**, *1*, 1143.

[182] E. Kriegler, N. Bauer, A. Popp, F. Humpenöder, M. Leimbach, J. Strefler, L. Baumstark, B. L. Bodirsky, J. Hilaire, D. Klein, *Global Environ. Chang.* **2017**, *42*, 297.

[183] C. McGlade, P. Ekins, *Nature* **2015**, *517*, 187.

[184] L. Zhang, Z.-J. Zhao, J. Gong, *Angew. Chem. In. Ed.* **2017**, *56*, 11326.

[185] D. D. Zhu, J. L. Liu, S. Z. Qiao, *Adv. Mater.* **2016**, *28*, 3423.

[186] K. Yang, R. Kas, W. A. Smith, *J. Am. Chem. Soc.* **2019**, *141*, 15891.

[187] L. Friedrich, T. Rodrigues, C. S. Neuhaus, P. Schneider, G. Schneider, *Angew. Chem. In. Ed.* **2016**, *55*, 6789.

[188] M. Ma, K. Djanashvili, W. A. Smith, *Angew. Chem. In. Ed.* **2016**, *55*, 6680.

[189] C. Li, B. Jiang, N. Miyamoto, J. H. Kim, V. Malgras, Y. Yamauchi, *J. Am. Chem. Soc.* **2015**, *137*, 11558.

[190] V. Malgras, H. Ataee - Esfahani, H. Wang, B. Jiang, C. Li, K. C. W. Wu, J. H. Kim, Y. Yamauchi, *Adv. Mater.* **2016**, *28*, 993.

[191] G. S. Attard, J. M. Corker, C. G. Göltner, S. Henke, R. H. Templer, *Angew. Chem. Int. Ed. Engl.* **1997**, *36*, 1315.

[192] P. Roy, S. Berger, P. Schmuki, *Angew. Chem. In. Ed.* **2011**, *50*, 2904.

[193] K. Lee, A. Mazare, P. Schmuki, *Chem. Rev.* **2014**, *114*, 9385.

[194] G. K. Mor, K. Shankar, M. Paulose, O. K. Varghese, C. A. Grimes, *Nano Lett.* **2006**, *6*, 215.

[195] N. T. Nguyen, M. Altomare, J. Yoo, P. Schmuki, *Adv. Mater.* **2015**, *27*, 3208.

[196] S. Zhang, F. Peng, H. Wang, H. Yu, S. Zhang, J. Yang, H. Zhao, *Catal. Commun.* **2011**, *12*, 689.

[197] G. Loget, P. Schmuki, *Langmuir* **2014**, *30*, 15356.

[198] S. Huang, Z. Si, X. Li, J. Zou, Y. Yao, D. Weng, *Sensor. Actuat. B-Chem.* **2016**, *234*, 264.

[199] D. Gao, H. Zhou, F. Cai, D. Wang, Y. Hu, B. Jiang, W.-B. Cai, X. Chen, R. Si, F. Yang, S. Miao, J. Wang, G. Wang, X. Bao, *Nano Res.* **2017**, *10*, 2181.

[200] D. Gao, H. Zhou, F. Cai, J. Wang, G. Wang, X. Bao, *ACS Catal.* **2018**, *8*, 1510.

[201] D. Gao, H. Zhou, J. Wang, S. Miao, F. Yang, G. Wang, J. Wang, X. Bao, *J. Am. Chem. Soc.* **2015**, *137*, 4288.

[202] A. Vasileff, C. Xu, Y. Jiao, Y. Zheng, S.-Z. Qiao, *Chem* **2018**.

[203] M. Iqbal, C. Li, K. Wood, B. Jiang, T. Takei, O. m. Dag, D. Baba, A. S. Nugraha, T. Asahi, A. E. Whitten, *Chem. Mater.* **2017**, *29*, 6405.

[204] C. Li, B. Jiang, N. Miyamoto, J. H. Kim, V. Malgras, Y. Yamauchi, *J. Am. Chem. Soc.* **2015**, *137*, 11558.

[205] Y. Zhao, C. Wang, G. G. Wallace, *J. Mater. Chem. A* **2016**, *4*, 10710.

[206] F. Kadirgan, B. Beden, J. M. Leger, C. Lamy, *J. Electroanal. Chem. Interf. Electrochem.* **1981**, *125*, 89.

[207] P. Alexandridis, J. F. Holzwarth, T. A. Hatton, *Macromolecules* **1994**, *27*, 2414.

[208] J. H. Park, N. M. Schneider, D. A. Steingart, H. Deligianni, S. Kodambaka, F. M. Ross, *Nano Lett.* **2018**, *18*, 1093.

[209] H. Wang, L. Wang, T. Sato, Y. Sakamoto, S. Tominaka, K. Miyasaka, N. Miyamoto, Y. Nemoto, O. Terasaki, Y. Yamauchi, *Chem. Mater.* **2012**, *24*, 1591.

[210] A. L. Luna, D. Dragoe, K. Wang, P. Beaunier, E. Kowalska, B. Ohtani, D. Bahena Uribe, M. A. Valenzuela, H. Remita, C. Colbeau-Justin, *J. Phys. Chem. C* **2017**, *121*, 14302.

[211] B. I. Podlovchenko, E. A. Kolyadko, S. Lu, *J. Electroanal. Chem.* **1994**, *373*, 185.

[212] T. Takashima, T. Suzuki, H. Irie, *Electrochemistry* **2019**, *87*, 134.

[213] B. Jiang, X.-G. Zhang, K. Jiang, D.-Y. Wu, W.-B. Cai, *J. Am. Chem. Soc.* **2018**, *140*, 2880.

[214] M. Melchionna, M. V. Bracamonte, A. Giuliani, L. Nasi, T. Montini, C. Tavagnacco, M. Bonchio, P. Fornasiero, M. Prato, *Energy Environ. Sci.* **2018**, *11*, 1571.

[215] A. Bandi, *J. Electrochem. Soc.* **1990**, *137*, 2157.

[216] J. Lee, J. M. Yoo, Y. Ye, Y. Mun, S. Lee, O.-H. Kim, H.-W. Rhee, H. I. Lee, Y.-E. Sung, J. Lee, *Adv. Energy Mater.* **2015**, *5*, 1402093.

[217] B. Jähne, G. Heinz, W. Dietrich, *J. Geophys, Res.-Ocean* **1987**, *92*, 10767.

[218] Z. Liu, X. Zhang, S. Nishimoto, M. Jin, D. A. Tryk, T. Murakami, A. Fujishima, *J. Phys. Chem. C* **2008**, *112*, 253.

[219] J. Zhang, B. Zhou, Q. Zheng, J. Li, J. Bai, Y. Liu, W. Cai, *Water Res.* **2009**, *43*, 1986.

[220] D. Gao, J. Wang, H. Wu, X. Jiang, S. Miao, G. Wang, X. Bao, *Electrochem. Commun.* **2015**, *55*, 1.

[221] M. Mahmood, D. Masheder, C. Harty, *J. Appl. Electrochem.* **1987**, *17*, 1159.

[222] C. Adán, J. Marugán, E. Sánchez, C. Pablos, R. Van Grieken, *Electrochim. Acta* **2016**, *191*, 521.

[223] C. Xiang, A. C. Meng, N. S. Lewis, *Proc. Natl. Acad. Sci.* **2012**, *109*, 15622.

[224] D. Moreira, J. C. Pires, *Bioresource Technol.* **2016**, *215*, 371.

[225] T. R. Anderson, E. Hawkins, P. D. Jones, *Endeavour* **2016**, *40*, 178.

[226] K. Zickfeld, A. H. MacDougall, H. D. Matthews, *Environ. Res. Lett.* **2016**, *11*, 055006.

[227] Q. Lu, F. Jiao, *Nano Energy* **2016**, *29*, 439.

[228] M. Koper, B. Roldan Cuenya, in *Research Needs towards Sustainable Production of Fuels and Chemicals*, Energy-X, 2019, 19.

[229] G. A. El-Nagar, A. M. Mohammad, M. S. El-Deab, B. E. El-Anadouli, *ACS Appl. Mater. Inter.* **2017**, *9*, 19766.

[230] F. Joó, *ChemSusChem* **2018**, *1*, 805.

[231] M. Grasemann, G. Laurenczy, *Energy Environ. Sci.* **2012**, *5*, 8171.

[232] R. Hegner, L. F. Rosa, F. Harnisch, *Appl. Catal. B: Environ.* **2018**, *238*, 546.

[233] X. Lu, Y. Wu, X. Yuan, H. Wang, *Angew. Chem.* **2019**, *131*, 4071.

[234] M. Azuma, K. Hashimoto, M. Hiramoto, M. Watanabe, T. Sakata, *J. Electrochem. Soc.* **1990**, *137*, 1772.

[235] A. S. Agarwal, Y. Zhai, D. Hill, N. Sridhar, *ChemSusChem* **2011**, *4*, 1301.

[236] F. Lei, W. Liu, Y. Sun, J. Xu, K. Liu, L. Liang, T. Yao, B. Pan, S. Wei, Y. Xie, *Nat. Commun.* **2016**, *7*, 1.

[237] Y. Li, J. Qiao, X. Zhang, T. Lei, A. Girma, Y. Liu, J. Zhang, *ChemElectroChem* **2016**, *3*, 1618.

[238] J. Gu, F. Héroguel, J. Luterbacher, X. Hu, *Angew. Chem.* **2018**, *130*, 2993.

[239] C. Chen, Y. Pang, F. Zhang, J. Zhong, B. Zhang, Z. Cheng, *J. Mater. Chem. A* **2018**, *6*, 19621.

[240] E. Hwang, H. Kim, H. Park, T. Lim, Y.-T. Kim, S. H. Ahn, S.-K. Kim, *J. Nanosci. Nanotechnol.* **2017**, *17*, 7547.

[241] B. Zhang, Z. Guo, Z. Zuo, W. Pan, J. Zhang, *Appl. Catal. B: Environ.* **2018**, *239*, 441.

[242] K. Hara, A. Tsuneto, A. Kudo, T. Sakata, *J. Electroanal. Chem.* **1997**, *434*, 239.

[243] H.-K. Lim, H. Shin, W. A. Goddard III, Y. J. Hwang, B. K. Min, H. Kim, *J. Am. Chem. Soc.* **2014**, *136*, 11355.

[244] T. Burdyny, W. A. Smith, *Energy Environ. Sci.* **2019**, *12*, 1442.

[245] C.-T. Dinh, T. Burdyny, M. G. Kibria, A. Seifitokaldani, C. M. Gabardo, F. P. G. De Arquer, A. Kiani, J. P. Edwards, P. De Luna, O. S. Bushuyev, *Science* **2018**, *360*, 783.

[246] H. Li, S. Chen, Y. Zhang, Q. Zhang, X. Jia, Q. Zhang, L. Gu, X. Sun, L. Song, X. Wang, *Nat. Commun.* **2018**, *9*, 1.

[247] J. D. Dwyer, E. J. Diaz, T. E. Webber, A. Katzenberg, M. A. Modestino, E. S. Aydil, *Nanotechnology* **2019**, *30*, 245705.

[248] T. S. Reddy, M. S. Kumar, *RSC Adv.* **2016**, *6*, 95680.

[249] M. Li, Y. Wu, T. Li, Y. Chen, H. Ding, Y. Lin, N. Pan, X. Wang, *RSC Adv.* **2017**, *7*, 48759.

[250] M. Choi, W. William, J. Hwang, D. Yoon, J. Kim, *J. Ind. Eng. Chem.* **2018**, *59*, 160.

[251] Y. Shiga, N. Umezawa, N. Srinivasan, S. Koyasu, E. Sakai, M. Miyauchi, *Chem. Commun.* **2016**, *52*, 7470.

[252] L. Fan, Z. Xia, M. Xu, Y. Lu, Z. Li, *Adv. Funct. Mater.* **2018**, *28*, 1706289.

[253] S. Zhang, P. Kang, T. J. Meyer, *J. Am. Chem. Soc.* **2014**, *136*, 1734.

[254] C. Zhao, J. Wang, *Chem. Eng. J.* **2016**, *293*, 161.

[255] Y. Chen, M. W. Kanan, *J. Am. Chem. Soc.* **2012**, *134*, 1986.

[256] Q. Lv, Q. Meng, W. Liu, N. Sun, K. Jiang, L. Ma, Z. Peng, W. Cai, C. Liu, J. Ge, *J. Phys. Chem. C* **2018**, *122*, 2081.

[257] J. J. Lv, M. Jouny, W. Luc, W. Zhu, J. J. Zhu, F. Jiao, *Adv. Mater.* **2018**, *30*, 1803111.

[258] F. Safizadeh, E. Ghali, G. Houlachi, *Int. J. Hydrogen Energy* **2015**, *40*, 256.

[259] N.-T. Suen, S.-F. Hung, Q. Quan, N. Zhang, Y.-J. Xu, H. M. Chen, *Chem. Soc. Rev.* **2017**, *46*, 337.

[260] J. Liu, Y. Zheng, Z. Wang, Z. Lu, A. Vasileff, S.-Z. Qiao, *Chem. Commun.* **2018**, *54*, 463.

[261] M. Görlin, J. Ferreira de Araújo, H. Schmies, D. Bernsmeier, S. r. Dresp, M. Gliech, Z. Jusys, P. Chernev, R. Kraehnert, H. Dau, *J. Am. Chem. Soc.* **2017**, *139*, 2070.

[262] M. Xie, L. Yang, Y. Ji, Z. Wang, X. Ren, Z. Liu, A. M. Asiri, X. Xiong, X. Sun, *Nanoscale* **2017**, *9*, 16612.

[263] E. Özer, C. Spöri, T. Reier, P. Strasser, *ChemCatChem* **2017**, *9*, 597.

[264] J. Kibsgaard, T. R. Hellstern, S. J. Choi, B. N. Reinecke, T. F. Jaramillo, *ChemElectroChem* **2017**, *4*, 2480.

[265] P. He, X. Y. Yu, X. W. D. Lou, *Angew. Chem.* **2017**, *129*, 3955.

[266] P. Cai, J. Huang, J. Chen, Z. Wen, *Angew. Chem.* **2017**, *129*, 4936.

[267] M. Xie, X. Xiong, L. Yang, X. Shi, A. M. Asiri, X. Sun, *Chem. Commun.* **2018**, *54*, 2300.

[268] J. S. Kim, B. Kim, H. Kim, K. Kang, *Adv. Energy Mater.* **2018**, *8*, 1702774.

[269] H. Yang, C. Wang, Y. Zhang, Q. Wang, *Small* **2018**, *14*, 1703273.

[270] M. Lee, H.-S. Oh, M. K. Cho, J.-P. Ahn, Y. J. Hwang, B. K. Min, *Appl. Catal. B-Environ.* **2018**, *233*, 130.

[271] X.-Y. Yu, Y. Feng, B. Guan, X. W. D. Lou, U. Paik, *Energ. Environ. Sci.* **2016**, *9*, 1246.

[272] S. Keltie, *J. Mater. Chem. A* **2018**, *6*, 24988.

[273] B. Han, A. Grimaud, L. Giordano, W. T. Hong, O. Diaz-Morales, L. Yueh-Lin, J. Hwang, N. Charles, K. A. Stoerzinger, W. Yang, *J. Phys. Chem. C* **2018**, *122*, 8445.

[274] H. Bandal, K. K. Reddy, A. Chaugule, H. Kim, *J. Power Sources* **2018**, *395*, 106.

[275] W. Xia, J. Li, T. Wang, L. Song, H. Guo, H. Gong, C. Jiang, B. Gao, J. He, *Chem. Commun.* **2018**, *54*, 1623.

[276] J. Zhao, X. Ren, Q. Han, D. Fan, X. Sun, X. Kuang, Q. Wei, D. Wu, *Chem. Commun.* **2018**, *54*, 4987.

[277] S. H. Ye, Z. X. Shi, J. X. Feng, Y. X. Tong, G. R. Li, *Angew. Chem. In. Ed.* **2018**, *57*, 2672.

[278] C.-Y. Lee, Y. Zhao, C. Wang, D. R. Mitchell, G. G. Wallace, *Sustain. Energ. Fuels* **2017**, *1*, 1023.

[279] L. Zhuang, L. Ge, Y. Yang, M. Li, Y. Jia, X. Yao, Z. Zhu, *Adv. Mater.* **2017**, *29*, 1606793.

[280] F. Song, X. Hu, *Nat. Commun.* **2014**, *5*, 4477.

[281] F. Yan, C. Zhu, S. Wang, Y. Zhao, X. Zhang, C. Li, Y. Chen, *J. Mater. Chem. A* **2016**, *4*, 6048.

[282] L. S. Zhong, J. S. Hu, H. P. Liang, A. M. Cao, W. G. Song, L. J. Wan, *Adv. Mater.* **2006**, *18*, 2426.

[283] Y. Jin, L. Dang, H. Zhang, C. Song, Q. Lu, F. Gao, *Chem. Eng. J.* **2017**, *326*, 292.

[284] L. Wang, C. Y. Lee, A. Mazare, K. Lee, J. Müller, E. Spiecker, P. Schmuki, *Chem. Eur. J.* **2014**, *20*, 77.

[285] X. Wen, S. Wang, Y. Ding, Z. L. Wang, S. Yang, *J. Phys. Chem. B* **2005**, *109*, 215.

[286] T. Vincent, M. Gross, H. Dotan, A. Rothschild, *Int. J. Hydrogen Energy* **2012**, *37*, 8102.

[287] R. L. Doyle, I. J. Godwin, M. P. Brandon, M. E. Lyons, *Phys. Chem. Chem. Phys.* **2013**, *15*, 13737.

[288] M. E. Lyons, M. P. Brandon, *Phys. Chem. Chem. Phys.* **2009**, *11*, 2203.

[289] L. D. Burke, M. E. Lyons, *J. Electroanal. Chem. Interf. Electrochem.* **1986**, *198*, 347.

[290] R. L. Doyle, M. E. Lyons, *Phys. Chem. Chem. Phys.* **2013**, *15*, 5224.

[291] J. M. V. Nsanzimana, V. Reddu, Y. Peng, Z. Huang, C. Wang, X. Wang, *Chem. Eur. J.* **2018**, *24*, 18502.

[292] P. M. Hallam, M. Gómez-Mingot, D. K. Kampouris, C. E. Banks, *RSC Adv.* **2012**, *2*, 6672.

[293] A. Liu, J. Liu, B. Pan, W.-x. Zhang, *RSC Adv.* **2014**, *4*, 57377.

[294] H. Wang, X. Zhang, Y. Xie, *Mat.Sci. Eng. R* **2018**, *130*, 1.

[295] W. Luo, C. Jiang, Y. Li, S. A. Shevlin, X. Han, K. Qiu, Y. Cheng, Z. Guo, W. Huang, J. Tang, *J. Mater. Chem. A* **2017**, *5*, 2021.

[296] W. D. Chemelewski, J. R. Rosenstock, C. B. Mullins, *J. Mater. Chem. A* **2014**, *2*, 14957.

[297] D. Inohara, H. Maruyama, Y. Kakihara, H. Kurokawa, M. Nakayama, *ACS omega* **2018**, *3*, 7840.

[298] X. Zhang, L. An, J. Yin, P. Xi, Z. Zheng, Y. Du, *Sci. Rep.* **2017**, *7*, 1.

[299] W. Ren, C. Zhao, *Natl. Sci. Rev.* **2020**, *7*, 7.

[300] R. A. Tufa, D. Chanda, M. Ma, D. Aili, T. B. Demissie, J. Vaes, Q. Li, S. Liu, D. Pant, *Appl. Energ.* **2020**, *277*, 115557.

[301] D. Wu, W. Chen, X. Wang, X.-Z. Fu, J.-L. Luo, *J. CO_2 Util.* **2020**, *37*, 353.

[302] J. Medina-Ramos, R. C. Pupillo, T. P. Keane, J. L. DiMeglio, J. Rosenthal, *J. Am. Chem. Soc.* **2015**, *137*, 5021.

[303] B. Ávila-Bolívar, L. García-Cruz, V. Montiel, J. Solla-Gullón, *Molecules* **2019**, *24*, 2032.

[304] W. Lv, J. Zhou, J. Bei, R. Zhang, L. Wang, Q. Xu, W. Wang, *Appl. Surf. Sci.* **2017**, *393*, 191.

[305] R. Zhang, W. Lv, L. Lei, *Appl. Surf. Sci.* **2015**, *356*, 24.

[306] J. Zou, C.-Y. Lee, G. G. Wallace, *Adv. Sci.* **2021**, 2004521.

[307] X. Zhang, X. Hou, Q. Zhang, Y. Cai, Y. Liu, J. Qiao, *J. Catal.* **2018**, *365*, 63.

[308] S. X. Guo, Y. Zhang, X. Zhang, C. D. Easton, D. R. MacFarlane, J. Zhang, *ChemSusChem* **2019**, *12*, 1091.

[309] H. Yang, Z. Chen, P. Guo, B. Fei, R. Wu, *Appl. Catal. B: Environ.* **2020**, *261*, 118240.

[310] W. Ma, R. Ma, J. Wu, P. Sun, X. Liu, K. Zhou, T. Sasaki, *Nanoscale* **2016**, *8*, 10425.

[311] R. Ma, Z. Liu, L. Li, N. Iyi, T. Sasaki, *J. Mater. Chem.* **2006**, *16*, 3809.

[312] D. Pan, S. Ge, J. Zhao, Q. Shao, L. Guo, X. Zhang, J. Lin, G. Xu, Z. Guo, *Dalton T.* **2018**, *47*, 9765.

[313] G. Zhao, C. Li, X. Wu, J. Yu, X. Jiang, W. Hu, F. Jiao, *Appl. Surf. Sci.* **2018**, *434*, 251.

[314] L. Wu, L. Yu, F. Zhang, D. Wang, D. Luo, S. Song, C. Yuan, A. Karim, S. Chen, Z. Ren, *J. Mater. Chem. A* **2020**, *8*, 8096.

[315] C. Wu, H. Li, Z. Xia, X. Zhang, R. Deng, S. Wang, G. Sun, *ACS Catal.* **2020**, *10*, 11127.

[316] J. Yang, X. Wang, Y. Qu, X. Wang, H. Huo, Q. Fan, J. Wang, L. M. Yang, Y. Wu, *Adv. Energy Mater.* **2020**, *10*, 2001709.

[317] H. Xiang, H. A. Miller, M. Bellini, H. Christensen, K. Scott, S. Rasul, H. Y. Eileen, *Sustain. Energy Fuels* **2020**, *4*, 277.

[318] U. O. Nwabara, A. D. Hernandez, D. A. Henckel, X. Chen, E. R. Cofell, M. P. De-Heer, S. Verma, A. A. Gewirth, P. J. Kenis, *ACS Appl. Energ. Mater.* **2021**, *4*, 5175.

[319] J. Hussain, H. Jónsson, E. Skúlason, *ACS Catal.* **2018**, *8*, 5240.

[320] M. R. Singh, J. D. Goodpaster, A. Z. Weber, M. Head-Gordon, A. T. Bell, *PNAS* **2017**, *114*, E8812.

[321] Z. Tian, C. Priest, L. Chen, *Adv. Theory Simul.* **2018**, *1*, 1800004.

[322] A. KS, N. Chandrasekaran, V. Chakrapani, *Front. Chem.* **2020**, *8*, 137.

[323] M. Dunwell, X. Yang, B. P. Setzler, J. Anibal, Y. Yan, B. Xu, *ACS Catal.* **2018**, *8*, 3999.

[324] Y. Zhu, J. Wang, H. Chu, Y.-C. Chu, H. M. Chen, *ACS Energy Lett.* **2020**, *5*, 1281.

[325] K. Yang, R. Kas, W. A. Smith, T. Burdyny, *ACS Energy Lett.* **2020**, *6*, 33.

[326] J. E. Huang, F. Li, A. Ozden, A. S. Rasouli, F. P. G. de Arquer, S. Liu, S. Zhang, M. Luo, X. Wang, Y. Lum, *Science* **2021**, *372*, 1074.

[327] L. Tijing, Y. Woo, M. Yao, J. Ren, H. Shon, *Comprehensive Membrane Science and Engineering; Elsevier: Oxford, UK* **2017**, 418.

[328] S. Sarp, N. Hilal, *Membrane-based salinity gradient processes for water treatment and power generation*, Elsevier, 2018.

[329] T. Sata, *Ion exchange membranes: preparation, characterization, modification and application*, Royal Society of chemistry, 2007.

Appendix Permission Letter

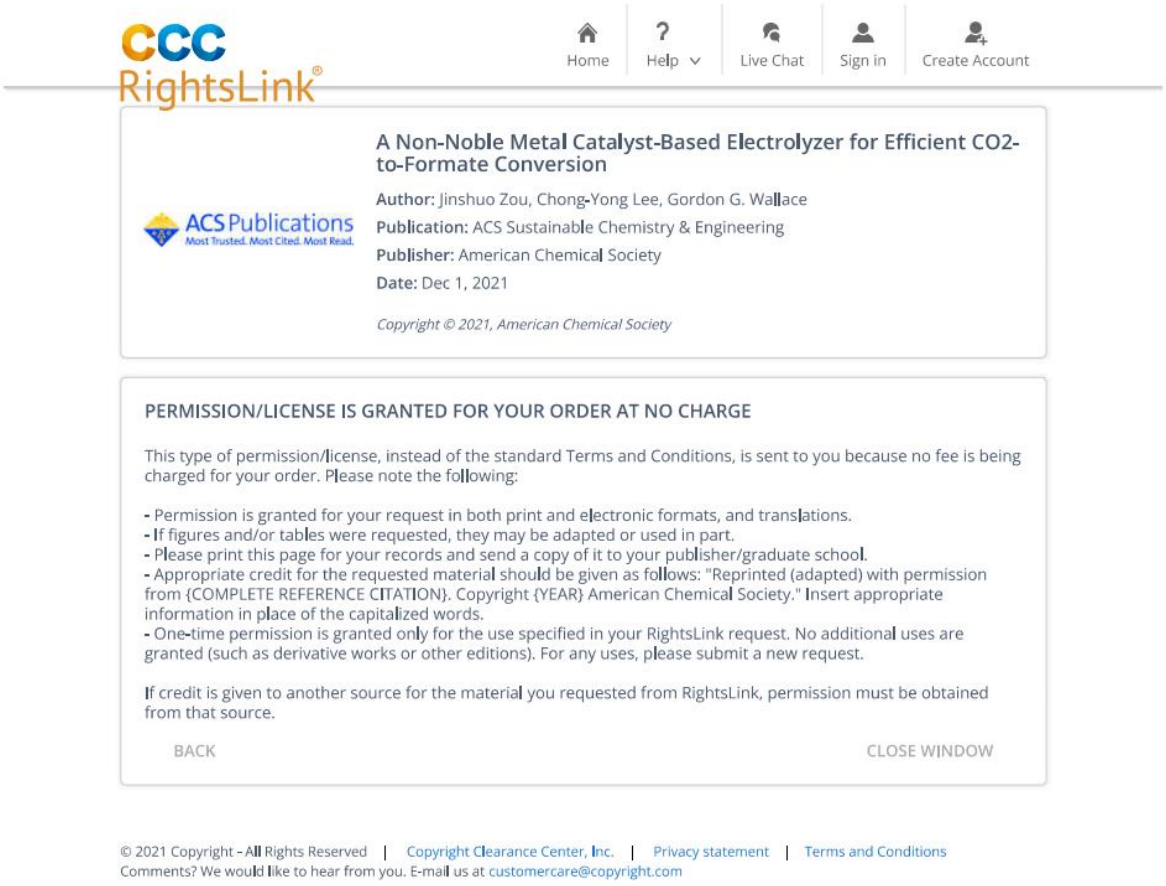

CCC RightsLink

Home | Help | Live Chat | Sign in | Create Account

ACS Publications
Most Trusted. Most Cited. Most Read.

A Non-Noble Metal Catalyst-Based Electrolyzer for Efficient CO2-to-Formate Conversion

Author: Jinshuo Zou, Chong-Yong Lee, Gordon G. Wallace

Publication: ACS Sustainable Chemistry & Engineering

Publisher: American Chemical Society

Date: Dec 1, 2021

Copyright © 2021, American Chemical Society

PERMISSION/LICENSE IS GRANTED FOR YOUR ORDER AT NO CHARGE

This type of permission/license, instead of the standard Terms and Conditions, is sent to you because no fee is being charged for your order. Please note the following:

- Permission is granted for your request in both print and electronic formats, and translations.
- If figures and/or tables were requested, they may be adapted or used in part.
- Please print this page for your records and send a copy of it to your publisher/graduate school.
- Appropriate credit for the requested material should be given as follows: "Reprinted (adapted) with permission from {COMPLETE REFERENCE CITATION}. Copyright {YEAR} American Chemical Society." Insert appropriate information in place of the capitalized words.
- One-time permission is granted only for the use specified in your RightsLink request. No additional uses are granted (such as derivative works or other editions). For any uses, please submit a new request.

If credit is given to another source for the material you requested from RightsLink, permission must be obtained from that source.

BACK CLOSE WINDOW